INSTITUTO POTOSINO DE INVESTIGACIÓN CIENTÍFICA Y TECNOLÓGICA, A.C.

POSGRADO EN GEOCIENCIAS APLICADAS

Nature of Petrological, Geochemical, Geochronological Settings and Evolution of Bundelkhand Greenstone Complexes in the Bundelkhand Craton, India

Tesis que presenta

Pradip Kumar Singh

Para obtener el grado de

Doctor en Geociencias Aplicadas

Director de la Tesis

Dr. Sanjeet Kumar Verma

San Luis Potosí, S.L.P., 11 Julio 2019

IPICYT

Constancia de aprobación de la tesis

La tesis ***"Nature of Petrological, Geochemical, Geochronological Settings and Evolution of Greenstone Complexes in the Bundelkhand Craton, India"*** presentada para obtener el Grado de Doctor en Geociencias Aplicadas, fue elaborada por **Pradip Kumar Singh** y aprobada el once de julio del dos mil diecinueve por los suscritos, designados por el Colegio de Profesores de la División de Geociencias Aplicadas del Instituto Potosino de Investigación Científica y Tecnológica, A.C.

Dr. Sanjeet Kumar Verma
Director de la tesis

Dr. Aaron James Martin
Miembro del Comité Tutoral

Dr. Elson Paiva Oliveira
Miembro del Comité Tutoral

Dr. Surendra Pal Verma
Miembro del Comité Tutoral

Créditos Institucionales

- Esta tesis fue elaborada en el Laboratorio de la División Geociencias Aplicadas del Instituto Potosino de Investigación Científica y Tecnológica, A.C., bajo la dirección del Dr. Sanjeet Kumar Verma.
- Durante la realización del trabajo el autor recibió una beca académica del Consejo Nacional de Ciencia y Tecnología (No. 612752) y del Instituto Potosino de Investigación Científica y Tecnológica, A. C.
- Becas mixtas 2017 movilidad en el extranjero del Consejo Nacional de Ciencia y Tecnología (No. 291212), ha sido elegido para participar en una estancia de investigación en Universidade Estadual de Campinas (UNICAMP), Brasil.
- Department of Geology, Institute of Earth Sciences, Bundelkhand University, Jhansi, India.
- Department of Geology and Natural Resources, Institute of Geosciences, University of Campinas – UNICAMP, Campinas, São Paulo, Brazil.
- Newton Advance Fellowship, The Royal Society, United Kingdom.
- Unidad de Geocronología, CAI de Ciencias de la Tierra y Arqueometría, Facultad de Ciencias Geológicas, Universidad Complutense de Madrid, Spain.
- Wadia Institute of Himalayan Geology, Dehradun, India.
- Association of Applied Geochemist (AAG) and Australian Laboratory Services Pty. Ltd., Malaga, Western Australia, Australia.

IPICYT

Instituto Potosino de Investigación Científica y Tecnológica, A.C.

Acta de Examen de Grado

El Secretario Académico del Instituto Potosino de Investigación Científica y Tecnológica, A.C., certifica que en el Acta 009 del Libro Primero de Actas de Exámenes de Grado del Programa de Doctorado en Geociencias Aplicadas está asentado lo siguiente:

En la ciudad de San Luis Potosí a los 11 días del mes de julio del año 2019, se reunió a las 10:30 horas en las instalaciones del Instituto Potosino de Investigación Científica y Tecnológica, A.C., el Jurado integrado por:

Dr. Surendra Pal Verma	**Presidente**	**UNAM**
Dr. Elson Paiva Oliveira	**Secretario**	**UNICAMP**
Dr. Aaron James Martin _	**Sinodal**	**IPICYT**
Dr. Sanjeet Kumar Verma _	**Sinodal**	**IPICYT**

a fin de efectuar el examen, que para obtener el Grado de:

DOCTOR EN GEOCIENCIAS APLICADAS

sustentó el C.

Pradip Kumar Singh

sobre la Tesis intitulada:

Nature of Petrological, Geochemical, Geochronological Settings and Evolution of Greenstone Complexes in the Bundelkhand Craton, India

que se desarrolló bajo la dirección de

Dr. Sanjeet Kumar Verma _

El Jurado, después de deliberar, determinó

APROBARLO

Dándose por terminado el acto a las 12:00 horas, procediendo a la firma del Acta los integrantes del Jurado. Dando fe el Secretario Académico del Instituto.

A petición del interesado y para los fines que al mismo convengan, se extiende el presente documento en la ciudad de San Luis Potosí, S.L.P., México, a los 11 días del mes de julio de 2019.

Dr. Marcial Bonilla Marín
Secretario Académico

Mtra. Ivonne Lizette Cuevas Vélez
Jefa del Departamento del Posgrado

INSTITUTO POTOSINO DE INVESTIGACIÓN CIENTÍFICA Y TECNOLÓGICA, A.C.
IPICYT
SECRETARIA ACADEMICA

Dedications

मेरी मातृका और मेरे माता-पिता को समर्पित

Dedicated to my grandmother and my parents

Dedicado a mi abuela y a mis padres

Acknowledgements

First of all, I give thanks, praise and honor to Paramātmā who makes all things possible.

I would like to thank and acknowledge my parents Śrīmatī Pushpa Devī and Śrī Paraśhurām Singh. They have been and still are my best (and First) gurus, apart from being the greatest source of love, support and inspiration in my life.

I owe profound thanks to my supervisor, Dr. Sanjeet Kumar Verma, for his patience, encouragement, kindness and generosity. Verma always found time to share his vast and deep knowledge of geology in a highly intelligible manner with me. His enthusiasm for geology was decidedly infectious and I hope that towards the later stages of my thesis he found mine to be as well. Without Dr. Verma's support, scientific, moral and monetary, it is highly doubtful that I would have finished this thesis. I also thank Dr. Renu Verma, Verma's wife, for hosting us at their place on various occasions and her exceptional kindness.

Thanks to my friend Dr. Courtney G. Parkins-Ferrón. His unwavering support, guidance, encouragement and English language training that immensely help me for completing this thesis. I would not have been able to improve my language and writing skills without his help. And also thanks for helping me to improve my public speaking skills and speaks lower during presentations.

Thanks to Prof. Vinod Kumar Singh for his spirited and guiding discussions and geologic expertise relevant to my research, which simultaneously echoed the past when I was a student of his at the Bundelkhand University and later a research collaborator. His support and guidance enormously valuable during field works in the research area. I also would especially thank Singh's wife Radha Singh for kindly hosting me at the Bundelkhand University and her constant support and love.

Thanks to Prof. Elson Paiva Oliveira for providing the direction, geochronological expertise, and support during my doctoral stay at University of Campinas, Brazil. I have greatly benefitted from his mentorship and guidance throughout my time in the institute, and truly feel that I have grown not only as a geologist but as a scientist in general. I am also grateful to Dr. Marcos Pereira and Drs. Veronica and Paola for their hospitality and great help during stay at the university.

Thanks to my doctoral committee members Dr. Aaron Martin, Dr. Juan Antonio Moreno, Prof. Vinod Kumar Singh, Prof. Elson Paiva Oliveira and Prof. Surendra Pal Verma for their valuable guidance and suggestions, and for regularly reminding me of the need to complete my thesis in a firm, but gentle manner. I would especially thank Dr. Juan for his energetic and guiding discussions relevant to my research

during manuscripts preparation. I thank Dr. Aaron for valuable suggestions and comments during semestral assessment. I also thank Prof. Verma for his teaching and for sharing his knowledge on analytical geochemistry and geology in general.

Thanks to my IPICYT colleagues for all their encouragement and support: Drs. Yadira Jazmín Mendoza Chávez, Cecilia Reyes, Sócrates Figueroa Miranda, Darío Torres Sánchez, Vivian Ruiz Mendoza, Lorena Elisa, Maria Mercedes and Dr. Sonia.

Thanks to every person at IPICYT, for their contributions, whether small or big, to my amazing experience. The last three years at IPICYT, within the Division of Applied Geosciences, have been life altering. Although IPICYT is an academic and research institution, and I have been here to research, my time here has meant so much more to me. It has enriched my life with friendships, opportunity, adventure and passion. I would particularly like to thank Dr. Jose Alfredo Ramos, Dr. Pablo Davila Harris, Dr. Omar Delgado, Dr. Nadia Valentina, Dr. Héctor López Loera. I am also thankful to Ivonne Lizette Cuevas Velez and Edith Rodriguez Delgadillo for their speedy help and support.

Thanks to my uncle and informal mentor, lieutenant Pritesh Singh, who has never stopped enquiring about my academic progress and offering his thoughtful advice. It has kept my feet in an even place.

Thanks to my friend, Keren Gurrion. She always made her apartment and hotel in Huatulco available to me when I needed it to spend the holidays in a beautiful and pleasant place, away from the crowd.

Thanks to Ramesh Singh, Pooja Singh, Shivam Sachan, Dr. Kailash Singh, Dr. Saurabh Singh, Sanjeet Sharma, Praveen Sharma, Prof. Trilok Nath Singh, Prof. Divya Prakash, Prof. Arun Jaitly, Prof. Nanhi Singh, Prof. Vijay Singh, Prof. Nand Lal Singh, Dr. Vishal Vikram, Dr. Vivek Malviya Shivkumar Singh, Martin Almendarez Gomez, Hasan Ansari, Shateesh, Rajan Gangaputra, Gurvindar Singh, Dr. Carmen Galindo Francisco, Dr. Jose Manuel Fuenlabrada Perez, Dr. Erica, Drs. Margrates, Dr. Mauricio, Drs. Bia, Drs. Paola, Ankur Gupta, Chaheta Gupta, Tankush Sardhana, Neeraj Chaudhary, Eloisa, Shivam Savita, Patricia and Sumit Misra for their help and moral support.

Finally, thanks to my brothers, Pravin and Sandeep and my sister-in-law, Pratima and Rima, for their inimitable support. My brother, Pravin, in particular, kept me motivated and enthusiastic. And, also thanks to all the other people who help and support me.

Contents

Constancia de aprobación de la tesis **ii**
Créditos institucionales **iii**
Acta de examen **iv**
Dedications **v**
Acknowledgements **vi**
Contents **viii**
List of Tables **xiii**
List of Figures **xiv**
Abstract **xix**
Resumen **xxiii**

Introduction

Introduction

1. Introduction **1**
   1.1. Research objectives of the PhD project **7**
   1.2. Hypothesis **8**
      1.2.1. Testing of hypothesis **9**
   1.3. Thesis outline **9**
References **12**

Chapter 1

Geological Setting of Central Bundelkhand Greenstone Complex

1. Regional geology and tectonic framework **18**
2. Lithological units, metamorphic events and mineral deposits of the CBGC **26**
   2.1. Lithologies **26**
      2.1.1. TTG gneisses **26**
      2.1.2. Greenstone sequences **31**
      2.1.3. Granodiorites and sanukitoids **36**

2.1.4. Anatectic granites **40**
2.2. Metamorphic events **42**
2.3. Mineral deposits in the Bundelkhand Craton **43**
References **45**

Chapter 2

Geochemistry and Sm–Nd isotope systematics of mafic-ultramafic rocks from the Babina and Mauranipur greenstone belts **49**

Abstract **50**
1. Introduction **50**
2. Geological Setting **52**
3. Geology and field description of the Babina and Mauranipur greenstone belts **54**
3.1. Babina greenstone belt **54**
3.2 Mauranipur greenstone belt **54**
4. Petrography and mineralogy **54**
4.1. Mafic rock–Babina greenstone belt **54**
4.2. Mafic rock–Mauranipur greenstone belt **54**
4.3. Ultramafic rocks–Babina and Mauranipur greenstone belts **54**
4.4. Ultramafic cumulate from the Mauranipur greenstone belt **54**
5. Analytical procedures **55**
5.1. Whole rock geochemistry **56**
5.2. Sm–Nd isotope systematics **56**
6. Results **56**
6.1. Major and trace elements geochemistry **56**
6.2. Sm–Nd isotopic data **57**
7. Discussion **58**
7.1. Effect of post-magmatic alteration **58**
7.2. Fractional crystallization and crustal contamination **61**
7.3. Mafic rocks and mantle source characteristic **62**

7.4. Geochronological aspects **63**
7.5. Geodynamic evolution and tectonic setting of the Babina and Mauranipur greenstone belts **63**
7.6. Period of Archean mafic emplacement of Indian cratons **65**
8. Conclusions **65**
Acknowledgements **65**
References **66**

Chapter 3

Geochemistry and petrogenesis of sanukitoids and high-K anatectic granites **68**

Abstract **69**
1. Introduction **69**
2. Geological Setting **72**
3. Sampling, field relationships and petrography **73**
3.1. Sanukitoids (s.l.) **73**
3.2. High-K anatectic granites **74**
4. Analytical methods **74**
4.1. Whole-rock geochemistry **74**
4.2. Zircon U–Pb dating **74**
4.3. Sm–Nd isotopes **75**
5. Results **75**
5.1. Whole-rock geochemistry **75**
5.1.1. Sanukitoids (s.l.) **75**
5.1.2. High-K anatectic granites **76**
5.2. Zircon U–Pb dating **79**
5.3. Whole-rock Sm–Nd isotopes **79**
6. Discussion **80**
6.1. Late Archean magmatism in the Bundelkhand Craton **80**
6.2. Petrogenesis **80**
6.2.1. Sanukitoids (s.l.) **80**
6.2.2. High-K anatectic granites **82**

6.3. Tectonic settings and geodynamics for the late-Archean evolution in the Bundelkhand Craton
6.3.1. Tectonic setting **83**
6.3.2. Geodynamic model **83**
6.4. Comparison with other Archean cratonic terrains: implications for late-Archean crustal evolution **83**
7. Conclusion **83**
Conflict of interest **86**
Acknowledgements **86**
References **86**
87

Chapter 4

Zircon geochronology, geochemistry and petrogenesis of the TTG gneisses and high-K granitoids **89**
Abstract **90**
1. Introduction **93**
2. Geological background **98**
3. Sample description and petrography **105**
3.1. Paleoarchean TTG gneiss **106**
3.2. Neoarchean TTG gneiss **108**
3.3. High-K granitoids **110**
4. Analytical techniques **110**
4.1. Zircon CL imaging and LA–ICP–MS U–Pb dating **110**
4.2. Whole-rock elements **111**
4.3. TIMS Sm–Nd isotope bulk-rock analyses **112**
5. Results **112**
5.1. Zircon CL images and U–Th–Pb systematics **112**
5.1.1. Paleoarchean TTG gneiss **113**
5.1.2. Neoarchean TTG gneiss **118**
5.1.3. Neoarchean High-K granitoids **120**
5.2. Whole-rock geochemistry **121**

5.2.1. Major elements **121**
5.2.2. Trace elements **123**
5.3. Whole-rock Sm–Nd systematics **124**
6. Discussion **127**
6.1. Geochronology, zircon inheritance and metamorphic events **127**
6.2. Petrogenesis **136**
6.2.1. TTG gneiss **136**
6.2.2. High-K granitoids **142**
6.3. Implications for crustal evolution and reworking **143**
6.4. Comparison with Archean cratons globally **150**
7. Conclusions **154**
Acknowledgements **156**
References **157**

Chapter 5

Conclusions **167**

Appendices **170**

List of Tables

Chapter 1

Table 1. Lithostratigraphic units of the BC. **23**

Chapter 2

Table 1. Geodynamic features of the Bundelkhand Craton. **52**

Table 2. Sm-Nd isotopes data on mafic-ultramafic rocks from the Babina and Mauranipur greenstone belts, Bundelkhand Craton, India. **56**

Table 3. The list of Indian cratons and their previous records of mafic-ultramafic rocks. **65**

Chapter 3

Table 1. Major lithostratigraphic units of the Bundelkhand Craton inferred from previous literature discussed in the text. **71**

Table 2. Sample description, locality and GPS coordinates of the sanukitoids (s.l.) and high-K anatectic granites of the BC **72**

Table 3. Results of U-Pb dating of zircons on sanukitoids (s.l.). **81**

Table 4. Sm-Nd isotopic data for sanukitoids (s.l.). **82**

Chapter 4

Table 1. Sample locations, description, petrography and summary of LA-ICP-MS U-Pb zircon results obtained from TTG gneisses and high-K granitoids in the CBGGT. **104**

Table 2. TIMS whole-rock Sm–Nd isotopic data for TTG gneisses and high-K granitoids from the CBGGT. **127**

List of Figures

Introduction

Figure 1. World cratonic map showing exposed Archean terranes **2**

Figure 2. Generalized geological map of the Indian shield **5**

Figure 3. Geology map of the Bundelkhand Craton. **6**

Chapter 1

Figure 1. Generalized geological map of the Indian shield. **19**

Figure 2. Geological map of the Bundelkhand Craton. **21**

Figure 3. Detailed Geological map of the CBGC. **27**

Figure 4. Representative field photographs and photomicrographs of TTG gneisses from the CBGC. **30**

Figure 5. Representative field photographs and photomicrographs of the greenstone sequences. **33**

Figure 6. Representative field photographs and photomicrographs of sanukitoids and granodiorites. **38**

Figure 7. Representative field photographs and photomicrographs of anatectic granites. **41**

Chapter 2

Figure 1. Geological map of India showing Archean cratons, Tectonic Divisions, and simplified map of the Bundelkhand Craton. **51**

Figure 2. Geological maps of the Babina and Mauranipur greenstone belts, Bundelkhand Craton. **53**

Figure 3. Representative field photographs and photomicrographs from the Babina and Mauranipur greenstone belts, Bundelkhand Craton. **55**

Figure 4. Sample classification in the TAS diagram, Nb/Y vs. Zr/Ti diagram and muti-dimensional (*MagClaMSys*) classification Diagram for the mafic-ultramafic rocks of the Babina and Mauranipur greenstone belts, Bundelkhand Craton. **57**

Figure 5. Fenner's binary diagram showing moderate to strong fractionation trends for selected major elements oxide versus MgO. **58**
Figure 6. Fenner's binary diagram showing correlation for selected trace elements versus MgO. **59**
Figure 7. Primitive mantle-normalized multi-element plots and chondrite-normalized rare-earth element plots for the Babina and Mauranipur greenstone belts, BC. **60**
Figure 8. Sm-Nd whole-rock isochron for mafic-ultramafic rocks from the Babina greenstone belt, Bundelkhand Craton. **61**
Figure 9. Cr vs. Ni, and Cr vs. V bi-variate diagrams. **61**
Figure 10. MgO vs. $\varepsilon_{Nd}t$, and SiO_2 vs. εNdt bi-variate diagrams for the mafic-ultramafic rocks from the Babina and mafic rocks from the Mauranipur greenstone belts **62**
Figure 11. Petrogenetic modelling of the Nb/Yb–Th/Yb projection. **63**
Figure 12. Time (Ga) vs. $\varepsilon_{Nd}t$, composition of komatiites and mafic-ultramafic rocks. **63**
Figure 13. (a-b) Application of log–ratio transformed immobile trace element–based discriminant function DF1–DF2 discrimination diagrams. (c) Primitive mantle normalized Nb/Th vs. Nb/La diagram. (d) Bivariate TiO_2 vs. Al_2O_3/TiO_2 discrimination diagram for mafic-ultramafic rocks from the Babina and Mauranipur greenstone belts. **64**
Figure 14. Schematic cartoon representing the geodynamic evolution of the Babina and Mauranipur greenstone belts. **65**

Chapter 3

Figure 1. Generalized geological map of the Indian shield with Archean cratonic blocks. **70**
Figure 2. Simplified geological map of the Bundelkhand Craton. **71**
Figure 3. Representative field photographs, field relationships, and rock textures of sanukitoids (s.l.) and high-K anatectic

granites. **73**
Figure 4. Representative photomicrographs. **74**
Figure 5. TAS (total alkalis vs. SiO2) diagram and ternary diagram ((Na2O/K2O)–2 * A/CNK (molar Al2O3/[CaO+Na2O+K2O])–2 * [(FeOt+MgO) wt.% * (Sr+Ba) wt.%] =FMSB)) for sanukitoids (s.l.) and high-K anatectic granites. **75**
Figure 6. Composition of the Bundelkhand sanukitoids (s.l.) and high-K anatectic granites intrusions presented in: (a) SiO2 vs. MALI-index; (b) SiO2 vs. (FeOt/(FeOt+MgO); (c) A/CNK [Al2O3/(CaO+Na2O+K2O)] vs. SiO2 and (d) K2O vs. SiO2 diagrams. **76**
Figure 7. Hacker's binary plots for selected major elements for sanukitoids (s.l.) and high-K anatectic granites, as well as average plots of sanukitoids from other cratonic bodies. **77**
Figure 8. Binary diagrams for selected trace elements vs. SiO2 for sanukitoids (s.l.) and high-K anatectic granites, and average data of various cratonic bodies also plotted. **78**
Figure 9. Primitive mantle-normalized multi element and chondrite-normalized REE plots for the Bundelkhand sanukitoids. **79**
Figure 10. Primitive mantle-normalized multi element and chondrite-normalized REE plots for the Bundelkhand high-K anatectic granites. **79**
Figure 11. CL and BSE images of zircon, U-Pb Disconcordia and Concordia plots for sample BC-16-18 **80**
Figure 12. εNd(t) vs. formation age (in Ma) diagram for late-Archean Bundelkhand sanukitoids (s.l.) and anatectic granites. **82**
Figure 13. Classification diagrams of Sanukitoids (s.l.) and high-K anatectic granites. **83**
Figure 14. Relationships between Th/Nb, La/Nb and Ce/Pb in the Bundelkhand Craton granitoids. **84**
Figure 15. Major element–based multidimensional discrimination and

immobile trace element–based multidimensional discrimination diagrams for the acid rocks. **84**

Figure 16. Schematic, conceptual cartoon illustrating the proposed geodynamic model for evolution of late-Archean rocks in the Bundelkhand Craton. **85**

Figure 17. Exposed Archean cratons and late-Archean geologic events distribution of various cratonic terrains. **86**

Chapter 4

Figure 1. Schematic geological map of the Indian shield showing major Precambrian cratons and Phanerozoic outcrops and geological outline map of the BC. **95**

Figure 2. Geological map of the CBGGT, central part of the BC showing the sample locations. **97**

Figure 3. Demonstrative field photos of the TTG gneisses and high-K granitoids of the CBGGT. **107**

Figure 4. Representative photomicrographs. **109**

Figure 5. Representative CL and BSE images of zircons for TTG gneisses and high-K granitoids of the CBGGT. **114**

Figure 6. Zircon U–Pb Concordia diagrams for TTG gneisses from the CBGGT. **116**

Figure 7. Zircon U–Pb Concordia diagrams for TTG gneisses and high-K granitoids from the CBGGT in the BC. **119**

Figure 8. TAS (total alkalis vs. SiO2) diagram, Normative Ab-An-Or triangular diagram and ternary diagram and ((Na_2O/K_2O)–2 * A/CNK (molar $Al_2O_3/[CaO+Na_2O+K_2O]$)–2* [(FeO_t+MgO) wt.% * (Sr+Ba) wt.%] =FMSB)). **125**

Figure 9. (a) SiO_2 vs. MALI-index; (b) SiO_2 vs. ($FeO_t/(FeO_t+MgO)$; (c) A/CNK[$Al_2O_3/(CaO+Na_2O+K_2O)$] vs. SiO_2 and (d) K_2O vs. SiO_2 diagrams. **126**

Figure 10. Hacker's binary plots for selected major elements for TTG gneisses and high-K granitoids. **128**

Figure 11. Chondrite-normalized REE patterns and Primitive mantle-normalized multi element plots. **129**

Figure 12. (a) $\varepsilon_{Nd}(t)$ *vs.* MgO. (b) $\varepsilon_{Nd}(t)$ *vs.* SiO_2. (c) $\varepsilon_{Nd}(t)$ *vs.* formation age (in Ma). **130**

Figure 13. Classification diagrams for TTG gneisses and high-K granitoids. **137**

Figure 14. Sr/Y *vs.* Y and $(La/Yb)_N$ *vs.* versus $(Yb)_N$ diagrams. **139**

Abstract

Nature of Petrological, Geochemical, Geochronological Settings and Evolution of Bundelkhand Greenstone Complexes in the Bundelkhand Craton, India

This doctoral thesis describes the geology, petrography, geochemistry, mineralogy, Sm–Nd isotope geochemistry and geochronology of mafic–ultramafic rocks, TTG (tonalite-trondhjemite-granodiorite) gneisses and high-K granitoids to decipher the nature and origin of the geodynamic changes that took place between ~3.59 and 2.50 Ga in the Central Bundelkhand Greenstone Complex (CBGC), Bundelkhand Craton (BC), India. The CBGC consists of mainly two greenstone belts: (1) the Babina greenstone belt (2) the Mauranipur greenstone belt. The petrography and mineral assemblages of these mafic–ultramafic volcanic rocks indicate that they experienced greenschist to amphibolite facies metamorphism. The mafic volcanic rocks from the Babina belt are characterized by SiO_2 = 43.9–51.2 wt%, MgO = 5.4–11.0 wt% and Mg# = 44–77 [Mg# = 100 × (Mg^{2+}/(Mg^{2+} + Fe^{2+}))], whereas those from the Mauranipur belt are characterized by higher silica (51.8–55.6 wt%), MgO = 6.9–9.5 wt% and Mg# = 59–70. The ultramafic rocks of the Babina and Mauranipur belts contain SiO_2 = 46.9–50.3 wt%, MgO = 20.2–21.1 wt% and Mg# = 77–82. The Babina mafic rocks show a nearly flat REE and HFSE profile [$(La/Yb)_{CN}$ = 0.87–1.40] with negative Nb (Nb/Nb^* = 0.13–0.77) and positive Pb anomalies that could be attributed to subduction-related metasomatic agents. On the other hand, the Mauranipur mafic rocks have total REE (26.0–40.7 ppm) and display flat chondrite normalized LREE [$(La/Yb)_{CN}$ = 1.1–1.7; $(La/Sm)_{CN}$ = 1.1–2.0] with no Eu anomalies (Eu/Eu* = 0.89–

1.0) and negative Nb anomalies (Nb/Nb* = 0.13–0.77), which are most probably the effects of crustal contamination. Additionally, the whole-rock isotopic (Sm–Nd) data of the mafic–ultramafic volcanic rocks from the Babina belt yield an isochron age of ~3.44 Ga, which represents the first estimation of the age of these rocks. Isotopic and geochemical characteristics of mafic–ultramafic volcanic rocks of the CBGC reveal that they were generated from a mantle source with long-term depletion. The outcrops mafic–ultramafic volcanic rocks in the Babina and Mauranipur belts are remnants of oceanic crust possibly emplaced in a subduction-related setting.

LA-SF-ICP-MS zircon dating reveals that TTG magmatism mainly developed around ~3.51–3.20 Ga at regular intervals of 100 Myr although it has also found evidence of younger Neoarchean TTG magmatism at 2.71–2.67 Ga. In addition, TTG and mafic–ultramafic magmatisms suggest contemporary felsic plutonism and mafic volcanism at ~3.44 Ga. Subsequently, high-K granitoids magmatism (sanukitoids and anatectic granites) occurred during the two discrete episodes during Neoarchean between ~2.58 and 2.50 Ga and suggest synchronous emplacement. These high-K granitoids commonly represent the last Archean magmatic event represented by large scale crustal melting (anatexis) that seems to be related to the final stabilization of the craton. The TTG gneisses and high-K granitoids contain inherited zircons, which suggest the participation of ancient crust in their origin. In addition, the combined zircon CL images and U–Pb data allowed unraveling different metamorphic events/overprint at ~3.31–3.10 Ga and 2.64 Ga that may have formed mainly by recrystallization in the BC.

Paleoarchean TTG gneisses display SiO_2 (64–73 wt%) and Neoarchean TTG gneisses contain SiO_2 (66–74 wt%). In contrast, sanukitoids show a range of SiO_2

contents from 61 to 71 wt.% and anatectic granites display high content of SiO_2 from 70 to 78 wt.%. The Paleoarchean TTG gneisses are characterized by moderate to high total REE (78–319 ppm) and moderately fractionated REE patterns [$(La/Yb)_{CN}$ = 3.88–41.12] with variable negative Eu anomalies. In contrast, Neoarchean TTG gneisses contain moderate total REE (107–142 ppm) and strongly fractionated REE patterns [$(La/Yb)_{CN}$ = 9.83–26.44] without any significant Eu anomalies signifying the role of garnet in source residue. Sanukitoids are characterized by enrichment in the LREE compared with the HREE and show a clear LREE/HREE fractionation, whereas anatectic granites display enrichment in the LREE with respect to the HREE with strong to moderate negative Eu anomalies. In the Primitive Mantle (PM) normalized incompatible elements diagram, Paleoarchean TTG gneiss samples show enrichment in Ba, U, K and Pb and slightly elevated values for Sr, and Zr, with large negative Nb and Ti anomalies and weak negative Ce, P and Ta anomalies. A similar pattern also recognized in Neoarchean TTG gneisses and high-K granitoids, which suggest for subduction-related origin.

The values of $\varepsilon_{Nd}(t)$ ranging from +4.3 to +0.3 (excepting one sample showing –0.5) along with their whole-rock geochemical nature indicate that the low-HREE type TTGs were produced through melting of subducted oceanic arc crust at different depths which probably interacted variably with felsic crustal melts in a stability fields of garnet and ilmenite, probably plagioclase-free source. On the other hand, high-HREE type TTG suggest a likely originated from a plagioclase and garnet-amphibolite at low pressure. Further, a Neoarchean TTG gneiss shows $\varepsilon_{Nd}(t)$ values of +4.5 belonging to the low-HREE group, formed by the partial melting of deep-

seated mafic crust in the garnet stability field with trivial involvement of ancient felsic crustal material in a subduction setting.

Sanukitoids show $\varepsilon_{Nd}(t)$ values between −3.6 to −1.6 along with their whole-rock geochemical characteristics reveal that they were formed by the mixing of mantle melts with anatectic melts followed by homogenization at shallow intrusion levels within a subduction environment. In contrast, anatectic granites display highly negative $\varepsilon_{Nd}(t)$ values (−3.4 to −8.7) which indicate that they were formed purely by partial melting of crustal materials (anatexis) in a collisional setting.

Finally, the amalgamation of diverse micro-blocks occurred by arc-continent collision and repeated slab break-off between north and south terranes of the BC during late Archean. These pieces of evidence suggest that the BC was not assembled until ~2.50 Ga. The anatectic granites were generated by intensive partial melting of the continental crust in an arc-continent collision, representing the final stabilization of the BC.

Keywords: Archean, TTG, greenstone, mafic–ultramafic volcanic rocks, sanukitoids, anatectic granites, zircon geochronology, Sm–Nd isotopes, geochemistry, juvenile and reworked ancient crust, mantle evolution, geodynamics and Bundelkhand Craton

Resumen

Nature of Petrological, Geochemical, Geochronological Settings and Evolution of Bundelkhand Greenstone Complexes in the Bundelkhand Craton, India

Esta tesis doctoral describe la geología, petrografía, geoquímica, mineralogía, geoquímica de isótopos Sm–Nd y geocronología de rocas máficas–ultramáficas, gneises de TTG (tonalita-trondhjemita-granodiorita) y granitoides de alto potasio para descifrar la naturaleza y el origen de los cambios geodinámicos ocurridos en el Bundelkhand Central Bundelkhand Greenstone Complex (CBGC) del cratón Bundelkhand (CB) de la India, en el periodo de tiempo comprendido entre ~3.59 y 2.50 Ga. El CBGC está constituido principalmente por dos cinturones de rocas verdes: (1) el cinturón de rocas verdes de Babina (2) el cinturón de rocas verdes de Mauranipur. A partir de las características petrográficas y las asociaciones minerales que muestran las rocas volcánicas máficas–ultramáficas se infiere que estas rocas pasaron de facies de esquistos verdes a facies de anfibolitas. Las rocas máficas del cinturón de Babina se caracterizan por contenidos de 43.9–51.2 % (en peso) de SiO_2, 5.4–11.0 % de MgO y unos valores de Mg# [Mg# = 100 × (Mg^{2+}/(Mg^{2+} + Fe^{2+}))] que varían entre 44 y 77, mientras que las del cinturón de Mauranipur se caracterizan por un mayor contenido de sílice (51.8–55.6 % en peso), MgO = 6.9–9.5 % y Mg# = 59–70. Las rocas ultramáficas de los cinturones de Babina y Mauranipur presentan unos valores de SiO_2 de 46.9–50.3 % (en peso), MgO de 20.2–21.1 % y Mg# de 77–82. Las rocas máficas de Babina muestran un perfil casi planos [$(La/Yb)_{CN}$ = 0.87–1.40] de tierras raras (REE) y elementos traza con

anomalías de negativas de Nb (Nb/Nb* = 0.13–0.77) y anomalías positivas de Pb que podrían ser atribuidas a la acción de agentes metasomáticos en un contexto de subducción. Por otro lado, las rocas máficas de Mauranipur muestran patrones de tierras raras [$(La/Yb)_{CN}$ = 1.1–1.7; (La/Sm)CN = 1.1–2.0] ligeramente enriquecidos en tierras raras ligeras y patrones de elementos traza con anomalías negativas de Nb (Nb/Nb* = 0.13–0.77), que probablemente sean consecuencia de un proceso de contaminación cortical. Además, los datos isotópicos de roca total (Sm–Nd) de las rocas volcánicas máficas–ultramáficas del cinturón de Babina arrojan una edad (obtenida a partir de una isócrona) de aproximadamente 3,44 Ga, siendo esta la primera estimación de la edad de estas rocas. Las características isotópicas y geoquímicas de las rocas máficas–ultramáficas del CBGC revelan que fueron generadas a partir de un manto empobrecido. Los afloramientos de rocas volcánicas máficas–ultramáficas en los cinturones de Babina y Mauranipur representan retazos de la corteza oceánica posiblemente emplazados en un contexto de subducción.

La datación de circones mediante LA-SF-ICP-MS revela que el magmatismo TTG se desarrolló en el periodo de tiempo entre 3.51 Ga y 3.20 Ga a intervalos regulares de 100 millones de años, aunque también se han encontrado evidencias de un magmatismo TTG Neoarcaico más joven (2.71–2.67 Ga). Además, las edades del magmatismo TTG y del magmatismo máfico–ultramáfico sugieren un desarrollo contemporáneo de un plutonismo félsico y el vulcanismo máfico hace aproximadamente 3.44 Ga. Posteriormente, durante el Neorcaico tuvo lugar un magmatismo rico en K, constituido por sanukitoides y granitos anatécticos que fueron probablemente emplazados de forma coetánea en dos episodios discretos entre ~2.58 y 2.50 Ga. Estos granitoides de alto K representan comúnmente el

último evento magmático del Arcaico que resultaría de una fusión de la corteza a gran escala (anatexis) que parece estar relacionado con la estabilización final del cratón. La presencia de circones heredados tanto en los gneises TTG como en los granitoides de alto contenido en K, sugiere la participación de corteza antigua en su origen. Además, las imágenes de CL en circón y los datos de U–Pb nos permitieron desentrañar diferentes eventos metamórficos a ~3.31–3.10 Ga, y 2.64 Ga que pueden haberse formado principalmente por recristalización en el BC.

Los gneises TTG Paleoarcaicos muestran valores de 64–73 % en peso de SiO_2, mientras que los gneises Neoarcaicos presentan valores de 66–74 %. Por el contrario, los sanukitoides tienen contenidos de SiO_2 que van del 61 al 71 % en peso y los granitos anatecticos presentan un alto contenido de SiO_2 variando entre 70 y 78 % en peso. Los gneises TTG Paleoarcaicos se caracterizan por un contenido de REE total moderado a alto (78–319 ppm) y patrones de REE moderadamente fraccionados [$(La/Yb)_{CN}$ = 3.88–41.12] con variables anomalías negativas de Eu. Por otra parte, los gneises TTG Neoarcaicos contienen valores totales moderados de REE (107–142 ppm) y patrones de REE fuertemente fraccionados [$(La/Yb)_{CN}$ = 9.83–26.44] sin ninguna anomalía significativa de Eu, lo que pone de manifiesto el papel del granate en el residuo de la fuente. Los sanukitoides se caracterizan por un enriquecimiento en LREE en comparación con los HREE y muestran un fraccionamiento claro de LREE/HREE, mientras que los granitos anatécticos muestran un enriquecimiento en LREE con respecto a HREE con anomalías negativas de Eu que varían de fuertes a moderadas. En el diagrama de elementos incompatibles normalizados al manto primitivo (PM), las muestras de gneises TTG Paleoarcaicos muestran enriquecimiento en Ba, U, K y Pb y valores ligeramente

elevados de Sr, y Zr, con grandes anomalías negativas de Nb y Ti y anomalías negativas poco marcadas de Ce, P y Ta. Un patrón similar se reconoce en los gneises TTG Neoarcaicos y en los granitoides de alto contenido en K, lo que parece sugerir un origen relacionado con un contexto de subducción.

Los valores de $\varepsilon_{Nd}(t)$ que van de +4,3 a +0,3 (excepto una muestra con un valor de –0,5) junto con los datos de geoquímica de roca total revelan que los TTGs de bajo HREE fue producido a través de la fusión de la corteza oceánica subducida a diferentes profundidades con una probable y variable interacción con fundidos félsicos corticales. Por otro lado, los TTGs con altos contenidos de HREE sugiere un probable origen desde plagioclasa y anfibolita de granate a baja presión. Además, un gneis TTG Neoarcaico con características de TTG de bajo contenido en HREE muestra valores de $\varepsilon_{Nd}(t)$ de +4,5, pudiendo haberse formado por fusión parcial de la corteza máfica profunda asentada en el campo de estabilidad del granate, con una participación trivial del material de la corteza antigua en un entorno de subducción.

Los sanukitoides muestran valores de $\varepsilon_{Nd}(t)$ entre –3,6 y –1,6, los cuales junto con sus características geoquímicas de roca total parecen indicar que se formaron por la mezcla de fundidos de manto con fundidos anatécticos seguidos de homogeneización a niveles de emplazamiento someros en un ambiente de subducción. Por el contrario, los granitos anatécticos presentan valores negativos elevados (–3,4 a –8,7) que indican que se originaron exclusivamente por la fusión parcial de los materiales de una corteza antigua (anatexis) en un contexto colisional. Finalmente, la acreción de diversos microbloques se produjo por la colisión arco-continente y la repetida ruptura de la losa entre los terrenos norte y sur del CB

durante el final del Arcaico. Estas evidencias sugieren que el CB no fue ensamblado hasta hace ~2.50 Ga. Los voluminosos granitos anatécticos fueron generados por una intensa fusión parcial de la corteza continental en un ambiente extensional después de la colisión arco-continente, representando así la estabilización final del CB.

Palabras clave: Arcaico, TTG, greenstone, rocas volcánicas máficas–ultramáficas, sanukitoides, granitos anatécticos, geocronología de circón, isótopos Sm–Nd, geoquímica, corteza juvenil, corteza retrabajada, evolución del manto, geodinámica, Bundelkhand Cratón.

INTRODUCTION

1. Introduction

Globally, Archean granite-greenstone terranes represent important components of ancient cratons. They consist of volcano-sedimentary sequences and tonalite-trondhjemite-granodiorite (TTG) suites, which are generally associated with syn- and post-tectonic high-K granitoids (Fig. 1; Sylvester, 1994; De Wit, 1998; Condie, 2000; Martin et al., 2005; Anhaeusser, 2014; Furnes et al., 2014; Laurent et al., 2014a, b; Manikyamba et al., 2015; Dall'Agnol et al., 2017; Terentiev and Santosh, 2018). These terranes have preserved history of the Earth's oldest rocks (~3.8 Ga) and host various important mineral deposits. The complex mechanism of origin and stabilization of these early cratons is still incompletely understood (Fig. 1; e.g., Stern and Bleeker, 1998; Peschler et al., 2004; Groves and Bierlein, 2007; Gallardo and Thebaud, 2012; Anhaeusser, 2014; Komiya et al., 2015; Shimojo et al., 2016; Tang and Santosh, 2018). However, the geodynamic processes for forming Archean granite-greenstone terranes have been the subject of intense on-going scientific debate varying from plume-type models (Condie, 1997; Hamilton,1998; Kerr et al., 2000; Nebel et al., 2014; Van Kranendonk et al., 2015), plume-arc interaction (Wyman, 1999; Hollings and Wyman,1999; Polat et al., 2006; Wyman et al., 2002; Manikyamba and Kerrich, 2012) to a subduction-accretion processes (Kusky and Polat, 1999; Polat and Kerrich, 2001; Saha et al., 2004; Cawood et al., 2009; Kusky et al., 2013; Taylor et al., 2016; Smithies et al., 2018).

A great deal of research has concluded that Archean greenstone volcanic sequences can be divided into three groups: komatiitic to tholeiitic basalt suites, tholeiitic to calc-alkaline associations, and bimodal basalt to rhyolite volcanism (Condie, 1981; Kerrich and Polat, 2006; Anhaeusser, 2014; Furnes et al., 2015; Thurston, 2015; Verma et al., 2017; Smithies et al., 2018). Petrological and geochemical fingerprints of various volcanic rocks have been shown to be useful in constraining the petrogenesis of these rocks.

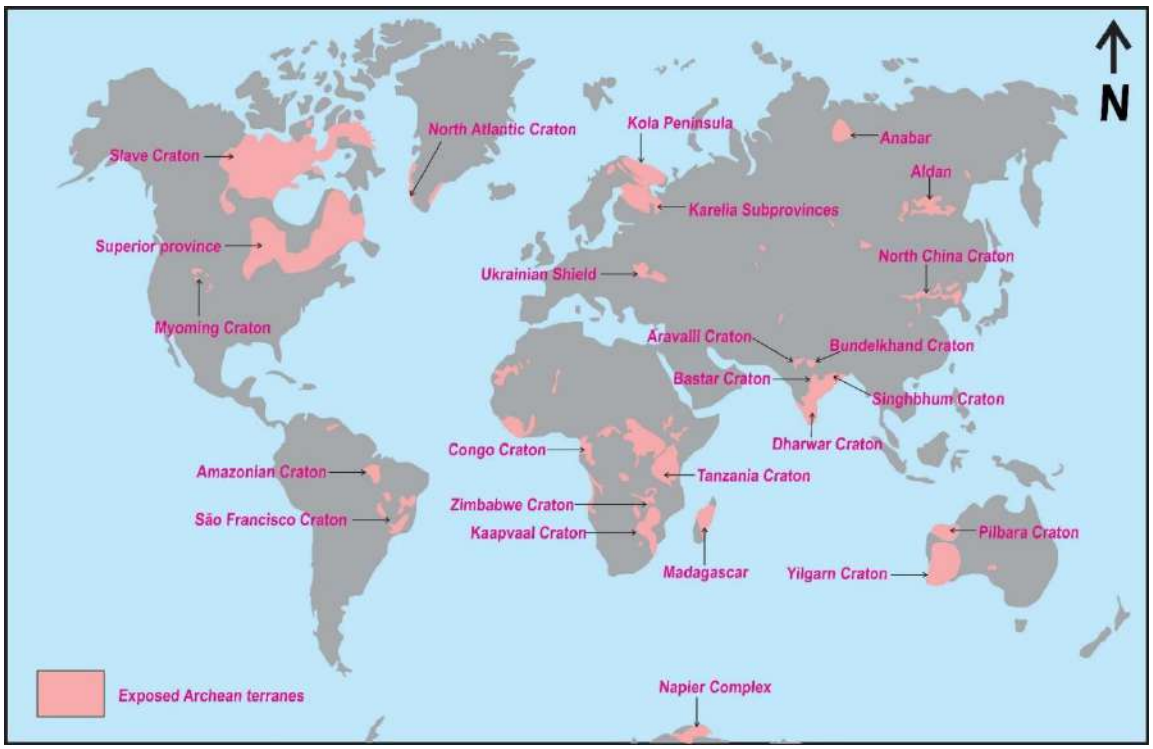

Fig. 1. World cratonic map showing exposed Archean terranes (modified after Bleeker, 2003).

They also provide insights into the geodynamic origin of Archean greenstone belts worldwide as well as the mechanism of continental growth during the early history of the Earth (Kusky and Polat, 1999; Polat and Kerrich, 2000; Sandeman et al., 2004; Wang et al., 2004; Polat et al., 2005; Manikyamba et al., 2009, 2012; Ordóñez-

Calderón et al., 2009, 2011; O'Neil et al., 2011; Condie and Kröner, 2013; Deng et al., 2013; Kröner et al., 2018; Smithies et al., 2018).

TTGs and high-K granitoids are also very important components of Archean crust that occupied a major part of Archean granite-greenstone terranes (Condie, 1981; Drummond and Defant, 1990; Martin, 1994; Smithies and Champion, 2000; Martin and Moyen, 2002; Moyen et al., 2003a, b; Martin et al., 2005; Moyen, 2011; Anhaeusser, 2014; Laurent et al., 2014a, b). TTGs were produced by episodic partial melting of hydrated basaltic oceanic crust (Foley et al., 2002; Johnson et al., 2014), and represent first-generation continental crust. High-K granitoids formed individual, syn- to post tectonic plutons, usually intrusive in greenstone belts and TTG suites (Goodwin, 1991; Sylvester, 1994). High-K granitoid magmatism was formed typically in the late stages of many Archean crustal evolution cycles, but not all potassic granites belongs to Neoarchean; for example, in the Pilbara Craton, the potassic granites have dated between 2.93 and 2.85 Ga (Champion and Smithies, 2007). These granitoids generally represent the last Archean magmatic event in every craton worldwide and appear to be related to final stabilization of the Archean craton. Although, this event is diachronous from one craton to another and occurred between 3.0 and 2.5 Ga on a planetary scale (Condie, 1981; Martin, 1994; Sylvester, 1994; Frost et al., 1998; Champion and Sheraton, 1997; Moyen et al., 2003a; Oliveira et al., 2009; Heilimo et al., 2013; Almeida et al., 2011, 2013; Romano et al., 2013; Laurent et al., 2014a). These late Archean events indicate a dramatic change in composition and tectonics as well as a first order secular change in felsic magmatism on the Earth (Moyen, 2011). To understand how TTGs and high-K

granitoids formed throughout the Archean is to comprehend much about the origin and generation of continental crust and its geochemical evolution at the early stage in the Earth's history.

The Bundelkhand Craton (BC) was formed largely in the Paleo- to Neoarchean with multi-stage crustal growth (Fig. 2 and 3; Basu, 1986; Mondal et al., 2002; Malviya et al., 2006; Kaur et al., 2014, 2016; Singh and Slabunov, 2015, 2016; Saha et al., 2016; Verma et al., 2016; Joshi et al., 2017; Slabunov et al., 2017; Singh et al., 2018; Singh et al., 2019a) and has attracted worldwide attention from geoscientists in the past decades. However, the Paleo- to Neoarchean tectonic evolution and continental growth mechanism of the BC have been controversial (Mondal et al., 2002; Kaur et al., 2014, 2016; Singh and Slabunov, 2015, 2016; Saha et al., 2016; Verma et al., 2016; Joshi et al., 2017; Slabunov et al., 2017; Slabunov and Singh, 2019; Singh et al., 2019a, b).

The BC has two greenstone complexes: the central Bundelkhand greenstone complex (CBGC) and the south Bundelkhand greenstone complex (Fig. 3; Singh and Slabunov, 2015, 2016). This PhD project concerns to the first one. The CBGC is located in the central part of the BC and mainly consists of volcano-sedimentary sequences, TTG suites and a variety of high-K granitic intrusive rocks (Mondal et al., 2002; Kaur et al., 2014, 2016; Singh and Slabunov, 2015; Saha et al., 2016; Verma et al., 2016; Joshi et al., 2017; Slabunov and Singh, 2019; Singh et al., 2019a, b). However, few studies have focused on the CBGC. To date, there has never been any report in the literature about the ages of mafic–ultramafic units of the greenstone belts. This explains the lack of understanding of formation age. Further, there is

some inconsistency in ideas about the tectonic evolution of this complex. Some researchers suggest that the rocks in the complex were generated in a subduction-accretion tectonic environment (Malviya et al., 2006; Singh and Slabunov, 2015; Kaur et al., 2016; Joshi et al., 2017) and one favor plume-type and plume-arc interaction (Singh et al., 2018).

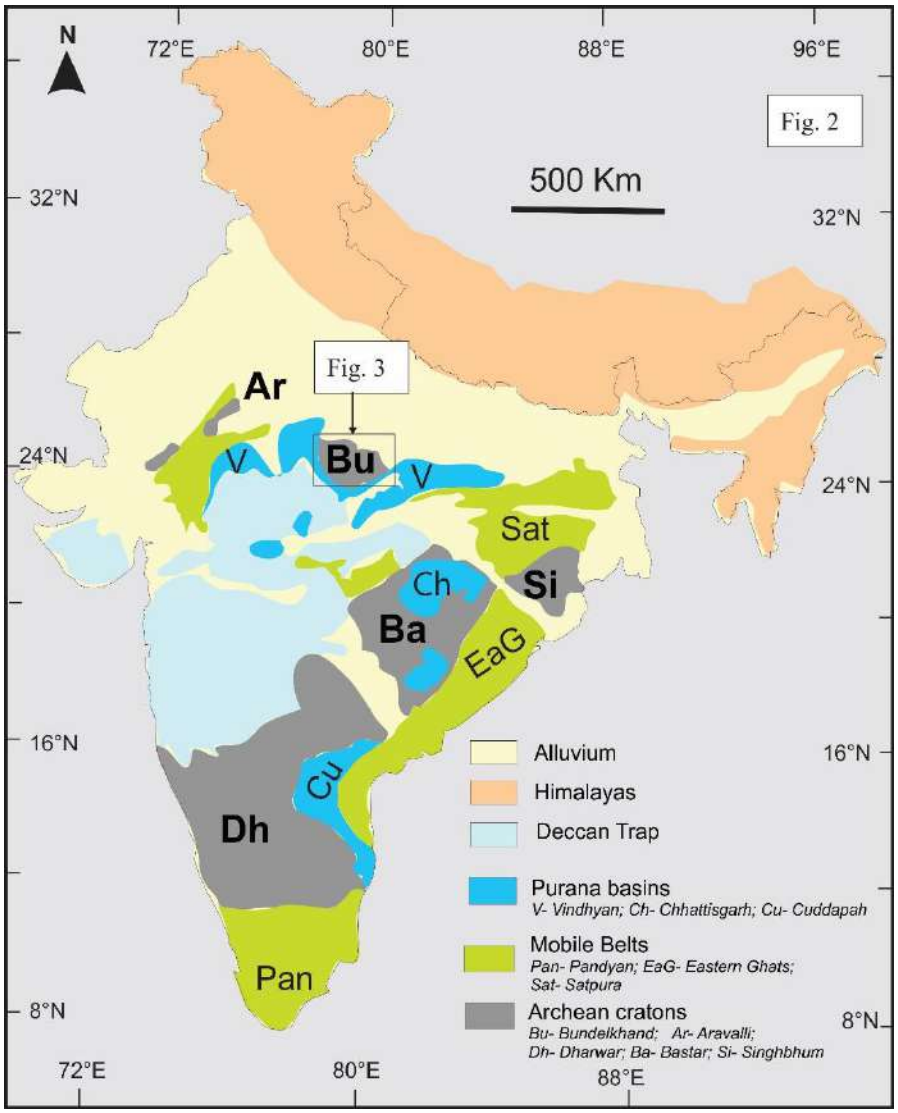

Fig. 2. Generalized geological map of the Indian shield (modified after: Ramakrishnan and Vaidyanadhan, 2010; Verma et al., 2016).

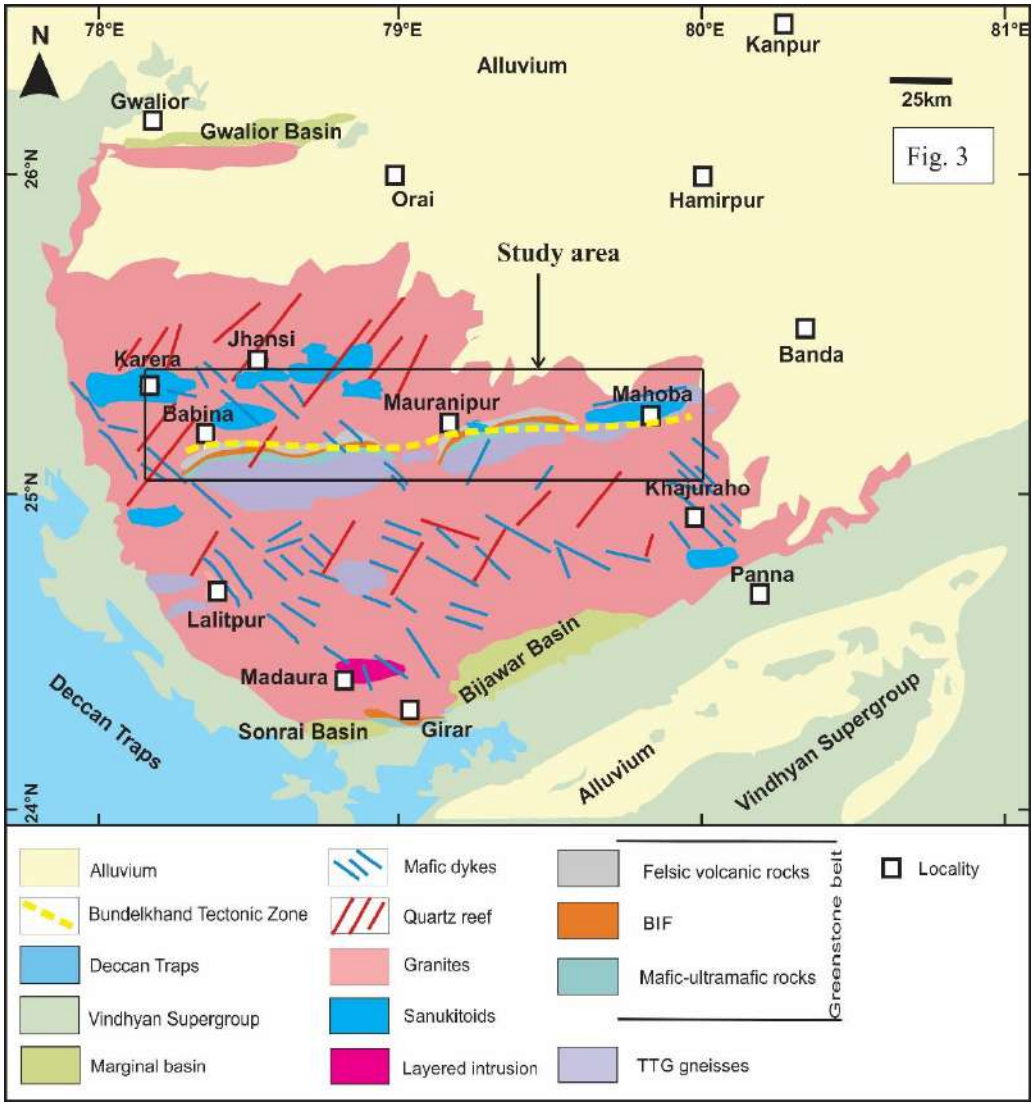

Fig. 3. Geological map of the Bundelkhand Craton (after Basu, 1986; Malviya et al., 2006; Singh and Slabunov, 2015; Verma et al., 2016; Joshi et al., 2017).

Zircon ages of TTGs have been reported as between 3.5 and 3.2 Ga in the CBGC and suggest four phases (~3.55 Ga, 3.40 Ga, 3.33 Ga and 3.20 Ga) of Paleoarchean TTG magmatism. However, Verma et al. (2016) reported one Neoarchean age (~2.7 Ga.) of TTG magmatism from the Babina belt, which is so far the youngest TTG rock in the BC. But as these authors did not provide geochemistry, it is difficult to determine whether it is a TTG *sensu stricto* or a granodiorite gneiss. Therefore,

further geochronological and geochemical studies are required for the identification of TTG and for understanding how many TTG magmatic phases occurred in the BC. Additionally, but very importantly, research on high-Mg granitoids (sanukitoids) and their petrogenetic connection between TTG and high-K anatectic granites remain scarce. However, they are crucial to understanding the Earth's crust and mantle evolution during Neoarchean and cratonization of the BC. The abovementioned shows that the CBGC had a complicated evolutionary history with a multi-stage crustal growth, recording all the important geological events of the early history of the Earth. Therefore, it is noteworthy that there is still lack of research, especially about CBGC in the BC.

1.1 Research objectives of the PhD project

In light of the issues mentioned above, the current PhD project contributes to the state of knowledge on the formation and evolution of the Earth’s early continental crust in the BC. This was achieved by petrological, geochemical, mineralogical and geochronological study of the various rock types (mafic–ultramafic volcanic, TTGs and high-K granitoid rocks) that constitute the CBGC. The present study provides new insight into the Archean crustal evolution, plate tectonics and continental growth of the BC.

The research questions of PhD project are as follows:

- What were the formation ages of the mafic–ultramafic volcanic rocks, and what was their geodynamic evolution?

- Did the greenstone belts (mafic-felsic components) originate mainly in a plume-type, plume-arc interaction, a subduction-accretion setting or in a transitional phase from one to another setting?
- What was the petrogenetic emplacement of sanukitoids and granites?
- What was the geodynamic evolution of the granites and TTG, and their role in the evolution of the Earth's crust versus mantle?
- Did zircon come from juvenile continental crust or from reworked ancient crust?

These questions have not been satisfactorily addressed in previous studies. They are the key to understanding the generation of continental crust and its geochemical evolution at an early stage in Earth history.

1.2 Hypothesis

The research hypotheses of the project are as follows:

1. The CBGC formed in a subduction-related setting.
2. The mafic–ultramafic volcanic rocks were emplaced in the Paleoarchean Era.
3. The sanukitoid plutons originated through an enriched mantle wedge.
4. The Neoarchean TTG magmatism occurred in the CBGC.
5. In the CBGC, more crust was recycled back to the mantle than was extracted from the mantle.

1.2.1 Testing of hypothesis

Major-trace and rare earth elements geochemistry will be used to understand the tectonic environment. Bulk-rock and isotopic geochemistry, geochronology, will be carried out to understand formation ages, petrogenesis and geodynamic evolution of the CBGC.

1.3 Thesis outline

This doctoral thesis is based on two published research papers and one submitted manuscript, which addresses all of the above-mentioned research objectives. Output of research works are presented in individual chapters dealing with various aspects of geochemistry, mineralogy, isotope geochemistry, geochronology and petrogenesis of the Archean mafic–ultramafic volcanic, TTG and high-K granitoid rocks.

The outline of the thesis is as follows:

Chapter **One** describes the geological setting of the study area. Chapter **Two** presents geochronology, geochemistry and petrogenesis of mafic–ultramafic volcanic rocks and reports ^{147}Sm–^{143}Nd whole-rock isochron age of ca. 3.44 Ga for the first time in the BC. Whole-rock Sm-Nd isotopes, major, trace and rare earth element compositions of the mafic–ultramafic volcanic rocks are measured using isotope dilution-thermal ionization mass spectrometry (ID-TIMS), X-ray fluorescence (XRF) and Inductively coupled plasma mass spectrometry (ICP-MS). The

geochemical characters of ultramafic–mafic volcanic rocks have serpentinite, basalts and basaltic andesites and have similar geochemical signatures to Archean subduction-related rocks. The age of magmatism and petrogenesis of mafic-ultramafic volcanic rocks are discussed. Research findings of this chapter have published in the “Lithos” that addresses the first and second research objectives of the present project. Chapter **Three** comprises the second paper, published in the “Journal of Asian Earth Sciences”, which focuses on the petrogenetic connections between sanukitoids and high-K anatectic granites, mantle-crustal melts interactions and their implication for crustal growth and cratonization of the BC during Neoarchean Era. Results are achieved by an isotopical, geochemical, petrological and geochronological study using ID–TIMS, XRF, ICP-MS and Laser Ablation Inductively Coupled Plasma Mass Spectrometry (LA-ICP-MS). This chapter represents the third research objective of the project. The submitted manuscript is covered in Chapter **Four** and investigates episodic crustal growth and the reworking of the CBGC. Whole-rock geochemical, Sm-Nd isotopical compositions and *in situ* U-Pb zircon dating of TTGs and high-K granitoids were determined by using ICP-MS, ID–TIMS and LA-ICP-MS. Zircon dating reveals that TTG magmatic events mainly took place in four discrete episodes during Paleoarchean (~3.51–3.20 Ga) and two distinct periods during Neoarchean Era (~2.71–2.67 Ga) at regular intervals of 100 Myr in the CBGC. Subsequently, high-K granitoids magmatism happened in the two discrete episodes during Neoarchean between ~2.57 and 2.50 Ga. These high-K granitoids commonly represent the last Archean magmatic event with a large-scale crustal melting (anatexis) that seems to be related to the final stabilization of the craton. This article deals with the fourth and fifth research objectives of the PhD

project. Chapter **Five** provides a summary of the main findings and suggests how this work can be extended and improved.

References:

Almeida, J. D. A. C., Dall'Agnol, R., de Oliveira, M. A., Macambira, M. J. B., Pimentel, M. M., Rämö, O. T., da Silva Leite, A. A., 2011. Zircon geochronology, geochemistry and origin of the TTG suites of the Rio Maria granite-greenstone terrane: Implications for the growth of the Archean crust of the Carajás province, Brazil. Precambrian Research 187, 201–221.

Almeida, J. D. A. C., Dall'Agnol, R., da Silva Leite, A. A., 2013. Geochemistry and zircon geochronology of the Archean granite suites of the Rio Maria granite-greenstone terrane, Carajás Province, Brazil. Journal of South American Earth Sciences 42, 103–126.

Anhaeusser, C. R., 2014. Archaean greenstone belts and associated granitic rocks–a review. Journal of African Earth Sciences 100, 684–732.

Basu, A. K., 1986. Geology of parts of the Bundelkhand granite massif central India. In: Records, Geological Survey of India (Ed.) 117, 61–124.

Bleeker, W., 2003. The late Archean record: a puzzle in ca. 35 pieces. Lithos 71, 99–134.

Cawood, P. A., Kröner, A., Collins, W. J., Kusky, T. M., Mooney, W. D., Windley, B. F., 2009. Accretionary orogens through Earth history. Geological Society, London, Special Publications 318, 1–36.

Champion, D. C., Sheraton, J. W., 1997. Geochemistry and Nd isotope systematics of Archaean granites of the Eastern Goldfields, Yilgarn Craton, Australia: implications for crustal growth processes. Precambrian Research 83, 109–132.

Champion, D.C., Smithies, R.H., 2007. In: Van Kranendonk, M.J., Smithies, R.H., Bennett, V.C. (Eds.), Geochemistry of Paleoarchean Granites of the East Pilbara Terrane, Pilbara Craton, Western Australia: Implications for Early Archean Crustal Growth. Earth's Oldest Rocks, Developments in Precambrian Geology 15. Elsevier, Amsterdam, 369–410.

Condie, K. C., 1981. Archean greenstone belts (Vol. 3). Elsevier.

Condie, K. C., 2000. Episodic continental growth models: afterthoughts and extensions. Tectonophysics 322, 153–162.

Condie, K. C., Kröner, A., 2013. The building blocks of continental crust: evidence for a major change in the tectonic setting of continental growth at the end of the Archean. Gondwana Research 23, 394–402.

Condie, K. C., 1997. Contrasting sources for upper and lower continental crust: the greenstone connection. The Journal of Geology 105, 729–736.

Dall'Agnol, R., da Cunha, I. R. V., Guimarães, F. V., de Oliveira, D. C., Teixeira, M. F. B., Feio, G. R. L., Lamarão, C. N., 2017. Mineralogy, geochemistry, and petrology of Neoarchean ferroan to magnesian granites of Carajás Province, Amazonian Craton: The origin of hydrated granites associated with charnockites. Lithos 277, 3–32.

De Wit, M.J., 1998. On Archaean granites, greenstones, cratons and tectonics: does the evidence demand a verdict?: Precambrian Research 91, 181–226.

Deng, H., Kusky, T., Polat, A., Wang, L., Wang, J., Wang, S., 2013. Geochemistry of Neoarchean mafic volcanic rocks and late mafic dikes in the Zanhuang Complex, Central Orogenic Belt, North China Craton: implications for geodynamic setting. Lithos 175, 193–212.

Drummond, M.S., Defant, M.J., 1990. Amodel for trondhjemite–tonalite–dacite genesis and crustal growth via slab melting: Archaean to modern comparisons. Journal of Geophysical Research 95, 21503–21521.

Foley, S., Tiepolo, M., Vannucci, R., 2002. Growth of early continental crust controlled by melting of amphibolite in subduction zones. Nature 417, 837.

Frost, C. D., Frost, B. R., Chamberlain, K. R., Hulsebosch, T. P., 1998. The Late Archean history of the Wyoming province as recorded by granitic magmatism in the Wind River Range, Wyoming. Precambrian Research 89, 145–173.

Furnes, H., De Wit, M., Dilek, Y., 2014. Four billion years of ophiolites reveal secular trends in oceanic crust formation. Geoscience Frontiers 5, 571–603.

Furnes, H., Dilek, Y., De Wit, M., 2015. Precambrian greenstone sequences represent different ophiolite types. Gondwana Research 27, 649–685.

Gallardo, L. A., Thebaud, N., 2012. New insights into Archean granite-greenstone architecture through joint gravity and magnetic inversion. Geology, 40, 215–218.

Goodwin, A.M., 1991. Precambrian Geology. Academic Press, New York, 666 pp.

Groves, D. I., Bierlein, F. P., 2007. Geodynamic settings of mineral deposit systems. Journal of the Geological Society 164, 19–30.

Hamilton, W. B.,1998. Archean magmatism and deformation were not products of plate tectonics. Precambrian Research 91, 143–179.

Heilimo, E., Halla, J., Andersen, T., Huhma, H., 2013. Neoarchean crustal recycling and mantle metasomatism: Hf–Nd–Pb–O isotope evidence from sanukitoids of the Fennoscandian shield. Precambrian Research 228, 250–266.

Hollings, P., Wyman, D., 1999. Trace element and Sm–Nd systematics of volcanic and intrusive rocks from the 3 Ga Lumby Lake Greenstone belt, Superior Province: evidence for Archean plume–arc interaction. Lithos 46, 189–213.

Johnson, T. E., Brown, M., Kaus, B. J., VanTongeren, J. A., 2014. Delamination and recycling of Archaean crust caused by gravitational instabilities. Nature Geoscience 7, 47.

Kaur, P., Zeh, A., Chaudhri, N., 2014. Characterisation and U–Pb–Hf isotope record of the 3.55 Ga felsic crust from the Bundelkhand Craton, northern India. Precambrian Research 255, 236–244.

Kaur, P., Zeh, A., Chaudhri, N., Eliyas, N., 2016. Unravelling the record of Archaean crustal evolution of the Bundelkhand Craton, northern India using U–Pb zircon–monazite ages, Lu–Hf isotope systematics, and whole-rock geochemistry of granitoids. Precambrian Research 281, 384–413.

Kerr, A. C., Tarney, J., Kempton, P. D., Spadea, P., Nivia, A., Marriner, G. F., & Duncan, R. A., 2002. Pervasive mantle plume head heterogeneity: Evidence from the late Cretaceous Caribbean-Colombian oceanic plateau. Journal of Geophysical Research: Solid Earth 107, ECV–2.

Kerrich, R., Polat, A., 2006. Archean greenstone-tonalite duality: Thermochemical mantle convection models or plate tectonics in the early Earth global dynamics?. Tectonophysics 415, 141–165.

Komiya, T., Yamamoto, S., Aoki, S., Sawaki, Y., Ishikawa, A., Tashiro, T., Collerson, K. D., 2015. Geology of the Eoarchean,> 3.95 Ga, Nulliak supracrustal rocks in the Saglek Block, northern Labrador, Canada: The oldest geological evidence for plate tectonics. Tectonophysics 662, 40–66.

Kröner, A., Nagel, T. J., Hoffmann, J. E., Liu, X., Wong, J., Hegner, E., Liu, D. 2018. High-temperature metamorphism and crustal melting at ca. 3.2 Ga in the eastern Kaapvaal craton, southern Africa. Precambrian Research 317, 101–116.

Kusky, T. M., Polat, A., 1999. Growth of granite–greenstone terranes at convergent margins, and stabilization of Archean cratons. Tectonophysics 305, 43–73.

Kusky, T. M., Windley, B. F., Safonova, I., Wakita, K., Wakabayashi, J., Polat, A., Santosh, M., 2013. Recognition of ocean plate stratigraphy in accretionary orogens through Earth history: A record of 3.8 billion years of sea floor spreading, subduction, and accretion. Gondwana Research 24, 501–547.

Laurent, O., Martin, H., Moyen, J. F., Doucelance, R., 2014a. The diversity and evolution of late-Archean granitoids: Evidence for the onset of “modern-style” plate tectonics between 3.0 and 2.5 Ga. Lithos 205, 208–235.

Laurent, O., Rapopo, M., Stevens, G., Moyen, J. F., Martin, H., Doucelance, R., Bosq, C., 2014b. Contrasting petrogenesis of Mg–K and Fe–K granitoids and implications for post-collisional magmatism: case study from the Late-Archean Matok pluton (Pietersburg block, South Africa). Lithos 196, 131–149.

Malviya, V. P., Arima, M., Pati, J. K., Kaneko, Y., 2006. Petrology and geochemistry of metamorphosed basaltic pillow lava and basaltic komatiite in the Mauranipur area: subduction related volcanism in the Archean Bundelkhand craton, Central India. Journal of Mineralogical and Petrological Sciences 101, 199–217.

Manikyamba, C., Kerrich, R., 2012. Eastern Dharwar Craton, India: continental lithosphere growth by accretion of diverse plume and arc terranes. Geoscience Frontiers 3, 225–240.

Manikyamba, C., Ganguly, S., Santosh, M., Saha, A., Chatterjee, A., Khelen, A. C., 2015. Neoarchean arc–juvenile back-arc magmatism in eastern Dharwar Craton, India: geochemical fingerprints from the basalts of Kadiri greenstone belt. Precambrian Research 258, 1–23.

Manikyamba, C., Kerrich, R., Khanna, T. C., Satyanarayanan, M., Krishna, A. K., 2009. Enriched and depleted arc basalts, with Mg-andesites and adakites: a potential paired arc–back-arc of the 2.6 Ga Hutti greenstone terrane, India. Geochimica et Cosmochimica Acta 73, 1711–1736.

Manikyamba, C., Kerrich, R., Polat, A., Raju, K., Satyanarayanan, M., Krishna, A. K. 2012. Arc picrite–potassic adakitic–shoshonitic volcanic association of the Neoarchean Sigegudda Greenstone Terrane, Western Dharwar Craton: transition from arc wedge to lithosphere melting. Precambrian Research 212, 207–224.

Martin, H., Moyen, J.-F., 2002. Secular changes in TTG composition as markers of the progressive cooling of the Earth. Geology 30, 319–322.

Martin, H., 1994. The Archaean grey gneisses and genesis of continental crust. In: Condie, K.C. (Ed.), Archaean Crustal Evolution, Developments in Precambrian Geology 11, 205–259.

Martin, H., Smithies, R. H., Rapp, R., Moyen, J. F., Champion, D., 2005. An overview of adakite, tonalite–trondhjemite–granodiorite TTG, and sanukitoid: relationships and some implications for crustal evolution. Lithos 79, 1–24.

Mohan, M. R., Singh, S. P., Santosh, M., Siddiqui, M. A., Balaram, V., 2012. TTG suite from the Bundelkhand Craton, Central India: geochemistry, petrogenesis and implications for Archean crustal evolution. Journal of Asian Earth Sciences 58, 38–50.

Mondal, M. E. A., Goswami, J. N., Deomurari, M. P., Sharma, K. K., 2002. Ion microprobe 207Pb/206Pb ages of zircons from the Bundelkhand massif, northern India: implications for crustal evolution of the Bundelkhand–Aravalli protocontinent. Precambrian Research 117, 85–100.

Moyen, J.-F., 2011. The composite Archaean grey gneisses: petrological significance, and evidence for a non-unique tectonic setting for Archaean crustal growth. Lithos 123, 21–36.

Moyen, J.-F., Martin, A., Jayananda, M., Auvray, B., 2003a. Late Archaean granites: a typology based on the Dharwar craton (India). Precambrian Research 127, 102–123.

Moyen, J.-F., Martin, H., Jayananda, M., Auvray, B., Mahabaleswar, B., 2003b. Late Archean granites: a typology based on the Dharwar Craton (India). Precambrian Research 127, 103–123.

Nebel, O., Campbell, I. H., Sossi, P. A., Van Kranendonk, M. J., 2014. Hafnium and iron isotopes in early Archean komatiites record a plume-driven convection cycle in the Hadean Earth. Earth and Planetary Science Letters 397, 111–120.

O'Neil, J., Francis, D., Carlson, R. W., 2011. Implications of the Nuvvuagittuq greenstone belt for the formation of Earth's early crust. Journal of Petrology 52, 985–1009.

Oliveira, M. A., Dall'Agnol, R., Althoff, F. J., da Silva Leite, A. A., 2009. Mesoarchean sanukitoid rocks of the Rio Maria granite-greenstone terrane, Amazonian Craton, Brazil. Journal of South American Earth Sciences 27, 146–160.

Ordóñez-Calderón, J. C., Polat, A., Fryer, B. J., Appel, P. W. U., van Gool, J. A. M., Dilek, Y., Gagnon, J. E., 2009. Geochemistry and geodynamic origin of the Mesoarchean Ujarassuit and Ivisaartoq greenstone belts, SW Greenland. Lithos 113, 133–157.

Ordóñez-Calderón, J. C., Polat, A., Fryer, B. J., Gagnon, J. E., 2011. Field and geochemical characteristics of Mesoarchean to Neoarchean volcanic rocks in the Storø greenstone belt, SW Greenland: evidence for accretion of intra-oceanic volcanic arcs. Precambrian Research 184, 24–42.

Peschler, A. P., Benn, K., oest, W. R., 2004. Insights on Archean continental geodynamics from gravity modelling of granite–greenstone terranes. Journal of Geodynamics 38, 185–207.

Polat, A., Kerrich, R., 2000. Archean greenstone belt magmatism and the continental growth–mantle evolution connection: constraints from Th–U–Nb–LREE systematics of the 2.7 Ga Wawa subprovince, Superior Province, Canada. Earth and Planetary Science Letters 175, 41–54.

Polat, A., Kerrich, R., 2001. Magnesian andesites, Nb-enriched basalt-andesites, and adakites from late-Archean 2.7 Ga Wawa greenstone belts, Superior Province, Canada: implications for late Archean subduction zone petrogenetic processes. Contributions to Mineralogy and Petrology 141, 36–52.

Polat, A., Kusky, T., Li, J., Fryer, B., Kerrich, R., Patrick, K., 2005. Geochemistry of Neoarchean (ca. 2.55–2.50 Ga) volcanic and ophiolitic rocks in the Wutaishan greenstone belt, central orogenic belt, North China craton: implications for geodynamic setting and continental growth. Geological Society of America Bulletin 117, 1387–1399.

Polat, A., Li, J., Fryer, B., Kusky, T., Gagnon, J., Zhang, S., 2006. Geochemical characteristics of the Neoarchean (2800–2700 Ma) Taishan greenstone belt, North China Craton: evidence for plume–craton interaction. Chemical Geology 230, 60–87.

Romano, R., Lana, C., Alkmim, F. F., Stevens, G., Armstrong, R., 2013. Stabilization of the southern portion of the São Francisco craton, SE Brazil, through a long-lived period of potassic magmatism. Precambrian Research 224, 143–159.

Saha, A., Basu, A. R., Garzione, C. N., Bandyopadhyay, P. K., Chakrabarti, A., 2004. Geochemical and petrological evidence for subduction–accretion processes in the Archean Eastern Indian Craton. Earth and Planetary Science Letters 220, 91–106.

Saha, L., Frei, D., Gerdes, A., Pati, J. K., Sarkar, S., Patole, V., Nasipuri, P., 2016. Crustal geodynamics from the Archaean Bundelkhand Craton, India: constraints from zircon U–Pb–Hf isotope studies. Geological Magazine 153, 179–192.

Sandeman, H. A., Hanmer, S., Davis, W. J., Ryan, J. J., Peterson, T. D., 2004. Neoarchaean volcanic rocks, Central Hearne supracrustal belt, Western Churchill Province, Canada: geochemical and isotopic evidence supporting intra-oceanic, supra-subduction zone extension. Precambrian Research 134, 113–141.

Shimojo, M., Yamamoto, S., Sakata, S., Yokoyama, T. D., Maki, K., Sawaki, Y., Tashiro, T., 2016. Occurrence and geochronology of the Eoarchean, ~ 3.9 Ga, Iqaluk Gneiss in the Saglek Block, northern Labrador, Canada: Evidence for the oldest supracrustal rocks in the world. Precambrian Research 278, 218–243.

Singh, S. P., Subramanyam, K. S. V., Manikyamba, C., Santosh, M., Singh, M. R., Kumar, B. C. 2018. Geochemical systematics of the Mauranipur-Babina greenstone belt, Bundelkhand Craton, Central India: Insights on Neoarchean mantle plume-arc accretion and crustal evolution. Geoscience Frontiers 9, 769–788.

Singh, V. K., Slabunov, A., 2016. Two types of Archaean supracrustal belts in the Bundelkhand craton, India: Geology, geochemistry, age and implication for craton crustal evolution. Journal of the Geological Society of India 88, 539–548.

Singh, V.K., Slabunov, A., 2015. The central Bundelkhand Archaean greenstone complex, Bundelkhand craton, central India: geology, composition, and geochronology of supracrustal rocks. International Geology Review 57, 1347–1362.

Slabunov, A., Singh, V.K., Kumar, B., Xiaoli, L., 2017. Paleoarchean zircons from quartzite of South Bundelkhand Supracrustal Complex: origin and implications for crustal evolution in Bundelkhand Craton, Central India. Current Science 112, 794–801.

Smithies, R. H., Champion, D. C., 2000. The Archaean high-Mg diorite suite: links to tonalite–trondhjemite–granodiorite magmatism and implications for early Archaean crustal growth. Journal of Petrology 41, 1653–1671.

Smithies, R. H., Ivanic, T. J., Lowrey, J. R., Morris, P. A., Barnes, S. J., Wyche, S., Lu, Y. J., 2018. Two distinct origins for Archean greenstone belts. Earth and Planetary Science Letters 487, 106–116.

Stern, R. A. Bleeker, W., 1998. Age of the world's oldest rocks refined using Canada's SHRIMP: The Acasta Gneiss Complex, Northwest Territories, Canada. Geoscience Canada 25.

Sylvester, P. J., 1994. Archean granite plutons. In Developments in Precambrian geology 11, 261–314.

Tang, L., Santosh, M., 2018. Neoarchean granite-greenstone belts and related ore mineralization in the North China Craton: an overview. Geoscience Frontiers 9, 751–768.

Taylor, J., Zeh, A., Gerdes, A., 2016. U–Pb–Hf isotope systematics of detrital zircons in high-grade paragneisses of the Ancient Gneiss Complex, Swaziland: Evidence for two periods of juvenile crust formation, Paleo-and Mesoarchaean sediment deposition, and 3.23 Ga terrane accretion. Precambrian Research 280, 205–220.

Terentiev, R. A., Santosh, M., 2018. High magnesian granitoids in the Precambrian continental crust: Implication for the continuum between ferro–potassic and magnesio–potassic rock suites. Lithos 314, 669–682.

Thurston, P. C., 2015. Igneous Rock Associations 19. Greenstone Belts and Granite−Greenstone Terranes: Constraints on the Nature of the Archean World. Geoscience Canada 42, 437–484.

Van Kranendonk, M. J., Smithies, R. H., Griffin, W. L., Huston, D. L., Hickman, A. H., Champion, D. C., Pirajno, F., 2015. Making it thick: a volcanic plateau origin of Palaeoarchean continental lithosphere of the Pilbara and Kaapvaal cratons. Geological Society, London, Special Publications 389, 83–111.

Verma S.K., Oliveira E.P., Silva P.M., Moreno J.A., Amaral W.S., 2017. Geochemistry of komatiites and basalts from the Rio das Velhas and Pitangui greenstone belts, São Francisco Craton, Brazil: Implications for the origin, evolution, and tectonic setting. Lithos 284–285, 560 577.

Verma, S.K., Verma, S.P., Oliveira, E.P., Singh, V.K., Moreno, J.A., 2016. LA-SF-ICP-MS zircon U–Pb geochronology of granitic rocks from the central Bundelkhand greenstone complex, Bundelkhand craton, India. Journal of Asian Earth Sciences 118, 125–137.

Wang, Z., Wilde, S. A., Wang, K., Yu, L., 2004. A MORB-arc basalt–adakite association in the 2.5 Ga Wutai greenstone belt: late Archean magmatism and crustal growth in the North China Craton. Precambrian Research 131, 323–343.

Wyman, D. A., 1999. A 2.7 Ga depleted tholeiite suite: evidence of plume-arc interaction in the Abitibi greenstone belt, Canada. Precambrian Research 97, 27–42.
Wyman, D. A., Kerrich, R., Polat, A., 2002. Assembly of Archean cratonic mantle lithosphere and crust: plume–arc interaction in the Abitibi–Wawa subduction–accretion complex. Precambrian Research 115, 37–62.

CHAPTER 1

Geological Setting of the Central Bundelkhand Greenstone Complex

1. Regional geology and tectonic framework

The Indian shield has five main cratons; they are composite, consolidated and rigid blocks that evolved during the Archean Eon. The ENE–WSW trending Central Indian Tectonic Zone (Fig. 1) broadly divides the Indian Shield into two cratonic blocks (see, for example, Acharyya (2003)): the southern cratonic block consists of Dharwar, Bastar, and Singhbhum cratons, and the northern cratonic block comprises Aravalli and Bundelkhand cratons (Fig. 1; Naqvi and Rogers, 1987; Yedekar et al., 1990; Ramakrishnan and Vaidyanadhan, 2010; Valdiya, 2010).

The Bundelkhand Craton (BC) is located north–central part of the Indian shield, and delimited to the west by the Great Boundary Fault, to the northeast by the Indo-Gangetic alluvial plains and to the south and southeast by the Narmada–Son lineament (Ahmad and Tarney, 1994; Ramakrishnan and Vaidyanadhan, 2010; Radhakrishna et al., 2013). The BC also bounded by marginal sedimentary basins of the Paleoproterozoic (2.0–1.8 Ga), Gwalior (Northwest), Sonrai (South) and Bijawar (Southeast), all of which are homotaxial and characterized by clastic sedimentary rocks at their base, and by top most units composed of carbonates with the banded iron formations (BIFs) (Fig. 2; Absar et al., 2009). Rocks of the Vindhyan Supergroup (Mesoproterozoic: 1.1–1.0 Ga) overlay these marginal basins,

discussed in detail by Meert et al. (2010) and Turner et al. (2014). Whereas the northern side of the craton is covered by Gangetic alluvial plains (Fig. 2; Manglik et al., 2015).

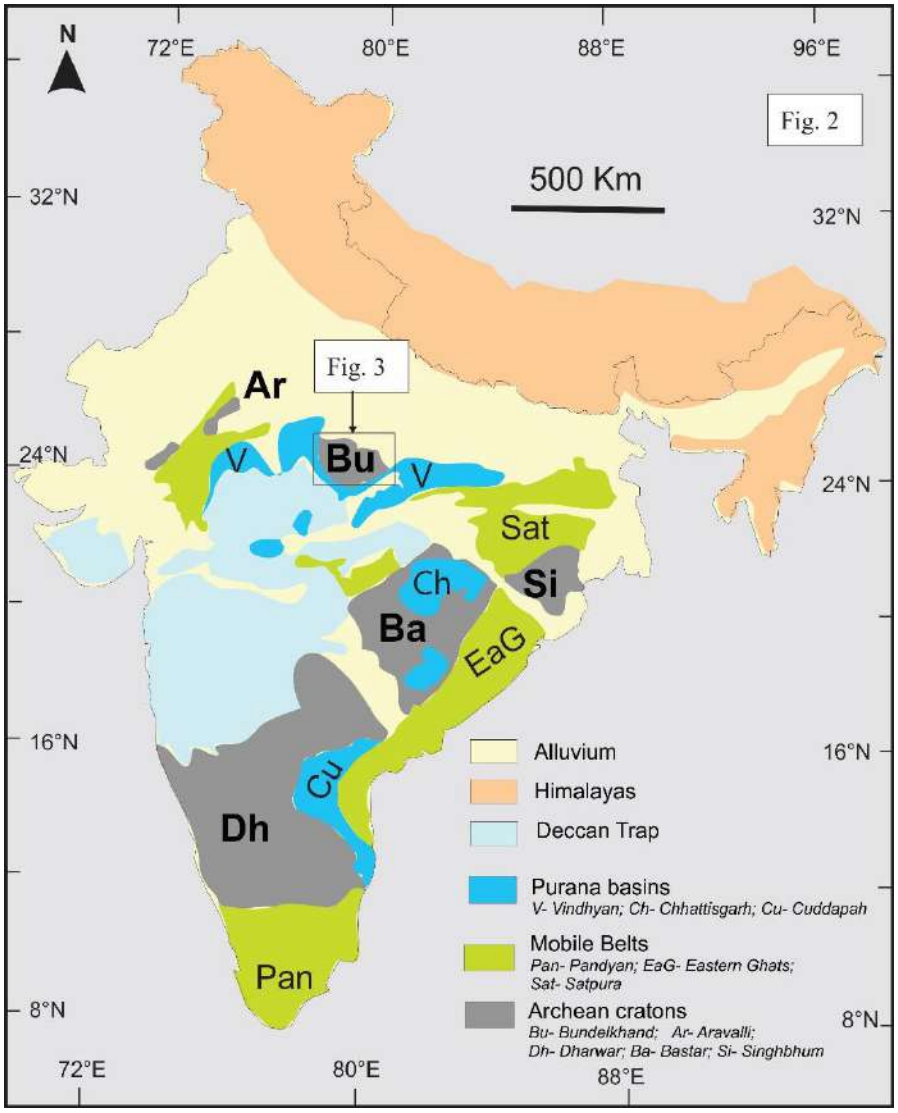

Fig. 1. General geology map of the Indian shield (modified after: Ramakrishnan and Vaidyanadhan, 2010; Verma et al., 2016).

The BC is a composite mosaic of Archean crustal nuclei, exposed in semicircular shape, which occupied about ~26,000 sq. km. It mainly consists of TTG gneisses,

volcanic-sedimentary greenstone sequences and voluminous high-K granitoids (granodiorites, sanukitoids and anatectic granites), ranging in age from Paleoarchean to Neoarchean (Fig. 2; Table 1; Mondal et al., 2002; Kaur et al., 2014, 2016; Singh and Slabunov, 2015; Joshi et al., 2017; Singh et al., 2018; Singh et al., 2019a, b, c). The craton is generally divided into two segments (central and southern) based on the geological signatures that is exposures of basement rock (TTG gneisses), greenstone belts, layered mafic-ultramafic intrusions, deformation, metamorphic events and degree of anataxis (older crusts) (Mondal et al., 2002; Kaur et al., 2014, 2016; Singh and Slabunov, 2015; Verma et al., 2016; Joshi et al., 2017; Singh et al., 2019a, b, c). An important structural feature, about 200 km long an E–W trending, brittle–ductile shear zone, known as the Bundelkhand Tectonic Zone, which represents a tectonic contact between above two segments (Malviya et al., 2006; Gokarn et al., 2013).

The TTG gneisses are the most widespread basement lithology spatially associated with supracrustals (greenstone belts), exposed mainly in central part of the craton. They are polyphase deformed and sporadic occurrences in linear E–W trending belt in central part, whereas patchy basement outcrops (TTGs) around Rungaon area in the southern part of the BC (Table 1; Mondal et al., 2002; Kaur et al., 2014, 2016; Joshi et al., 2017; Nasipuri et al., 2019). TTG gneisses represent oldest felsic crust in the BC and reported geochronological data show four distinct episodes of TTG magmatism between 3.55 and 3.20 Ga (Mondal et al., 2002; Kaur et al., 2014, 2016; Saha et al., 2016; Joshi et al., 2017; Singh et al., 2019c). Additionally, two distinct phases of Neoarchean TTG magmatism between 2.71 and 2.67 Ga have been

reported from the Babina and Mauranipur terranes by Verma et al. (2016) and Singh et al. (2019c).

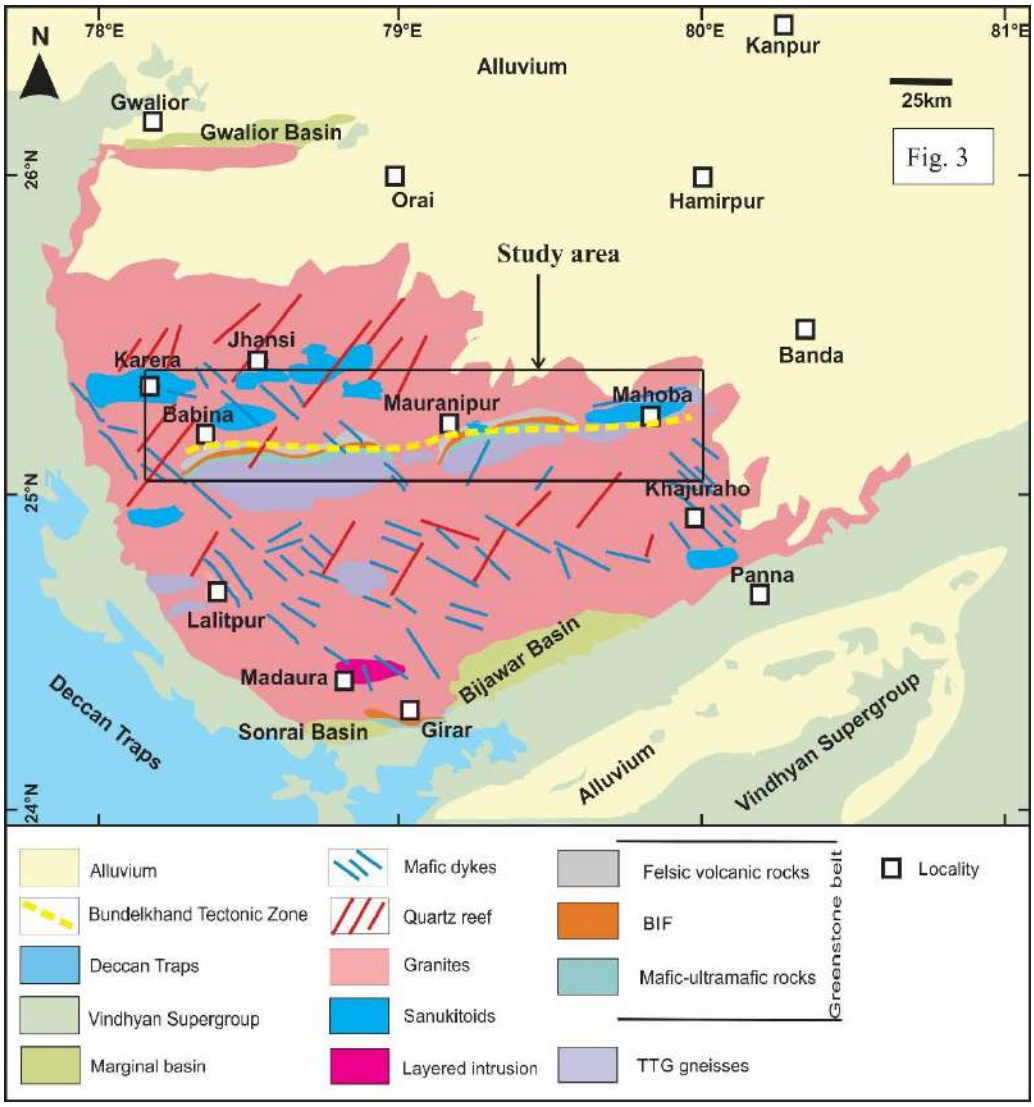

Fig. 2. Geology map of the Bundelkhand Craton (after Basu, 1986; Malviya et al., 2006; Singh and Slabunov, 2015; Verma et al., 2016; Joshi et al., 2017; Singh et al., 2019a, b).

Two distinct greenstone complexes: (i) the central Bundelkhand and (ii) the southern Bundelkhand have been recognized by detailed field and stratigraphic relationships in the BC (Malviya et al., 2006; Singh and Slabunov, 2015, 2016; Singh et al., 2018;

Singh et al., 2019b, c). The central Bundelkhand greenstone complex (CBGC) is located in the central part of the BC and comprises TTG suites, greenstone sequences (ultramafic-mafic volcanics, BIFs and felsic volcanics), granodiorite and anatectic granites (Fig. 2, Malviya et al., 2006; Singh and Slabunov, 2015, 2016; Singh et al., 2018; Slabunov and Singh, 2019, Singh et al., 2019a, b, c). The CBGC is further divided into Babina and Mauranipur greenstone belts (*see for details: next section*). Whereas, the southern Bundelkhand greenstone complex located in the southern part of the craton. It occurs around Rungaon and Girar areas, comprise mostly thick metasedimentary units (variety of quartzites and BIFs) and ultramafic-mafic volcanic rocks (Farooqui and Singh, 2006; Singh and Slabunov, 2016). Slabunov et al. (2017a) reported detrital zircons from the quartzite that were 3.4–3.3 Ga older, which indicates the existence of an Archean crustal block in the provenance.

The layered ultramafic-mafic complex outcrops also occur around the Madawara-Ikauna and Lalitpur areas in the southern parts of the BC. It is considered that layered igneous complexes (*age?*) are older than the high-K granitoids and younger than TTG gneisses (Fig. 2; Farooqui and Singh, 2006; Balaram et al., 2013; Manavalan et al., 2015; Singh and Slabunov, 2016; Slabunov et al., 2017; Mohanty et al., 2018; Ramiz et al., 2018). The Madawara-Ikauna layered ultramafic-mafic complex comprised two types of lithostratigraphic unit: (i) undeformed ultramafic-mafic plutonic rocks (gabbro, harzburgite, lherzolite, and olivine websterite) and (ii) high-Mg ultrabasic-basic rocks (serpentinites, schists and spinel-bearing schists).

The former one has experienced low-grade metamorphism (Farooqui and Singh, 2006; Mohanty et al., 2018; Ramiz et al., 2018; Slabunov et al., 2018).

Table 1. Lithostratigraphic units of the BC.

Rock type	Age (Ga)	Occurrence	Field characteristics and relations
Tonalite–trondhjemite–granodiorite (TTG) gneisses	~3.55–3.20	Babina, Baragaon, Roni, Kuraicha, Mahoba, Karera, Charkhari, Rungaon	Basement unit, polyphase deformed and multiphase emplacement by amphibolites, granodiorite and porphyritic and pink granites. Last phase emplacement by quartz reefs and showing cross cut relationship.
Greenstone units: Ultramafic-mafic volcanics	~3.44	Babina, Baragaon, Roni, Kuraicha	Supracrustal successions intruded on basement unit and have sheared and faulted contact with TTGs. Emplaced by granodiorites, granites, quartz reefs and Mafic dykes. Intense deformation.
Meta sedimentary units	~3.43–3.25	Babina, Pura, Baragaon, Roni, Kuraicha, Prithvipur, Girar, Bedaura	Metasedimentary successions having contact relation with metavolcanic and with felsic volcanic association. Some places have highly intense deformed contact with mafic-ultramafic units.
Felsic volcanics	~2.81–2.54	Babina, Baragaon, Kararkhera, Umri, Mahoba town	Felsic volcanic associations forming top-most unit of greenstone belt. Easily identifiable with other units in the field because of undeformed nature.
layered ultramafic-mafic complex	Age?	Around Madawara, Ikauna and Lalitpur areas	Sporadic outcrops of gabbro, harzburgite, lherzolite, and olivine websterite rocks.
Transitional TTGs	2.71–2.67	Babina, Near Ghisoli and Baghora areas, Kuraicha Village, Mauranipur	Mainly exposed around South of Babina town and intensely intruded by pink granite and mafic dykes. Cut by thick pegmatite veins. It has similar magmatic age of Aravalli Craton. Small outcrop exposed South of Babina town and highly deformed gneiss. High grade metamorphic event (White schist).
Sanukitoids, granodiorites, hybrid granites and anatectic granites	2.59–2.46	Throughout craton	Undeformed outcrops, multiphase emplacement in all older units. Cover almost 75 % of craton.
Giant quartz reefs	2.40–1.80	Series of NE–SW to NNE–SSW trending quartz vein throughout craton,	Giant quartz veins intruded almost everywhere in the craton, having NE-SW trend.
Mafic dykes	1.98–1.10	Throughout craton	NW-SE trends, mafic dyke swarms evidence of extesional tectonic and last phase of magmatic activity, no effects of deformation
Paleoproterozoic marginal basins	2.0-1.8	Gwalior (Northwest), Sonrai (South) and Bijawar (Southwest)	Homotaxial and characterized by clastic sedimentary rocks and carbonates with Banded Iron Formations (BIFs)

Detailed petrological and mineralogical studies suggest that high-Mg ultrabasic rocks are generated by the partial of metasomatized mantle at shallow depth, whereas the undeformed ultramafic-mafic plutonic rocks were originated as a consequence of asthenospheric upwelling from a greater depth that induced the

melting in the overlying lithosphere (Mohanty et al., 2018; Ramiz et al., 2018; Slabunov et al., 2018).

The voluminous undeformed plutons of the high-K granitoid (granodiorites, sanukitoids, anatectic granites) rocks are occupied most of the BC and intruded in the TTG-greenstone association during Neoarchean (2.58–2.50 Ga; Figs. 2, 3; Table 1, Mondal et al., 2002; Kaur et al., 2016; Saha et al., 2016; Joshi et al., 2017; Singh et al., 2019b, c). Anatectic granites generally crop out large part (80%) of the craton, whereas sanukitoids and granodiorites in subordinate amount (Figs. 2 and 3). They locally display intrusive relationship with TTG gneisses and/or greenstone sequences. Most high-K granitoids plutons are undeformed to feebly foliated, but some of them show a moderate to well-developed foliation. These granitoids show multiple episodes of magmatism and crustal reworking mostly during Neoarchean Era (2.58–2.50 Ga) throughout craton mainly in a subduction related setting. Geochemical and isotopic studies reveal that sanukitoids plutons were produced by the mixing of metasomatized mantle melts with anatectic melts, and their homogenization at the lower crust level. Whereas, high-K anatectic granitic plutons suggest that they were originated by the reworking (partial melting) of earlier rocks and were vastly emplaced during cratonic stabilization at 2.5 Ga (Singh et al., 2019b). Mafic magmatic enclaves recognized in the Neoarchean high-K granitoids, which also suggest mantle involvement in the emplacement of the high-K granitic plutons in the BC (Joshi et al., 2017; and Singh et al., 2019b). Ramiz and Mondal, (2017) discussed their petrogenesis and suggest that these mafic enclaves are

contemporaneous with the granitic melt and are a result of rapid crystallization of the mafic melt in the same emplacement event.

An important magmatic structure is recognized in the BC which is well-developed orbicular structures, ranging in age between 2.55–2.50 Ga (Pati and Mamgain, 1996; Srivastava et al., 2004; Ramiz and Mondal, 2015). They are preserved in the medium grained-pink porphyritic granitoids, and exposed at the NW and NE extremities of the craton. There are two main exposures of the orbicular structured granitoids: (i) preserved in the porphyritic granites of Pichhore area of Shivpuri district, NW of the craton and (ii) the other around the Rauli Kalyanpur area of Banda district, NE of the craton. The orbicular structures indicate that they were produced by the magma mixing processes while the whole region was undergoing voluminous granitic magmatism during late Neoarchean (Pati and Mamgain, 1996; Srivastava et al., 2004; Ramiz and Mondal, 2015).

Important post-Neoarchean magmatic events of the BC are recorded in the mafic dyke swarms and giant quartz reefs, which were emplaced into the granite-greenstone terranes (Pati et al. 1998, 1999, 2008; Mondal and Ahmad 2001; Rao et al., 2005, 2008; Pradhan et al., 2012; Slabunov et al., 2017b). Mafic dyke swarms show variable orientations, generally NW–SE (Mondal and Ahmad 2001; Rao et al., 2005, 2008; Pradhan et al., 2012). On the other hand, quartz reefs are commonly aligned along NE–SW directions Pati et al., 1998, 1999). The entire craton is dissected by E–W, NE–SW, NW–SE, and N–S trending shears, fractures/joints.

2. Lithological units, metamorphic events and mineral deposits of the central Bundelkhand greenstone Complex (CBGC)

A summary of lithological units, deformation and metamorphic events of the Archean CBGC is presented below, which mainly relates to the volcano-sedimentary greenstone belts, TTG gneisses and high-K granitoids (granodiorites, sanukitoids and anatectic granites) and are known as constituents of the CBGC (Fig. 3). It preserves multi-stage igneous magmatic events between Paleo- to Neoarchean, which provide a "window" to the composition, structure and physical conditions of continental crust and its geochemical evolution at the early stage in Earth history.

2.1. Lithologies

2.1.1. TTG gneisses

The TTG gneisses are basement units along with supracrustals, and generally sporadic occurrences around the Mauranipur, Baragaon, Kuraicha, Babina, Karitoran, Mahoba and Charkhari in the CBGC (Fig. 3 and Fig. 4a–h). These TTG gneisses were variably metamorphosed and reworked in the late Neoarchean to Paleoproterozoic. TTG gneisses contain either of several banded deformed and/or migmatized magmatic phases intruding each other (Figs. 4a–c and f–g), or of a single, homogeneous orthogneiss (Fig. 4e). They show well-developed gneissose structure; foliation generally strikes NW–SE (Fig. 4f). In some areas weakly- to un-deformed TTGs plutons are recognized, for example Neoarchean TTGs around the Babina greenstone belt (Fig. 4e–g). Some TTG gneisses outcrops have dismembered boudin of mafic rocks occur in the gneisses which are often rotated and traversed by leucocratic veins along shear zones (Fig. 4a–b).

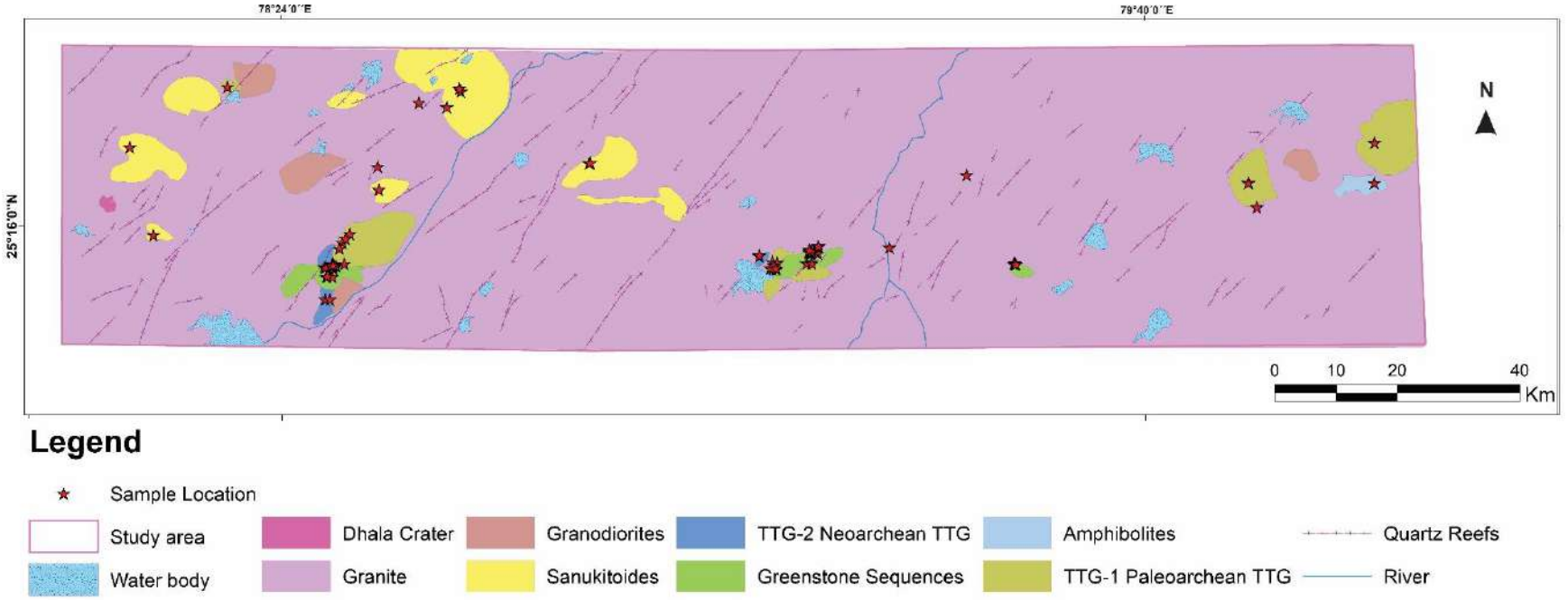

Fig. 3. Detailed Geological map of the CBGC.

TTG gneisses are emplaced by high-K granites (Fig. 4f–g). They generally whitish to gray in color varying generally between leucocratic to mesocratic, medium- to coarse-grained (Figs. 4a–c and f–g). They are characterized by high modal abundance of sodic plagioclase and quartz with respect to alkali feldspar. The main minerals are plagioclase, quartz, hornblende, biotite, and K-feldspar (Figs. 4d and h). Plagioclase is generally anhedral to subhedral in shape with multiple (polysynthetic) twinning. Furthermore, the anti-perhite lamellae are also common some plagioclase crystals are partially altered to sericite. Microcline exhibits characteristic cross-hatched twinning. Ilmenite, titanite, zircon, apatite, and garnet (rarely) are accessory minerals. The less evolved TTG have relatively more mafic minerals which belongs Neoarchean magmatic events. In some places TTGs show evidence of grain size reduction or cataclasis (Fig. 2b in the Kaur et al., 2016).

Two types of TTG gneisses recognized based on field, petrography and age relations which comprise Paleoarchean TTG gneisses (classical type) and Neoarchean TTG gneisses (transitional TTGs). The former gneisses mainly occur in the CBGC, as basement unit (Mondal et al., 2002; Kaur et al., 2014, 2016; Saha et al., 2016; Nashipuri et al., 2019; Singh et al., 2019c) whereas, recently by Verma et al. (2016) and Singh et al. (2019c) have identified Neoarchean TTG gneissic plutons around Babina, Baghora and Kuraicha (Mauranipur) areas in the CBGC. The Paleoarchean TTG gneisses are typically characterized by tonalitic to trondhjemitic in compositions whereas Neoarchean TTGs are mainly granodioritic in nature.

Published U-Pb zircons dating reveal that TTG gneisses accretion is episodic, and occurred at ~3.55 Ga, ~3.44 Ga, ~3.33 Ga, ~3.20 Ga during Paleoarchean (Mondal

et al., 2002; Kaur et al., 2014, 2016; Saha et al., 2016), whereas Neoarchean TTG magmatism at ~2.70 Ga and ~2.60 Ga in the CBGC (Verma et al., 2016; Singh et al., 2019c). The oldest rock of the BC is identified as a TTG gneiss (~3.55 Ga) in the Mauranipur belt, near Kuraicha Village (Kaur et al., 2016), whereas ~3.59 Ga year old xenocrystic zircons are reported from most abundant TTG gneisses (~3.44 Ga) of the Babina (Saha et al., 2016). The most abundant TTG gneisses are of 3.44–3.28 Ga age group recognized in various localities mostly within the CBGC (Mondal et al., 2002; Kaur et al., 2014, 2016; Saha et al., 2016; Verma et al., 2016; Singh et al., 2019c), while some plutons of similar ages are also identified around Girar and Rungaon in the southern part of the craton (Kaur et al., 2016). Additionally, a TTG gneiss pluton have identified significantly older than thus far assumed in the eastern part of the study area, which reveals the existence of TTG gneiss ~3.34 Ga around the Charkhari area (Singh et al., 2019c). Recently, a very interesting finding concerning common Paleoarchean TTG magmatism and mafic-ultramafic volcanism of the Babina belt which is advocate that they were sub-contemporaneous at 3.4 Ga (Mondal et al., 2002; Kaur et al., 2016; Singh et al., 2019, 2019a, c). This finding endorse that Paleoarchean felsic plutonism and mafic-ultramafic volcanism were coeval. Recently, Singh et al. (2019c) have reported two Neoarchean TTG plutons from the Babina belt whereas one from Kuraicha in the Mauranipur belt, for the first time. These finding suggest that two episodes of Neoarchean TTG magmatism took place between ~2.71 Ga and ~2.67 Ga in the CBGC (Verma et al., 2016; Singh et al., 2019c). By comparing ages of felsic volcanics and Neoarchean TTGs reveal that the Neoarchean felsic plutonism and volcanism were coeval in the Mauranipur belt (Slabunov and Singh, 2019; Singh et al., 2019c).

Fig. 4. Representative field photographs and photomicrographs of TTG gneisses from the CBGC. (a–d) Paleoarchean TTG gneisses. (e–h) Neoarchean TTG gneisses.

Geochemically, TTG gneisses are divided broadly into two groups: sodic and potassic. Sodic TTGs are the true TTG whereas potassic TTGs belongs to the transitional TTG gneisses (Mohan et al., 2012; Kaur at al., 2014, 2016; Saha et al., 2016; Joshi et al., 2017, Singh et al., 2019c). A number of studies on TTG gneisses have been reported, and suggesting two petrogenetic environments for Paleoarchean TTGs; (i) oldest TTG gneisses (~3.55 Ga) were generated by the partial melting of an ancient deep-seated mafic crust in the garnet stability field (Mohan et al. 2012; Kaur et al. 2014, 2016; Saha et al., 2016; Singh et al., 2019c), (ii) common TTGs (3.4-3.2 Ga) produced from partial melting of relatively shallow mafic sources in the plagioclase stability field, with involvement of the older TTG crust (Mohan et al. 2012; Kaur et al. 2014, 2016; Joshi et al., 2017; Singh et al., 2019c). In contrast, Neoarchean TTGs (~2.7 Ga) were originated by the partial melting of hydrated garnetiferous mafic rocks interacted with the overlying mantle melts to form the TTG (granodioritic) plutons. Thus it is quite evident that the depth of melting of the subducted slab has changed through time (Singh et al., 2019a, c). Nd and Hf-isotope datasets also unravel reworking of older mafic and felsic crusts between ~3.55 and ~2.50 Ga (Kaur et al., 2014, 2016; Saha et al., 2016; Singh et al., 2019a, b, c).

2.1.2. Greenstone sequences

The CBGC has complex lithology and diverse in field geology (Fig. 3). The greenstone belts are dominated by komatiitic basalts, basalts, BIFs and felsic volcanics (andesites and rhyolites). The CBGC has two distinct greenstone belts that is the Mauranipur and Babina, which are exposed in a linear belt with E-W trend. It

is recognized by Singh and Slabunov (2015) representing an association of ultramafic/mafic-felsic volcanics and metasedimentary rocks (BIFs), which are formed on the highly deformed TTG gneissic basement rock (Mondal et al., 2002; Kaur et al., 2014; Saha et al., 2016; Singh et al., 2019b, c). All these lithologies were multiple intruded by Neoarchean high-K granitoids and Paleoproterozoic quartz reefs and mafic dykes (Kaur et al., 2016; Joshi et al., 2017; Singh et al., 2019a). The age of ultramafic-mafic volcanic rocks has been never reported whereas in this PhD project an attempt has been made for the first time to establish emplacement ages. The Sm-Nd isochrone result reveal that they were emplaced at ca. 3.44 Ga which is sub-contemporaneous with Paleoarchean TTGs (~3.44 Ga) (Singh et al., 2019a, c). The Mauranipur greenstone sequences have well preserved outcrops around the Baragaon village where belt-like exposures, of 4 km long and 1 km wide. They show sparse outcrops around the Raspahari, Kuraicha, and Roni areas (Figs. 2 and 5a–h; Malviya et al., 2006; Singh and Slabunov, 2015; Singh et al., 2017; Slabunov and Singh, 2019).

Pillow lava outcrop is observed in the Saprar river section NW of Kuraicha village. Mafic-ultramafic rocks are usually black and dark gray color (Figs. 5a and c), have sheared and faulted contact with metasedimentary rocks (Fig. 5f). Recently, Singh et al, (2019c) recognized contact between Paleoarchean TTG gneisses and mafic unit of the greenstone belt in Baragaon and Roni areas whereas emplaced by high-K granitoids and quartz veins (Fig. 5a).

Fig. 5. Representative field photographs and photomicrographs of the greenstone sequences. (a–b) Metabaslts. (c–d) Metamorphosed ultramafic rock from Mauranipur belt. (e–f) BIFs outcrops from the Babina and Mauranipur belts. (g–h) Outcrops of the felsic volcanics from the Mauranipur belt.

Mauranipur belt comprised of three different lithologies: (i) Paleoarchean medium to low-grade metamorphosed basalts and basaltic komatiites (Malviya et al., 2006; Singh et al., 2019a); (ii) BIFs (Singh and Slabunov, 2015; Alfimova et al., 2019); and (iii) 2.81–2.56 Ga felsic volcanics (Slabunov and Singh, 2019). The lithology of the Mauranipur belt are similar to those of the Babina belt and emplaced in the similar timeframe (Paleoarchean). The petrographical and mineralogical studies of the mafic-ultramafic rocks display that they were gone through greenschist to amphibolite facies metamorphism (Fig. 5b). Metabasalts are the most common rock in the belt (Slabunov and Singh, 2019; Singh et al., 2018, 2019a), which comprises amphibolites with retrograde chlorite (Figure 4(a) in Slabunov and Singh, 2019) and pillow (Figure 4(b) in Slabunov and Singh, 2018) structures are occasionally present (Malviya et al. 2006; Slabunov and Singh, 2019; Singh et al., 2019b). The lithology of the Mauranipur belt are similar to those of the Babina belt and emplaced in the similar timeframe (Paleoarchean). The petrographical and mineralogical studies of the mafic-ultramafic rocks display that they were gone through greenschist to amphibolite facies metamorphism (Fig. 5b). Metabasalts are the most common rock in the belt (Slabunov and Singh, 2019; Singh et al., 2018, 2019a), which comprises amphibolites with retrograde chlorite (Figure 4(a) in Slabunov and Singh, 2019) and pillow (Figure 4(b) in Slabunov and Singh, 2018) structures are occasionally present (Malviya et al. 2006; Slabunov and Singh, 2019; Singh et al., 2019b). At places, the ultramafic rocks occur as extensively serpentinized dark green color occurring generally in low lying area but a few samples collected from well cuts have well preserved primary olivine and chromium spinel (Fig. 5c–d). These ultramafic rocks are interpreted as basaltic komatiite (Malviya et al. 2006). The metasediments

intercalate with metamorphosed pillow basalt. The BIF is fine- to medium-grained rock with distinct mm- to cm-scale inter-layering of iron oxide and quartzite (Fig. 5f). Recently, Singh et al. (2019a) determined Sm-Nd isochrone age of the ultramafic-mafic rocks, which suggest a Paleoarchean magmatism (~3.44 Ga) contemporaneous with some TTG gneiss plutons in the CBGC. BIFs was formed probably after ultramafic-mafic volcanism in this belt, which could be a Mesoarchean event (Singh and Slabunov, 2013, 2015). SHRIMP U-Pb dating of the felsic volcanic rocks display 2810 ± 13 Ma, 2687 ± 11 Ma (metasomatic age), and 2557 ± 33 Ma, which endorse a two episode of felsic volcanic magmatism during Meso- to Neoarchean (Slabunov and Singh, 2019). The metasomatic age somehow similar to Neoarchean TTG gneisses. Zircons of basalts produce a concordant age of 2687 ± 11 Ma, which is considered age of metamorphism in the Mauranipur greenstone belt (Slabunov and Singh, 2019). Isotope geochemistry of ultramafic-mafic unit reveals a subduction-related setting for their origin, through the magmas underwent fractional crystallization and minor crustal contamination. On the other hand, Singh et al. (2018) proposed a plume-arc accretionary tectonics for the greenstone belt.

The Babina greenstone belt located in the central part of the BC, well exposed about 40 km long and up to 4 km wide in E–W trending. This belt comprises three distinct litho-units: i) ultramafic-mafic volcanic rocks, ii) metasedimentary rocks, and iii) felsic volcanic rocks, in stratigraphy order (Singh and Slabunov, 2015). These greenstone sequences intruded by high-K granitoids, mafic dykes and quartz reefs. The ultramafic-mafic unit comprises of basaltic komatiites, basalts and tholeiitic basalt to basaltic andesite that were variably metamorphosed between greenschist to

amphibolite facies (Malviya et al., 2006; Singh and Slabunov, 2015; Singh et al., 2018; Singh et al., 2019a). It constitutes about 5-10 % of the total outcrop of the greenstone belt. Metasedimentary unit about 10–200 m wide and about 1–10 cm thick BIFs bed occur (Fig. 5f) in the Babina belt (Singh and Slabunov, 2015; Alfimova et al., 2019). Alternating beddings are included dominantly of hematite-magnetite grains and quartz grain layers. Silicate phases also find at some outcrops (Singh and Slabunov, 2015). The ultramafic-mafic volcanic unit yield Sm–Nd whole rock ages of ca. 3.44 Ga, which indicate Paleoarchean volcanism in the Babina belt as similar to Mauranipur belt (Singh et al., 2019a). The felsic volcanic rocks, in this belt, yielded a SHRIMP U-Pb zircon age of 2542 ± 17, which endorse a Neoarchean age for the felsic volcanic unit in the Babina Belt (Singh and Slabunov, 2015). The felsic volcanic age is similar to the abundant anatectic granites magmatic age which suggest a synchronous felsic plutonism and volcanism occurred at ~2.55 Ga. BIFs was deposited presumably at ca ~2.8 Ga in this belt that propose a Mesoarchean event (Singh and Slabunov, 2013, 2015). Until, no age has not been reported so far for the metasedimentary rocks in this belt. Additionally, scares knowledge of the metamorphic history in the BC and is still great matter of research. However, Saha et al. (2011) have recognized a high-P metamorphism from white-mica gneiss and zircon dating reveal metamorphic event at 2.78 Ga.

2.1.3. Granodiorites and sanukitoids

Plutons of sanukitoid and granodiorite have been found in the various localities in the CBGC, e.g., Jhansi, Kochhabhanwar, Sakrar, Sankargarh, Kherai, Nand, Babina, Baghora, Mauranipur and Bilbai (Table 1; Fig. 6a–f). In the Jhansi terrane,

several sanukitoids intrusion form large E-W striking batholiths which vastly intruded by anatectic granites (Fig. 6a; Kaur et al., 2016; Joshi et al; 2017; Ramiz and Mondal, 2017; Singh et al., 2019b, c). In contrast, granodiorites form large plutons some places in the Babina and Jhansi terranes. Granodiorite plutons are typically medium to coarse grained, undeformed to slightly deformed and with foliation (Fig. 6c). Mostly sanukitoids are mesocratic, medium- to coarse-grained, moderate to crude foliated and locally contain mafic minerals (biotite and amphiboles) in aggregates or clots (Figs. 6a, c, and e–f). They do not show any deformation except local sharing and pegmatite and quartz veins intrusion. Mafic magmatic enclaves (MME) is common feature of the sanukitoids and anatectic granites throughout craton (Fig. 6c and e). At numerous outcrops, mingling or mixing between sanukitoids and light grey anatectic granites can be seen, with disrupted boudins within the diatexites. Granitoid plutons show boudins of sanukitoids enclave in high-K anatectic granites around Kochhabhanwar in the Jhansi terranes (Singh et al., 2019b). In addition, few places, large granitoid plutons show sharp contact between sanukitoids and anatectic granites whereas some huge outcrops display synchronous magmatism relations (Joshi et al., 2017; Singh et al., 2019b). Sanukitoids comprise mainly plagioclase, hornblende, biotite and quartz (Figs. 6b and d). Plagioclase is moderately to severely sericitised (Singh et al., 2019b). K-feldspars show perthitic and myrmekitic intergrowths (Fig. 6d) and mostly affected by albitization (Kaur et al., 2016). K-feldspar of sanukitoids (s.l.) is Carlsbad-twinned perthitic microcline. Titanite, apatite, zircon and opaque minerals are the common accessory minerals of the sanukitoids and granodiorites.

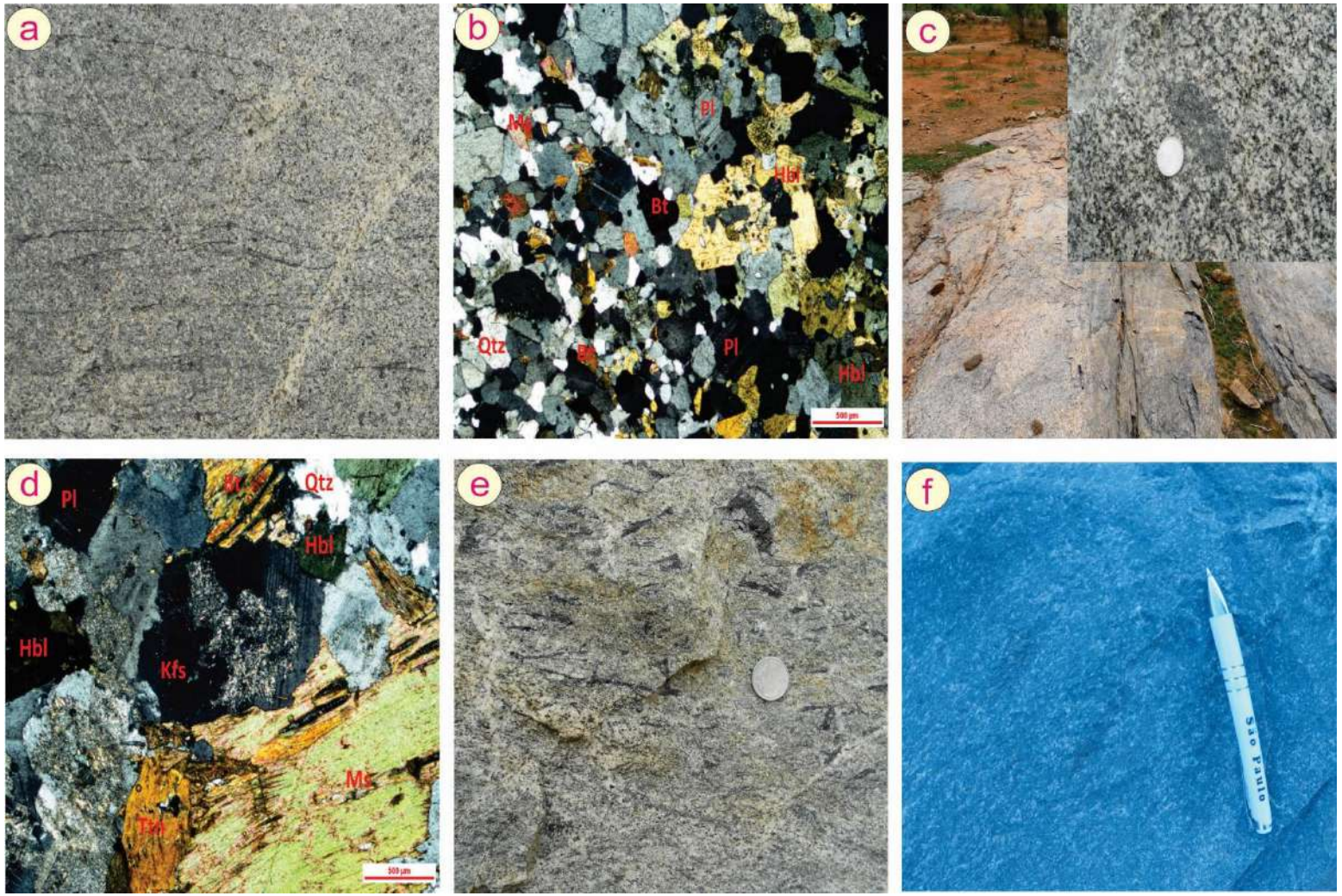

Fig. 6 (a–f). Representative field photographs and photomicrographs of sanukitoids and granodiorites.

Based on whole-rock geochemistry, calc-alkaline granitoids classified into granodiorite, sanukitoids and Closepet-type (Kaur et al., 2016; Joshi et al., 2017; Singh et al., 2019b, c). They were plotted in the fields of diorite, syenodiorite, and granodiorite with characteristics features ranging from alkali to calcic, magnesian and mostly metaluminous in nature. They display a wide range of SiO_2 contents, high MgO and have high contents of mantle-compatible elements such as Mg, Cr, and Ni. Sanukitoids show enrichment in large-ion lithophile elements (LILE), along with negative Ba, Sr, P, Nb-Ta and Ti anomalies. They are elevated Ba+Sr and enrichment in the LREE compared with the HREE, and low Yb and Y contents. Based on overall geochemical and isotopic characteristics, it has been interpreted that the granodiorites and sanukitoids were originated from the mixing of metasomatized mantle with crustal-generated melts and were followed by homogenization at shallow levels of incursions in a subduction environment. The occurrence of xenocrystic zircons with older ages (2914 ± 8 Ma, 2842 ± 3 Ma, 2644 ± 25 and 2619 ± 24 Ma) from sanukitoids also supporting to the ancient crustal material contributions in their genesis (Joshi et al., 2017; Singh et al., 2019b, c). The sanukitoid intrusions happened during Neoarchean in the BC, as similar to other cratonic terranes of the Indian shield and globally (Condie and Aster, 2010; Jayananda et al., 2018). Geochronological studies reveal that sanukitoid rocks were emplaced ca. 2.56 Ga. However, field relationships and chronology of sanukitoids and anatectic granites unravel for the contemporaneous magmatism at ca. 2.55 Ga (Mondal et al., 2002; Kaur et al., 2016; Joshi et al., 2017; Singh et al., 2019b, c).

2.1.4. Anatectic granites

Undeformed anatectic granites are known throughout in the BC and occupying ~80 % of the cratonic part (Fig. 3). In the CBGC, large discrete potassic plutons are intruded TTG-greenstone association during Neoarchean and covering about 75 percent total area of this terrane. Anatectic granites are medium- to coarse-grained, equigranular, undeformed excepting locally shear zone deformation (Fig. 7a–c). Few plutons locally show a porphyritic texture and foliation generally strikes NW–SE with northeasterly dips (55–60) around Kuraicha and Panchora, while the foliation in granitoids at Dinara and Rungaon trends NE–SW with northwesterly dip (35–60) (Kaur et al., 2016). These granitic plutons are intruded by pegmatite veins, porphyry dykes and dyke swarms (Fig. 7b). Anatectic granites contain mainly quartz, bimodal quartz, K-feldspar, but in others, plagioclase, biotite (Fig. 7d–f). The biotite is partly to completely replaced by chlorite and rarely muscovite (Kaur et al., 2016). The titanite, apatite, epidote zircon, allanite some opaques are common accessory minerals. Multi episode generations of anatectic granites are documented in the BC and intruded in to TTG-greenstone associations. The major granite intrusions occurred during ca. 2.58–2.50 Ga that are connected to the stabilization of the BC ~2.50 Ga (Fig. 3; Table 1, Mondal et al., 2002; Kaur et al., 2016; Saha et al., 2016; Joshi et al., 2017). The anatectic granites share similar geochemical characteristics of Cordilleran-type granitoids (Frost et al., 2001) produced in arcs and post-collisional settings; their primarily magnesian character may indicate a formation under oxidizing conditions (e.g., Frost and Frost, 2008). Their metaluminous to slightly peraluminous composition.

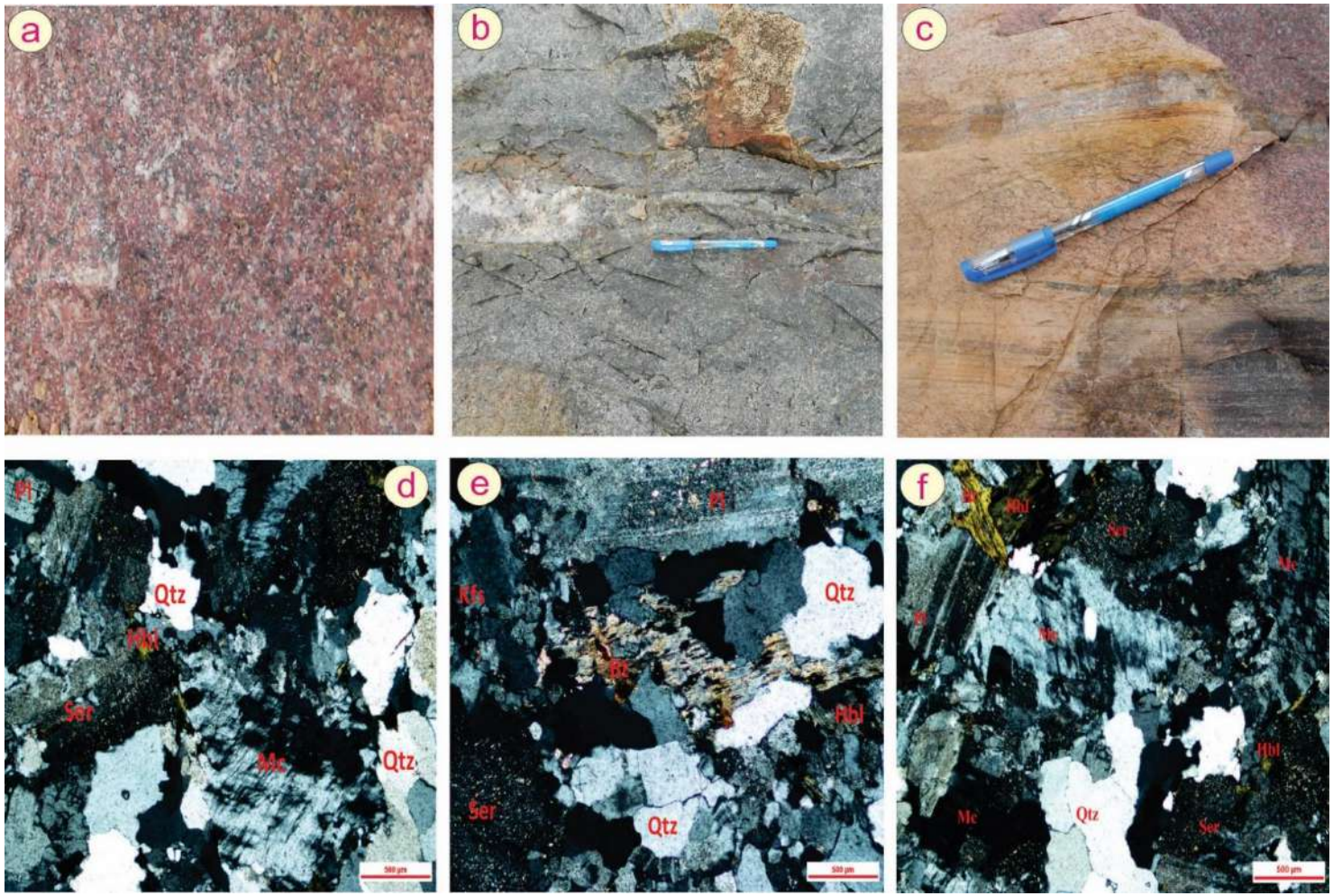

Fig. 7 (a–f). Representative field photographs and photomicrographs of anatectic granites.

The occurrence of the xenocrystic zircons also support for anataxis origin. Therefore, these granites might consequence of the partial melting of igneous rocks, probably TTGs and granodiorite in the shallow to lower continental crust (Moyen, 2011; Singh et al., 2019b) but under conditions that inhibit zircon survival (Bea et al., 2007). The field relations and similar emplacement ages unravel that sanukitoids magmatism could also have played an important role in providing the necessary heat flux for crustal melting in order to produce anatectic melts. Although, the Neoarchean-Paleoproterozoic transition period was recorded an important time in the Earth history. This time period was a period for cratonization and stabilization of the cratonic bodies globally including the BC.

Finally, at ~2.50 Ga, cratonization occurred through the arc-continent collision and repetitive slab break-off of the diverse micro-blocks in the CBGC. Additionally, ample anatectic granites were generated by concentrated partial melting of the ancient rocks in a post-collision extensional environment after a collision event. The occurrence of these processes would then suggest that Neoarchean crust-mantle interaction played an important role in the evolution and cratonization of the BC.

2.2. Metamorphic events

Few studies have discussed the metamorphic history of BC (Saha et al., 2011; Nashipuri et al., 2019). TTG and ultramafic-mafic rocks have deformed and metamorphosed, showing at least three phases of metamorphism. A high-pressure metamorphism event (18-20 kbar and ca. 630 C) took place at ~ 2.78 Ga, recorded in the white schist (corundum-bearing) of the Babina belt (Saha et al., 2011). These

metamorphic events were followed by voluminous high-K granitoid magmatism at ~2.50 Ga (Mondal et al., 2002; Kaur et al., 2016; Verma et al., 2016; Joshi et al., 2017; Singh et al., 2019b, c). In addition, a Paleoarchean metamorphic overprint (~ 3.20 Ga) has been recognized in TTG by Kaur et al. (2016) and recently, Nashipuri et al. (2019) have published on the structural and metamorphic evolution of the basement unit (TTG) of the Babina belt that reveals a metamorphism with P - T ranges of ~ 6.5-8.5 kbar, 630-720 ° C (hornblende-plagioclase-quartz bearing assemblage) attained during the final stages of the crystallization of magma. In conclusion, Integrated zircon imaging and U-Pb data reveal metamorphic events at ~3.30 Ga, 3.29 Ga, 3.20 Ga, ~2.78 Ga, ~2.55 Ga, ~2.48 Ga and ~2.13 Ga (Mondal et al., 2002; Saha et al., 2011, 2016; Kaur et al., 2014, 2016; Joshi et al., 2017; Slabunov and Singh, 2019; Nasipuri et al., 2019; Singh et al., 2019b, c).

2.3. Mineral deposits in the Bundelkhand Craton

Most Archean granite-greenstone terranes host important economic mineral deposits (e.g. Cu, Ni, Fe, Au and Cr). Concerning the BC, no significant economic metal deposits have been reported. But, diaspore and pyrophyllite are some nonmetal deposits that are deposited in the BC. They are commercially mined for ceramic industry. In addition, BIFs (iron ore), occur mainly in the greenstone belts of the BC. BIFs are low-grade iron deposits and mainly occur around the Babina, Mauranipur and Prithvipur in the central part and around Girar area in the southern part of the BC. Slag and waste dump materials indicate the mining of iron ore and other base metals for local purposes in these areas since ancient times. The

mineralization of molybdenite hosted in granitoids have also reported and associated mainly with the Central Bundelkhand Tectonic Zone, Raksa Shear Zone and localized shear zones that coincide mainly with the recognized trend in the case of gold mineralization (Pati et al., 1997, 2014). Pyrophyllite and Diaspore are the only minerals that are commercially mine in the BC. The diaspore is found as geodes, veins and dissemination in pyrophyllite (Misra 1947). They are deposited mainly in the Jhansi and Lalitpur districts and approximately 2,30,000 and 40,000 tons are reserved, respectively. The deposits occur at the junction of the Kuraicha and Palar formations of the Mehroni Group in the BC. The deposits appear to be of the laterite-type products of the Mahoba–Baghora gneisses that were subjected to metamorphism (Sharma 1979). These deposits are linked with the NE–SW trending quartz reefs (Valdiya, 2010). Currently, new minerals are found as rare earth elements in the area of Khajra Bujurg in Jhansi and diamonds in the districts of Banda, but it remains a major topic of research and exploration (DGM, UP). In addition, there are many mining exploration programs underway in the BC, which include platinum and palladium mineralization in the layered ultramafic-mafic complex, asbestos deposits in the greenstone belt of Mauranipur and the mineralization of are earth elements in the carbonatites in the Jhansi area (DGM, UP). Research and exploration of gold mineralization in the Girar greenstone belt and placer gold deposits in the Berwar area are still ongoing in the Lalitpur district.

Finally, the above-mentioned shows that the BC needs a series of investigations and explorations to find its mineral deposits.

References:

Absar, N., Raza, M., Roy, M., Naqvi, S. M., Roy, A. K., 2009. Composition and weathering conditions of Paleoproterozoic upper crust of Bundelkhand craton, Central India: records from geochemistry of clastic sediments of 1.9 Ga Gwalior Group. Precambrian Research 168, 313–329.

Acharyya, S. K., 2003. The nature of Mesoproterozoic Central Indian Tectonic Zone with exhumed and reworked older granulites. Gondwana Research 6, 197–214.

Ahmad, T. and Tarney, J., 1994. Geochemistry and petrogenesis of late Archaean Aravalli volcanics, basement enclaves and granitoids, Rajasthan. Precambrian Research 65, 1–23.

Alfimova, N., Raza, M. B., Felitsyn, S., Matrenichev, V., Bogomolov, E., Nasipuri, P., Kumar, V., 2019. Isotopic Sm-Nd signatures of Precambrian Banded Iron Formation from the Fennoscandian shield, East-European Platform, and Bundelkhand craton, India. Precambrian Research 328, 1–8.

Balaram, V., Singh, S.P., Satyanarayanan, M., Anjaiah, K.V., 2013. Platinum group elements geochemistry of ultramafic and associated rocks from Pindar in Madawara Igneous Complex, Bundelkhand massif, central India. Journal of Earth System Science 122, 79–91.

Basu, A. K., 1986. Geology of parts of the Bundelkhand granite massif central India. In: Records, Geological Survey of India (Ed.) 117, 61–124.

Bea, F., Montero, P., González-Lodeiro, F. and Talavera, C., 2007. Zircon inheritance reveals exceptionally fast crustal magma generation processes in Central Iberia during the Cambro-Ordovician. Journal of Petrology 48, 2327–2339.

Condie, K. C., Aster, R. C., 2010. Episodic zircon age spectra of orogenic granitoids: the supercontinent connection and continental growth. Precambrian Research 180, 227–236.

Department of Geology and Mining, Uttar Pradesh (DGM UP), Lucknow.

Farooqui, S. A., Singh, A. K., 2006. Platinum mineralization in Ikauna Area, Lalitpur District, Uttar Pradesh. Journal-Geological Society of India 68, 582–584.

Frost, B. R., Barnes, C. G., Collins, W. J., Arculus, R. J., Ellis, D. J. and Frost, C. D., 2001. A geochemical classification for granitic rocks. Journal of Petrology 42, 2033–2048.

Frost, B. R., Frost, C. D., 2008. A geochemical classification for feldspathic igneous rocks. Journal of Petrology 49, 1955–1969.

Gokarn, S. G., Rao, C. K., Selvaraj, C., Gupta, G., Singh, B. P., 2013. Crustal evolution and tectonics of the Archean Bundelkhand craton, Central India. Journal of the Geological Society of India 82, 455–460.

Jayananda, M., Santosh, M., Aadhiseshan, K. R., 2018. Formation of Archean 3600–2500 Ma continental crust in the Dharwar Craton, southern India. Earth Science Review 181, 12–42.

Joshi, K. B., Bhattacharjee, J., Rai, G., Halla, J., Ahmad, T., Kurhila, M., Choudhary, A. K., 2017. The diversification of granitoids and plate tectonic implications at the Archaean–Proterozoic boundary in the Bundelkhand Craton, Central India. Geological Society, London, Special Publications 449, 123–157.

Kaur, P., Zeh, A., Chaudhri, N., 2014. Characterisation and U–Pb–Hf isotope record of the 3.55 Ga felsic crust from the Bundelkhand Craton, northern India. Precambrian Research 255, 236–244.

Kaur, P., Zeh, A., Chaudhri, N., Eliyas, N., 2016. Unravelling the record of Archaean crustal evolution of the Bundelkhand Craton, northern India using U–Pb zircon–monazite ages,

Lu–Hf isotope systematics, and whole-rock geochemistry of granitoids. Precambrian Research 281, 384–413.
Laurent, O., Martin, H., Moyen, J. F., Doucelance, R., 2014. The diversity and evolution of late-Archean granitoids: Evidence for the onset of “modern-style” plate tectonics between 3.0 and 2.5 Ga. Lithos 205, 208–235.
Malviya, V. P., Arima, M., Pati, J. K., Kaneko, Y., 2006. Petrology and geochemistry of metamorphosed basaltic pillow lava and basaltic komatiite in the Mauranipur area: subduction related volcanism in the Archean Bundelkhand craton, Central India. Journal of Mineralogical and Petrological Sciences 101, 199–217.
Manavalan, S., Singh, SP, Balaram, V., Niranjan, M., 2015. Geochemistry of the Madawara Igneous Complex, Bundelkhand Craton, Central India: Implications for PGE Metallogeny. Open Geosciences 7.
Manglik, A., Adilakshmi, L., Suresh, M., Thiagarajan, S., 2015. Thick sedimentary sequence around Bahraich in the northern part of the central Ganga foreland basin. Tectonophysics 653, 33–40.
Meert, J.G., Pandit, M.K., Pradhan, V.R., Banks, J., Sirianni, R., Stroud, M., Newstead, B., Gifford, J., 2010. Precambrian crustal evolution of Peninsular India: a 3.0 billion year odyssey. Journal of Asian Earth Sciences 39, 483–515.
Mohan, M. R., Singh, S. P., Santosh, M., Siddiqui, M. A., Balaram, V., 2012. TTG suite from the Bundelkhand Craton, Central India: geochemistry, petrogenesis and implications for Archean crustal evolution. Journal of Asian Earth Sciences 58, 38–50.
Mohanty, N., Singh, S. P., Satyanarayanan, M., Jayananda, M., Korakoppa, M. M., Hiloidari, S., 2018. Chromian spinel compositions from Madawara ultramafics, Bundelkhand Craton: Implications on petrogenesis and tectonic evolution of the southern part of Bundelkhand Craton, Central India. Geological Journal.
Mondal, M. E. A. and Ahmad, T., 2001. Bundelkhand mafic dykes, central Indian shield: implications for the role of sediment subduction in Proterozoic crustal evolution. Island Arc 10, 51–67.
Mondal, M. E. A., Goswami, J. N., Deomurari, M. P., Sharma, K. K., 2002. Ion microprobe $^{207}Pb/^{206}Pb$ ages of zircons from the Bundelkhand massif, northern India: implications for crustal evolution of the Bundelkhand–Aravalli protocontinent. Precambrian Research 117, 85–100.
Mondal, M. E. A., Sharma, K. K., Rahman, A., Goswami, J. N., 1998. Ion microprobe ^{207} Pb/^{206} Pb zircon ages for gneiss-granitoid rocks from Bundelkhand massif: Evidence for Archaean components. Current Sceince 70–75.
Moyen, J. F., 2011. The composite Archaean grey gneisses: petrological significance, and evidence for a non-unique tectonic setting for Archaean crustal growth. Lithos 123, 21–36.
Naqvi, S.M., Rogers, J.J.W., 1987, Precambrian Geology of India: Oxford monographs on geology and geophysics, no. 6, Oxford, Oxford University Press 223.
Nasipuri, P., Saha, L., Hangqiang, X., Pati, J.K, Satyanaryanan, M., Sarkar, S., Bhandari, A., Gaur, Y., 2019. Paleoarchean Crustal Evolution of the Bundelkhand Craton, North Central India. Earth’s Oldest Rocks, Chapter 31, 793–817.
Pandey, U. K., Bhattacharya, D., Sastry, D. V. L. N., Pandey, B. K., 2011. Geochronology Rb-Sr, Sm-Nd and Pb-Pb, isotope geochemisty and evolution of the granites and andesites hosting Mohar Cauldron, Bundelkhand Granite Complex, Shivpuri district, Central India. Exploration Research Atomic Mineral 21, 103–116.
Pati, J. K., Patel, S. C., Pruseth, K. L., Malviya, V. P., Arima, M., Raju, S., Prakash, K., 2007. Geology and geochemistry of giant quartz veins from the Bundelkhand Craton, central India and their implications. Journal of Earth. System Sciences 116, 497–510.

Pati, J. K., Raju, S., Malviya, V. P., Bhushan, R., Prakash, K. and Patel, S. C., 2008. Mafic dykes of Bundelkhand craton, Central India: field, petrological and geochemical characteristics. Indian dykes: geochemistry, geophysics and geochronology. Narosa Publishing House, New Delhi 547–569.

Pati, J.K., 1997. Gold mineralization in parts of Bundelkhand Granitoid Complex (BGC). Journal Geological Society of India 50, 601–606.

Pati, J.K., 1998. Specialized thematic studies of quartz reefs and mylonite zones in parts of Bundelkhand Granitoid Complex, southern UP. Resources Geological Survey of India 130, 88–89.

Pati, J.K., 1999. Study of granitoid mylonites and reef/vein quartz in parts of Bundelkhand Granitoid Complex (BGC). Resources Geological Survey of India 131, 95–96.

Pati, J.K., Mamgain, V.D., 1996. A note on the occurrence of orbicular rocks in Bundelkhand Granitoid Complex. Journal of Geological Society of India 48, 345–348.

Pradhan, V. R., Meert, J. G., Pandit, M. K., Kamenov, G., Mondal, M. E. A., 2012. Paleomagnetic and geochronological studies of the mafic dyke swarms of Bundelkhand craton, central India: implications for the tectonic evolution and paleogeographic reconstructions. Precambrian Research 198, 51–76.

Radhakrishna, T., Chandra, R., Srivastava, A. K., Balasubramonian, G., 2013. Central/Eastern Indian Bundelkhand and Bastar cratons in the Palaeoproterozoic supercontinental reconstructions: A palaeomagnetic perspective. Precambrian Research 226, 91–104.

Ramakrishnan, M., Vaidyanadhan, R., 2010. Geology of India (Vol. 1 & 2). GSI Publications 2.

Ramiz, M. M., Mondal, M. E. A., 2015. Orbicular structures near Pichhore, Shivpuri district, Bundelkhand Craton: forerunner for geoheritage site. Current Science 109, 684–687.

Ramiz, M. M., Mondal, M. E. A., 2017. Petrogenesis of mafic magmatic enclaves of the Bundelkhand granitoids near Orchha, Central Indian shield: evidence for rapid crystallization. Geological Society, London, Special Publications 449, 159–173.

Ramiz, M. M., Mondal, M. E. A., Farooq, S. H., 2018. Geochemistry of ultramafic–mafic rocks of the Madawara Ultramafic Complex in the southern part of the Bundelkhand Craton, Central Indian Shield: Implications for mantle sources and geodynamic setting. Geological Journal.

Rao, J.M., 2004. The wide-spread 2 Ga dyke activity in the Indian shield–evidences from Bundelkhand mafic dyke swarm, Central India and their tectonic implications. Gondwana Research 7, 1219–1228.

Rao, J.M., Rao, G.V.S.P., Widdowson, M., Kelley, S.P., 2005. Evolution of Proterozoic mafic dyke swarms of the Bundelkhand Granite Massif, Central India. Current Science 88, 502–506.

Saha, L., Frei, D., Gerdes, A., Pati, J. K., Sarkar, S., Patole, V., Nasipuri, P., 2016. Crustal geodynamics from the Archaean Bundelkhand Craton, India: constraints from zircon U–Pb–Hf isotope studies. Geological Magazine 153, 179–192.

Saha, L., Pant, N. C., Pati, J. K., Upadhyay, D., Berndt, J., Bhattacharya, A., Satynarayanan, M., 2011. Neoarchean high-pressure margarite–phengitic muscovite–chlorite corona mantled corundum in quartz-free high-Mg, Al phlogopite–chlorite schists from the Bundelkhand craton, north central India. Contributions to Mineralogy and Petrology 161, 511–530.

Sarkar, A., 1996. Geochronology and Geochemistry of Mid Archaean Trondhjemitic gneisses from Bundelkhand craton, Central India. Recent Res. Geol. 16, 76–92.

Shrivastava, S.K., Nambiar, K.V., and Gaur, V.P., 2004. Orbucular structures in Bundelkhand Granitoid Complex near Pichhore, Shivpuri district, Madhya Pradesh. Journal of Geological Society of India 64, 677–684.

Singh, P.K., Verma, S.K., Moreno, J.A., Singh, V.K., Malviya, V.P., Oliveira, E.P., Mishra, M., Arima, M., 2019a. Geochemistry and Sm–Nd isotope systematics of mafic-ultramafic rocks from the Babina and Mauranipur greenstone belts, Bundelkhand Craton, India: Implications for tectonic setting and Paleoarchean mantle evolution. Lithos 330, 90–107.

Singh, P.K., Verma, S.K., Singh, V.K., Moreno, J.A., Oliveira, E.P., Mehta, P., 2019b. Geochemistry and petrogenesis of sanukitoids and high-K anatectic granites from the Bundelkhand Craton, India: Implications for late-Archean crustal evolution. Journal of Asian Earth Sciences 174, 263–282.

Singh, P.K., Verma, S.K., Singh, V.K., Moreno, J.A., Oliveira, E.P., 2019c. Zircon geochronology, geochemistry and petrogenesis of the TTG gneisses and high-K granitoids from the central Bundelkhand granite-greenstone terrane in the Bundelkhand Craton, India: Implications for Archean crustal evolution. Lithos.

Singh, S. P., Subramanyam, K. S. V., Manikyamba, C., Santosh, M., Singh, M. R., Kumar, B. C., 2018. Geochemical systematics of the Mauranipur-Babina greenstone belt, Bundelkhand Craton, Central India: Insights on Neoarchean mantle plume-arc accretion and crustal evolution. Geoscience Frontiers 9, 769–788.

Singh, V. K., Slabunov, A., 2016. Two types of Archaean supracrustal belts in the Bundelkhand craton, India: Geology, geochemistry, age and implication for craton crustal evolution. Journal of Geological Society of India 88, 339–348.

Singh, V.K., Slabunov, A., 2015. The central Bundelkhand Archaean greenstone complex, Bundelkhand craton, central India: geology, composition, and geochronology of supracrustal rocks. International Geology Review 57, 1347–1362.

Slabunov, A., Egorova, S., Singh, VK, Svetov, S., Kumar, S., 2019. Archean mafic-ultramafic Ikauna layered intrusion, Bundelkhand craton, India: petrography and geochemistry. Archeology andAnthropology 49-55.

Slabunov, A., Singh, V.K., Kumar, B., Xiaoli, L., 2017a. Paleoarchean zircons from quartzite of South Bundelkhand Supracrustal Complex: origin and implications for crustal evolution in Bundelkhand Craton, Central India. Current Science 112, 794–801.

Slabunov, A.I., Singh, V.K., Shchiptsov, V.V., Lepekhina E. N., Kevlich V.I., 2017b. A new Paleoproterozoic 1.9–1.8 Ga event in the crustal evolution of the Bundelkhand Craton, India: the results of SHRIMP Dating of zircons from giant quartz veins. In: Slabunov, A.I., Svetov, S.A., Baltibaev, Sh.K. eds., Early Precambrian vs Modern Geodynamics. Extended Abstracts and Field Trips Guide. Petrozavodsk: KarRC RAS pp. 239–241.

Slabunov, A. I., Singh, V. K., 2019. Meso–Neoarchaean crustal evolution of the Bundelkhand Craton, Indian Shield: new data from greenstone belts. International Geology Review 61, 1409–1428.

Turner, C.C., Meert, J.G., Pandit, M.K., Kamenov, G.D., 2014. A detrital zircon U-Pb and Hf isotopic transect across the Son Valley sector of the Vindhyan Basin, India: implications for basin evolution and paleogeography. Gondwana Research 26, 348–364.

Valdiya, K.S., 2010. The Making of India: Geodynamic Evolution, Macmillan Publishers. New Delhi 848.

Verma, S. K., Verma, S. P., Oliveira, E. P., Singh, V. K., Moreno, J. A., 2016. LA-SF-ICP-MS zircon U–Pb geochronology of granitic rocks from the central Bundelkhand greenstone complex, Bundelkhand craton, India. Journal of Asian Earth Sciences 118, 125–137.

Yedekar, D.B., 1990. The central Indian collision suture. Geological Survey of India, Special Publication 28, 1–43.

CHAPTER 2

Geochemistry and Sm-Nd isotope systematics of mafic-ultramafic rocks from the Babina and Mauranipur greenstone belts, Bundelkhand Craton, India: Implications for tectonic setting and Paleoarchean mantle evolution

A presentation of the published research paper

This research paper is published in *Lithos*, in which the author of this thesis actively participated. I am the first author, and Dr. Sanjeet K. Verma, Dr. Juan A. Moreno, Prof. Vinod K. Singh, Dr. Vivek P Malviya, Prof. Elson Oliveira, Sumit Mishra and Prof. Makoto Arima are the co-authors of the research article.

My Contribution in this research work can be summarized as follows:

1. Field work and sample collection
2. Sample preparation and experiments
3. Data calculation and diagram preparation
4. Data interpretation and write-up of the work

Lithos 330–331 (2019) 90–107

Contents lists available at ScienceDirect

Lithos

journal homepage: www.elsevier.com/locate/lithos

Geochemistry and Sm—Nd isotope systematics of mafic-ultramafic rocks from the Babina and Mauranipur greenstone belts, Bundelkhand Craton, India: Implications for tectonic setting and Paleoarchean mantle evolution

Pradip K. Singh [a], Sanjeet K. Verma [b,*], Juan A. Moreno [c], Vinod K. Singh [d], Vivek P. Malviya [e,f], Elson P. Oliveira [g], Sumit Mishra [d,h], Makoto Arima [e]

[a] Posgrado de la División de Geociencias Aplicadas, Instituto Potosino de Investigación Científica y Tecnológica (IPICYT), Camino a la Presa San José 2055, San Luis Potosí 78216, Mexico
[b] División de Geociencias Aplicadas, Instituto Potosino de Investigación Científica y tecnológica (IPICYT), Camino a la Presa San José 2055, San Luis Potosí 78216, Mexico
[c] Centro de Investigaciones en Ciencias de la Tierra (CICTERRA), Consejo Nacional de Investigaciones Científicas y Técnicas, Facultad de Ciencias Exactas, Físicas y Naturales, Universidad Nacional de Córdoba, Av. Vélez Sarsfield 1611, Edificio de CICTERRA, X5016CGA Córdoba, Argentina
[d] Department of Geology, Institute of Earth Sciences, Bundelkhand University, Jhansi, India
[e] Graduate School of Environmental and Information Sciences, Yokohama National University, 79-7 Tokiwadai, Hodogaya-Ku, Yokohama 240-8501, Japan
[f] 24E Mayur Residency Ext, Indra Nagar, Lucknow 226015, India
[g] Department of Geology and Natural Resources, Institute of Geosciences, PO Box 6152, University of Campinas – UNICAMP, 13083-970 Campinas, SP, Brazil
[h] Department of Geology, School of Earth Sciences, H.N.B. Garhwal University, Srinagar, Pauri Garhwal 246174, India

ARTICLE INFO

Article history:
Received 13 June 2018
Accepted 11 February 2019
Available online 16 February 2019

Keywords:
Mafic-ultramafic rocks
Sm-Nd geochronology
Geochemistry
Paleoarchean mantle evolution
Tectonic setting
Bundelkhand Craton

ABSTRACT

The Paleoarchean geodynamical evolution of the Bundelkhand Craton is discussed based on the geochemistry (major, trace and rare earth elements) and Sm—Nd isotope systematic of mafic-ultramafic rocks from volcano-sedimentary succession of the Babina and Mauranipur greenstone belts. The petrography and mineral assemblages of these mafic-ultramafic rocks imply that they were gone through greenschist to amphibolite facies metamorphism. Geochemical analyses indicate that mafic rocks from the Babina are characterized by SiO_2 = 43.9–51.2 wt%, MgO = 5.4–11.0 wt%, TiO_2 = 0.3–1.14 wt% and Mg# = 44–77, whereas the Mauranipur are characterized by higher silica (51.8–55.6 wt%), MgO = 6.9–9.5 wt% and Mg# = 59–70. The ultramafic rocks from the Babina and Mauranipur contain SiO_2 = 46.9–50.3 wt%, MgO = 20.2–21.1 wt%, TiO_2 = 0.33–0.46 wt% and Mg# = 77–82. Six samples of mafic-ultramafic rocks from the Babina greenstone belt yield ^{147}Sm—^{143}Nd whole rock isochron age of ca. 3.4 Ga. Sm—Nd isotopic studies of mafic rocks from the Babina and Mauranipur reveal that they were derived from a depleted mantle source. Bivariate diagrams such as Cr vs. Ni and V suggest that these magmas might have evolved through fractionation of clinopyroxene and olivine. The mafic rocks from the Babina displayed almost a flat REE and HFSE profile [$(La/Yb)_{PM}$ = 0.87–1.40] with negative Nb (Nb/Nb^* = 0.13–0.77) and positive Pb anomalies that could be attributed to metasomatic agents derived from subducting crustal rocks. The Mauranipur mafic rocks show slightly enriched REE [$(La/Yb)_{PM}$ = 1.1–1.7; $(La/Sm)_{PM}$ = 1.1–2.0] with negative Nb anomalies (Nb/Nb^* = 0.13–0.77), which are most likely the effects of crustal contamination. The ultramafic rocks from both areas and ultramafic cumulate rock from the Mauranipur display a progressive enrichment from Th, La to Yb, with negative Nb anomalies (Nb/Nb^* = 0.40–0.73) with lack of Zr anomalies (Zr/Zr^* = 0.10–0.30) that could be attributed to their derivation from shallower mantle. These data collectively suggest that the mafic-ultramafic rocks have been interpreted to be derived from oceanic crust in a subduction-related setting with depleted mantle composition.

1. Introduction

Mafic-ultramafic volcanic rocks (i.e. komatiite, basaltic komatiite, basalt and high–Mg basalt) are key components of greenstone belt of Archean cratons (Anhaeusser, 2014; Condie, 2000; Verma et al., 2017a). Along with mafic-ultramafic volcanics, banded iron formations (BIF) and felsic volcanic rocks also comprise a minor but

* Corresponding author.
E-mail addresses: pradip.singh@ipicyt.edu.mx (P.K. Singh), sanjeet.verma@ipicyt.edu.mx (S.K. Verma), jmoreno_2@ugr.es (J.A. Moreno), vinodksingh@bujhansi.ac.in (V.K. Singh), vivek.geology@gmail.com (V.P. Malviya), elson@ige.unicamp.br (E.P. Oliveira), arima@ynu.ac.jp (M. Arima).

https://doi.org/10.1016/j.lithos.2019.02.010
0024-4937/

important part of greenstone belts (Anhaeusser, 2014; Kump and Barley, 2007; Parman et al., 1997, 2004). However, mafic-ultramafic volcanic and associated rocks provide vital clue to understand whether the greenstone belt formed by mantle-derived magma in continental or in oceanic environment due to subduction-accretion processes (Bédard et al., 2014; Manikyamba et al., 2005; Pearce, 2008; Stott and Mueller, 2009).

Mafic component provides much insight into understanding the geodynamics of early Earth history, because they are upper mantle derived melts (Condie et al., 2016; Herzberg et al., 2010). For example, geochemistry of modern basalt shows heterogeneous composition of mantle by extraction and separation of continental crust through time (Arndt et al., 2008; Condie, 2000; Herzberg et al., 2010; Hofmann, 2003; Iwamori and Nakamura, 2015; Williams and Bizimis, 2014). However, Condie (2005) has geochemically explained that many Archean basalts are derived from a mantle source, and that the state of mantle depletion in the Archean is uncertain. If most of the Archean mantle had a primitive composition it may have serious implications for our understanding of continent evolution and formation. It is worth noting that the composition of the mantle from which most modern basalts have been extracted is similar to the composition of modern MORB and OIB, and their major and trace element geochemistry favor that the Archean mantle may have had a similar composition to the present day mantle (Pearce, 2008). Furthermore, geochemical variation and magma generation temperatures suggest that Archean enriched mantle was part of an undifferentiated or well-mixed mantle similar in composition to calculated primitive mantle (Condie et al., 2016). Thus, the mantle thermal regimes play a key role in change of mantle geodynamics/plate tectonic style from Archean to present day (Condie et al., 2016; Keller and Schoene, 2018).

The Bundelkhand Craton is one of the oldest Archean cratons, which is situated in north central part of the Indian shield (Fig. 1a, Basu, 1986; Malviya et al., 2004, 2006; Saha et al., 2016; Singh and Slabunov, 2015; Verma et al., 2016). The central Bundelkhand Craton is mainly composed of the Paleo–Mesoarchean Tonalite–Trondhjemite–Granodiorite (TTG) gneisses of 3551 Ma and 3270 Ma (Joshi et al., 2017; Kaur et al., 2014; Mondal et al., 2002; Saha et al., 2016), Neoarchean granitoids of 2583–2516 Ma (Joshi et al., 2017; Kaur et al., 2016; Mondal et al., 2002) and mafic-ultramafic volcanic, felsic volcanic, quartzite, BIF, calc silicates and volcanoclastic metasediments (Fig. 1b, Basu, 1986; Malviya et al., 2006; Kaur et al., 2014; Singh and Slabunov, 2015; Singh et al., 2018). The Babina and Mauranipur greenstone belts are located in the central part of the Bundelkhand Craton (Fig. 1b). It is worthwhile to note that TTG and granitoids have been widely studied in terms of geochemistry and geochronology to understand the extent of reworking vs juvenile crustal growth during Paleo–Neoarchean time and magmatism of the Bundelkhand Craton (Joshi et al., 2017; Kaur et al., 2014, 2016; Mohan et al., 2012; Mondal et al., 2002; Saha et al., 2016; Singh et al., 2019; Singh and Slabunov, 2015; Verma et al., 2016), whereas, limited studies of mafic-ultramafic rocks were reported by Malviya et al. (2006) and Singh et al. (2018). These authors have explained about tectonic setting along with the style and nature of magmatism, and their observation is solely based on whole-rock geochemistry. Further, whole-rock geochemical data allow to evaluate the compositional variation in these rocks. In addition, new Sm—Nd isotope data may provide valuable information about the sources of magmatic rocks and aid a discussion about possible processes of generation. Thus in order to get robust insights, additional geochemical data are required. In this work, we report for the first time ID–TIMS Sm—Nd isotope data, whole-rock isochron age, as well as major and high precision ICP-MS trace element data of mafic-ultramafic rocks of the Babina and Mauranipur greenstone belts, Bundelkhand Craton to deduce the important information of early evolution of the crust-mantle source composition, age, petrogenesis and tectonic setting.

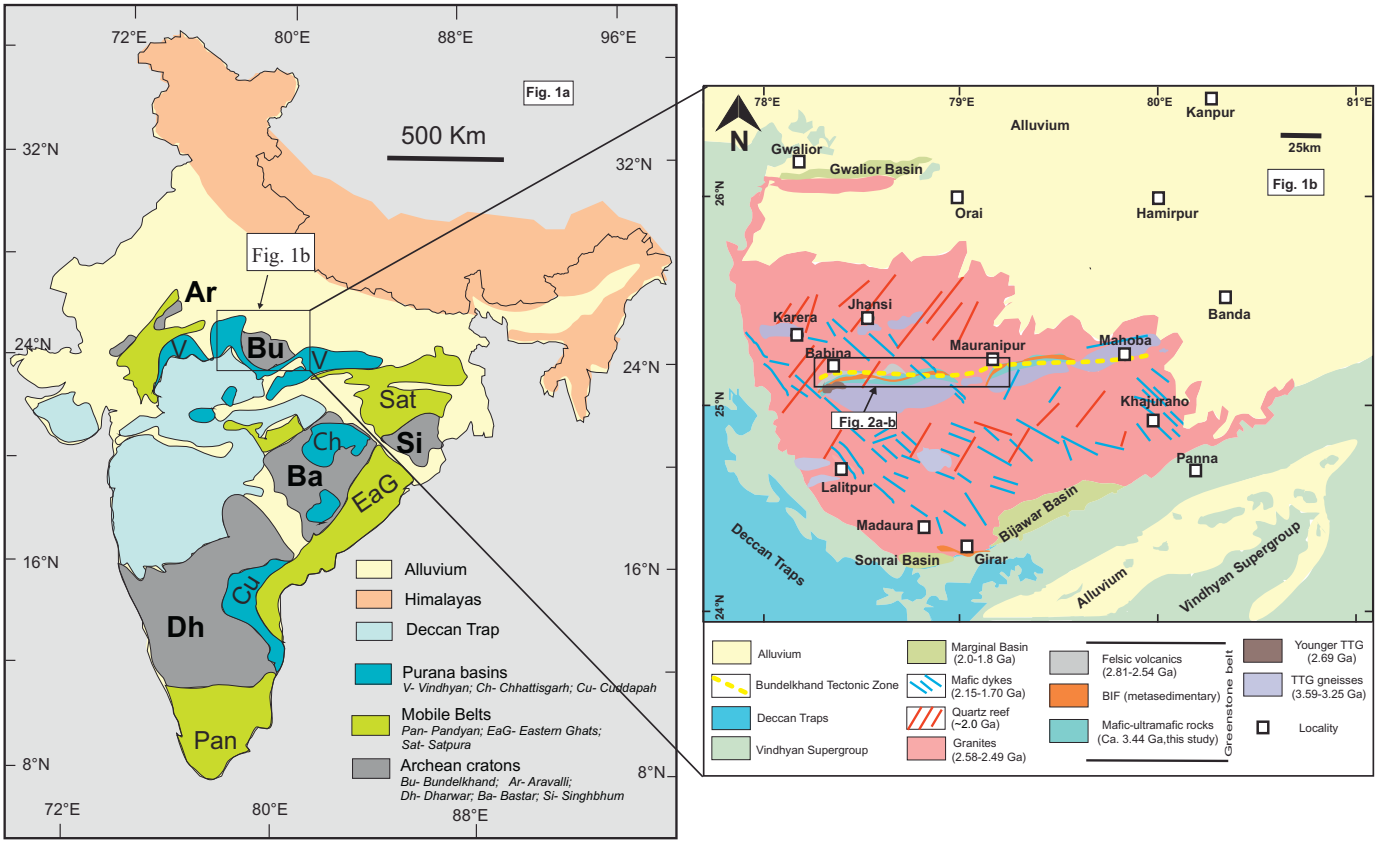

Fig. 1. (a) Geological map of India showing Archean cratons, Tectonic Divisions and (b) simplified map of the Bundelkhand Craton (after Basu, 1986; Malviya et al., 2006; Singh and Slabunov, 2015).

2. Geological setting

The Indian shield has five Archean cratons (Fig. 1a). These five cratons are broadly divided into two Archean cratonic blocks (southern and northern) by the ENE–WSW trending Central Indian Tectonic Zone (CITZ) (Naqvi and Rogers, 1987). The southern block consists of the Dharwar, Bastar and Singhbhum cratons, and northern block comprises of the Aravalli and Bundelkhand cratons (Fig. 1a; Naqvi and Rogers, 1987). The NE–SW trending great boundary fault divides the Aravalli Craton to the west and the Bundelkhand Craton to the east (Basu, 1986; Mondal et al., 2002).

The Bundelkhand Craton is one of the oldest Archean crustal nuclei and occurs in a semicircular shape of an area of approximately 26,000 km^2 and consists predominantly of granite–greenstone terranes (Basu, 1986; Kaur et al., 2014, 2016; Mondal et al., 2002; Saha et al., 2016). It is bounded by Paleoproterozoic (2.0–1.8 Ga) Gwalior (Northwest), Sonrai (South) and Bijawar (Southeast) marginal basins (see Fig. 1b), all of which are homotaxial and identified by clastic sedimentary rocks at the base and carbonates with BIF as topmost rock units (Absar et al., 2009). These marginal basins are overlain by rocks of the Mesoproterozoic Vindhyan Supergroup that occur at three sides of the craton, the northern side of the craton is covered by Gangetic alluvial plains (Fig. 1b; Basu, 1986; Manglik et al., 2015). The geologic investigations of the Bundelkhand Craton indicate a sequence of events as follows in Table 1 (for references see supplementary file-SR1). Basu (1986) and Sharma and Rahman (1995) considered TTG gneisses as a basement of the Bundelkhand Craton, whereas Singh and Slabunov (2015) observed that greenstone successions are younger than TTG gneisses. The oldest basement TTG gneisses were emplaced around 3.59–3.55 Ga and are reported from the Babina and Mauranipur greenstone belts (Kaur et al., 2014; Saha et al., 2016). However, the most abundant TTG gneisses are of 3.3–3.2 Ga, which also occur around the Babina, Mauranipur, Charkhari and Kabrai area (Joshi et al., 2017; Kaur et al., 2016; Mondal et al., 2002).

Singh and Slabunov (2015) reported two Archean supracrustal complexes in the Bundelkhand Craton. First, central Bundelkhand complex, which consists of the Babina and Mauranipur greenstone belts, and second, southern Bundelkhand complex comprises of the Rungaon–Girar greenstone belt. The central Bundelkhand complex consists of mafic-ultramafic and felsic volcanics, less often metasedimentary or BIF rocks (Malviya et al., 2006; Singh and Slabunov, 2015). The generally E-W trending granite–greenstone terrane in central part of the craton is 200 km long, stretches from the Mahoba to Babina via Mauranipur (Fig. 1b, Malviya et al., 2006; Singh and Slabunov, 2015), and follow the trend of Bundelkhand Tectonic Zone (BTZ) (Pati et al., 2007). The Mauranipur greenstone belt has geochemical characteristics of island arc setting and underwent greenschist to amphibolite facies metamorphism (Malviya et al., 2004, 2006). A metamorphic imprint at 2.78 Ga of white schist occur in the Babina belt (Saha et al., 2011). The felsic volcanics exposed around the Babina, Baragaon, Kararkhera, Umri, Maheshpura, Nayakhera and west of the Mahoba town that are of Neoarchean age (ca. 2.5 Ga, Singh and Slabunov, 2015; Joshi et al., 2017). Sensitive High Resolution Ion Micro Probe (SHRIMP) ages of zircon from felsic volcanic outcrops of the Babina and Mauranipur areas yielded age of 2.54 Ga and 2.81 Ga, respectively (Fig. 2a, b, Singh and Slabunov, 2015; Slabunov and Singh, 2018). The southern Bundelkhand complex consists of sericite schist, quartzite and BIFs (Slabunov et al., 2017). The Madawara–Ikauna igneous intrusive complex comprises peridotite, harzburgite, serpentinite, pyroxenites and associated diorite and gabbro (Ramiz et al., 2018). Disseminated lensoid exposures of these rocks occur around the Madawara area for >400 km^2 in the southern part of the craton (Ramiz et al., 2018; Slabunov et al., 2017; and references therein).

A post-Archean important feature in the Bundelkhand Craton is emplacement of the giant quartz reefs (Pati et al., 2007) and mafic dyke

Table 1
Geodynamic features of the Bundelkhand Craton.

Geological events	Age (Ga)	Occurrence in the craton	Field characteristics and relations	References*[1–24]
Tonalite–trondhjemite–granodiorite (TTG) gneisses, highly fractionated REE pattern with low HREE contents, and positive Eu anomalies	3.59–3.25	Babina, Roni, Kuraicha, Mahoba, Karara, Charkhari, Rungaon	Multiphase emplacement and polyphase deformation show pre to syn genetic evidence with greenstone unit.	1, 2, 3, 4, 5, 6, 7, 8
Greenstone units: Mafic-ultramafic volcanics (metabasalts)	~3.44 (in this study)	Babina, Baragaon (Mauranipur)	Supracrustal successions coexisted with TTG and have sheared and faulted contact with TTG. Low-grade metamorphism and mildly deformation.	9, 10, 11, 12, 13, 14
Metasedimentary units (BIF, Pelagic sediments, volcanoclastic sediments)	2.78 (Metamorphic age)	Babina, Pura, Baragaon, Roni, Kuraicha, Prithvipur, Girar, Bedaura	Metasedimentary successions cofolded with mafic-ultramafic rocks having highly intense deformed contact relation. Small outcrop exposed south of Babina town within highly deformed gneiss. High-grade metamorphic event (white schist).	15, 16, 10, 11, 14, 7
Felsic volcanics (rhyolite-rhyodacite-dacite)	2.81–2.54	Babina, Baragaon, Kararkhera, Umri, west of Mahoba town	2.54 Ga felsic volcanic association forming top most unit of greenstone belt in the Babina region. Easily identifiable with other units in the field because of their undeformed nature, whereas 2.81 Ga felsic volcanic occurs at base of BIF in the Mauranipur greenstone belt.	11, 12, 13, 14, 17
Younger phase TTG	2.69	Babina, Near Ghisoli Village	Mainly exposed around south of Babina town and intruded by pink granite and mafic dykes. Cut by pegmatite veins.	18
Undeformed granitic rock	2.58–2.49	Throughout craton	Undeformed outcrops, multiphase intrusion in all older units. Cover almost 75% of craton.	1, 3, 5
Quartz reefs	~2.0 Ga	NE–SW to NNE–SSW trending quartz vein throughout craton	Giant quartz veins intruded almost everywhere in the craton, having NE-SW trend.	19
Giant mafic dykes	2.15–1.7 Ga	Throughout craton	NW-SE trends, mafic dyke swarms evidence of extensional tectonic activity, no effects of deformation.	20, 8
	~1.1 Ga	Mahoba dyke	ENE-WSW trending.	21
Paleoproterozoic Marginal basins	2.0–1.8 Ga	Gwalior (Northwest), Sonrai (South) and Bijawar (southeast)	Homotaxial and characterized by clastic sedimentary rocks and carbonates with BIF.	22, 23, 24

*[1–24] (for references see supplementary file-SR1).

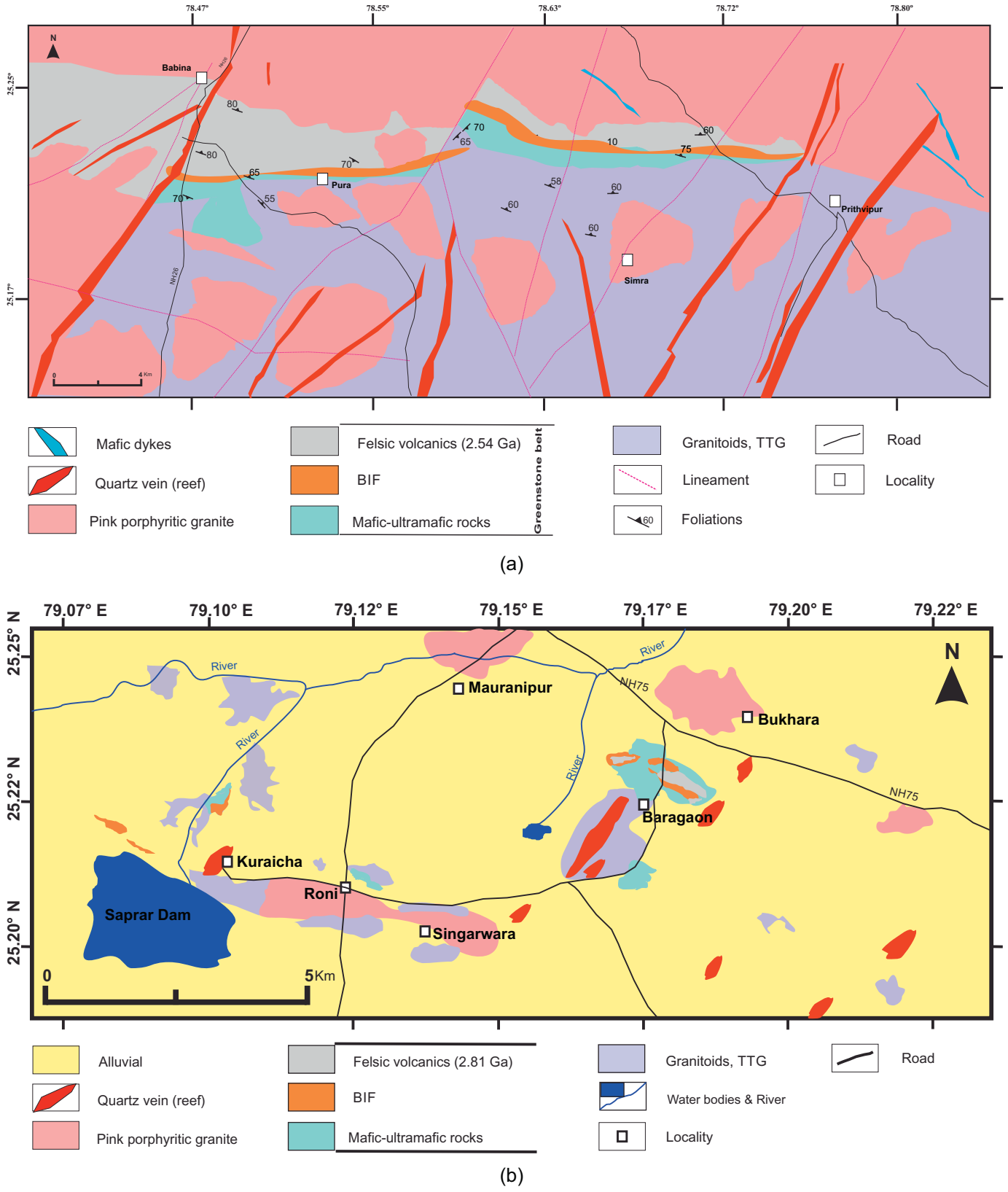

Fig. 2. Geological map of the Babina (a) and Mauranipur (b) greenstone belts, Bundelkhand Craton.

swarms (Pradhan et al., 2012). The NW–SE trending mafic dyke swarms occur along a discontinuous >50 km long of exposures. Geochemical characteristics of these dykes indicate partial melting of heterogeneous mantle sources followed by fractional crystallization of the parental magmas, which are grouped as low Ti–tholeiite (Pati et al., 2008; Pradhan et al., 2012).

3. Geology and field description of the Babina and Mauranipur greenstone belts

3.1. Babina greenstone belt

The east–west trending volcano-sedimentary succession of the Babina greenstone belt is about 40 km long and up to 4 km wide, and exposed around the Babina town (Fig. 2a). This belt consists of mafic-ultramafic rocks and BIF. The BIF occurs in association with mafic rocks (Figs. 1b, 2a) and is well exposed around south of the Babina to Pura village (Fig. 1b, 2a). The mafic-ultramafic rocks in the Babina area occur as lowermost units of greenstone successions (Fig. 3a). The mafic sequence is exposed about 1.5 m thick and having sheared and intense weathered contact with BIF (Fig. 3b).

Three phases of deformation fabrics were observed in these greenstone components. The S_1 schistosity dominantly parallel to S_o BIF bedding and F_1 folds are tight to isoclinal type with thickened hinge. The F_1 folds are inclined in nature and marked as first deformational event (D_1). The fold F_2 is close fold and dominantly defined by puckers in quartzite (Fig. 3b). The crenulations cleavage (S_2) shows NNW–SSE strike with varying dips 45°-85° due east. The fold F_2 shows plunge due NW and the axial planar schistosity show NW–SE trend with sub-vertical dip observed in greenstone rocks and granite gneisses, marked as second deformational event (D_2). The third and final phase of deformation (D_3) is observed as E–W trending shearing. All D1, D2 and D3 deformational imprints are observed in TTG gneiss and greenstone components while D3 is postdate to quartz reef intrusions ca ~2.15 Ga (Pati et al., 2007).

3.2. Mauranipur greenstone belt

The Mauranipur greenstone belt has well preserved outcrops around the Baragaon village (co-ordinates 79.17°E, 25.23°N), whereas sparse outcrops are found around the Raspahari, Kuraicha, and Roni villages (Figs. 1b, 2b, Malviya et al., 2006; Singh and Slabunov, 2015; Singh et al., 2018; Slabunov and Singh, 2018). Outcrops of pillow lava are observed in the Saprar river section NW of Kuraicha village. Mafic-ultramafic rocks are usually black and dark gray color, have sheared and faulted contact with metavolcano-sediments.

This greenstone belt indicates little deformation but at some places the mafic rocks have well preserved pillow structure (Fig. 3c). The pillow lavas are spatially associated with ultramafic rocks (Malviya et al., 2006; Singh and Slabunov, 2015) exposed at the base of the greenstone belt. At places, the ultramafic rocks occur as extensively serpentinized dark green rock occurring generally in low lying area but a few samples collected from well cuts have well preserved primary olivine and chromium spinel (Fig. 3d). These ultramafic rocks were interpreted as basaltic komatiite (Malviya et al., 2006). The metasediments intercalate with metamorphosed pillow basalt. The BIF is fine- to medium-grained rock with distinct mm- to cm-scale inter-layering of iron oxide and quartzite.

Intercalated BIF with metamorphosed pillow lava is well exposed at the NE side of the Baragaon, Mauranipur. Field observation suggests the stratigraphic sequences of the greenstone rocks consist of ultramafic and ultramafic rocks followed by the pillow and massive basalt and volcaniclastic metasediment, which is overlain by the BIF from bottom to top. This greenstone belt was intruded by granites and quartz reefs (Joshi et al., 2017; Kaur et al., 2014, 2016; Malviya et al., 2006; Mondal et al., 2002).

Malviya et al. (2006) reported that the Mauranipur greenstone rocks have experienced intensive heterogeneous deformation of at least three phases. Primary structure in the form of bedding (So) is observed in the BIF with strike of N 40° W which is almost parallel to the schistosity (S1, N39° W). The moderately plunging tight to isoclinal fold (F1) with axial plane trending N45°W marks the D1 deformation phase observed in the BIF, volcaniclastic metasediments and mafic rock. Second phase of deformation (D2) is marked by the northwesterly plunging (~40°) refolded fold and the development puckers on S1 marked as (F2). F1 and F2 are coaxial. Third phase of deformation (D3) is clearly observed in the greenstone rocks as well as younger granites and is marked as E–W shearing event.

4. Petrography and mineralogy

4.1. Mafic rock–Babina greenstone belt

The mafic rocks are fine-grained, dark colored and relatively foliated. Greenschist to amphibolite facies metamorphism and secondary alteration obliterated almost the primary igneous texture. Well-developed foliation is defined by the hornblende, actinolite and chlorite (Fig. 3e). The other minerals include plagioclase, magnetite, quartz and epidote. Relict minor orthopyroxene is identified by X-ray powder diffraction (XRD) quantitative analysis in some samples. Powder XRD analysis reveals that amphibole are 60–65% (Table S1) includes hornblende, Fe gedrite and actinolite in increasing order of abundance. Plagioclase is 15–18%, chlorite 12–15%, talc 3–5%, orthopyroxene (Opx) 3–6%, and minor amount of sericite (Table S1).

4.2. Mafic rock–Mauranipur greenstone belt

The mineral assemblages in mafic rocks have hornblende, tremolite-actinolite, magnetite, plagioclase and quartz. Amphibole and plagioclase occur as tabular to prismatic and/or needle-shaped grains (Fig. 3f). Powder XRD quantitative analysis of these rocks reveal that amphibole is 60–70% (Table S1) comprise of hornblende, tremolite-actinolite in increasing order of abundance, plagioclase is 25–30% (Table S1), mostly labradoritic in composition, clinopyroxenes (Cpx) 2–3% and minor amount of magnetite and quartz (Table S1). In some places, the mafic rock are deformed with the distinct S1-foliation, which is defined by elongated amphibole (Hbl) and plagioclase grains. Quartz occurs as an interstitial phase and in the secondary veins. Chlorite, sericite and actinolite are the product of retrograde metamorphism. These retrograde phases exhibit no preferred orientation (Fig. 3f).

4.3. Ultramafic rocks–Babina and Mauranipur greenstone belts

Most of the serpentinite rocks are chlorite-serpentinite-tremolite with highly deformed fabrics. At places tremolite needles are seen to develop within serpentine. The primary olivines were serpentinized, which was later replaced by talc (Fig. 3g). Powder XRD quantitative analysis reveals mineralogical assemblages as (nimite 35%, clinochlore 21%, lizardite 4%, talc 13%, edenite18%, Fe- gedrite 5%, and tremolite 4%, Table S1).

4.4. Ultramafic cumulate from the Mauranipur greenstone belt

The ultramafic cumulate exhibits equigranular texture and no sign of deformation texture was identified in the primary minerals. The rock has relict olivine and chromium spinel in a serpentine-chlorite matrix (Fig. 3h). Secondary amphibole and chlorite also occur; along with serpentine these minerals are possibly alteration product of clinopyroxene. Secondary magnetite occurs along boundary of olivine grain, released during serpentinization (Fig. 3h). In addition, these rocks reveal mineralogical assemblages such as (clinochrysotile 36%, lizardite10%, edenite 20%, ferro-gedrite 6%, nimite 17%, magnetite 1–2%, olivine 6–7% and Cr-Spinel 2–3%, Table S1).

The mineral chemistry of same cumulative rocks from the Mauranipur area is reported by Malviya et al. (2006). According to them, the forsterite (Fo) content in the olivine ranges from 81 to 83% and the spinel grains contain 36–39 wt% Cr_2O_3, 0.61–2.08 wt% MnO, and 1.38–2.67 wt% TiO_2 and Cr number [Cr/ (Cr + Al)] and Mg number

[Mg/ (Mg + Fe^{2+})] ranges 0.69 to 0.75 and 0.16 to 0.20, respectively. The central part of spinel grain tends to contain lower MnO and TiO_2 and higher in Cr and Mg numbers. The Fo content of olivine and the Cr number ratio of spinel in the rock plot (not shown) in a low-Fo region, away from the olivine-spinel mantle array.

5. Analytical procedures

The mafic-ultramafic rocks of the study area were sampled to encompass the entire area of the Babina and Mauranipur greenstone belts (Table S2- provided in the Supplementary material file; Fig. 2a, b).

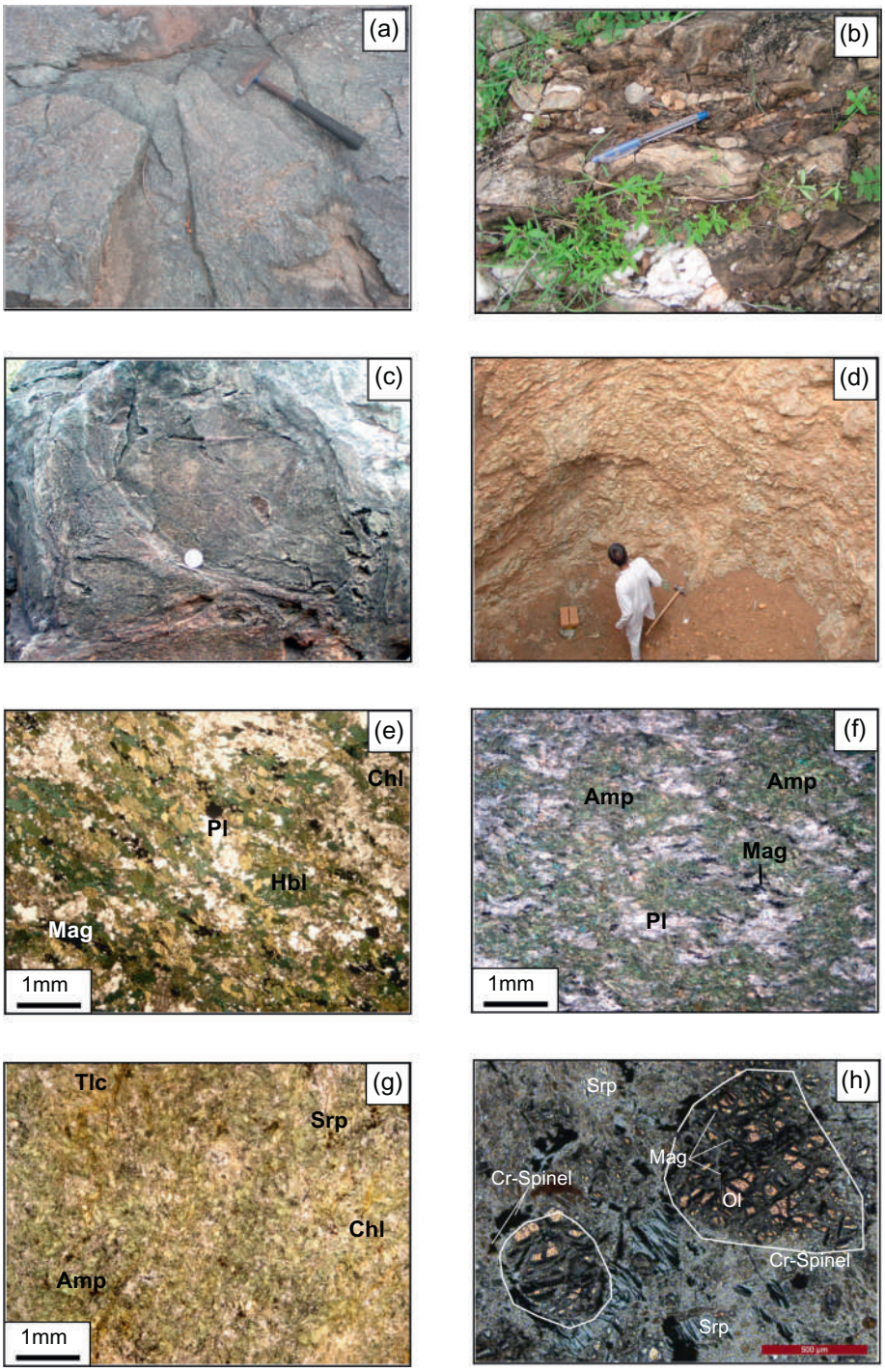

Fig. 3. Representative field photographs and photomicrographs from the Babina and Mauranipur greenstone belts, Bundelkhand Craton. These representative petrographic features are typical of greenschist to amphibolite–facies from both regions. Field photographs (a–d): (a) deformed mafic rocks from the Babina greenstone belt, (b) deformed mafic rocks co-folded with quartzite from the Babina greenstone belt, (c) deformed massive mafic rocks with pillowed structure from the Baragaon area, Mauranipur greenstone belt, (d) showing outcrop of ultramafic in a well section from the Baragaon area, Mauranipur greenstone belt. Photomicrographs (e–h): (e) deformed mafic rocks from the Babina greenstone belt showing texture and mineral assemblages, (f) deformed mafic rocks from the Mauranipur greenstone belt is showing aligned long axes of amphibole, plagioclase, magnetite grains and quartz occur as an interstitial phase (plain polarized light), (g) deformed ultramafic rocks from the Babina greenstone belt showing texture and mineral assemblages, (h) ultramafic rocks from the Mauranipur greenstone belt showing cumulate texture. Relict olivine (Ol) grains are occur within serpentine-chlorite matrix with magnetite (Mag) distributed along the foliation planes subhedral to euhedral chrome spinel (Spl) is present in the serprntinised matrix, (Cross nicol). Abbreviations: Srp–serpentine, Ol–olivine, Mag–magnetite, Cr-Spl–Cr spinel, Tlc–talc, Pl–plagioclage, Chl–chlorite, Hbl–hornblende, and Amp–amphibole.

Sites of intrusions, severe deformation and veins were avoided during sampling. Although all samples are altered and metamorphosed to some extent, the fresh samples were selected for geochemical analysis after detailed petrographic studies.

5.1. Whole rock geochemistry

A total of forty-three rock samples were collected and analyzed for the whole rock geochemistry (Table S2). Major oxides concentrations were determined by X-ray fluorescence spectrometer (XRF) on fusion beads obtained using lithium borate fusion techniques; and trace elements by inductively coupled plasma-mass spectrometry (ICP-MS) after acid dissolution. The loss on ignition (LOI) was determined by TGA furnace. The base metals were analyzed using four acid digestions method by inductively coupled plasma atomic emission spectroscopy (ICP-AES). Geochemical analyses were obtained in two different laboratories (1) Australian Laboratory services Pty. Ltd., Malaga, Western Australia, Australia, the detail analytical procedure could be found at www.alsglobal.com, and (2) Institute of Geosciences, University of Campinas (UNICAMP), Brazil, the each of two certified standard (W-2, BHVO and RGM-1, WSE) have been used for the major and trace elements, respectively, the precision and accuracy was considered <5% for major and up to 10% for the trace elements (Vendemiatto and Enzweiler, 2001).

Trace element and REE compositions of whole rocks were determined by solution in a quadrupole Thermo (Xseries2) ICP-MS at the Isotope Geology Laboratory, Institute of Geosciences, University of Campinas, Brazil (Table S2), following the detail sample preparation and analytical procedures of Cotta and Enzweiler, 2009. Three standards (BRP-1, RGM-1 and GSP-2) were used to calibrate the analytical data quality, having <10% deviation from the recommended values for the international standards.

5.2. Sm—Nd isotope systematics

Eleven samples were selected for the Sm—Nd isotopic analyses, which were performed at the Centro de Geocronología y Geoquímica Isotópica from the Universidad Complutense de Madrid, Spain. These analyses were performed in whole-rock powders using a ^{150}Nd—^{149}Sm tracer by Isotope Dilution-Thermal Ionization Mass Spectrometry (ID-TIMS). The weighted samples in Teflon® vessels were dissolved in 5 ml of ultrapure HF and 3 ml of ultrapure HNO_3 (Merck-Suprapur™). Along with the samples, enriched spike solution (^{149}Sm—^{150}Nd - Oak Ridge) was added and placed inside an oven for 65 h at 120 °C temperature. After that time, cold vials were evaporated on a hot plate at 120 °C. Once samples were completely dried, 1 ml of ultrapure HNO_3 (Merck-Suprapur™) was added and place back on the heat plate for evaporation at 120 °C. Furthermore, 4 ml of 6 N distilled HCL 6 N were added to the dried samples and placed in an oven overnight at 120 °C. After that, samples were centrifuged at 4000 r.p.m. for 10 min, in order to separate the dissolved fraction from the residue if any. Chromatographic separation of the complete group of REE was performed using cation exchange resin DOWEX 50 W-X8 200–400 mesh (previously calibrated). REE fractions recovered from the previous chromatographic stage were dried completely before dissolved again in 200 μL HCl 0.18 N. These solutions were passed through a new chromatographic step (Ln-Resin). The result is a complete separation between the Nd (using 0.3 N HCl as eluent) and the Sm (using 0.4 N HCl as eluent) fractions of the samples, being ready for the subsequent analysis in the mass spectrometer (TIMS).

Dried Sm and Nd samples dissolved with 2 μl of 0.05 M phosphoric acid were loaded onto a side Rhenium (Re) filament of a triple Re filament arrangement. Nd ratios were analyzed in a mass spectrometer TIMS-Phoenix®, following a dynamic multicollection method, through 160 cycles at a stable intensity of 1 V for the ^{144}Nd mass. In turn, Sm ratios were analyzed in the same spectrometer, following a single static method through 112 cycles maintaining 1 V intensity for the ^{149}Sm mass.

The measured $^{143}Nd/^{144}Nd$ isotopic ratios were corrected for possible isobaric interferences from ^{142}Ce and ^{144}Sm and normalized to $^{146}Nd/^{144}Nd = 0.7219$ to correct for mass fractionation (Table 2). Nd isotopic standard (JNdi-1, Tanaka et al., 2000) was analyzed during sample measurement, and gave an average value of $^{143}Nd/^{144}Nd = 0.512107$ for 9 replicas, with an internal precision of ±0.000005 (2σ). The estimated error for the $^{147}Sm/^{144}Nd$ ratio is 0.1% and $^{143}Nd/^{144}Nd$ is 0.006%. Procedural blanks were always below 0.01 ng/ml.

6. Results

6.1. Major and trace elements geochemistry

The mafic rocks from the Babina display variable contents of SiO_2 = 43.9–51.2 wt%, except one sample with SiO_2 = 52.1 wt%, MgO = 5.4–11.0 wt% and TiO_2 = 0.31–1.14 wt%, with Mg-numbers (Mg#) of 44–77 (Table S2). The Cr and Ni contents are in the ranges of 58–700 ppm and 22–325 ppm, respectively. In addition, mafic rocks from the Mauranipur have SiO_2 = 51.8–55.6 wt%, MgO = 6.9–9.5 wt%, and TiO_2 = 0.61–0.85 wt%, with Mg# of 59–70 (Table S2). The Cr and Ni contents are in the ranges of 150–660 ppm and 50–200 ppm, respectively (Table S2). The ultramafic rocks from the Babina and Mauranipur possess variable contents of SiO_2 = 46.9–50.3 wt%, narrow range of MgO = 20.2–21.1 wt% and TiO_2 = 0.33–0.46 wt% (Table S2). Mg# range from 77 to 82, Ni from 852 ppm to 1590 ppm, Cr from 2070 ppm to 2930 ppm (Table S2). In addition, one sample of ultramafic cumulate rock from the Mauranipur displays SiO_2 = 44.5 wt%, MgO = 34.2 wt%, TiO_2 = 0.11 wt%, with

Table 2
Sm—Nd isotopes data on mafic-ultramafic rocks from the Babina and Mauranipur greenstone belts, Bundelkhand Craton, India. The εNd_t values were calculated for $_t$ = 3435 Ma. For both places the depleted mantle values for $^{143}Nd/^{144}Nd = 0.51315$ and $^{147}Sm/^{144}Nd = 0.2137$ were taken from Dickin, 1995.

Sample	Rock unit	Sm (ppm)	Nd (ppm)	$^{147}Sm/^{144}Nd$	$^{143}Nd/^{144}Nd$	±2σ	$f_{Sm/Nd}$	εNd_t	T_{DM} (Ga)
	Babina								
BCB-05	Mafic	1.35	4.3	0.195538	0.512688	$2*10^{-6}$	−0.0059	4.06	3.84
BCB-06	Mafic	1.92	5.9	0.201119	0.512838	$1*10^{-6}$	0.0225	3.91	3.75
BCB-07	Mafic	0.66	2.3	0.182034	0.512410	$1*10^{-6}$	−0.0745	5.89	3.53
BCB-09	Mafic	1.9	6.6	0.174289	0.512231	$2*10^{-6}$	−0.1139	2.00	3.52
BCB-12	Mafic	4.32	19.3	0.140302	0.511443	$1*10^{-6}$	−0.2867	4.04	3.52
BCB-17	Ultramafic	1.21	4.5	0.169341	0.512135	$2*10^{-6}$	−0.1391	5.36	3.46
	Mauranipur								
BCB-25	Mafic	1.65	5.5	0.191754	0.512575	$1*10^{-6}$	−0.0251	5.61	3.95
BCB-31	Mafic	1.66	6.1	0.184093	0.512369	$2*10^{-6}$	−0.0641	9.09	3.98
BCB-39	Mafic	1.55	4.89	0.191460	0.512535	$2*10^{-6}$	−0.0266	0.24	4.17
BCB-40	Mafic	1.66	5.33	0.187780	0.512511	$2*10^{-6}$	−0.0453	1.26	3.72
BCB-41	Mafic	1.56	4.89	0.192681	0.512579	$2*10^{-6}$	−0.0204	0.55	4.09

Mg# = 84.7 and high Cr and Ni contents 3829 ppm and 957 ppm (Table S2). TAS—total alkalis vs. silica, Nb/Yb–Zr-Ti diagram and MagClaMSys—Magma Classification Major-element based System diagrams (Le Bas et al., 1986; Winchester and Floyd, 1977; Verma et al., 2017b, Fig. 4a–c), have been used to classify these rock samples. Samples are characterized as ultrabasic-basic to intermediate in composition, and plotted in the field of basalt to basaltic andesite (Figs. 4a–c). Fenner's binary diagrams show a negative correlation with most of the major oxides and immobile and incompatible elements, whereas positive correlations between Cr and Ni are shown in Figs. 5 and 6.

Primitive mantle-normalized multi-element patterns (McDonough and Sun, 1995, Fig. 7a–c) indicate that mafic rocks from the Babina (Fig. 7a) have almost flat REE profiles [$(La/Yb)_{PM}$ = 0.87–1.40; $_{PM}$-primitive mantle normalized (McDonough and Sun, 1995), $(La/Sm)_{PM}$ = 0.91–1.21; $(Gd/Yb)_{PM}$ = 0.91–1.00]. Three samples (BCB-01, BCB-10, BCB-12) display enriched REE patterns [$(La/Yb)_{PM}$ = 3.4–12.8; $(La/Sm)_{PM}$ = 2.1–3.9]. These rocks also show negative Nb anomalies (Nb/Nb^* = 0.13–0.78) with a positive Pb anomalies (Fig. 7a). The mafic rocks from the Mauranipur show slightly enriched REE [$(La/Yb)_{PM}$ = 1.1–1.7; $(La/Sm)_{PM}$ = 1.1–2.0; $(Gd/Yb)_{PM}$ = 0.85–1.4] with negative Nb anomalies (Nb/Nb^* = 0.13–0.77) (Fig. 7b). The ultramafic rocks from the Babina and Mauranipur and ultramafic cumulate rock from the Mauranipur display a progressive enrichment from Th, through La to Yb, with negative Nb anomalies (Nb/Nb^* = 0.40–0.73) with lack of Zr anomalies (Zr/Zr^* = 0.10–0.3) (Fig. 7c).

Chondrite-normalized (McDonough and Sun, 1995) rare-earth element (REE) plots are shown in Fig. 7d–f. The Babina mafic rocks have total REE contents of 12.6–42.1 ppm, except three samples (BCB-01, BCB-10, BCB-12) with total REE (63.3–148.8 ppm) and display flat chondrite normalized LREE patterns (Fig. 7d) with weak or no negative Eu anomalies (Eu/Eu^* = 0.81–1.15), $(La/Yb)_{CN}$ = 0.87–1.4 ($_{CN}$ noting chondrite-normalized after McDonough and Sun, 1995), $(La/Sm)_{CN}$ = 0.9–1.2, and $(Gd/Yb)_{CN}$ = 0.9–1.0, except three samples (BCB-01, BCB-10, BCB-12), which display enriched LREE patterns (Fig. 7d) $(La/Yb)_{CN}$ = 3.4–12.7, $(La/Sm)_{CN}$ = 2.1–3.9 and $(Gd/Yb)_{CN}$ = 1.4–2.0. The mafic rocks from the Mauranipur have total REE (26.0–40.7 ppm) and display flat chondrite normalized LREE (Fig. 7e) with no Eu anomalies (Eu/Eu^* = 0.89–1.0), $(La/Yb)_{CN}$ = 1.1–1.7, $(La/Sm)_{CN}$ = 1.1–2.0 and $(Gd/Yb)_{CN}$ = 0.85–1.4 (Fig. 7e). The ultramafic rocks from the Babina and Mauranipur are characterized by lower total REE (17.4–24.0 ppm), except one sample (BCB-20) with total REE (43.1 ppm) and displays flat chondrite normalized LREE pattern (Fig. 7f) marked by negative Eu anomalies (Eu/Eu^* = 0.50–0.69), $(La/Yb)_{CN}$ = 2.3–2.9, $(La/Sm)_{CN}$ = 1.5–1.8 and $(Gd/Yb)_{CN}$ = 1.3–1.6 (Table S2). One ultramafic cumulate rock from the Mauranipur has total REE (5.3 ppm) shows enriched LREE pattern (Fig. 7f) with ratio values of $(La/Yb)_{CN}$ = 7.6, $(La/Sm)_{CN}$ = 4.9 and $(Gd/Yb)_{CN}$ = 1.3 (Table S2).

6.2. Sm—Nd isotopic data

Sm—Nd isotopic data for mafic-ultramafic rock samples are listed in Table 2. Six samples (BCB-05, 06, 07, 09, 12 and 17) of the Babina–mafic-ultramafic rocks define a whole rock isochron (MSWD = 0.71) with an initial $^{143}Nd/^{144}Nd$ ratio of 0.508268 ± 0.000183 and a slope corresponding to 3435 ± 161 Ma (Fig. 8). However, the poor correlation between $^{147}Sm/^{144}Nd$ and $^{143}Nd/^{144}Nd$ data obtained for the Mauranipur mafic rocks did not allow us to obtain a reasonable age. So, the initial radiogenic isotope ratios were calculated at 3435 Ma (see discussion below) for rocks from both areas. The Babina–mafic-ultramafic rocks have εNd_t values (calculated according Goldstein et al., 1984) of +2.0 to +5.89 and depleted-mantle model ages (T_{DM}, calculated according to Goldstein et al., 1984) of 3.46–3.84 Ga (Table 2), whereas the Mauranipur–mafic rocks have epsilon Nd_t (Goldstein et al., 1984) of +0.24 to +9.09 and model ages (T_{DM}) of 3.72–4.17Ga (Table 2).

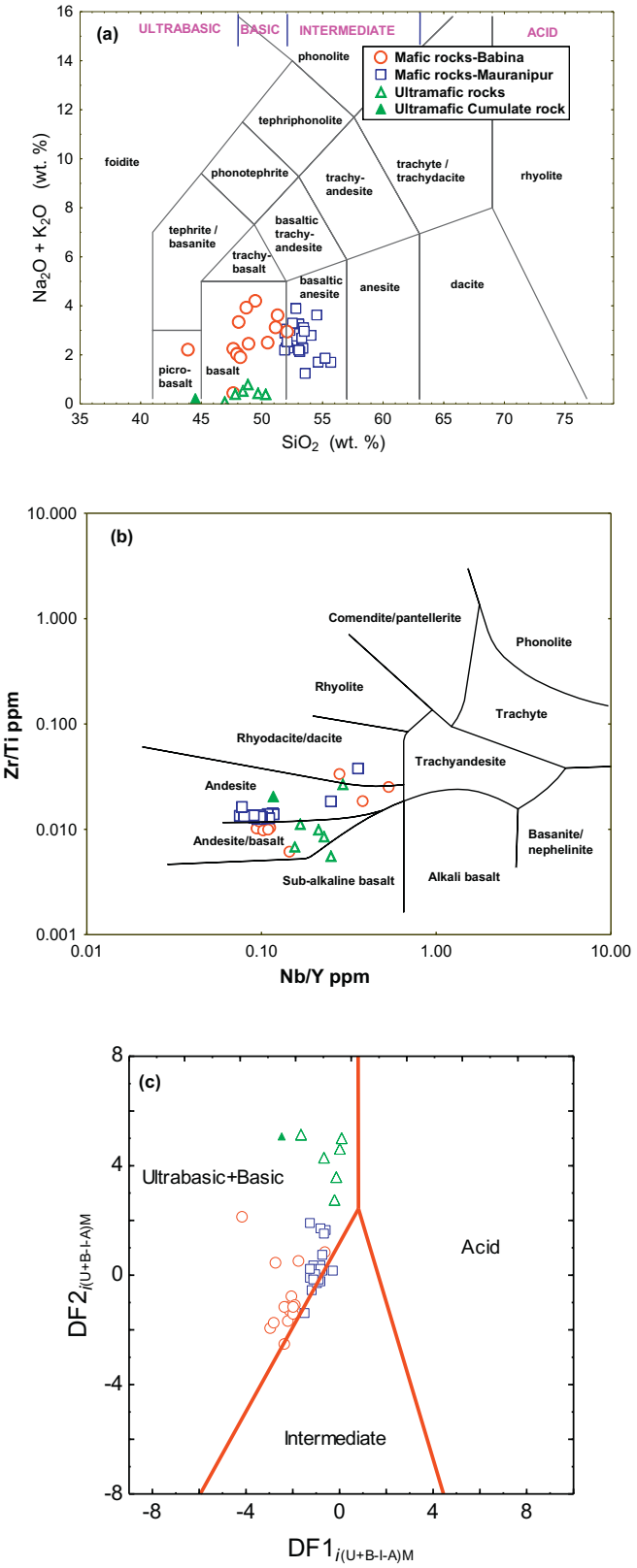

Fig. 4. (a) Sample classification in the TAS diagram of Le Bas et al. (1986) obtained from the IgRoCS computer program (Verma and Rivera-Gómez, 2013) (b) Nb/Y vs. Zr/Ti diagram (Winchester and Floyd, 1977) (c) muti-dimensional (MagClaMSys) classification diagram (Verma et al., 2017b) for the mafic-ultramafic rocks of the Babina and Mauranipur greenstone belts, Bundelkhand Craton.

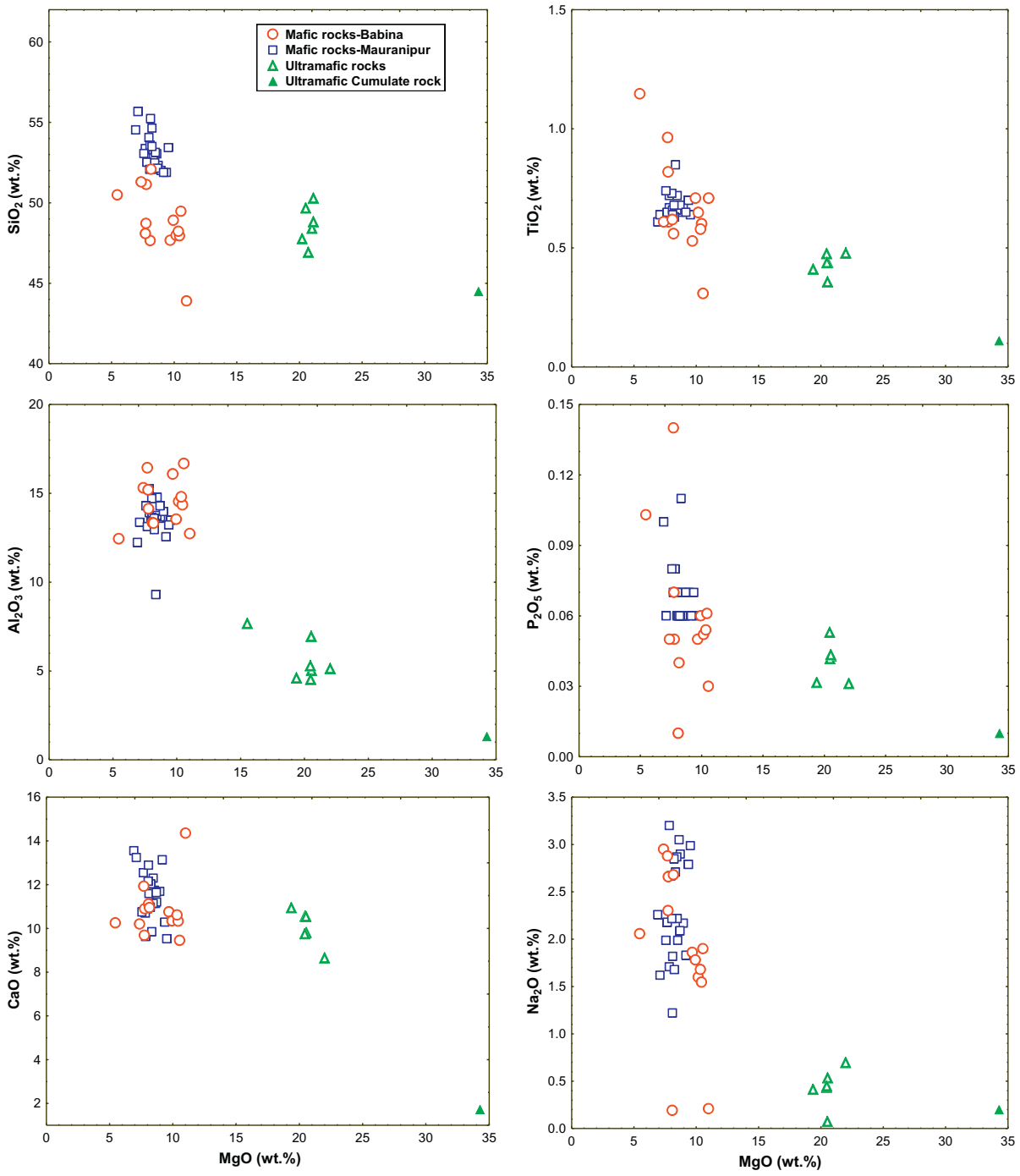

Fig. 5. Fenner's binary diagram showing moderate to strong fractionation trends for selected major elements oxide versus MgO.

7. Discussion

7.1. Effect of post-magmatic alteration

All Archean basalts can present variable degree of alteration that is normally controlled by secondary processes, such as metamorphism or hydrothermal alteration (Chavagnac, 2004). Element mobility is a critical concern in the study of Archean greenstone metamorphosed and deformed volcanic rocks (Polat et al., 2002). It is important to estimate the effects of the metamorphism on the geochemistry of the basalts accordingly before considering any petrogenetic interpretation. Mafic-ultramafic rocks from the Babina and Mauranipur greenstone belts were affected by low-grade metamorphism and are composed mainly of serpentine, actinolite-tremolite, chlorite, plagioclase, and minor hornblende with rarely preserved primary mineralogy (olivine, pyroxene, and plagioclase). The petrographic observations, however, do not indicate the coexistence of carbonate minerals in the mafic-ultramafic rocks. Furthermore, the replacement of olivine into serpentine, pyroxene into actinolite–tremolite and chlorite, and plagioclase into epidote are consistent with a metasomatic origin at lower temperatures (<700 °C; Abbott and Raymond, 1984). The studied mafic-ultramafic rocks have not undergone significant secondary alteration as inferred from their low loss on ignition mostly <3% (average LOI = 1.6%), absence of Ce anomalies and lack of carbonization (Van Acken et al., 2016). Zr is one of the least mobile elements to understand post-magmatic alteration (Pearce and Peate, 1995; Polat et al., 2002).

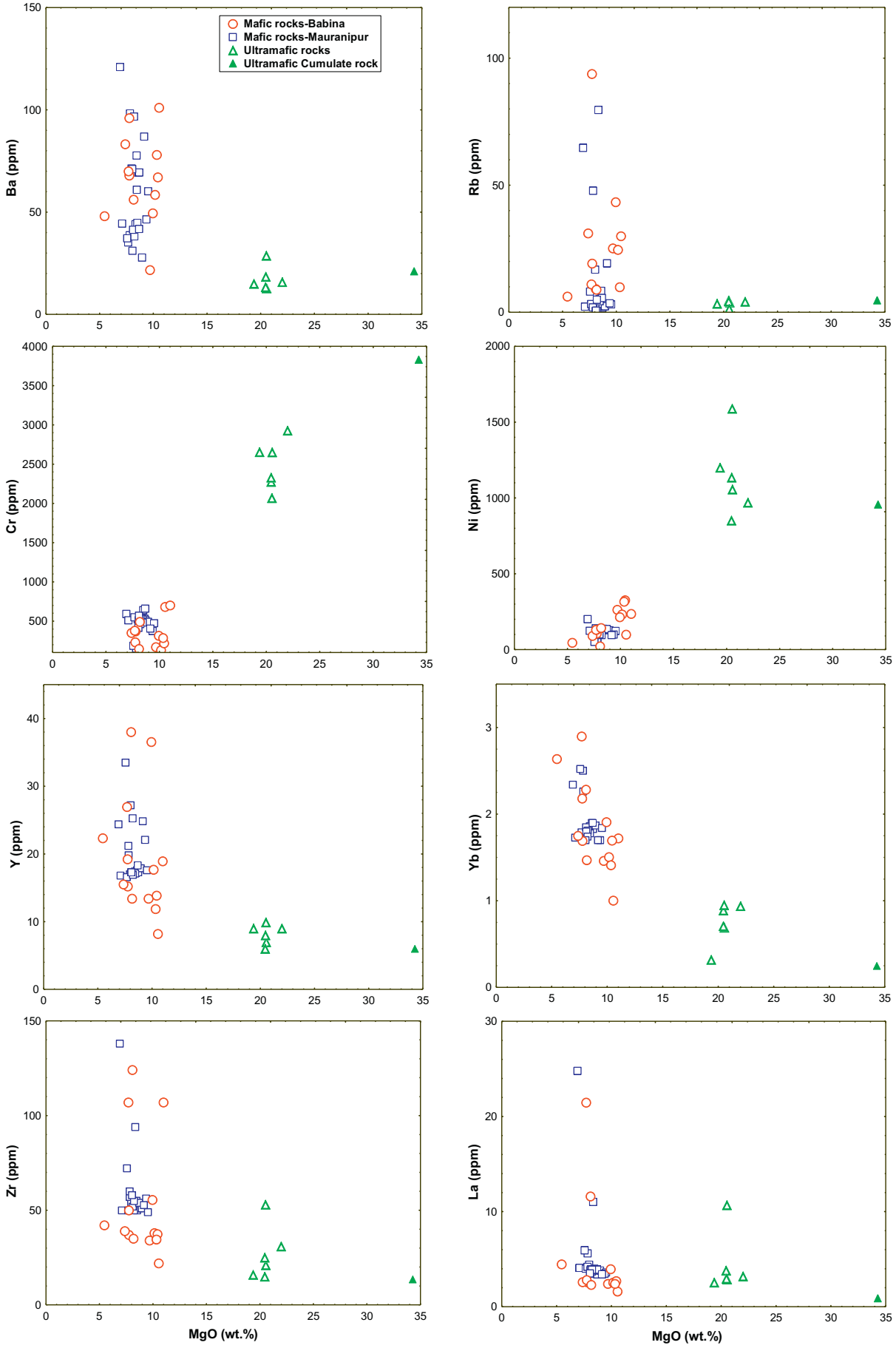

Fig. 6. Fenner's binary diagram showing correlation for selected trace elements versus MgO.

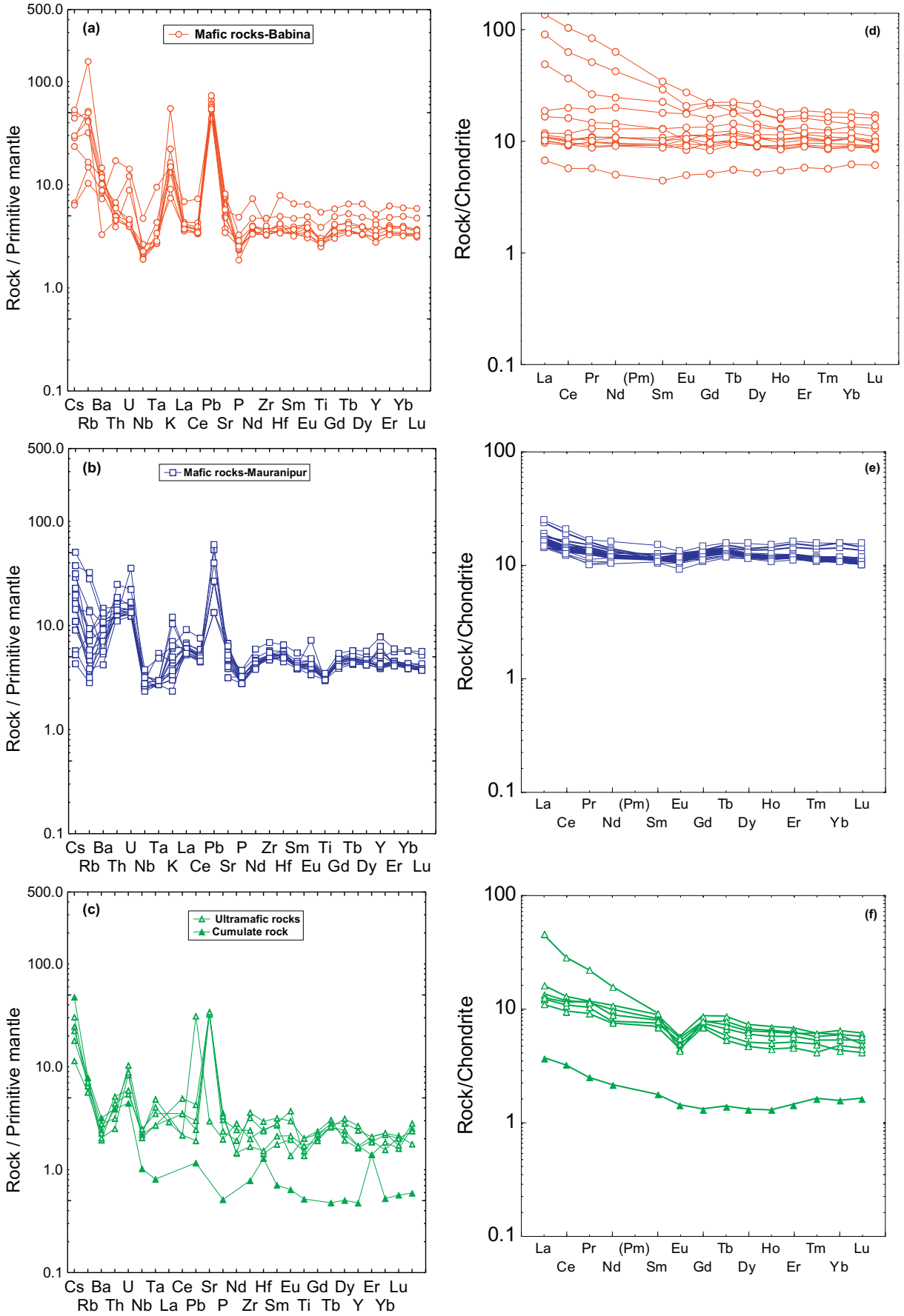

Fig. 7. (a–c) Primitive mantle-normalized multi-element plots; and (7d–f) chondrite-normalized rare-earth element plots (McDonough and Sun, 1995) for the Babina and Mauranipur greenstone belts, Bundelkhand Craton.

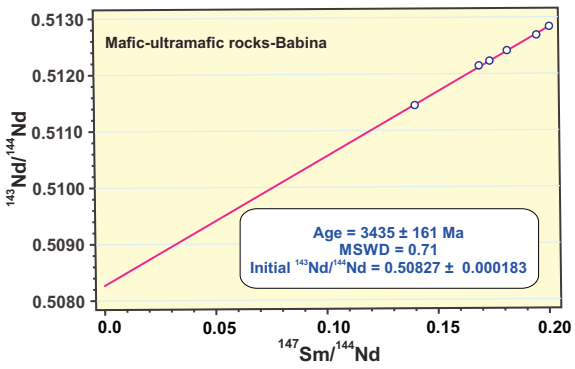

Fig. 8. Sm—Nd whole-rock isochron for mafic-ultramafic rocks from the Babina greenstone belt, Bundelkhand Craton.

We correlated Zr versus other elements to test their mobility. Zr shows consistent correlations with some other elements such as Nb, Th, U and Hf indicating that these elements have not been significantly mobilized during late stage metamorphism (Fig. S1, see supplementary material). Moreover, the studied mafic-ultramafic rocks have a narrow range of the $^{147}Sm/^{144}Nd$ ratios, which also support low degree of mobility during metamorphism. Published works indicate that Ce anomalies occur in response to oxidation of Ce^{3+} to Ce^{4+} from solution as CeO_2 (Braun et al., 1993). Ce/Ce* ratios between 0.9 and 1.1 display limited LREE mobility whereas those with Ce/Ce* <0.9 and >1.1 are characterized by large LREE mobility (Polat et al., 2002). In this study, two samples (BCB-12 and BCB-21) indicate Ce/Ce* ratios 0.88 and 0.84. With the exception of these two samples, all the other samples have Ce/Ce* within the range of 0.9 to 1.1 indicating limited LREE mobility. In some greenstone belts, Eu anomalies have been used to disclose hydrothermal secondary alteration processes (Arndt et al., 2008). Accordingly, studied ultramafic rocks indicate negative Eu anomalies (Fig. 7e) that are generally attributed to secondary alteration processes. However their LOI data indicate least altered nature of majority of the samples which display smooth and coherent REE patterns. Thus, we conclude that the protoliths were little affected by elemental mobility during metamorphism. Therefore, major- and trace-element and isotopic compositions of these rocks can be used to constrain their magmatic processes and infer mantle source characteristics.

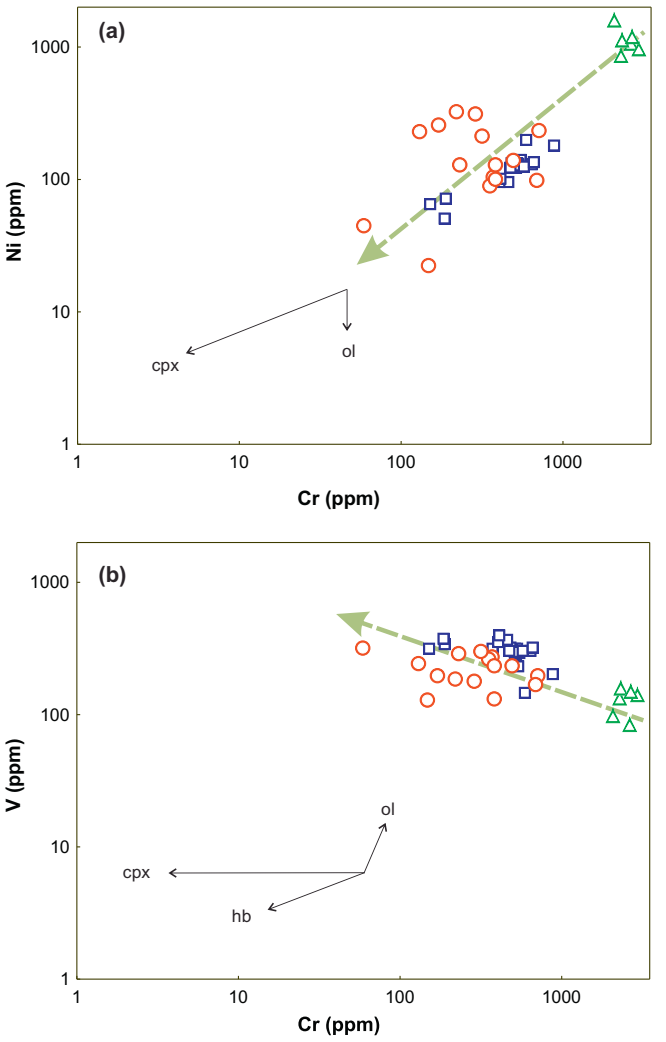

Fig. 9. (a) Cr vs. Ni, and (b) Cr vs. V bi-variate diagrams. The dashed arrow lines show clinopyroxene and olivine-dominated fractionation in the evolution of the mafic-ultramafic rocks from the Babina and Mauranipur greenstone belts, Bundelkhand Craton. Partition coefficients are taken from Rollinson (1993).

7.2. Fractional crystallization and crustal contamination

The mafic-ultramafic rocks from the Babina and Mauranipur greenstone belts present variation between MgO, Mg#, and compatible elements such as Ni, Cr, V, etc. (Table S2). The correlation of these elements reveals that these are affected by significant fractional crystallization. For example, Cr vs. Ni, and Cr vs. V diagrams (Fig. 9a–b) suggest that the original magmas might have evolved through fractionation of clinopyroxene and olivine in lesser extent whereas little or non-fractionation of plagioclase is observed as suggested by the presence of negligibly negative or positive Eu anomalies (Fig. 7a–c; Table S2). In addition, the trends of CaO and Al_2O_3 with MgO indicate fractional crystallization of clinopyroxene and plagioclase (Fig. 5).

The elements Al, Ti, REE, HFSE (Nb, Ta, Zr, Hf), Y, Sc and V are considered the least mobile during hydrothermal alteration and greenschist facies metamorphism of mafic volcanic rocks (e.g. Kerrich et al., 1999). Crustal contamination can account for variations in the Sm—Nd isotopic and geochemical composition of mafic rocks (Hofmann, 1997). Regarding Sm—Nd isotope data, the Babina mafic-ultramafic rocks have high εNd_t values ranging from +2.00 to +5.89 and an average T_{DM} of 3.6 ± 0.2 Ga, which together with the absence of any correlation between MgO and SiO_2 vs. εNd_t (Fig. 10a–b) may indicate little or no crustal contamination in their generation. Nonetheless, few samples display enriched REE patterns that most likely are the effects of alteration or crustal contamination (Fig. 7a; Polat and Hofmann, 2003; Lahaye et al., 1995). In addition, the Mauranipur mafic rocks have highly variable εNd_t with values that vary between +0.24 and + 9.09, which along with their older T_{DM} (3.9 ± 0.3 Ga) suggest a likely crustal contamination or derivation from a heterogeneous mantle source. On the other hand, in the bi-variate diagram of Pearce (2008), which is based on petrogenetic modelling of immobile trace elements (Nb/Yb vs. Th/Yb), the samples from the two greenstone belts plot above the MORB-OIB array (Fig. 11a), mainly following the AFC trend from a depleted mantle source (Fig. 11b). This suggests a variable degree of crustal assimilation that seems to be more important in the Mauranipur mafic rocks (Fig. 11a), which agrees well with the Nd isotopic data variation presented here. This also corroborates the crust-mantle interaction previously suggested by Singh et al. (2018) for some mafic-ultramafic rocks from the Babina and Mauranipur greenstone belts, based on variations in the La/Sm and La/Ta ratios. Archean mafic-ultramafic greenstone belt rocks with high Th/Nb ratios, with a possible crust-mantle interaction, have been described in other Archean shields worldwide such as the Pilbara Craton, Yilgarn Craton, Abitibi Craton and Northern Superior Province (Pearce, 2008, reference therein). From above evidence, it seems that the studied rocks from the Babina and Mauranipur greenstone belts came from mantle sources and evolved through fractional

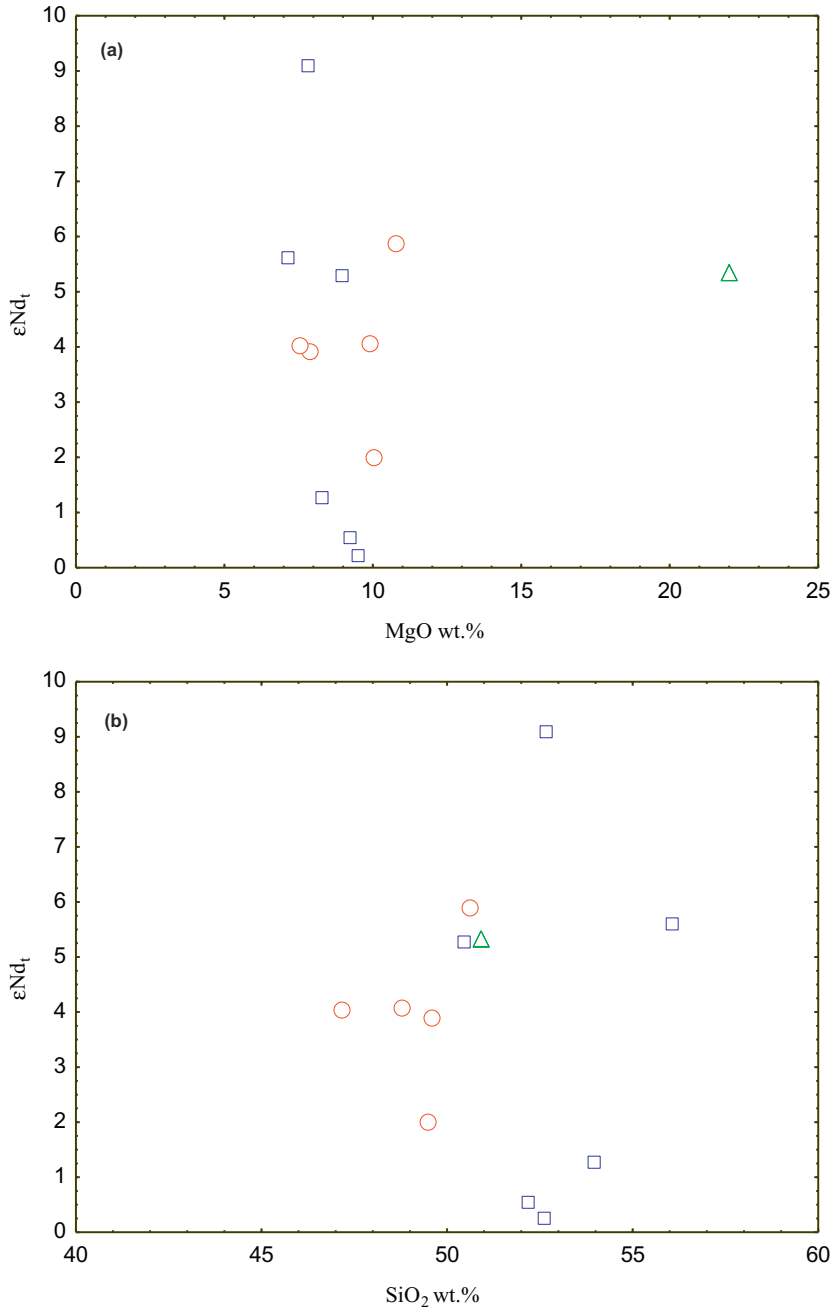

Fig. 10. (a) MgO vs. εNd_t and (b) SiO_2 vs. εNd_t bi-variate diagrams for the mafic-ultramafic rocks from the Babina and mafic rocks from the Mauranipur greenstone belts, Bundelkhand Craton.

crystallization with variable degree of crustal contamination (i.e., AFC processes) that seems to be more efficient in the Mauranipur greenstone belt.

7.3. Mafic rocks and mantle source characteristic

In the bivariate (Nb/Th vs. Th/Yb) diagrams of Pearce (2008), the most primitive rocks were plotted nearby the MORB-OIB mantle array, which indicates a significant involvement of depleted mantle sources (Fig. 11a–b). Positive εNd_t values indicate a juvenile source derived from a depleted mantle. In Table 2, all samples from the Babina area and three most depleted samples from the Mauranipur have positive εNd_t values (+1.26 to +5.89). Interestingly, they resemble the majority of Archean mafic components worldwide without significant crustal contamination (Fig. 12), with positive εNd_t values between +1.0 and + 4.5 (DePaolo, 1988; Dickin, 1995).

Smithies et al. (2018) discussed the performance of the bivariate diagrams Th/Yb vs. Nb/Yb of Pearce (2008) to assess how mantle-derived magmas and crust has interacted by applying to basaltic rocks from well-studied Archean greenstone belts. Accordingly, greenstone belts with variable Th/Nb-Nb/Yb trends reflect mixing between low Th/Nb-Nb/Yb mantle-derived melts and high Th/Nb-Nb/Yb crust, whereas those belts with constant Th/Nb-Nb/Yb trends probably require derivation from a source already possessing a high and relatively constant Th/Nb-Nb/Yb trends (Smithies et al., 2018). Our study shows a distinct trends that traverses from primitive mantle to continental crust (variable Th/Nb-Nb/Yb trends; Fig. 11a) of Paleoarchean mafic-ultramafic rocks from the Babina and Mauranipur greenstone belts, which reflect interaction between mantle melts and continental crust (Fig. 11a).

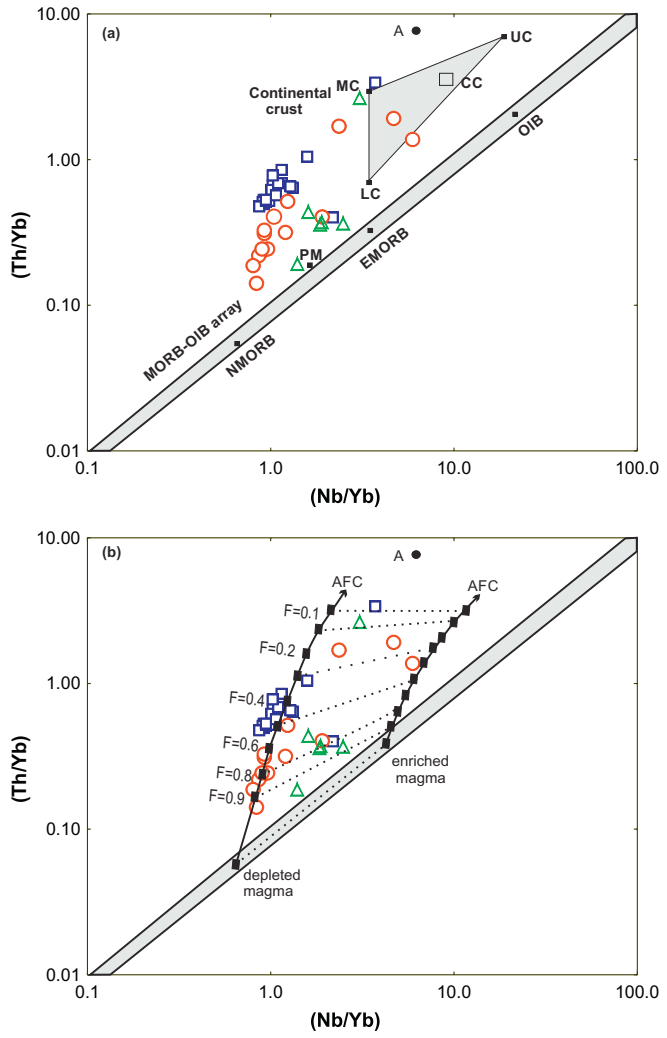

Fig. 11. (a) Petrogenetic modelling of the Nb/Yb–Th/Yb projection after Pearce (2008). a) Primordial Mantle (PM) and continental crust where (LC) average lower crust, (UC) upper crust, (CC) total continental crust, and (A) Archean crust for basaltic samples; nb) crustal contamination of depleted and enriched magmas with the continental crust; F denotes percentage of magma left.

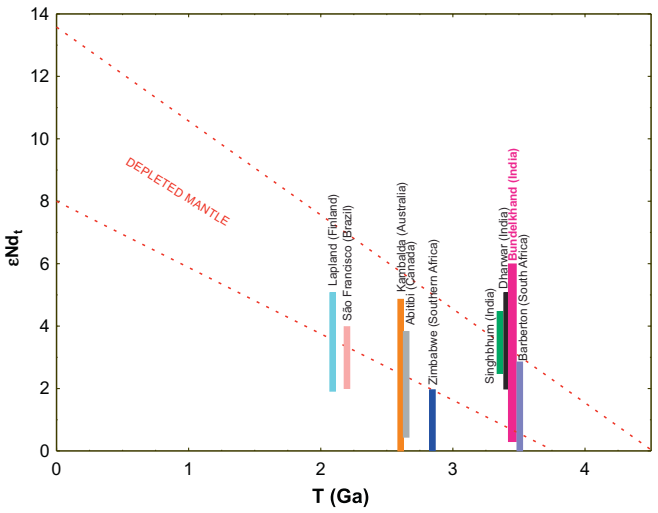

Fig. 12. Time (Ga) vs. εNd_t composition of komatiites and mafic-ultramafic rocks. The vertical bars represent the mantle source composition from different cratons worldwide, including the Bundelkhand data of present study. Age and εNd_t data were taken from (Arndt et al., 2008; Chaudhuri et al., 2017; Jayananda et al., 2008; Maya et al., 2017; Silva, 1992 and references therein).

This is also in accordance with an evolution of these magmas through AFC processes as discussed above.

7.4. Geochronological aspects

The whole-rock isochron presented here for the Babina mafic-ultramafic rocks yield an age of 3435 ± 161 Ma and an initial $^{143}Nd/^{144}Nd$ of 0.508268 (Fig. 8). The poor correlation between $^{147}Sm/^{144}Nd$ and $^{143}Nd/^{144}Nd$ data obtained for the Mauranipur mafic rocks did not give a reasonable precision in age. This poor isotopic correlation could be caused by the variable degree of crustal assimilation showed by these rocks as discussed in the previous section. However the field disposition and deformational features such as imprints of all the three major deformational features on it and Sm—Nd isochron age, altogether also supports Paleoarchean ages for the Mauranipur mafic-ultramafic rocks. Thus, the isochron age 3.44 ± 0.16 Ga is considered formation age of mafic-ultramafic rocks in the central Bundelkhand Craton.

The TTG and granite–monzogranite–syenogranite (GMS) series rocks in the Bundelkhand Craton can be grouped after available geochronological data as: (i) TTG suite emplaced approximately 3.5–3.3 Ga and (ii) the younger TTG (mainly 2.7 Ga) and GMS series plutons (emplaced approximately 2.58–2.35 Ga) occurring over large part of the belt and whose emplacements concur with the stabilization of the Bundelkhand Craton (Joshi et al., 2017; Kaur et al., 2016; Mondal et al., 2002; Saha et al., 2016; Singh et al., 2019; Verma et al., 2016). The felsic volcanic rocks emplaced about 2.54 Ga, were classified as calc–alkaline dacite, less commonly rhyolite in the Babina belt (Singh and Slabunov, 2015). 2.78 Ga high pressure muscovite minerals and the 2.73–2.47 Ga monazite ages reported from the Babina greenstone belt maybe conceivably connected to metamorphic events during accretion processes (Saha et al., 2011). According to Saha et al. (2016) and Verma et al. (2016), ca. 3.5–3.4 Ga, and ca. 2.7 Ga magmatic zircon ages were reported for TTG from the Babina, whereas ages of ca. 3.5–3.3 Ga, and ca. 3.2 were reported for the TTG from the Mauranipur (Kaur et al., 2016; Mondal et al., 2002). This finding supports that TTG and mafic-ultramafic rocks were emplaced during the Paleoarchean between 3.55 and 3.20 Ga.

7.5. Geodynamic evolution and tectonic setting of the Babina and Mauranipur greenstone belts

The geodynamics and tectonic setting of the Bundelkhand Craton has been controversial and a matter of debate as in the case of most of the Archean blocks worldwide. Subduction-related tectonic setting has been proposed (Malviya et al., 2006; Singh and Slabunov, 2015) for these greenstone belts, which have been recently complemented with processes such as slab breakoff (Joshi et al., 2017) and plume-arc accretion processes (Singh et al., 2018).

The petrology, geochemistry and Nd isotopic systematics of mafic-ultramafic rocks from the Babina and Mauranipur greenstone belts play a key role to contribute to this debate. These greenstone belts are located in the central part of the craton, along the “Tectonic Zone”. The ubiquitous association of mafic-ultramafic, ultramafic cumulate rocks, and closed association of BIF and metasediment strongly favor that these greenstone belts are remnant of oceanic crust. These rocks plot in a subduction-related setting in the tectonic discrimination diagrams (Verma and Agrawal, 2011, Fig. 13a–b). In addition, large variation of initial epsilon Nd values (Fig. 10a–b) suggest that mafic-ultramafic rocks were likely derived from depleted mantle sources and/or underwent crustal contamination, which hamper the use of tectonic setting discrimination diagrams. Thus, tectonic discrimination diagrams based on modern magmas are unsuitable for the purpose of

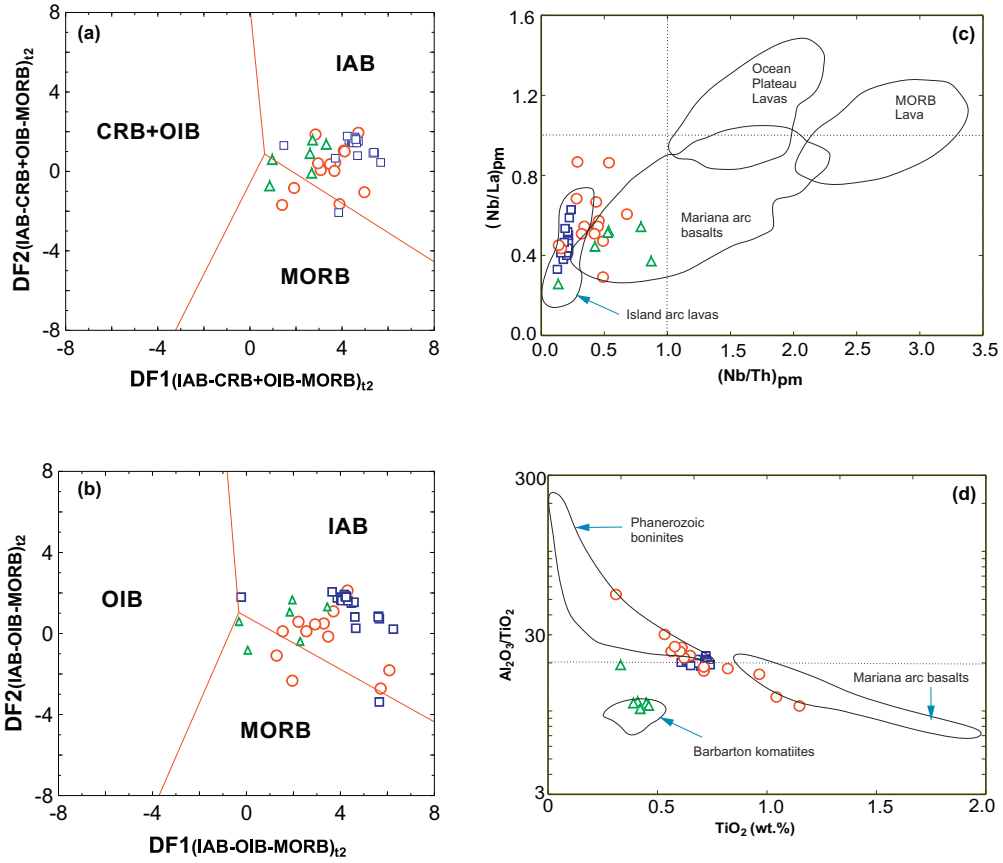

Fig. 13. (a-b) Application of log–ratio transformed immobile trace element–based discriminant function DF1–DF2 discrimination diagrams (Verma and Agrawal, 2011) for mafic-ultramafic rock samples from the Babina and Mauranipur greenstone belts. The four fields that can be discriminated are: IAB–island (and continental) arc mafic-ultramafic rocks; CRB–continental rift mafic-ultramafic rocks; OIB–ocean island mafic-ultramafic rocks; MORB–mid-ocean ridge mafic-ultramafic rocks; (c) Primitive mantle normalized Nb/Th vs. Nb/La diagram. Fields for island arc lavas, oceanic plateau lavas and MORB lavas is as shown in Puchtel et al. (1999); (d) Bivariate TiO_2 vs. Al_2O_3/TiO_2 discrimination diagram for mafic-ultramafic rocks from the Babina and Mauranipur greenstone belts, Bundelkhand Craton.

describing the conditions on the Archean Earth and will therefore focus our interpretations on a discussion on the likely sources of Archean magmas (Moyen and Laurent, 2018). Fig. 11a, the mafic-ultramafic rocks coincide with Primitive Mantle (PM), near MORB-OIB array, representing typical greenstone belt rocks sourced from PM like mantle and emplaced in oceanic settings (Pearce, 2008). Further, a subduction like rocks are well documented in Archean on the basis of their geochemical signature (Polat and Kerrich, 2006). These rocks are characterized by mafic to intermediate composition and attribute a degree of a subduction-related processes (i.e. fluid-fluxed melting of the mantle, or mixing of sediments into a depleted mantle).

Similarly, geochemical composition of mafic-ultramafic rocks from the Babina and Mauranipur greenstone belts are also attributed to a subduction related setting (Fig. 13c; Polat and Hofmann, 2003), although crustal contamination may also account for a subduction related signature. The high MgO, Mg#, and low HFSE characteristics of ultramafic rocks resembles to komatiites (Puchtel et al., 1999). However, ultramafic rocks from these greenstone belts exhibit negative Nb and Ti anomalies (Figs. 7b and 13c), which is typical of rocks generated in a subduction-related tectonic setting or due to assimilation with crustal material, probably with oceanic sediments (Pearce and Peate, 1995), and do not support typical tectonic setting of Archean komatiite. Moreover, they show marked similarities in geochemical composition with the modern boninites and the Barberton type komatiites, and komatiitic basalts (e.g., low Ti/Zr ratios, depleted Nb and Ti anomalies, flat REE patterns). According to Parman et al. (2004), Barberton komatiites were generated in subduction zone, and their origin relates to hydrous melting in mantle plume. Similarly, modern boninites generated by hydrous melting of mantle wedge in an arc setting: except that the mantle temperatures were relatively higher in the Archean, and that these komatiites represent Archean equivalents of modern boninites (Smithies et al., 2004). Thus, the ultramafic samples from the Babina and Mauranipur greenstone belts plotted in the field of the Barberton komatiites (Fig. 13d). The ultramafic rocks have higher Al_2O_3/TiO_2 ratio (average 21) that may be simply due to partial melting beyond garnet stabilization depth as compared to the lower Al_2O_3/TiO_2 ratio (10) for the Barberton komatiites (Fig. 13d; Parman et al., 2004). Finally, the Barberton komatiites are characterized by higher Nb/Th (8.3–14; Chavagnac, 2004), whereas the studied mafic-ultramafic samples indicate low (Nb/Th = 1.08–7.5) and CaO/Al_2O_3 (0.56–1.70) is almost identical to certain high calcium boninites (CaO/Al_2O_3 (0.49–1.02)); (Falloon and Crawford, 1991). The mineral chemistry of olivine and Cr spinel suggest its arc cumulate origin (Malviya et al., 2006).

Furthermore, it is proposed that during the Paleoarchean, the thick oceanic plateau provided as a base for subduction of oceanic crust generating basaltic rock in an arc affinity. The plausible geodynamic model based on geochemical data along with lithological framework of the Babina and Mauranipur greenstone belts have been schematically represented in Fig. 14. Based on all above discussion, it is proposed that the mafic-ultramafic rocks along with metasedimentary rocks from the Babina and Mauranipur greenstone belts were emplaced in intra oceanic arc-related tectonic setting during Paleoarchean time. Similar model has been proposed for other cratonic blocks of Indian shield (viz the Bastar, Dharwar and Singhbhum, cratons) during Paleoarchean

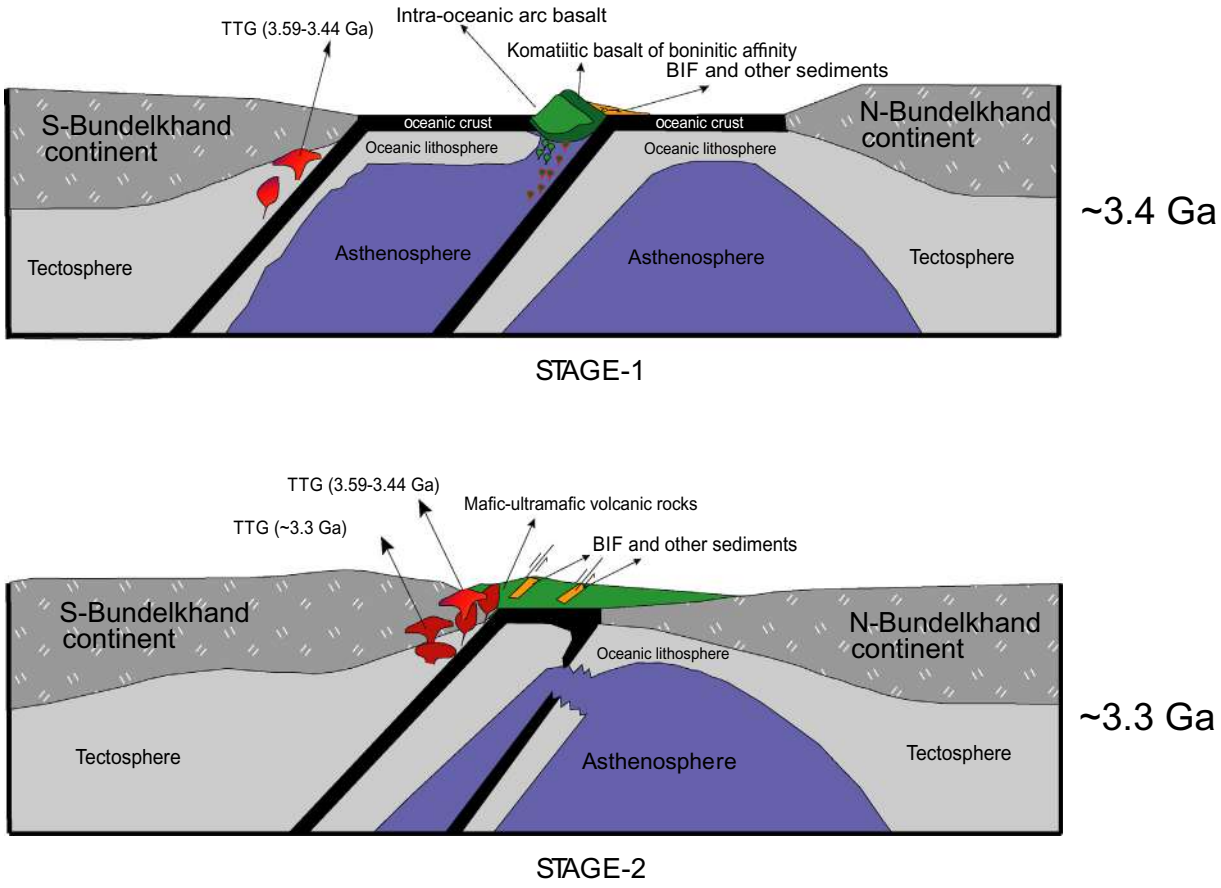

Fig. 14. Schematic cartoon representing the geodynamic evolution of the Babina and Mauranipur greenstone belts. Subducting oceanic crust and slab rollback under the oceanic plateau resulting in a volcanic island arc-related magma.

to Neoarchean time (Manikyamba et al., 2005; Manu Prasanth et al., 2018). Finally, these greenstone belts are interpreted as remnant oceanic crust formed in a subduction-related setting.

7.6. Period of Archean mafic emplacement of Indian cratons

It has been reported 3.44–3.14 Ga Archean mafic-ultramafic rocks in the Indian cratons (Bundelkhand, Dharwar, and Singhbhum; Table 3, for references see supplementary file-SR2). Present study reports mafic-ultramafic rocks Sm—Nd isochron age (ca.3.44 Ga) for the greenstone belts of the Bundelkhand Craton. This age is almost similar to the mafic-ultramafic rocks of ca. 3.35 Ga and 3.14 Ga komatiites (Jayananda et al., 2008; Maya et al., 2017) from the Sargur Group and Banasandra greenstone belts, Dharwar Craton and 3.34 Ga komatiites (Chaudhuri et al., 2017) and 3.30 Ga amphibolites (Sharma et al., 1994) from the Gorumahishani-Badampahar greenstone belt and Older Metamorphic Group, Singhbhum Craton (Table 3). The presence of similar lithology and age in the Bundelkhand, Singhbhum and Dharwar cratons may display similar tectonic style during Paleoarchean time in these cratons.

Table 3
The list of Indian cratons and their previous records of mafic-ultramafic rocks.

Indian craton	Sm-Nd age (Ga) of mafic-ultramafic rocks	References (SR2-see supplementary file)
Bundelkhand Craton	3.44, 3.3–4.9[a]	This study, 1
Dharwar Craton	3.35, 3.14	2, 3
Singhbhum Craton	3.4, 3.3, 3.6–5.6[a]	4, 5, 6

[a] T_{DM} Nd model age.

8. Conclusions

The synthesis of whole-rock geochemistry and Sm—Nd isotope systematics are in favor of the following conclusions:

1. The Babina mafic-ultramafic rocks define whole-rock Sm—Nd isochron indicating that they were formed at 3435 ± 161 Ma, whereas poor correlation between $^{147}Sm/^{144}Nd$ and $^{143}Nd/^{144}Nd$ data obtained for the Mauranipur mafic rocks did not provide reasonable precision in Sm—Nd isochron age.
2. Trace elements ratios suggest that the fractionation of clinopyroxene and minor olivine was the most likely process involved in the generation of the mafic-ultramafic rocks.
3. Whole-rock geochemical analysis and positive εNd_t values (+0.24 to +9.09) suggest that mafic magmas derived from a depleted mantle source and evolved through fractional crystallization associated with crustal assimilation.
4. The mafic-ultramafic and associated metasedimentary rocks from the Babina and Mauranipur greenstone belts are remnant of oceanic crust possibly emplaced in a subduction related environment and are post to syngenetic to oldest (ca. 3.59 Ga) TTG intrusion.

Acknowledgment

The first author (PKS) is thankful to the National Council of Science and Technology (CONACYT), Mexico for his doctoral fellowship [grant # 612752], whose doctoral thesis is in preparation under the guidance of SKV and Association of Applied Geochemist (AAG) for the partial analytical support. SKV is grateful to Newton Advanced Fellowship award–The Royal Society, UK for the grant [NA160116]. JAM thanks

CONICET for his postdoctoral grant. EPO thank to the São Paulo Research Foundation (FAPESP) for the grants [2012/15824-6], which were used in the analytical purpose, and to Brazilian CNPq for a productivity research grant. VKS thanks the Department of Science and Technology, Govt. of India for grant (INT/RUS/RFBR/P-279). VKS and SKV are thankful to the Bundelkhand University, Jhansi, India and IPICYT, Mexico, as supporting under MOU for field mapping. VPM and MA gratefully acknowledge the Ministry of Education Culture, Sports, Science and Technology, Govt. of Japan for their Monbukagakusho grant. We express our sincere gratitude to Dr. Carmen Galindo Francisco and Dr. Jose Manuel Fuenlabrada Perez to provide us isotopic analysis. We are grateful to the Ex-Editor-in-chief "Prof. Nelson Eby" and current Editor-in-chief "Prof. Michael Roden" and two reviewers (Dr. Aitor Cambeses and Dr. Trisrota Chaudhuri) for their helpful comments and suggestions to improve our final version of manuscript.

Appendix A. Supplementary data

Supplementary data to this article can be found online at https://doi.org/10.1016/j.lithos.2019.02.010.

References

Abbott, R.N., Raymond, L.A., 1984. The Ashe metamorphic suite, Northwest North Carolina: metamorphism and observations on geologic history. American Journal of Science 284, 350–375.
Absar, N., Raza, M., Roy, M., Naqvi, S.M., Roy, A.K., 2009. Composition and weathering conditions of Paleoproterozoic upper crust of Bundelkhand craton, Central India: records from geochemistry of clastic sediments of 1.9 Ga Gwalior Group. Precambrian Research 168, 313–329.
Anhaeusser, C.R., 2014. Archaean greenstone belts and associated granitic rocks–a review. Journal of African Earth Sciences 100, 684–732.
Arndt, N.T., Lesher, C.M., Barnes, S.J., 2008. Komatiites. Cambridge University, New York.
Basu, A.K., 1986. Geology of parts of the Bundelkhand Granite Massif, Central India. Records, Geological Survey of India, pp. 61–124 Ed.
Bédard, J.H., Harris, L.B., Thurston, P., 2014. The hunting of the snArc. Precambrian Research 229, 20–48.
Braun, J.J., Pagel, M., Herbillon, A., Rosin, C., 1993. Mobilization and redistribution of REEs and thorium in a syenitic lateritic profile: a mass balance study. Geochimica et Cosmochimica Acta 57, 4419–4434.
Chaudhuri, T., Satish-Kumar, M., Mazumder, R., Biswas, S., 2017. Geochemistry and Sm-Nd isotopic characteristics of the Paleoarchean Komatiites from Singhbhum Craton, Eastern India and their implications. Precambrian Research 298, 385–402.
Chavagnac, V., 2004. A geochemical and Nd isotopic study of Barberton komatiites (South Africa): implication for the Archean mantle. Lithos 75, 253–281.
Condie, K.C., 2000. Episodic continental growth models: afterthoughts and extensions. Tectonophysics 322, 153–162.
Condie, K.C., 2005. High field strength element ratios in Archean basalts: a window to evolving sources of mantle plumes? Lithos 79, 491–504.
Condie, K.C., Aster, R.C., van Hunen, J., 2016. A great thermal divergence in the mantle beginning 2.5 Ga: geochemical constraints from greenstone basalts and komatiites. Geoscience Frontiers 7, 543–553.
Cotta, A.J.B., Enzweiler, J., 2009. Quantification of major and trace elements in water samples by ICP–MS and collision cell to attenuate Ar and Cl-based polyatomic ions. Journal of Analytical Atomic Spectrometry 24, 1406–1413.
DePaolo, D.J., 1988. Neodymium Isotope Geochemistry: An Introduction. Springer-Verlag, Berlin.
Dickin, A.P.G., 1995. Radiogenic Isotope Geochemistry. Cambridge.
Falloon, T.J., Crawford, A.J., 1991. The petrogenesis of high-calcium boninite lavas dredged from the northern Tonga ridge. Earth and Planetary Science Letters 102, 375–394.
Goldstein, S.L., O'Nions, R.K., Hamilton, P.J., 1984. A Sm–Nd isotopic study of atmospheric dust and particulates from major river systems. Earth and Planetary Science Letters 70, 221–236.
Herzberg, C., Condie, K., Korenaga, J., 2010. Thermal history of the Earth and its petrological expression. Earth and Planetary Science Letters 292, 79–88.
Hofmann, A.W., 1997. Mantle geochemistry: the message from oceanic volcanism. Nature 385, 219–229.
Hofmann, A.W., 2003. Sampling mantle heterogeneity through oceanic basalts: isotopes and trace elements. In: Carlson, R.W. (Ed.), Treatise on Geochemistry. Elsevier, pp. 61–101.
Iwamori, H., Nakamura, H., 2015. Isotopic heterogeneity of oceanic, arc and continental basalts and its implications for mantle dynamics. Gondwana Research 27, 1131–1152.
Jayananda, M., Kano, T., Peucat, J.-J., Channabasappa, S., 2008. 3.35 Ga komatiite volcanism in the western Dharwar craton, southern India: constraints from Nd isotopes and whole-rock geochemistry. Precambrian Research 162, 160–179.
Joshi, K.B., Bhattacharjee, J., Rai, G., Halla, J., Ahmad, T., Kurhila, M., Heilimo, E., Choudhary, A.K., 2017. The diversification of granitoids and plate tectonic implications at the Archean–Proterozoic boundary in the Bundelkhand craton, Central India. In: Halla, J., Whitehouse, M.J., Ahmad, T., Bagai, Z. (Eds.), Crust–Mantle Interactions and Granitoid Diversification: Insights from Archean Cratons. vol. 449. Geological Society, London, Special Publications, pp. 123–157.
Kaur, P., Zeh, A., Chaudhri, N., 2014. Characterisation and U–Pb–Hf record of the 3.55 Ga felsic crust from the Bundelkhand Craton, northern India. Precambrian Research 255, 236–244.
Kaur, P., Zeh, A., Chaudhri, N., Eliyas, N., 2016. Unravelling the record of Archean crustal evolution of the Bundelkhand Craton, northern India using U–Pb zircon–monazite ages, Lu–Hf isotope systematics, and whole-rock geochemistry of granitoids. Precambrian Research 281, 384–413.
Keller, B., Schoene, B., 2018. Plate tectonics and continental basaltic geochemistry throughout Earth history. Earth and Planetary Science Letters 481, 290–304.
Kerrich, R., Wyman, D., Hollings, P., Polat, A., 1999. Variability of Nb/Th and Th/La in 3.0 to 2.7 Ga Superior Province ocean plateau basalts: implications for the timing of continental growth and lithosphere recycling. Earth and Planetary Science Letters 168, 101–115.
Kump, L.R., Barley, M.E., 2007. Increased subaerial volcanism and the rise of atmospheric oxygen 2.5 billion years ago. Nature 448, 1033.
Lahaye, Y., Arndt, N.T., Byerly, G., Gruau, G., Fourcade, S., Chauvel, C., 1995. The influence of alteration on the trace-element and Nd isotope compositions of komatiites. Chemical Geology 126, 43–64.
Le Bas, M.J., Maitre, R.W.L., Streckeisen, A., Zanettin, B., 1986. A chemical classification ofvolcanic rocks based on the total alkali–silica diagram. Journal of Petrology 27, 745–750.
Malviya, V.P., Arima, M., Pati, J.K., Kaneko, Y., 2004. First report of metamorphosed pillow lava in central part of Bundelkhand craton–an island arc setting of possible late Archean age. Gondwana Research 7, 1338–1340.
Malviya, V.P., Arima, M., Pati, J.K., Kaneko, Y., 2006. Petrology and geochemistry of metamorphosed basaltic pillow lava and basaltic komatiite in the Mauranipur area: subduction related volcanism in the Archean Bundelkhand craton, Central India. Journal of Mineralogical and Petrological Sciences 101, 199–217.
Manglik, A., Adilakshmi, L., Suresh, M., Thiagarajan, S., 2015. Thick sedimentary sequence around Bahraich in the northern part of the central Ganga foreland basin. Tectonophysics 653, 33–40.
Manikyamba, C., Naqvi, S.M., Rao, D.S., Mohan, M.R., Khanna, T.C., Rao, T.G., Reddy, G.L.N., 2005. Boninites from the Neoarchaean Gadwal greenstone belt, Eastern Dharwar craton, India: implications for Archaean subduction processes. Earth and Planetary Science Letters 230, 65–83.
Manu Prasanth, M.P., Hari, K.R., Chalapathi Rao, N.V., Hou, G., Pandit, D., 2018. An island-arc tectonic setting for the Neoarchean Sonakhan Greenstone Belt, Bastar Craton, Central India: Insights from the chromite mineral chemistry and geochemistry of the siliceous high-Mg basalts (SHMB). Geological Journal 53, 1526–1542.
Maya, M., Bhutani, R., Balakrishnan, S., Sandhya, S.R., 2017. Petrogenesis of 3.15 Ga old Banasandra komatiites from the Dharwar craton, India: Implications for early mantle heterogeneity. Geoscience Frontiers 8, 467–481.
McDonough, W.F., Sun, S.S., 1995. The composition of the Earth. Chemical Geology 120, 223–253.
Mohan, M.R., Singh, S.P., Santosh, M., Siddiqui, M.A., Balaram, V., 2012. TTG suite from the Bundelkhand Craton, Central India: geochemistry, petrogenesis and implications for Archean crustal evolution. Journal of Asian Earth Sciences 58, 38–50.
Mondal, M.E.A., Goswami, J.N., Deomurari, M.P., Sharma, K.K., 2002. Ion microprobe $^{207}Pb/^{206}Pb$ ages of zircons from the Bundelkhand massif, northern India: implications for crustal evolution of the Bundelkhand–Aravalli protocontinent. Precambrian Research 117, 85–100.
Moyen, J.-F., Laurent, O., 2018. Archaean tectonic systems: a view from igneous rocks. Lithos 302–303, 99–125.
Naqvi, S.M., Rogers, J.J.W., 1987. Precambrian Geology of India: Oxford Monographs on Geology and Geophysics. Oxford University Press, Oxford, p. 223.
Parman, S.W., Dann, J.C., Grove, T.L., De Wit, M.J., 1997. Emplacement conditions of komatiite magmas from the 3.49 Ga Komati Formation, Barberton greenstone belt, South Africa. Earth and Planetary Science Letters 150, 303–323.
Parman, S.W., Grove, T.L., Dann, J.C., deWit, M.J., 2004. A subduction origin for komatiites and cratonic lithospheric mantle. South African Journal of Geology 107, 107–118.
Pati, J.K., Patel, S.C., Pruseth, K.L., Malviya, V.P., Arima, M., Raju, S., Prakash, K., 2007. Geology and geochemistry of giant quartz veins from the Bundelkhand Craton, Central India and their implications. Journal of Earth System Science 116, 497–510.
Pati, J.K., Raju, S., Malviya, V.P., Bhushan, R., Prakash, K., Patel, S.C., 2008. Mafic Dykes of Bundelkhand Craton, Central India: Field, Petrological and Geochemical Characteristics. Indian Dykes: Geochemistry, Geophysics and Geochronology. Narosa Publishing House, New Delhi, pp. 547–569.
Pearce, J.A., 2008. Geochemical fingerprinting of oceanic basalts with applications toophiolite classification and the search for Archean oceanic crust. Lithos 100, 14–48.
Pearce, J.A., Peate, D.W., 1995. Tectonic implications of the composition of volcanic arc magmas. Annual Review of Earth and Planetary Sciences 23, 251–285.
Polat, A., Hofmann, A.W., 2003. Alteration and geochemical patterns in the 3.7–3.8 Ga Isua greenstone belt, West Greenland. Precambrian Research 126, 197–218.
Polat, A., Kerrich, R., 2006. Reading the geochemical fingerprints of Archean hot subduction volcanic rocks: evidence for accretion and crustal recycling in a mobile tectonic regime. In: Benn, K., Mareschal, J.-C., Condie, K.C. (Eds.), Archean Geodynamics and Environments. American Geophysical Union, pp. 189–213.
Polat, A., Hofmann, A.W., Rosing, M.T., 2002. Boninite-like volcanic rocks in the 3.7–3.8 Ga Isua greenstone belt, West Greenland: geochemical evidence for intraoceanic, subduction zone processes in the early Earth. Chemical Geology 184, 231–254.
Pradhan, V.R., Meert, J.G., Pandit, M., Kamenov, G., Mondal, M.E.A., 2012. Paleomagnetic and geochronological studies of the mafic dyke swarms of Bundelkhand craton, Central India: implications for the tectonic evolution and paleogeographic reconstructions. Precambrian Research 198–199, 51–76.

Puchtel, I.S., Hofmann, A.W., Amelin, Yu.V., Garbe-Schonberg, C.D., Samsonov, A.V., Shchipansky, A.A., 1999. Combined mantle plume–island arc model for the formation of the 2.9 Ga Sumozero-Kenozero greenstone belt, SE Baltic Shield: isotope and traceelement constraints. Geochimica et Cosmochimica Acta 63, 3579–3595.

Ramiz, M.M., Mondal, M.E.A., Farooq, S.H., 2018. Geochemistry of ultramafic–mafic rocks of the Madawara Ultramafic complex in the southern part of the Bundelkhand Craton, Central Indian Shield: Implications for mantle sources and geodynamic setting. Geological Journal https://doi.org/10.1002/gj.3290 in press.

Rollinson, H.R., 1993. Using Geochemical Data: Evaluation, Presentation, Interpretation. Longman Scientific Technical, Essex, p. 344.

Saha, L., Pant, N.C., Pati, J.K., Berndt, J., Bhattacharya, A., Satynarayanan, M., 2011. Neoarchean high-pressure margarite-phengitic muscovite-chlorite corona mantled corundum in quartz-free high-Mg, Al phlogopite-chlorite schists from the Bundelkhand craton, North Central India. Contributions to Mineralogy and Petrology 161, 511–530.

Saha, L., Frei, D., Gerdes, A., Pati, J.K., Sarkar, S., Patoke, V., Bhandari, A., Nasipur, P., 2016. Crustal geodynamics from the Archean Bundelkhand Craton, India: constraints from zircon U–Pb–Hf isotope studies. Geological Magazine 153, 179–192.

Sharma, M., Basu, A.R., Ray, S.L., 1994. Sm-Nd isotopic and geochemical study of the Archean tonalite-amphibolite association from the eastern Indian Craton. Contributions to Mineralogy and Petrology 117, 45–55.

Sharma, K.K., Rahman, A., 1995. Occurrence and petrogenesis of Loda Pahar trondhjemitic gneiss from Bundelkhand craton, Central India: remnant of an early crust. Current Science 613–617.

Silva, M.G., 1992. Evidências isotópicas e geocronológicasde umfenômeno de acrescimentocristal transamazônico no craton do São Francisco, Estadoda Bahia. XXXVVII Congresso Brasileiro de Geologia, São Paulo, SBG, Anais. vol. 2, pp. 181–182.

Singh, V.K., Slabunov, A., 2015. The central Bundelkhand Archean greenstone complex, Bundelkhand craton, Central India: geology, composition, and geochronology of supracrustal rocks. International Geology Review 57, 1349–1364.

Singh, S.P., Subramanyam, K.S.V., Manikyamba, C., Santosh, M., Singh, M.R., Kumar, B.C., 2018. Geochemical systematics of the Mauranipur-Babina greenstone belt, Bundelkhand Craton, Central India: Insights on Neoarchean mantle plume-arc accretion and crustal evolution. Geoscience Frontiers 9, 769–788.

Singh, P.K., Verma, S.K., Singh, V.K., Moreno, J.A., Oliveira, E.P., Mehta, P., 2019. Geochemistry and petrogenesis of sanukitoids and high-K anatectic granites from the Bundelkhand Craton, India: Implications for late-Archean crustal evolution. Journal of Asian Earth Sciences https://doi.org/10.1016/j.jseaes.2018.12.013 in press.

Slabunov, A., Singh, V.K., 2018. Meso–Neoarchaean crustal evolution of the Bundelkhand Craton, Indian Shield: new data from greenstone belts. International Geology Review https://doi.org/10.1080/00206814.2018.1512906 in press.

Slabunov, A., Singh, V.K., Joshi, K.B., Li, X., 2017. Paleoarchean zircons from quartzite of South Bundelkhand Supracrustal complex: origin and implications for crustal evolution in Bundelkhand Craton, Central India. Current Science 112, 794–801.

Smithies, R.H., Champion, D.C., Sun, S.S., 2004. The case for Archaean boninites. Contributions to Mineralogy and Petrology 147, 705–721.

Smithies, R.H., Ivanic, T.J., Lowrey, J.R., Morris, P.A., Barnes, S.J., Wyche, S., Lu, Y.J., 2018. Two distinct origins for Archean greenstone belts. Earth and Planetary Science Letters 487, 106–116.

Stott, G., Mueller, W., 2009. Superior Province: the nature and evolution of th eArchean continental lithosphere. Precambrian Research 168, 1–3.

Tanaka, T., Togashi, S., Kamioka, H., Amakawa, H., Kagami, H., Hamamoto, T., Yuhara, M., Orihashi, Y., Yoneda, S., Shimizu, H., Kunimaru, T., Takahashi, K., Yanagi, T., Nakano, T., Fujimaki, H., Shinjo, R., Asahara, Y., Tanimizu, M., Dragusanu, C., 2000. JNdi-1: a neodymium isotopic reference in consistency with LaJolla neodymium. Chemical Geology 168, 279–281.

Van Acken, D., Hoffmann, J.E., Schorsher, J.H.D., Schulz, T., Heuser, A., Luhuet, A., 2016. Formation of high Al-komatiites from the Mesoarchean Quebra Osso Group, Minas Gerais, Brazil: trace elements, HSE systematics and Os isotope signatures. Chemical Geology 422, 108–121.

Vendemiatto, M.A., Enzweiler, J., 2001. Routine control of accuracy in silicate rock analysis by X-Ray fluorescence spectrometry. Geostandards and Geoanalytical Research 25, 283–291.

Verma, S.P., Agrawal, S., 2011. New tectonic discrimination diagrams for basic and ultrabasic volcanic rocks through log-transformed ratios of high field strength elements and implications for petrogenetic processes. Revista Mexicana de Ciencias Geológicas 28, 24–44.

Verma, S.P., Rivera-Gómez, M.A., 2013. Computer programs for the classification and nomenclature of igneous rocks. Episodes 36, 115–124.

Verma, S.K., Verma, S.P., Oliveira, E.P., Singh, V.K., Moreno, J.A., 2016. LA-SF-ICP-MS zircon U–Pb geochronology of granitic rocks from the central Bundelkhand greenstone complex, Bundelkhand craton, India. Journal of Asian Earth Sciences 118, 125–137.

Verma, S.K., Oliveira, E.P., Silva, P.M., Moreno, J.A., Amaral, W.S., 2017a. Geochemistry of komatiites and basalts from the Rio das Velhas and Pitangui greenstone belts, São Francisco Craton, Brazil: Implications for the origin, evolution, and tectonic setting. Lithos 284–285, 560–577.

Verma, S.P., Rivera-Gomez, M.A., Díaz-González, L., Pandarinath, K., Amezcua-Valdez, A., Rosales-Rivera, M., Verma, S.K., Quiroz-Ruiz, A., Armstrong Altrin, J.S., 2017b. Multidimensional classification of magma types for altered igneous rocks and application to their tectonomagmatic discrimination and igneous provenance of siliciclastic sediments. Lithos 278–281, 321–330.

Williams, H.M., Bizimis, M., 2014. Iron isotope tracing of mantle heterogeneity within the source regions of oceanic basalts. Earth and Planetary Science Letters 404, 396–407.

Winchester, J.A., Floyd, P.A., 1977. Geochemical discrimination of different magma series and their differentiation products using immobile elements. Chemical Geology 20, 325–343.

CHAPTER 3

Geochemistry and petrogenesis of sanukitoids and high-K anatectic granites from the Bundelkhand Craton, India: Implications for late-Archean crustal evolution

A presentation of the published research paper

This research paper is published in *Journal of Asian Earth Sciences*, in which the author of this thesis actively participated. I am the first author, and Dr. Sanjeet K. Verma, Prof. Vinod K. Singh, Dr. Juan A. Moreno, Prof. Elson P. Oliveira and Dr. Pankaj Mehta are the co-authors of the paper.

My Contribution in this research work can be summarized as follows:

1. Field work and sample collection
2. Sample preparation and analysis
3. Compilation of data from the literature
4. Data calculation and diagram preparation
5. Data interpretation and write-up of the work

Journal of Asian Earth Sciences 174 (2019) 263–282

Contents lists available at ScienceDirect

Journal of Asian Earth Sciences

journal homepage: www.elsevier.com/locate/jseaes

Full length article

Geochemistry and petrogenesis of sanukitoids and high-K anatectic granites from the Bundelkhand Craton, India: Implications for late-Archean crustal evolution

Pradip K. Singh[a], Sanjeet K. Verma[b,*], Vinod K. Singh[c], Juan A. Moreno[d], Elson P. Oliveira[e], Pankaj Mehta[f]

[a] Posgrado de la División de Geociencias Aplicadas, Instituto Potosino de Investigación Científica y Tecnológica (IPICYT), Camino a la Presa San José 2055, San Luis Potosí 78216, Mexico
[b] División de Geociencias Aplicadas, Instituto Potosino de Investigación Científica y Tecnológica (IPICYT), Camino a la Presa San José 2055, San Luis Potosí 78216, Mexico
[c] Department of Geology, Institute of Earth Sciences, Bundelkhand University, Jhansi, India
[d] Centro de Investigaciones en Ciencias de la Tierra (CICTERRA), Consejo Nacional de Investigaciones Científicas y Técnicas, Facultad de Ciencias Exactas, Físicas y Naturales, Universidad Nacional de Córdoba, Av. Vélez Sarsfield 1611, Edificio de CICTERRA, X5016CGA Córdoba, Argentina
[e] Department of Geology and Natural Resources, Institute of Geosciences, PO Box 6152, University of Campinas – UNICAMP, 13083-970 Campinas, SP, Brazil
[f] Department of Environmental Sciences, Central University of Jammu, J&K 181143, India

ARTICLE INFO

Keywords:
Sanukitoids
High-K anatectic granites
Sm–Nd isotope
Zircon age
Late Archean
Geodynamics
Bundelkhand Craton (India)

ABSTRACT

In this paper, we present in situ zircon U–Pb ages as well as whole-rock elemental and Sm-Nd isotopic compositions for late Archean sanukitoids of the Bundelkhand Craton, India. The LA–ICP–MS zircon U–Pb dating results of the sanukitoids (s.l.) indicate that these rocks were emplaced at 2577 ± 16 Ma, with inherited zircon at an age of 2644 ± 25 Ma, and are coeval with high-K anatectic granites (2544–2583 Ma). The sanukitoids (s.l.) are characterized by high-alumina (15–16 wt.%), Mg# (27–50) and TiO_2 (0.31–0.87 wt.%). They have a strongly enriched signature in terms of incompatible trace elements (LREEs and LILE) pointing to a subduction-related or crustal source. The high-K anatectic granites are characterized by Al_2O_3 (12–15 wt.%), Mg# (13–39) and TiO_2 (0.06–0.8 wt.%); they have enriched and variable concentrations of LILEs and REEs; and negative Eu anomalies (Eu/Eu* = 0.15–0.93). The whole-rock $\varepsilon_{Nd}(t)$ values (−3.64 to −1.66) indicate a crustal component. These isotopic and geochemical characteristics indicate that the sanukitoid plutons originated from the mixing of metasomatized mantle melts with anatectic melts and were followed by homogenization at shallow levels of emplacement, whereas the high-K anatectic granites indicate reworking of the pre-existing TTG crust during the cratonic stabilization ca. 2.5 Ga. This interpretation suggests a temporal evolution from TTG-domination through sanukitoids (s.l.) to anatectic leucogranites by an internal reworking of the continental crust, involving subduction-collision environments in the late Archean era. Such magmatic events and tectonics during the late-Archean in the Bundelkhand Craton resemble other Archean cratons, such as the Dharwar, North China, Karelian, Superior Province, Pilbara, Kaapvaal and Amazonian.

1. Introduction

It is generally accepted that most of the continental crust was formed in the Archean era, chiefly in the late Archean, although only < 10% of the crust of that age is still preserved (Hawkesworth et al., 2013, 2018). Thus, a knowledge of the evolution and reworking of the Archean continental crust is of great importance to understanding the early evolution of the Earth. The Archean cratons commonly consist of Tonalite-Trondhjemite-Granodiorite (TTG) suites, komatiites, and high-K granitoids. The former (TTGs and komatiites) are predominant in the Paleo- and Mesoarchean, whereas the high-K magmatism is predominant in the late Archean (e.g., Laurent et al., 2014). Consequently, late Archean crust is mostly composed of high-K granodiorite–granite (Barbarin, 1999; Laurent et al., 2014), which is generally interpreted as a change in the petrogenetic and geodynamic processes of crustal growth (Keller and Schoene, 2012; Moyen and

* Corresponding author.
E-mail addresses: pradip.singh@ipicyt.edu.mx (P.K. Singh), sanjeet.verma@ipicyt.edu.mx (S.K. Verma), vinodksingh@bujhansi.ac.in (V.K. Singh), jmoreno_2@ugr.es (J.A. Moreno), elson@ige.unicamp.br (E.P. Oliveira).

https://doi.org/10.1016/j.jseaes.2018.12.013
Received 11 July 2018; Accepted 21 November 2018
Available online 04 January 2019

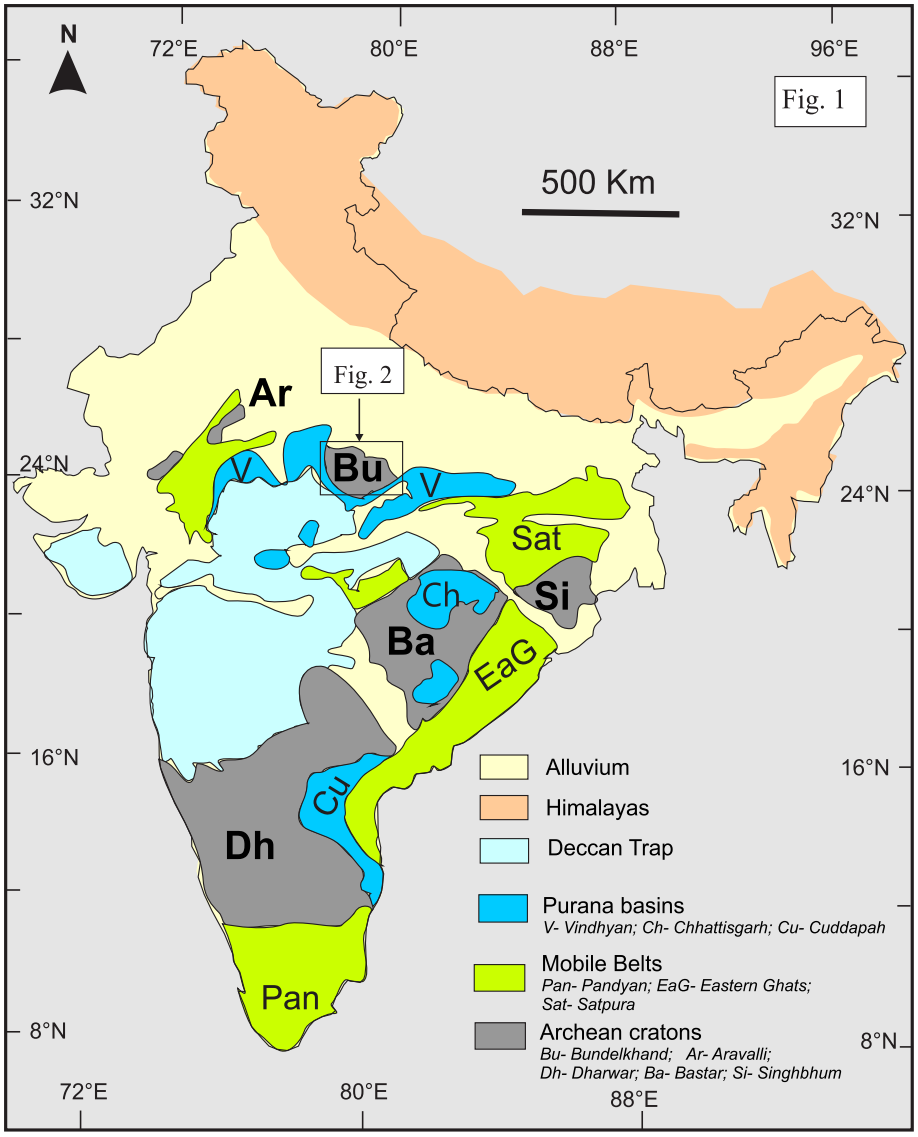

Fig. 1. Generalized geological map of the Indian shield with Archean cratonic blocks (modified after: Ramakrishnan and Vaidyanadhan, 2010; Verma et al., 2016).

Laurent, 2018). Such high-K magmatism mainly consists of high-Mg granitoids (sanukitoids), biotite-bearing granites and alkaline (A-type) granitoids (e.g., Moyen et al., 2003; Laurent et al., 2014). The so-called "sanukitoids" are a series of high-Mg dioritic-granodioritic rocks that are geochemically different from typical TTG, although they still share some features (e.g., Shirey and Hanson, 1984; Smithies and Champion, 2000; Heilimo et al., 2010; Dey et al., 2014, 2016; Jayananda et al., 2018).

Shirey and Hanson (1984) introduced the term sanukitoid to describe geochemical characteristics viz. SiO_2 = 55–60%, MgO > 6%, Mg# > 60, Sr > 600–1800 ppm, Ba > 600–1800 ppm, Cr > 100 ppm, Ni > 100 ppm and LREE enrichment over HREE. Prevailing models for the origin of sanukitoid petrogenesis include; (i) enrichment of mantle wedge peridotite by slab-derived melts or fluids from a subducting oceanic slab (Halla, 2005; Martin et al., 2010; Laurent et al., 2011), (ii) partial melting of a metasomatized mantle wedge (Stern and Hanson, 1991; Martin et al., 2010; Qian and Hermann, 2010) and (iii) interaction between mantle melts and TTG (crustal) melts (Oliveira et al., 2010, 2011; Semprich et al., 2015).

Late Archean high-K anatectic granites occur as syn- to post tectonic plutons usually in TTG-greenstone associations (Bleeker, 2003; Jayananda et al., 2006; Farina et al., 2015; Dall'Agnol et al., 2017). A great deal of research, conducted on anatectic granites in Archean terranes worldwide, reveals a high diversity in their mineral composition, geochemistry and tectonic setting during the late-Archean era, suggesting their formation by crustal melting (anatexis) (Laurent et al., 2014).

The Bundelkhand Craton is comprised of TTG gneisses, ultramafic-mafic rocks, banded iron formation (BIF), felsic volcanic rocks, and granodioritic–granitic rocks. The available geochronological data for the rocks of the Bundelkhand Craton suggest that TTG magmatism, granitoid formation, accretion and deformation all occurred during Paleo-Neoarchean times (Sarkar et al., 1996; Mondal et al., 2002; Kaur et al., 2014, 2016; Singh and Slabunov, 2015a; Saha et al., 2016; Verma et al., 2016; Joshi et al., 2017). The origin and evolution of such granitoid magmatism is the least understood in terms of petrogenesis and possible genetic linkage between anatectic granites and sanukitoids. Recently, a few studies have focused on this high-K granitoid magmatism (Kaur et al., 2016; Joshi et al., 2017), reporting major and trace element geochemical data in the attempt to propose an explanation for the petrogenesis of these diverse granitoids. In fact, Joshi et al. (2017) have established a comprehensive classification of the high-K granitoids in the Bundelkhand Craton, in which they identified for the first time the presence of sanukitoid granitoids and briefly discussed

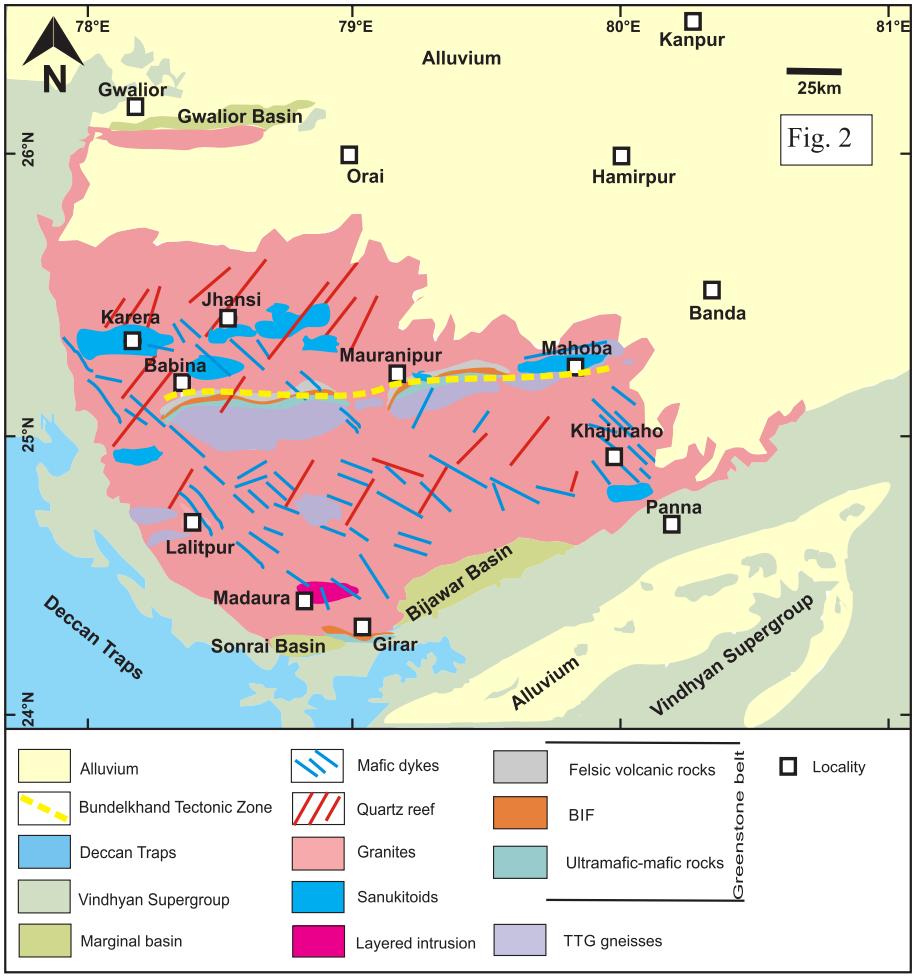

Fig. 2. Simplified geological map of the Bundelkhand Craton (after Basu, 1986; Malviya et al., 2006; Absar et al., 2009; Pradhan et al., 2012; Singh and Slabunov, 2015a; Verma et al., 2016; Joshi et al., 2017).

Table 1
Major lithostratigraphic units of the Bundelkhand Craton inferred from previous literature discussed in the text.

Geological events	Age (Ga)	Occurrence in the craton	Field characteristics and relations
Basement unit: Tonalite–trondhjemite–granodiorite (TTG) gneisses,	3.59–3.25	Babina, Baragaon, Roni, Kuraicha, Mahoba, Karera, Charkhari, Rungaon	Basement unit, polyphase deformed and sporadic occurrences mostly in central part
Greenstone belt: Mafic-ultramafic volcanics	~3.44	Babina, Baragaon, Roni, Kuraicha	Supracrustal successions intruded on basement unit and have sheared and faulted contact with TTGs. Low-grade metamorphism and mildly deformation
BIF		Babina, Pura, Baragaon, Roni, Kuraicha, Prithvipur, Girar	This volcano-sedimentary successions having contact relation with felsic volcanic association. Some places have highly deformed contact with basic ultramafic rocks
Felsic volcanics (rhyolite-rhyodacite-dacite)	2.81–2.54	Babina, Baragaon, Kararkhera, Umri, west of Mahoba town	Older felsic volcanic rocks occur at base of BIF near Baragaon, Mauranipur belt. While younger Felsic volcanics show in dike form at Baragaon and widely exposed around Babina region which forming top most unit of greenstone belt. These rocks are less deformed
TTG (granodioritic composition)	2.69	Babina, Near Ghisoli and Baghora areas, Kuraicha Village, Mauranipur	Mainly exposed around South of Babina town and high pressure metamorphism takes place. These have tectonic contact with basic ultramafic rocks
Sanukitoid suites, hybrid granites and anatectic granites	2.59–2.46	Throughout Bundelkhand craton	Undeformed outcrops, multiphase emplacement in all older units. Cover almost 75% of the Bundelkhand craton
Mafic dykes	2.15–1.7	Throughout Bundelkhand craton	NW-SE trends, mafic dyke swarms evidence of extesional tectonic
Quartz reefs	~2.0	Series of NE–SW to NNE–SSW trending quartz vein throughout craton.	Giant quartz veins intruded almost everywhere in the Bundelkhand craton, having NE-SW trend in general
Paleoproterozoic Marginal basins	2.0–1.8	Gwalior (Northwest), Sonrai (South) and Bijawar (Southeast)	Homotaxial and characterized by clastic sedimentary rocks and carbonates with Banded Iron Formations (BIFs)

Table 2
Sample description, locality and GPS coordinates of the sanukitoids (s.l.) and high-K anatectic granites of the Bundelkhand craton.

Sample	Locality	Lithology	GPS co-ordinates	
			Longitude (E)	Latitude (N)
BC-16-01	Jhansi	Sanukitoids (s.l.)	78°36′02″	25°26′52″
BC-16-02	Jhansi	Sanukitoids (s.l.)	78°36′00″	25°26′50″
BC-16-03	Shankargarh	Sanukitoids (s.l.)	78°38′29″	25°26′29″
BC-16-04	Kochhabhanwar	Sanukitoids (s.l.)	78°39′36″	25°28′07″
BC-16-05	Kochhabhanwar	Sanukitoids (s.l.)	78°39′44″	25°27′52″
BC-16-06	Kochhabhanwar	Sanukitoids (s.l.)	78°39′35″	25°28′07″
BC-16-07	Kherai	Sanukitoids (s.l.)	78°10′35″	25°22′57″
BC-16-08	Nand	Sanukitoids (s.l.)	78°12′39″	25°15′13″
BC-16-09	Kherai	Sanukitoids (s.l.)	78°10′35″	25°22′57″
BC-16-10	Babina	Sanukitoids (s.l.)	78°29′34″	25°14′54″
BC-16-11	Babina	Sanukitoids (s.l.)	78°29′18″	25°14′34″
BC-16-12	Babina	Sanukitoids (s.l.)	78°32′30″	25°19′12″
BC-16-13	Babina	Sanukitoids (s.l.)	78°29′02″	25°14′02″
BC-16-14	Babina	Sanukitoids (s.l.)	78°29′57″	25°15′20″
BC-16-15	Sakrar	Sanukitoids (s.l.)	78°51′05″	25°21′33″
BC-16-16	Sakrar	Sanukitoids (s.l.)	78°51′02″	25°21′32″
BC-16-17	Sakrar	Sanukitoids (s.l.)	78°51′07″	25°21′35″
BC-16-18	Sakrar	Sanukitoids (s.l.)	78°51′05″	25°21′33″
BC-16-19	Mauranipur	Sanukitoids (s.l.)	79°07′09″	25°12′51″
BC-16-20	Jhansi	Anatectic granites	78°36′02″	25°26′52″
BC-16-21	Ganj-Dinara	Anatectic granites	78°19′10″	25°28′16″
BC-16-22	Babina	Anatectic granites	78°29′34″	25°14′54″
BC-16-23	Babina	Anatectic granites	78°32′24″	25°21′14″
BC-16-24	Babina	Anatectic granites	78°27′57″	25°11′35″
BC-16-25	Baghora village	Anatectic granites	78°27′47″	25°09′43″
BC-16-26	Mauranipur	Anatectic granites	79°07′18″	25°12′33″
BC-16-27	Mauranipur	Anatectic granites	79°06′59″	25°12′18″
BC-16-28	Mauranipur	Anatectic granites	79°07′27″	25°12′16″
BC-16-29	Bukhara village	Anatectic granites	79°11′11″	25°14′15″
BC-16-30	Deori-Ghat	Anatectic granites	79°17′27″	25°14′07″
BC-16-31	Mahoba	Anatectic granites	79°24′14″	25°20′30″
BC-16-32	Kabrai	Anatectic granites	80°00′09″	25°23′21″
BC-16-33	Mahoba	Anatectic granites	79°49′48″	25°17′39″

their sources and tectonic setting. Nevertheless, our understanding of the crustal evolution in this craton, particularly regarding the sanukitoids and their relation to the anatectic granites, is still inadequate due to the paucity of isotopic data (Pandey et al., 2011; Kaur et al., 2016). Thus, new isotopic data may provide unambiguous information about the sources of magmatic rocks (in both the crust and mantle) and aid a discussion about possible processes of generation. In this paper, we report major and trace element whole-rock and Nd isotope data, as well as new zircon U–Pb dating of sanukitoids (s.l.), along with major and trace element whole-rock data of high-K anatectic granites from the Bundelkhand Craton in an effort to advance the current knowledge in the region. These data will be used to constrain the plausible sources of the sanukitoids and high-K anatectic granites, and explain their petrogenesis and possible relation, as well as their tectonic setting. The results are then compared to published data from the following various Archean terranes: Amazonian, Bundelkhand, Baltic shield, Dharwar, Kaapvaal, North China, and Superior Province.

2. Geological setting

Exposed areas of Archean crustal fragments in the Indian shield are generally divided into two main blocks: the Northern and Southern blocks. The Northern block consists of two crustal segments known as the Aravalli and Bundelkhand cratons (Fig. 1), whereas the Southern Block consists of the Dharwar, Bastar, and Singhbhum cratons (Fig. 1; Naqvi and Rogers, 1987). The ENE–WSW-trending Central Indian Tectonic Zone separates these two blocks (Ramakrishnan and Vaidyanadhan, 2010).

The Bundelkhand Craton is one of the Archean cratons that is located in the north-central part of India (Fig. 1). It covers an exposed area of approximately 26,000 km^2 and consists predominantly of granites and TTGs (Basu, 1986; Singh and Slabunov, 2015a). It is bounded by the Paleoproterozoic (2.0–1.8 Ga), Gwalior (Northwest), Sonrai (South) and Bijawar (Southeast) marginal basins (Fig. 2), all of which are homotaxial and characterized by clastic sedimentary rocks at their base, and by upper rock units composed of carbonates with BIFs (Absar et al., 2009). Rocks of the Mesoproterozoic Vindhyan Basin (1.1–1.0 Ga) overlay these marginal basins, discussed in detail by Meert et al. (2010) and Turner et al. (2014). The northern side of the craton is covered with Gangetic alluvial plains.

The Bundelkhand granite-greenstone terrane is chiefly composed of TTGs suites, volcano-sedimentary sequences, quartzite, schist, granodiorite and anatectic granites (Fig. 2 and Table 1) (Basu, 1986; Mondal et al., 2002; Malviya et al., 2006; Mohan et al., 2012; Kaur et al., 2014, 2016; Singh and Slabunov, 2015a, 2015b, 2016; Saha et al., 2016; Verma et al., 2016; Joshi et al., 2017). TTG gneisses are the oldest rocks in the region and the existing age data indicate three distinct phases of Paleoarchaean TTG crust formation: 3.55 Ga, 3.44 Ga and 3.30 Ga (Mondal et al., 2002; Kaur et al., 2014; Saha et al., 2016). In addition, Verma et al. (2016) reported a TTG phase (granodioritic composition) that is ca. 2.67 Ga younger and contains widespread ~2.53–2.51 Ga anatectic granites in the Bundelkhand Craton. The Bundelkhand Craton contains two greenstone complexes; the central Bundelkhand complex comprising the Babina–Mauranipur greenstone belt, and the southern Bundelkhand complex consisting of the Rungaon–Girar greenstone belt (Singh and Slabunov, 2015b). The central greenstone complex comprises mafic–ultramafic and felsic volcanics, less often metasedimentary, and BIFs (Fig. 2, Malviya et al., 2006; Singh and Slabunov, 2015a). The central greenstone complex is further divided into two greenstone belts (1) the Mauranipur greenstone belt, which consists of three different lithologies: (1) medium to low-grade metamorphosed basaltic pillow lava and basaltic komatiites (Malviya et al., 2006); (2) BIFs (Singh and Slabunov, 2015a); and (3) 2.81–2.56 Ga felsic volcanics (Slabunov and Singh, 2018), and (2) the Babina greenstone belt that is composed of three additional lithologies: (1) small scattered outcrops of ultramafic-mafic rocks, (2) BIFs, and (3) volcanic rocks represented by dacite-rhyolite association (2.54 Ga) (Singh and Slabunov, 2015a, 2015b). However, Saha et al. (2011) inferred a high-pressure metamorphism at ~2.78 Ga in the Babina belt on the basis of U–Th–Pb monazite chemical dating and U–Pb zircon dating.

The Rungaon–Girar greenstone belt consists of quartzites, BIFs and layered mafic-ultramafic rocks (Farooqui and Singh, 2006; Singh and Slabunov, 2016; Slabunov et al., 2017a). Slabunov et al. (2017a) reported detrital zircons from the quartzite that were 3.4–3.3 Ga older, which indicates the existence of an Archean crustal block in the provenance. The layered igneous suite is composed of gabbro, peridotite and diorite, which occur as scattered outcrops in the Madawara-Ikauna and Lalitpur areas in the southern parts of the Bundelkhand Craton and are older than the anatectic granites (Slabunov and Singh, 2018).

The undeformed plutons of the sanukitoids (s.l.) and voluminous granite-monzogranite-syenogranite series (GMS) rocks occupied most of the Bundelkhand Craton. These rocks intruded during ca. 2.6–2.35 Ga, and spread over a majority of the belt. Their emplacements agree with the stabilization of the Bundelkhand Craton (Fig. 2; Table 1, Mondal et al., 2002; Kaur et al., 2016; Saha et al., 2016; Joshi et al., 2017). These rocks contain K-feldspar as the main feldspar mineral and are inferred to have evolved due to partial melting of felsic rocks to intermediate rocks in a subduction-related tectonic setting during the late-Archean era (Kaur et al., 2016, Joshi et al., 2017). These granitic plutons are intruded by pegmatite veins, porphyry dykes and dyke swarms.

Mafic dyke swarms are also an integral part of the Bundelkhand Craton (Fig. 2, Table 1). Most of them form long discontinuous outcrops along fractures, extending from a few meters to > 50 km long and are mostly oriented in a NW–SE direction (Fig. 2), but a few also exhibit a NE–SW to ENE–WSW strike, suggesting at least two discrete events of

Fig. 3. a–p. Representative field photographs, field relationships, and rock textures of sanukitoids (s.l.) and high-K anatectic granites: (a) Sanukitoids from the Jhansi area, contact between sanukitoids and high-K anatectic granites (length of the hammer 35 cm). (b) Contact between sanukitoids and anatectic porphyritic granites from the Jhansi sample site (length of the pen 14 cm). (c) Field aspects of the Jhansi sanukitoids pluton, showing elongated and linear sheared mafic enclaves and moderate foliation. (d) Outcrop of the Kochhabhanwar high-K anatectic granites with boundins of sanukitoids enclave. Fabric intensity drops off away from the enclave margin and is absent in the body of the host granites, implying a synmagmatic origin. (e) BHEL, Babina sanukitoids, showing elongated mafic enclaves. (f) High-K anatectic granites from the Babina area (Baghora village). (g) Mingling between sanukitoids and light grey anatectic granites in the Sakrar pluton, showing mafic microgranular enclaves and appearance indicating weak deformation (pen is 14-cm long). (h) High-K anatectic granites outcrop of the Bukhara (Mauranipur) area, displaying typical porphyritic texture and a cross-cutting pegmatite vein. (i) Outcrop of the high-K anatectic pink granites from the Bukhara village, Mauranipur type-area. (j) Outcrop showing sharp contact between TTGs and anatectic pink granites Roni village, Mauranipur. (k) Contact between sanukitoids (s.l.) (upper coarse fine grained) and lower, coarse-grained high-K anatectic pink granites from the Deori-Ghat area (pen is 14 cm long). (l) Vein of coarse-grained high-K anatectic granites in a host rock of fine-grained sanukitoids (coin diameter is 2.5 cm) exposed near the Jhansi. (m) Emplacement of pegmatite dikes in the amphibolites outcrop exposed at the Kabrai. (n) High-K anatectic pink granites outcrop exposed ~5 km before the Mahoba city, left side of Jhansi-Mahoba road. (o) Coarse grained high-K anatectic pink granites from the Kabrai. (p) Vein of highly deformed mylonitic anatectic granites in a host rock of fine-grained amphibolites exposed near the Kabrai.

mafic dyke activity (Basu, 1986; Pradhan et al., 2012; Radhakrishna et al., 2013).

The dykes are nonfoliated dolerites and cross-cut the TTGs and granites (Pradhan et al., 2012). Based on $^{40}Ar/^{39}Ar$ and U–Pb zircon geochronology, Rao et al. (2005) and Pradhan et al. (2012) suggested that two phases of mafic dyke magmatic events occurred in the Bundelkhand Craton. First, NW–SE trending dykes formed ca. 2.0 Ga and then NE–SW oriented dykes formed at approximately 1.10 Ga.

The giant quartz reefs are emplaced in NE–SW and N–S directions in the granites and generally have widths of ~50–60 m and discontinuous lengths from 10 to 40 km (Pati et al., 2007). Their exposures vary from ~1 to 70 m with an evolution generally interpreted to be the result of tectonically controlled hydrothermal activity along vertical to subvertical shear zones that formed in response to extensional tectonics at 1.9–1.8 Ga (Pati et al., 2007; Slabunov et al., 2017b).

3. Sampling, field relationships and petrography

We collected representative samples from different localities of the Bundelkhand Craton (Fig. 2), where mapping and sampling were undertaken during two successive field seasons. The locations of intense deformation, later intrusions and veins were avoided during sampling. Total thirty-three samples were collected for whole-rock geochemistry among these; three sanukitoids (s.l.) samples were selected for Sm-Nd analyses. Then, of these three samples, one was selected for zircon U–Pb analyses. The localities and GPS coordinates of representative samples are summarized in Table 2.

3.1. Sanukitoids (s.l.)

Sanukitoid suites occur in small plutons (northern terrain: Jhansi,

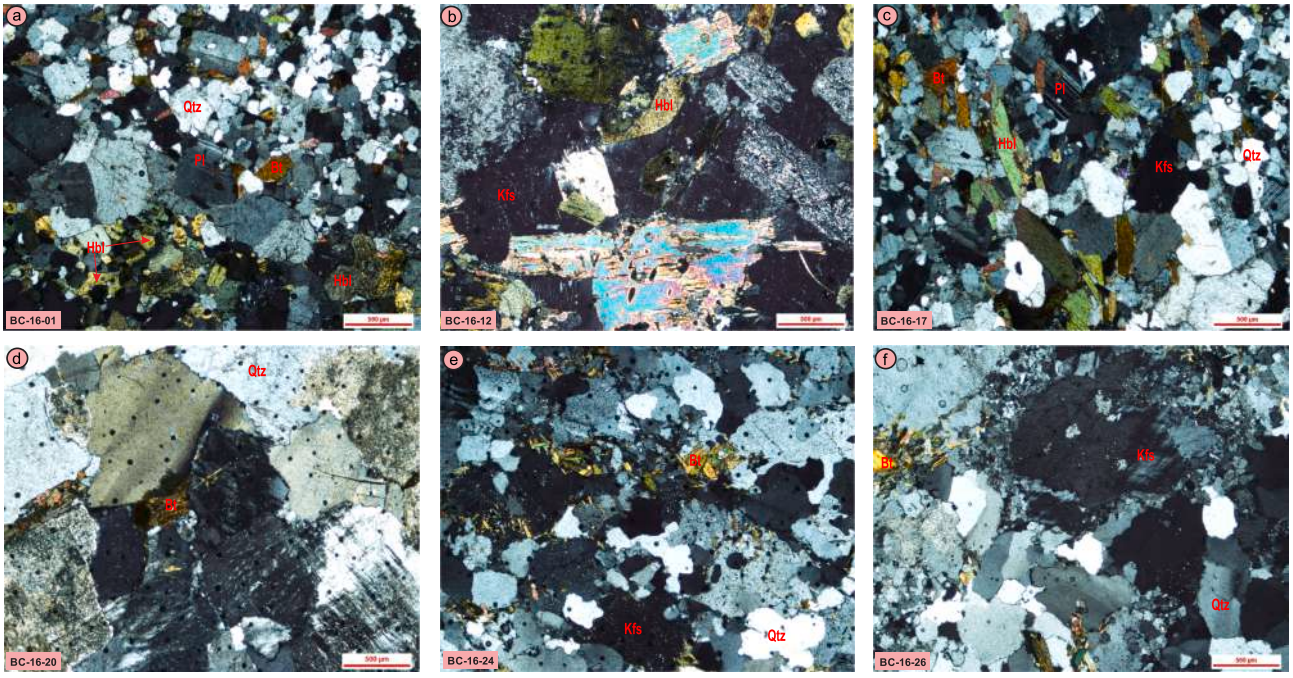

Fig. 4. Representative photomicrographs of mineral assemblages: (a–c) sanukitoids with quartz, plagioclase, K-feldspar, hornblende and biotite from northern and central terrains; (d–f) high-K anatectic granites with bimodal quartz, K-feldspar, and biotite. *Abbreviations:* Qtz-quartz, Pl-plagioclase, Hbl-hornblenbe, Kfs-K-feldspar and Bt-biotite. All photomicrographs with crossed nicols.

Sakrar, Sankargarh, Kherai and Nand; central terrain: Babina and Mauranipur, Fig. 2; Table 2) that were intruded by high-K granite. Sanukitoids (s.l.) rocks range in composition from diorite to granodiorites (Fig. 3a–p). Most sanukitoids (s.l.) are gray to light gray in color, moderate to crude foliated and locally contain mafic minerals (biotite and amphiboles) in aggregates or clots (Fig. 3c and e). The rocks are mesocratic, medium- to coarse-grained locally intruded by pegmatite and quartz veins. The main minerals in sanukitoids (s.l.) are plagioclase, hornblende, biotite and quartz (Fig. 4a–c). K-feldspar of sanukitoids (s.l.) is Carlsbad-twinned perthitic microcline. Smaller phenocrysts of antiperthitic plagioclase are also present. Titanite, apatite, zircon and opaque minerals are accessory phases (Fig. 4a–c).

3.2. High-K anatectic granites

Medium- to coarse-grained, equigranular high-K anatectic granites are exposed around the Jhansi, Kochhabhanwar, Kherai, Ganj-Dinara, Babina, Baghora, Sakrar, Bukhara, Deori-Ghat, Mahoba and Kabrai in the northern and central terrains of the Bundelkhand Craton (Fig. 2; Table 2). The anatectic granites are leucocratic, which consist of quartz, K-feldspar (perthite), minor plagioclase and very scarce or rare biotite (Fig. 4d–f). Zircon, apatite, monazite, titanite, allanite and some opaques are common accessory minerals. There are abundant microcline grains with cross-hatched ("tartan") multiple twinning and perthite (exsolution texture) (Fig. 4d–f).

4. Analytical methods

4.1. Whole-rock geochemistry

Thirty-three rock samples were collected and analyzed for the whole rock geochemistry. Major oxides and selected trace elements were analyzed by X-ray fluorescence spectrometer (XRF). For this procedure, 1.2 g-powdered sample were mixed with 6 g lithium borate flux (consisting of 35.3% tetraborate and 64.7% metaborate). Further, the fusion bead method was used to prepare the glass bead at 1000 °C for ≈8 min in Pt–Au crucible for only major elements analyses. For selected trace element analyses, 9 g of sample was pressed into a pellet using 1.2 g Wax binding agent. Both, glass bead and pressed pellet were analyzed at Institute of Geosciences, University of Campinas (UNICAMP), Brazil. The analytical precision for major oxides and trace elements, based on certified standards (W-2 and BHVO for major elements, and RGM-1 and WSE for trace elements), and accuracy was considered less than 5% for major oxides and up to 10% for trace elements (Vendemiatto and Enzweiler, 2001). Fe-oxidation adjustment followed the procedure of Middlemost (1989) on an anhydrous basis to 100%. This was easily achieved using the computer program, IgRoCS_M1 (Verma and Rivera-Gómez, 2013).

The remaining rare earth and other trace elements were analyzed on a quadrupole Thermo (Xseries2) ICP-MS at the Institute of Geosciences, University of Campinas. The analytical procedures were based on those of Liang et al. (2000). Cotta and Enzweiler (2009) described details of the instrument and sample preparation. The standards used for this work, were BRP-1, RGM-1 and GSP-2, with a 10% standard deviation.

4.2. Zircon U–Pb dating

One sample of sanukitoids (s.l.) (BC-16-18) was selected for zircon U–Pb dating. About 5–6 kg sample was crushed with a jaw crusher and powdered to approximately 300 μm using disc ball mill. Heavy mineral concentrates were obtained by panning and were subsequently purified using Nd magnets, a Frantz magnetic separator and methyleneiodide; after that obtained zircon grains were mounted in 1 in. round epoxy mounts resin, polished using diamond paste, and cleaned using 10% v/v HNO_3 followed by de-ionized water. Further, zircon grains were studied by cathodoluminescence imaging (CL) to reveal the internal structures of zircons and to help select optimum spot locations. Zircon U–Pb dating was obtained using an ICP-MS Element XR (Thermo Scientific) at the IG-UNICAMP, Brazil. U–Th–Pb ratios and absolute abundances were determined relative to the standard zircon 91,500 (Wiedenbeck et al., 1995). Data were reduced off-line using Iolite software (version 2.5) following the method described by Paton et al. (2010). Peixe zircon standard (ID-TIMS age of 564 ± 4 Ma; cf. Dickinson and Gehrels, 2003) was used to monitor the quality of the

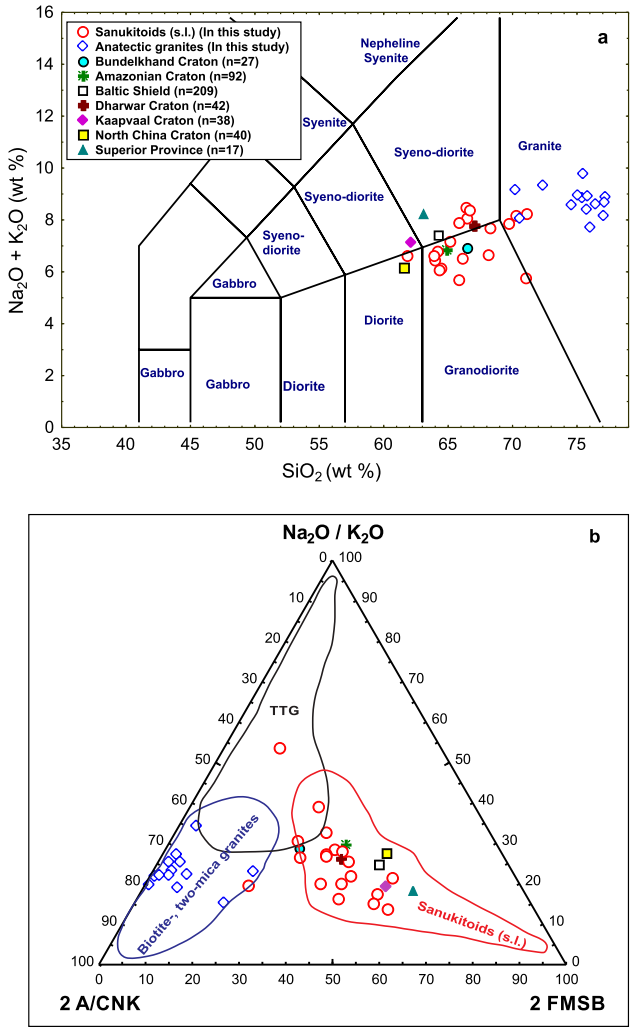

Fig. 5. a – TAS (total alkalis *vs.* SiO_2) diagram of Le Bas et al. (1986) obtained from the IgRoCS computer program (Verma and Rivera-Goméz, 2013); b – a ternary diagram ((Na_2O/K_2O)–2 * A/CNK (molar $Al_2O_3/[CaO + Na_2O + K_2O]$)–2 * [($FeO_t$ + MgO) wt.% * (Sr + Ba) wt.%] = FMSB)) of Laurent et al., 2014) for sanukitoids (s.l.) and high-K anatectic granites.

reduction procedures (further details are given in Moreno et al., 2017). All data are reported with 2 sigma uncertainties, and are plotted using the software *ISOPLOT 3.75* (Ludwig, 2012).

4.3. Sm–Nd isotopes

Three samples were selected for Sm–Nd isotopic analyses. Sm–Nd isotopic ratios were determined at the Centro de Geocronología y Geoquímica Isotópica from the Universidad Complutense de Madrid, Spain by thermal ionization mass spectrometry (TIMS-Phoenix®). Isotope Dilution-TIMS analysis were performed in whole-rock powder using a ^{150}Nd–^{149}Sm tracer. The weighted samples in Teflon® vessels were dissolved in 5 ml of ultrapure HF and 3 ml of ultrapure HNO_3 (Merck-Suprapur TM). Along with the samples, enriched spike solution (^{149}Sm–^{150}Nd - Oak Ridge) was added and placed inside an oven for 65 h at 120 °C temperature. After that time, cold vials were evaporated on a heat plate at 120 °C. Once samples were completely dried, 1 ml of ultrapure HNO_3 (Merck-Suprapur TM) were added and place back on the heat plate for evaporation at 120 °C. Furthermore, 4 ml of 6 N distilled HCL 6 N were added to the dried samples and placed in an oven overnight at 120 °C. After that, samples were centrifuged at 4000 r.p.m. for 10 min, in order to separate the dissolved fraction from the residue if any. Chromatographic separation of the complete group of REE was performed using cation exchange resin DOWEX 50W-X8 200–400 mesh (previously calibrated). REE fractions recovered from the previous chromatographic stage were dried completely before dissolution again in 200 µL HCl 0.18 N. These solutions were passed through a new chromatographic step (Ln-Resin). The result is a complete separation between the Nd (using 0.3 N HCl as eluent) and the Sm (using 0.4 N HCl as eluent) fractions of the samples, being ready for the subsequent analysis in the mass spectrometer (TIMS). Dried Sm and Nd samples dissolved with 2 µL of 0.05 M phosphoric acid were loaded onto a side Rhenium (Re) filament of a triple Re filament arrangement. Nd ratios were analyzed in a mass spectrometer TIMS-Phoenix®, following a dynamic multicollection method, through 160 cycles at a stable intensity of 1 V for the ^{144}Nd mass. In turn, Sm ratios were analyzed in the same spectrometer, following a single static method through 112 cycles maintaining 1 V intensity for the ^{149}Sm mass. The measured $^{143}Nd/^{144}Nd$ isotopic ratios were corrected for possible isobaric interferences from ^{142}Ce and ^{144}Sm and normalized to $^{146}Nd/^{144}Nd = 0.7219$ to correct for mass fractionation. Nd isotopic standard (JNdi-1, Tanaka et al., 2000) was analyzed during sample measurement, and gave an average value of $^{143}Nd/^{144}Nd = 0.512107$ for 9 replicas, with an internal precision of ± 0.000005 (2σ). The estimated error for the $^{147}Sm/^{144}Nd$ ratio is 0.1% and $^{143}Nd/^{144}Nd$ is 0.006%.

5. Results

5.1. Whole rock geochemistry

The new geochemical data for sanukitoids (s.l.) and high-K anatectic granites are summarized in Table S1 (see supplementary material). Geochemical data of sanukitoids (s.l.) averaged from values present in the various Archean terrane literature worldwide have been used in this work. The data used are as follows: Bundelkhand Craton (Joshi et al., 2017); Amazonian (Oliveira et al., 2009; Santos and Oliveira, 2016); Baltic shield (O'Brien et al., 1993; Halla, 2005; Kovalenko et al., 2005; Lobach-Zhuchenko et al., 2008; Kapyaho et al., 2006; Larionova et al., 2007; Heilimo et al., 2010; Kudryashow et al., 2013); Dharwar (Jayananda et al., 1995, 2000; Sarvothaman, 2001; Prabhakar et al., 2009; Dey et al., 2012); Kaapvaal (Laurent et al., 2011, 2014); North China (Wang et al., 2009; Ma et al., 2013; Jiang et al., 2016) and Superior Province (Stevenson et al., 1999).

5.1.1. Sanukitoids (s.l.)

Sanukitoids (s.l.) were plotted in the fields of diorite, syenodiorite, and granodiorite with characteristics of subalkaline suites (in TAS, Fig. 5a, Le Bas et al., 1986). In the Na_2O/K_2O–2A/CNK–2FMSB diagram (Fig. 5b, Laurent et al., 2014), the sanukitoid (s.l.) samples are plotted in the global typical Archean sanukitoid field. Sanukitoids (s.l.) exhibit geochemical features ranging from alkali to calcic, and include magnesian and mostly metaluminous features as well (Fig. 6a–c). According to the SiO_2 *vs.* K_2O diagram, sanukitoids (s.l.) were classified as medium- to high-K (Fig. 6d). Sanukitoids (s.l.) also show a range of SiO_2 contents from 61 to 71 wt.% and have high contents of mantle-compatible elements such as Mg, Cr, and Ni (MgO = 0.68–3.13 wt.%, Cr up to 92 ppm, and Ni up to 22 ppm). Consequently, they have relatively high Mg# (41–50, except three samples with 13–30) for such SiO_2-rich rocks, which is a typical characteristic of worldwide sanukitoids (e.g., Laurent et al., 2011, 2014; Dey et al., 2012). These samples are enriched in LIL elements such as K_2O (1.98–4.96 wt.%), Ba (400–2517 ppm) and Sr (184–693 ppm), and in ferromagnesian oxides (FeO_t + MgO + MnO + TiO_2 = 4.47–11.6 wt.%), whose concentrations are similar to those reported by Joshi et al. (2017). Bivariate plots of TiO_2, Al_2O_3, MgO, CaO and P_2O_5 versus SiO_2 display linear trends, and Na_2O, K_2O and Mg# display definite scatter but also exhibit apparent linear trends (Fig. 7). This may suggest that these magmas

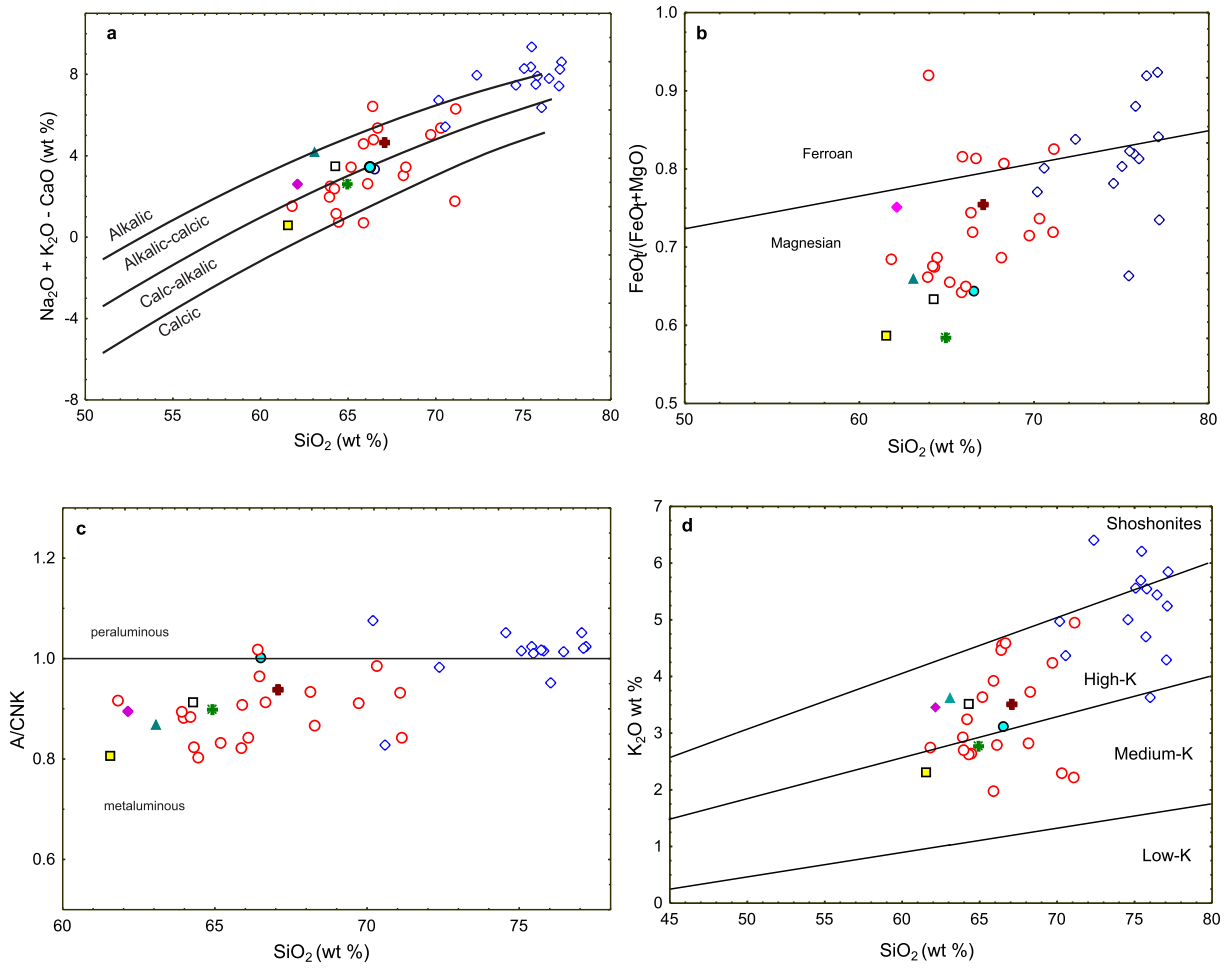

Fig. 6. Composition of the Bundelkhand sanukitoids (s.l.) and high-K anatectic granites intrusions represented in: a – SiO_2 *vs.* MALI-index diagram (after Frost et al., 2001); b – SiO_2 *vs.* (FeO_t/(FeO_t + MgO) diagram, line separating ferroan and magnesian fields (after Frost et al., 2001); c –A/CNK [Al_2O_3/(CaO + Na_2O + K_2O)] *vs.* SiO_2 diagram (after Shand, 1943); d – K_2O *vs.* SiO_2 diagram (after Laurent et al., 2011).

underwent fractional crystallization of ferromagnesian minerals, i.e., biotite and/or hornblende, and Ti-Fe oxides. SiO_2 displays a negative correlation with Cr, Ni, Zr and Sr (Fig. 8).

In the primitive mantle normalized multi-element diagram (Fig. 9a), most of the samples show enrichment in large-ion lithophile elements (LILE) (Fig. 9a), along with negative Ba, Sr, P, Nb-Ta and Ti anomalies. Negative Nb-Ta and positive Pb anomalies are generally interpreted as subduction-related magma and/or continental crust signature (Foley et al., 2000; Schmidt et al., 2004). Sanukitoids (s.l.) are depleted in high-field-strength elements (HFSE), such as Zr (129–337 ppm), Hf (3.2–10.7 ppm), Y (8.9–97.3 ppm), Nb (3.7–34 ppm) and Ta (0.5–3.3). Similarly, HFSE depletions are common in rocks, which are generated in arc environments that interact with continental crust and then underwent crystallization of Ti-rich phases (Foley et al., 2000, 2002).

The chondrite-normalized REE patterns of the sanukitoids (s.l.) are characterized by enrichment in the LREE compared with the HREE (Fig. 9b). These rocks have a clear LREE/HREE fractionation with $(La/Yb)_{CN}$ = 7.6–32.4 and $(La/Lu)_{CN}$ = 7.5–24.6, and a slightly negative or absent Eu anomaly (0.33–0.94). However, some samples show positive Eu anomalies (1.12–1.40) likely due to feldspar accumulation consistent with samples containing very high levels of Ba (> 2000 ppm).

5.1.2. High-K anatectic granites

High-K anatectic granites are silica rich (SiO_2 = 70–77 wt.%) with 12–15 wt.% Al_2O_3, 0.09–0.63 wt.% MgO, 0.42–2.90 wt.% FeO_t, 3.62–7.18 wt.% K_2O, and 0.28–2.6 wt.% CaO. The Na_2O contents vary from 2.93 to 5.49 wt.%, which is relatively higher than the sanukitoids (s.l.) samples. The Mg# number varies from 13 to 48. All these characteristics are typical of late-Archean anatectic granites. In the TAS diagram, these granites are plotted in the field of rhyolite equivalent to granite (Fig. 5a), and in the Na_2O/K_2O–2A/CNK–2FMSB diagram, they are plotted in the field of biotite and two mica granites (Laurent et al., 2014, Fig. 5b). These rocks are alkali to alkali-calcic and vary from magnesian to ferron (Fig. 6a and b). They are high-K to shoshonitic and weakly peraluminous rocks (Fig. 6c–d) with an Aluminium Saturation Index (ASI) of 0.84–1.08.

Harker diagrams display a negative correlation between TiO_2, Al_2O_3, MgO, CaO, and P_2O_5 with SiO_2, whereas Na_2O and K_2O are scattered without any clear correlation (Fig. 7). The trace elements of the high-K anatectic granites show a considerable spread in Harker diagrams, with the exception of Sr that seems to decrease with silica (Fig. 8). The Ba and Sr contents are variable but generally in the ranges of 51–1437 and 19–399 ppm, respectively (Table S1 and Fig. 8), whereas Th (up to 81 ppm) is relatively higher than that what is found in sanukitoids (s.l.). In the primitive mantle-normalized multi-element plots, negative Ba, Nb-Ta, Sr, Ce, P and Ti anomalies (Fig. 10a) characterize the high-K anatectic granites. These high-K anatectic granites are depleted in HFSE Zr (10–264 ppm), Hf (66–7.3 ppm), Y (5.0–68.0 ppm), Nb (2.1–64.2 ppm) and Ta (0.18–11.5). The chondrite-normalized REE patterns of the high-K anatectic granites are characterized by enrichment in the LREE with respect to the HREE having $(La/Lu)_{cn}$ = 1.45–27.13 (Fig. 10b). The REE patterns also show strong to moderate negative Eu anomalies (Eu/Eu* = 0.15–0.93) (Fig. 10b). The fractionation of REE is similar to what is found in sanukitoids (s.l.),

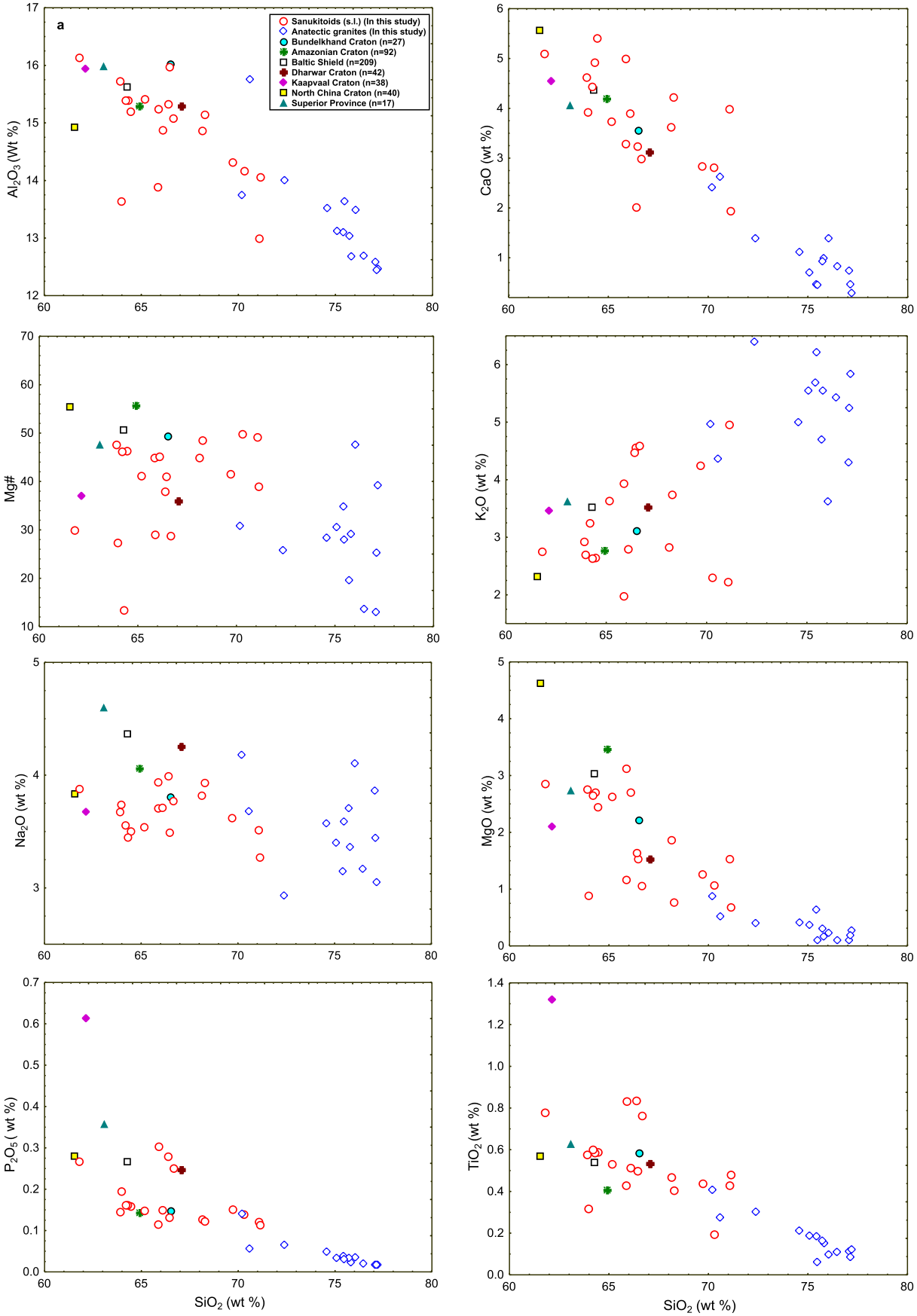

Fig. 7. Hacker's binary plots for selected major elements for sanukitoids (s.l.) and high-K anatectic granites, as well as average plots of sanukitoids from other cratonic bodies. Mg# *vs.* SiO_2 plot for sanukitoids (after Heilimo et al., 2010).

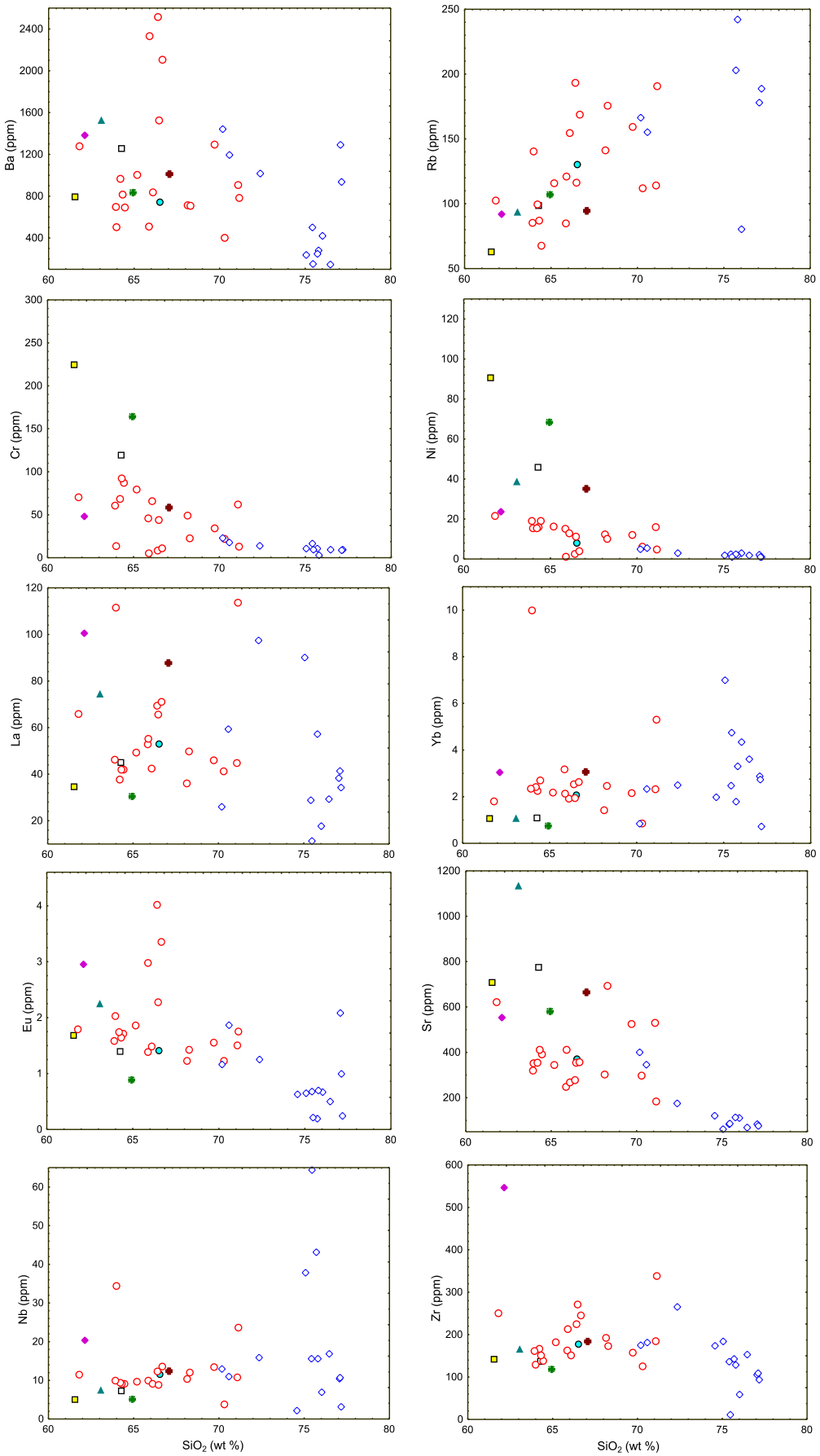

Fig. 8. Binary diagrams for selected trace elements *vs.* SiO_2 for sanukitoids (s.l.) and high-K anatectic granites, and average data of various cratonic bodies also plotted.

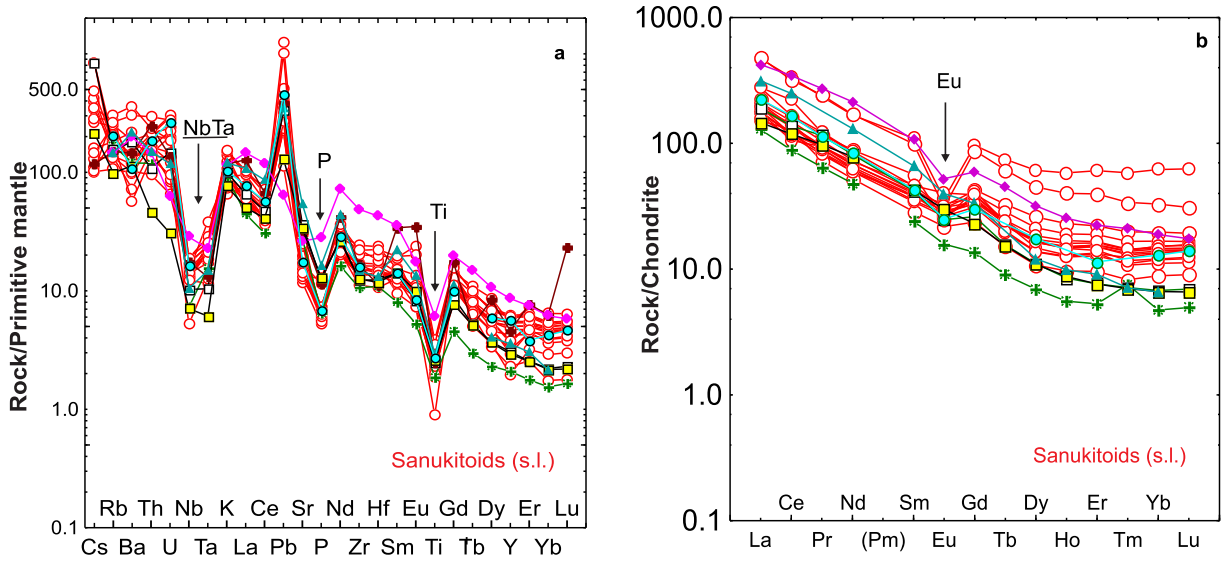

Fig. 9. a and b. Primitive mantle-normalized multi element (after McDonough and Sun, 1995) and chondrite-normalized REE (after McDonough and Sun, 1995) plots for the Bundelkhand sanukitoids (s.l.).

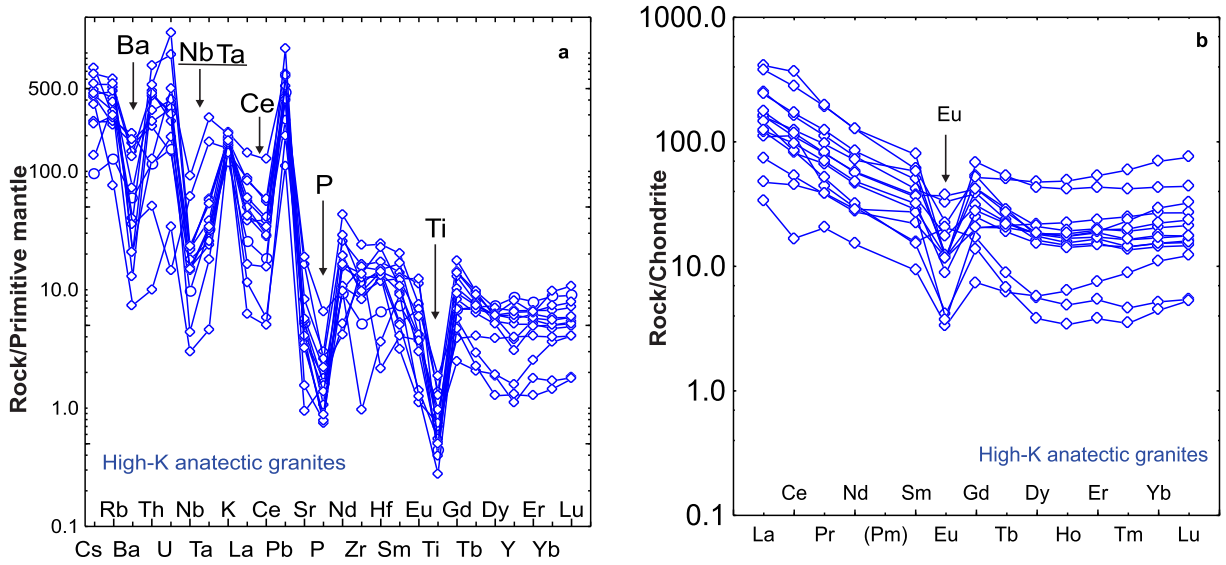

Fig. 10. a and b. Primitive mantle-normalized multi element (after McDonough and Sun, 1995) and chondrite-normalized REE (after McDonough and Sun, 1995) plots for the Bundelkhand high-K anatectic granites.

although certain samples show a slight enrichment in HREE.

5.2. Zircon U–Pb dating

One sample of sanukitoids (s.l.) (BC-16-18) was collected from the Sakrar region of the Bundelkhand Craton for zircon U–Pb dating. Cathodoluminescence (CL) images reveal that the zircons are euhedral and prismatic in morphology. In general, they range in length from 70 to 160 µm. Back scattered electron (BSE) images show concentric oscillatory zoning, and some grains display a narrow yet highly luminescent rim (Fig. 11a). The observed CL patterns indicate magmatic origin for most of the zircons. Twenty-two analyses were performed on twenty-two zircon grains. Most analyses reveal Th/U ratios that are between 0.49 and 1.3. The U–Pb dating values are listed in Table 3. The upper intercept age was calculated using seven zircons (< 10% discordance) and yielded an age of 2578 ± 13 Ma (MSWD = 0.74). The most discordant spots are also likely to represent the same population ($^{207}Pb/^{206}Pb$ ages = 2530–2570 Ma (Fig. 11b). Concordant zircons yielded a concordia age of 2577 ± 16 Ma (MSWD = 0.048; n = 4), which can be interpreted as the crystallization age of sanukitoids (s.l.) (Fig. 11c). Two analyzed zircon grains also provided ages of 2644 ± 25 and 2619 ± 24 Ma and are considered inherited ages. These findings are identical to the ages of 2563 ± 2, 2559 ± 7 and 2560 ± 7 Ma reported by Joshi et al. (2017).

5.3. Whole-rock Sm–Nd isotopes

The Sm–Nd isotopes of three whole-rock samples of sanukitoids (s.l.) are listed in Table 4. Samples BC-16-01 (Jhansi) and BC-16–03 (Sankargarh) have εNd_t ($_t$ = 2.56 Ga) values between −1.6 and −3.6 (Fig. 12), whereas BC-16-18 (Sakrar) has εNd_t ($_t$ = 2.57 Ga) value −2.6 (Fig. 12). The εNd_t values suggest a crustal imprint in the sanukitoids magma.

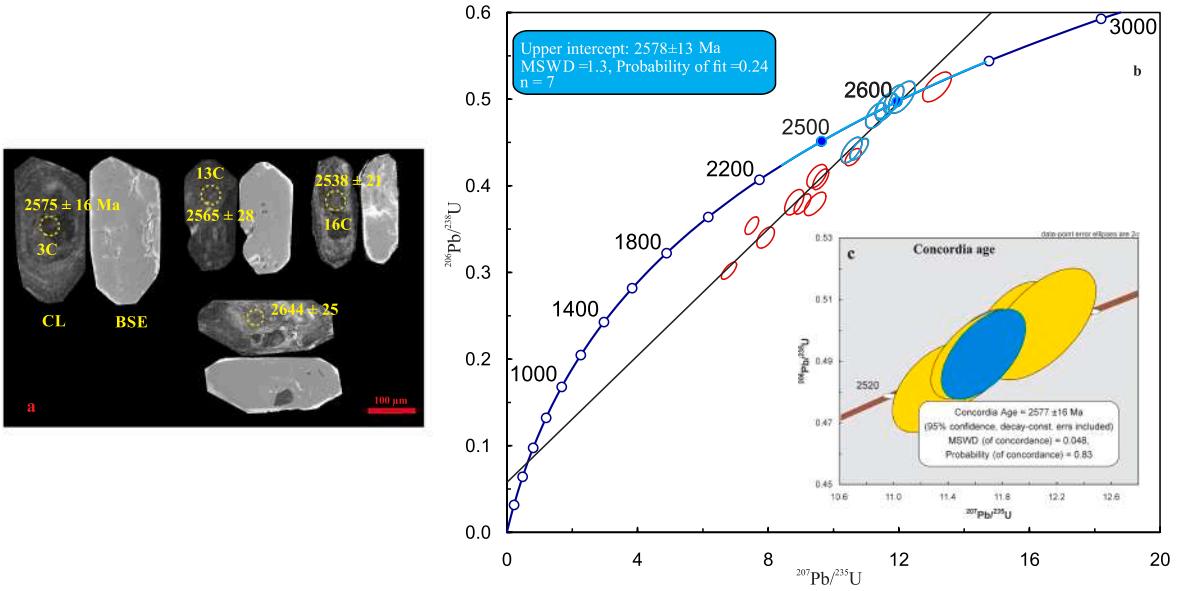

Fig. 11. a – Cathodoluminescence (CL) and BSE images of zircon, b – Zircon U-Pb Disconcordia plot for sample BC-16-18, c – Concordia plot for sample BC-16-18.

6. Discussion

6.1. Late Archean magmatism in the Bundelkhand Craton

The emplacement of sanukitoids and anatectic granites occurred extensively during the late Archean in most of the Archean cratons worldwide (Smithies and Champion, 2000; Moyen et al., 2003; Bibikova et al., 2005; Almeida et al., 2013; Laurent et al., 2014; Jiang et al., 2016; Santos and Oliveira, 2016; Jayananda et al., 2018). Similar granitoids magmatism occurred in the Bundelkhand Craton during the late Archean and specific age data in the present study including published geochronological studies of TTG, granodiorite, sanukitoids (s.l.), felsic volcanics and anatectic granites, are summarized in Table S2. Existing geochronological data indicate at least four episodes of Paleoarchean TTG magmatism between 3.55 Ga and 3.20 Ga (Mondal et al., 2002; Kaur et al., 2014, 2016; Saha et al., 2016), as well as Neoarchean TTG magmatism (2.7 Ga; Verma et al., 2016). This magmatism was followed by a voluminous high-K granitoid emplacement event during the Neoarchean era at 2.59–2.50 Ga (Mondal et al., 2002; Pandey et al., 2011; Kaur et al., 2016; Joshi et al., 2017).

In the present study, we report new geochronological data to qualitatively determine the possible time frame of sanukitoids petrogenesis in the Bundelkhand Craton. Sanukitoids (s.l.) yielded a discordant age with an upper intercept corresponding to an age of 2578 ± 13 Ma (Fig. 11b), and a concordia age of 2577 ± 16 Ma (Fig. 11c). This concordia age may be related to the crystallization of zircon during the emplacement of sanukitoids (s.l.) in the Sakrar region, located in the northern terrain of Bundelkhand Craton. Considering aging errors, this is almost identical to the reported ages (2564 ± 2 and 2544 ± 6 Ma) of sanukitoids in the Jhansi region, located in the northern Bundelkhand Craton (Joshi et al., 2017). This finding suggests that sanukitoid magmatism was contemporaneous with the whole Bundelkand Craton. On the other hand, published U–Pb zircon data indicate that the Bundelkhand Craton underwent a period of ca. 100 Myr (from 2.60 to 2.50 Ga) that is characterized by roughly coeval sanukitoid-like and high-K granitic magmatism. Field relationships in the central Bundelkand Craton also show evidence of contemporaneous magmatism (Fig. 3a and b). Simultaneously, previous studies reveal that high-K anatectic granites were emplaced between (2583–2482 Ma) in the entire Bundelkhand Craton, which is somehow contemporaneous with sanukitoids (s.l.) emplacement (Mondal et al., 1998, 2002; Pandey et al., 2011; Kaur et al., 2016; Joshi et al., 2017).

An interesting finding presented here is the older inherited ages of 2644 ± 25 and 2619 ± 24 Ma found in two zircon grains of the studied samples (Table 3, Fig. 11a). Similarly, Pandey et al. (2011) have reported a Rb-Sr whole rock age of 2622 ± 300 Ma for andesite from the Mohar region, in the central part of Bundelkhand Craton, which could reveal a possible linkage between the Jhansi and Mohar regions, but unfortunately, that age cannot be considered due to the large error of 300 Ma. Therefore, the inherited ages (2644 ± 25 and 2619 ± 24 Ma) together with those reported by Joshi et al. (2017) from Jhansi (2842 ± 3 Ma and 2914 ± 8 Ma) suggest the involvement of older Mesoarchean and Neoarchean crust in the genesis of these magmas. On the other hand, these values contrast with the apparent absence of inherited zircons in the high-K anatectic granites of clear crustal origin (Joshi et al., 2017). Although further studies are necessary, it may currently be suggested that: (1) sources of the anatectic granites were not saturated with zircon; (2) P-T conditions and kinetics of magmas may be different for sanukitoids and anatectic granites, preventing zircon dissolution in one case and favoring dissolution in the other (see discussion about zircon survival mechanisms in Bea et al., 2007).

6.2. Petrogenesis

6.2.1. Sanukitoids (s.l.)

As mentioned before, most of the sanukitoid plutons are situated in the northern and central parts of the Bundelkhand Craton, and only a few intrusions occur in the southern part, that is, the Khajuraho pluton (Joshi et al., 2017). The samples from northern and central terrains have the typical geochemical feature of Archean sanukitoids such as a relatively high Mg# (41–50), high Ba + Sr (700–2800 ppm) and enrichment in LILE and LREE. In addition, they are characterized by fractionated REE patterns and negative anomalies in Nb-Ta and Ti. Interestingly, they mostly plot as M-type granitoids in the discrimination diagrams of Bea et al. (2007) based on major elements (not shown), which is also typical of sanukitoids. However, independently, high concentrations of Ba and Sr in sanukitoids are thought to indicate their derivation from a mantle source enriched by fluids released from a subducting slab (Lobach-Zhuchenko et al., 2008). Several bivariate and ternary diagrams have been tested, i.e., (Na_2O/K_2O *vs.* Ba + Sr), (Ba + Sr *vs.* Er) and (Ba + Sr)/1000–1/Er–Er), respectively (Fig. 13). In

Table 3
Results of U-Pb dating of zircons on sanukitoids (s.l.).

Sample-Spot		Content ($mg \cdot g^{-1}$)								Isotopic ratios							Isotopic ages (Ma)						% conc
	f206 (%)	U	2s	Th	2s	Pb	2s	Th/U	$^{206}Pb/^{204}Pb$	$^{207}Pb/^{206}Pb$	2s	$^{207}Pb/^{235}U$	2s	$^{206}Pb/^{238}U$	2s	Rho	$^{207}Pb/^{206}Pb$	2s	$^{207}Pb/^{235}U$	2s	$^{206}Pb/^{238}U$	2s	
BC-16-18-2C	0.11	157	11.0	132.6	7.8	172	13.0	0.84	16,350	0.1659	0.0035	9.05	0.21	0.3789	0.0095	0.64	2534	20	2058	44	2332	21	81
BC-16-18-3C	0.08	183.5	8.4	217.7	7.2	286	13.0	1.19	23,000	0.1699	0.0029	10.78	0.23	0.4420	0.0100	0.68	2575	16	2346	44	2498	20	91
BC-16-18-4C	0.13	120.2	6.7	71.5	3.3	83.4	4.9	0.59	14,500	0.1700	0.0028	10.60	0.20	0.4330	0.0081	0.56	2583	16	2311	36	2482	17	89
BC-16-18-5C	0.25	94.2	3.1	95.2	4.1	78.1	4.3	1.01	7430	0.1645	0.0047	6.31	0.24	0.2677	0.0097	0.70	2532	29	1529	50	2019	33	60
BC-16-18-6C	0.15	115.7	3.2	133.2	4.9	151	6.7	1.15	12,440	0.1755	0.0044	9.44	0.27	0.3790	0.0110	0.64	2619	24	2059	53	2381	26	79
BC-16-18-7C	0.08	178.7	4.3	86.9	2.1	122.7	4.0	0.49	24,750	0.1650	0.0033	11.84	0.25	0.5000	0.0130	0.62	2523	18	2605	54	2588	20	103
BC-16-18-13C	0.12	140.3	5.3	147.8	5.3	150	5.5	1.05	15,450	0.1622	0.0041	9.49	0.25	0.4110	0.0110	0.52	2483	23	2212	52	2379	25	89
BC-16-18-16C	0.16	87.1	1.9	72.9	1.9	117.9	3.7	0.84	11,820	0.1767	0.0043	13.17	0.36	0.5140	0.0140	0.62	2644	25	2668	60	2683	26	101
BC-16-18-17C	0.13	396	15.0	151.6	5.3	230	12.0	0.38	14,755	0.1592	0.0038	3.77	0.21	0.1630	0.0089	0.87	2468	26	958	49	1504	50	39
BC-16-18-18C	0.10	151	5.4	168.7	5.6	202.8	7.5	1.12	19,150	0.1654	0.0036	11.60	0.26	0.4910	0.0130	0.57	2538	20	2568	54	2573	21	101
BC-16-18-19C	0.08	230.9	6.6	97.6	2.8	94.2	4.0	0.42	24,150	0.1652	0.0033	9.61	0.20	0.4075	0.0098	0.63	2540	19	2192	45	2390	20	86
BC-16-18-21C	0.20	94.7	3.0	129.2	3.3	132.8	4.9	1.36	9165	0.1643	0.0046	8.80	0.24	0.3810	0.0120	0.53	2524	29	2061	53	2310	25	82
BC-16-18-23C	0.12	133.4	4.6	113.2	3.7	124.8	6.1	0.85	15,150	0.1669	0.0038	10.55	0.26	0.4410	0.0120	0.61	2545	23	2344	52	2487	22	92
BC-16-18-24C	0.12	574	11.0	55.2	1.6	24.8	1.6	0.10	16,050	0.0974	0.0025	1.52	0.04	0.1093	0.0029	0.48	1595	32	668	17	937	17	42
BC-16-18-25C	0.13	116.2	4.4	89.9	3.2	100	4.5	0.77	13,900	0.1658	0.0038	11.30	0.26	0.4810	0.0120	0.52	2542	22	2522	50	2549	21	99
BC-16-18-26R	0.17	84.9	5.2	112	7.0	153	9.0	1.32	10,700	0.1686	0.0044	12.09	0.33	0.5020	0.0150	0.59	2565	28	2609	63	2593	25	102
BC-16-18-28R	0.23	91.2	3.9	60.7	1.8	62.5	2.7	0.67	8010	0.1647	0.0046	7.92	0.22	0.3401	0.0099	0.53	2512	27	1893	47	2221	24	75
BC-16-18-29C	0.09	294	12.0	658	37.0	262.8	9.7	2.24	21,500	0.1576	0.0027	6.80	0.19	0.3019	0.0081	0.72	2422	20	1696	40	2086	24	70
BC-16-18-33R	0.41	84.5	4.7	146.8	8.7	72.2	4.2	1.74	4510	0.1737	0.0071	5.32	0.21	0.2211	0.0069	0.49	2594	47	1283	36	1832	32	49
BC-16-18-36C	0.15	98.9	2.8	85.6	3.1	109.5	5.2	0.87	12,130	0.1659	0.0037	11.61	0.28	0.4920	0.0120	0.57	2538	21	2566	51	2571	22	101
BC-16-18-38C	0.10	298.1	9.1	251.6	6.0	162.4	4.4	0.84	18,015	0.1539	0.0036	5.48	0.19	0.2488	0.0078	0.72	2416	23	1426	40	1891	29	59
BC-16-18-44C	0.16	131.8	4.2	89.3	2.8	91.5	3.8	0.68	11,660	0.1486	0.0033	7.50	0.17	0.3539	0.0083	0.58	2354	22	1953	40	2169	21	83

% conc = (^{206}Pb-^{238}U age/^{207}Pb-^{206}Pb age) * 100, f206c (degree of concordance) = ($^{206}Pb^{204}Pb$model/$^{206}Pb^{204}Pb$ measured) × 100, Spot size = 25 μm, depth of crater ~20 μm.

Table 4
Sm-Nd isotopic data for sanukitoids (s.l.).

Sample	Rock type	Sm (ppm)	Nd (ppm)	$^{147}Sm/^{144}Nd$	$^{143}Nd/^{144}Nd$	$^{143}Nd/^{144}Nd_t$	t (Ma)	εNd_t	± 2σ
BC-16-01	Sanukitoids (s.l.)	5.04	25.53	0.119	0.511147	0.509132	2560[a]	−3.64	$1 * 10^{-6}$
BC-16-03	Sanukitoids (s.l.)	4.15	20.78	0.121	0.511271	0.509233	2560[a]	−1.66	$1 * 10^{-6}$
BC-16-18	Sanukitoids (s.l.)	5.54	32.31	0.104	0.510922	0.509161	2578[b]	−2.67	$1 * 10^{-6}$

t for calculations: [a] = age data from Joshi et al. (2017), [b] = age of sample BC-16-18 in this study.

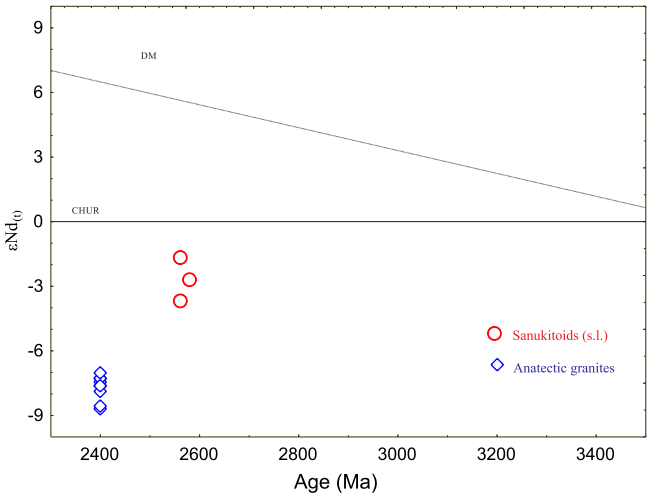

Fig. 12. $\varepsilon_{Nd}(t)$ *vs.* formation age (in Ma) diagram for late-Archean Bundelkhand sanukitoids (s.l.) and anatectic granites. $\varepsilon_{Nd}(t)$ data for anatectic granites are taken from Pandey et al. (2011).

these diagrams, most of the sanukitoids (s.l.) samples from the Bundelkhand Craton were discriminated as enriched source (Fig. 13). Thus, this finding indicates that these sanukitoids (s.l.) were also generated from the mantle source, having similar characteristics of typical Archean sanukitoids. To support this finding, Nd isotope systematic measurement was also used for the whole-rock.

The whole-rock ε_{Ndt} values are mostly negative between −3.64 and −1.66, indicating a crustal component involved in the origin of sanukitoids (Fig. 12). The presence of inherited zircons also suggests crustal reworking. La/Nb *vs*. Th/Nb ratios (Fig. 14a–c) also favor a crustal origin. However, these rocks present with high contents of compatible elements (Mg, Cr, Ni), which points to a mantle contribution. Furthermore, their high Ba and Sr contents are independent of the silica content point to a source enriched in such elements, possibly a metasomatized mantle as mentioned above. The high Nb/Y and La/Yb ratios of these rocks suggest a felsic melt as a metasomatic agent rather than a metasomatic fluid (Martin et al., 2010). Thus, a hypothesis may favor partial melting of a mantle source, previously metasomatized by TTG melts, in accordance with published experimental data and modeling of sanukitoids (e.g., Rapp et al., 2010; Semprich et al., 2015). However, as mentioned before, these rocks can be classified as low-Ti sanukitoids, in which the most likely scenario would be the contamination of slab TTG melts with a mantle peridotite and the concomitant generation of sanukitoids in a single event (Martin et al., 2005, 2010). The degree of interaction of metasomatized mantle melts with anatectic melts is high for the Bundelkhand sanukitoids (s.l.), similar to Banshentu pluton, North China Craton (Jahn et al., 1988; Wang et al., 2009; Ma et al., 2013), and some plutons in the Dharwar Craton (Moyen et al., 2003), as suggested by the negative epsilon values. This is in accordance with the enriched mantle source proposed by Joshi et al. (2017) that Closepet-type rocks could imply a different degree of mixing with crustal sources.

6.2.2. *High-K anatectic granites*

High-K anatectic granites were emplaced at 2.57–2.48 Ga in the Bundelkhand Craton. A crustal origin of high-K anatectic granites is generally interpreted and accepted, resulting from the partial melting of TTG rocks and/or the melting of metasedimentary rocks (see, for example, Mondal et al., 2002; Kaur et al., 2016; Joshi et al., 2017). The high-K anatectic granites constitute a major part of the Bundelkhand Craton and share similar geochemical characteristics of Cordilleran-type granitoids (Frost et al., 2001) formed in arcs and post-collisional settings; their primarily magnesian character may indicate a formation under oxidizing conditions (e.g., Frost and Frost, 2008). Their metaluminous to slightly peraluminous composition, along with the apparent absence of inherited zircons (Joshi et al., 2017), precludes a derivation from the partial melting of metasedimentary rocks. Therefore, these granites might result from the partial melting of igneous rocks, probably TTGs and granodiorite in the shallow to lower continental crust (Moyen, 2011) but under conditions that inhibit zircon survival (Bea et al., 2007). The field relations (Fig. 3) and geochronology suggest that sanukitoids magmatism could also have played an important role in providing the necessary heat flux for crustal melting in order to generate anatectic melts.

This study explores trace element ratios (Nb/Ta, Th/Nb, Y/Nb, Ce/Pb) that are sensitive to magma sources (see Moreno et al., 2014, 2016; and references therein) and can help to determine the origin of such granites (Fig. 14a–c). These high-K anatectic granites exhibit marked negative Nb and positive Pb anomalies that can indicate continental crustal and/or subduction-related sources. Accordingly, the relationships of their Th/Nb, Ce/Pb and La/Nb ratios mainly suggest an affinity for continental crust and/or subduction-related sources (Fig. 14a–c). This feature is also in conformance with the low Nb/Ta values in most of the samples (Table S1), which are close to or lower than the crustal value (11–12; Green, 1995).

Concerning the Bundelkhand Craton, the melting of the lower crust could be linked to the advective heat transfer and thermal blanketing caused by felsic volcanics (2542 ± 17 Ma; Singh and Slabunov, 2015a) and sanukitoids (s.l.) magma emplacement (ca. 2563 ± 2 Ma; Joshi et al., 2017). Field relationships between some sanukitoids (s.l.) and high-K anatectic granites in the Bundelkhand Craton suggest that they were intruded contemporaneously ca. 2.55 Ga (Table S2 and Fig. 3a and b). Granites from the Mohar area in the northern terrane, studied by Pandey et al. (2011), exhibit a wide range of T_{DM} (3.03–3.17 Ga) with ε_{Nd} values (t = 2400 Ma) that are mostly negative and ranging from −8.72 to −6.28; the values are more radiogenic than those obtained here for the sanukitoids (Table 4) and suggest a derivation from the crustal reworking of old crustal sources. The Nd isotope signatures of granites are in agreement with the Sr isotopic compositions (I.R. ~ 0.7069) indicating their derivation from heterogeneous crustal sources (Pandey et al., 2011). Kaur et al. (2016) reported major and trace element data of high-K anatectic granites and in situ Hf isotope data of zircon [$\varepsilon_{Hf}(t)$ = −2.5 to −11.4] that are consistent with their derivation from the reworking of a heterogeneous crustal source, which conforms to Nd isotope signatures $\varepsilon_{Nd}(t)$ = −6.28 to −8.729 (Pandey et al., 2011).

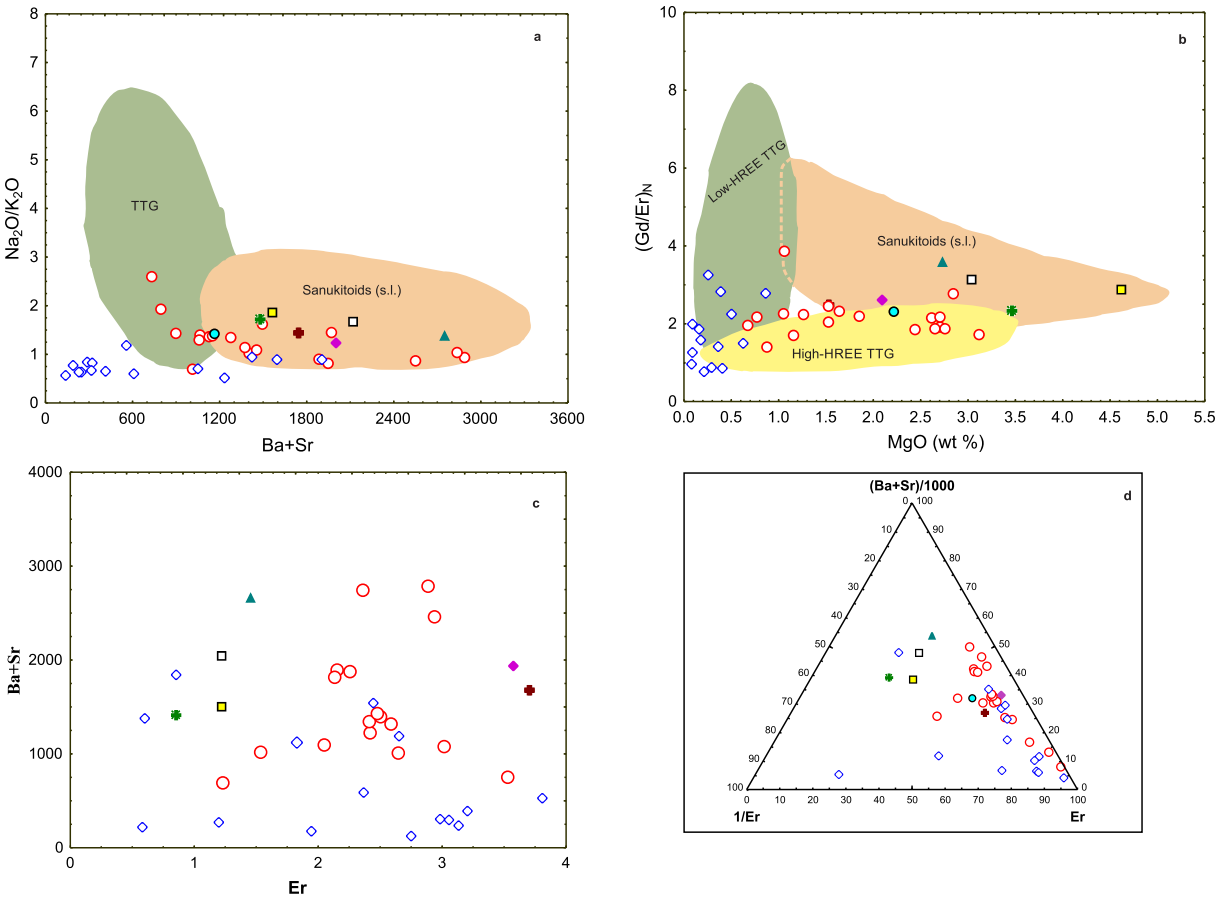

Fig. 13. Classification diagrams of Sanukitoids (s.l.) and high-K anatectic granites: a – Na_2O/K_2O *vs.* Ba + Sr (after Halla et al., 2009); b – (Gd/Er) *vs.* MgO (Halla et al., 2009); c – Ba + Sr *vs.* Er binary plot (after Heilimo et al., 2010); d – (Ba + Sr/1000) − 1/Er − Er triangular plot for distinguishing sources and role of garnet in residue (after Heilimo et al., 2010).

6.3. Tectonic settings and geodynamics for the late-Archean evolution in the Bundelkhand Craton

6.3.1. Tectonic setting

In the present study, two sets (major and immobile trace elements) based new multidimensional discrimination diagrams have been used to infer tectonic setting. As the older bi-variate or ternary discrimination diagrams have several problems, which are related to statistically wrong treatment of compositional data (Aitchison, 1986), eye-drawn subjective field boundaries for tectonic environment, and lack of representative data base (Verma et al., 2013). Therefore, new multi-dimensional discrimination diagrams (Verma et al., 2012, 2013) which are based on linear discriminant analysis (LDA) and log-ratio transformations were used for tectonic interpretation having four tectonic fields (Fig. 15a and b). Sanukitoids (s.l.) were plotted out in the combined field of island (IA) and continental arc (CA) setting, whereas most of anatectic granites were plotted in collision (Col) setting in both diagrams (Fig. 15a and b). Thus, the new multi-dimensional discrimination diagrams (Verma et al., 2012, 2013) indicated a subduction related setting for the sanukitoids (s.l.) whereas a collision setting for the high-K anatectic granites from the Bundelkhand Craton.

6.3.2. Geodynamic model

In this work, an integrated geodynamic model has been proposed to explain the formation and evolution of late-Archean rocks in the Bundelkhand Craton (Fig. 16a–c). At ca. 2.7 Ga, the oceanic slab was subducted to generate the TTG melt, and the partial melting of hydrated garnetiferous mafic rocks interacted with the overlying mantle to form the TTG (granodioritic) plutons (Fig. 16a, Verma et al., 2016). Furthermore, the mid-oceanic ridge was subducted and the lithospheric mantle was upwelled through the mantle windows to produce felsic volcanics (which are of a younger sequence), that constitute the central Bundelkhand greenstone belt (Fig. 16b). Progressive cooling occurred ca. 2.5 Ga, which caused the reduction in the degree of slab melting and consequently, the decrease in the rock/melt ratios (Martin et al., 2010). In such circumstances, the slab melts can be strongly contaminated by assimilation of mantle peridotite, thus giving rise to low-Ti sanukitoids (Fig. 16c). Therefore, sanukitoid suites (produced from crust-mantle magma), and high-K anatectic granites (resultant of crustal magma) have probably played a key role in the overall crustal stabilization of the Bundelkhand Craton. Finally, a crucial change took place after 2.5 Ga, when the Earth's heat production was very low for slab melting, except in relatively infrequent geodynamic conditions; most modern arc magmas originated in the melting of the mantle wedge peridotite, a result of dehydrated subducted slabs.

6.4. Comparison with other Archean cratonic terrains: implications for late-Archean crustal evolution

Late Archean crust forming events and continental growth of the Bundelkhand Craton can be correlated with other Archean cratons such as Dharwar, North China, Pilbara, Kaapvaal, Karelian, Amazonian and Superior Province (Fig. 17). All these cratonic terrains comprise three traditional types of late-Archean granitoids: TTG, sanukitoids, and high-K anatectic granites (Moyen et al., 2003; Laurent et al., 2014; Jayananda et al., 2018). Figs. 5 and 6 show that rocks from the Bundelkhand Craton apparently have similar geochemical characteristics, which indicate the occurrence of sanukitoids (s.l.) and anatectic

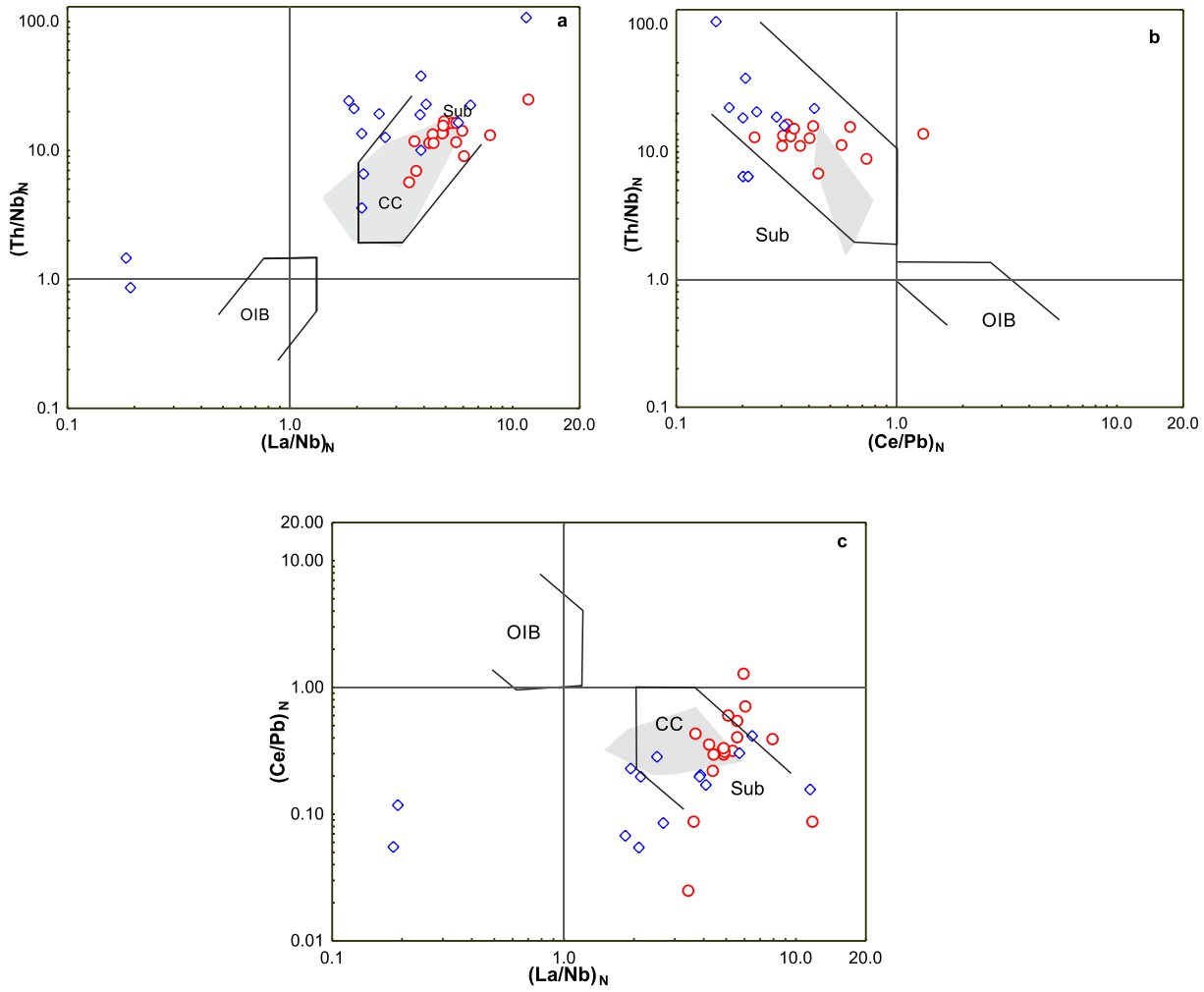

Fig. 14. a–c. Relationships between Th/Nb, La/Nb and Ce/Pb in the Bundelkhand Craton granitoids. Normalization values after McDonough and Sun (1995). Compositional fields after Moreno et al. (2016). Abbreviations: CA–Continental Arcs; CC–Continental Crust; IA–Island Arcs; OIB–Ocean Island Basalts; Sh, shoshonites; Sub, subduction-related magmatic suites.

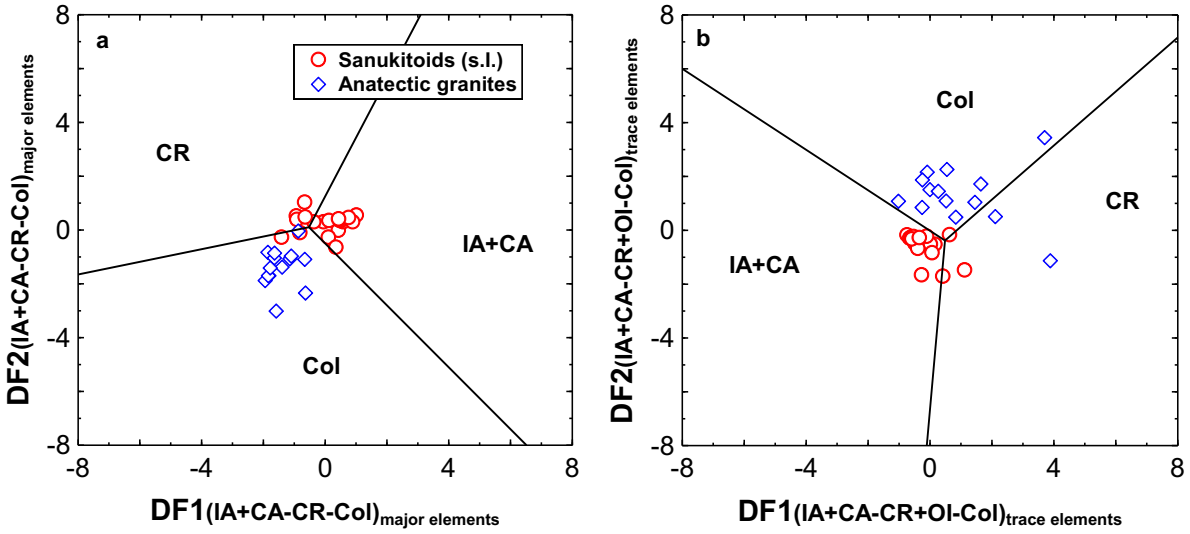

Fig. 15. a – Major element–based multidimensional discrimination diagrams (Verma et al., 2012), b – immobile trace element–based multidimensional discrimination diagrams (Verma et al., 2013) for the acid rocks. The four fields that can be discriminated are: IA–island arc; CA–continental arc; CR–continental rift; Col–collision setting.

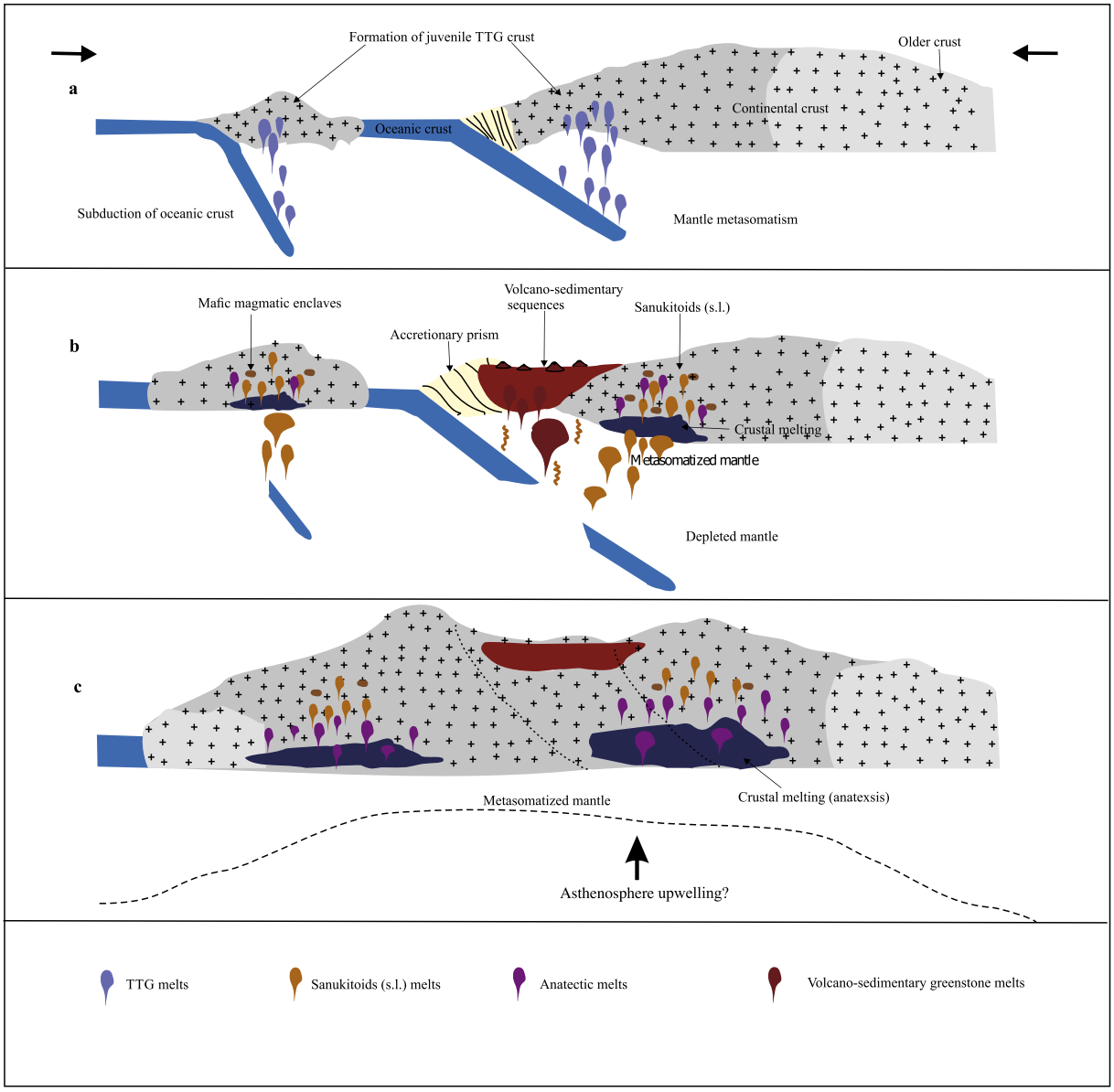

Fig. 16. Schematic, conceptual cartoon illustrating the proposed geodynamic model for evolution of late-Archean rocks in the Bundelkhand Craton, i.e., subduction–collision sequences: a – Geodynamic model showing the melting of subducted slab and mantle for the formation of TTGs at ~2.7 Ga, b – followed by a shift from slab melting to direct mantle melting as a consequence of slabs break off into asthenosphere leading to mantle upwelling which caused melting of previously enriched shallower mantle for origin of sanukitoids and also happened felsic volcanism. The sanukitoid melts were interacted with crustal melts (anatectic melts) at ~2.58 Ga, c– finally, at ~2.5 Ga collision was happened and it provided heat flux to generate voluminous anatectic melts (anatexis processes).

granites, and this is consistent with the commonly observed features on the abovementioned Archean cratons worldwide (Frost et al., 2001, Laurent et al., 2014).

However, during the late Archean era, sanukitoids (s.l.) and anatectic granites were emplaced between 2.58 and 2.50 Ga in the Bundelkhand Craton. The field observations and geochemical data indicate a gradual transition between the two rock types. Sanukitoids show many geochemical characteristics, such as enriched LREE compared with the HREE, and a negative Eu anomaly with some being positive, especially for those with higher Ba (> 2000 ppm) and Zr (337 ppm) content, and lower Nb (3.7 ppm) and Ta (0.5) content. Thus, it is very likely that the geochemical signatures of the sanukitoids (s.l.) were acquired during the partial melting of TTG crust. This interpretation is consistent with other Archean cratons (viz. Dharwar, North China, Pilbara, Kaapvaal, Karelian, and Amazonian), given that sanukitoids (s.l.) can be formed by enriched-mantle sources (Moyen et al., 2003; Heilimo et al., 2010; Laurent et al., 2014; Jiang et al., 2016; Santos and Oliveira, 2016; Jayananda et al., 2018). The anatectic granites are typically biotite- or two mica-granites (Fig. 5a), which is comparable to other Archean cratons such as Dharwar, India and North China, China (Laurent et al., 2014). Published data reveal that anatectic granites can be generated by the partial melting of a low-K TTG crust (Watkins et al., 2007). Thus, such anatectic granites may be formed solely by internal crust reworking, without the addition of melts from an external source, and may resemble the Archean Andean-type setting (Laurent and Zeh, 2015). In the Bundelkhand Craton, many researchers (Kaur et al., 2014, 2016; Joshi et al., 2017) have proposed a subduction-related geodynamic setting, which is somehow similar to the findings of this study, where multi-dimensional discrimination diagrams indicate arc and collision-related affinities, at least for the Neoarchean time (Verma et al., 2012, 2013).

The studied Nd isotope of sanukitoids (s.l.) exhibit εNd_t values ranging between −1.0 and −3.0 and can provide robust constraints on the nature of magma sources. The ε_{Nd} values (T = 2577 Ma) of the

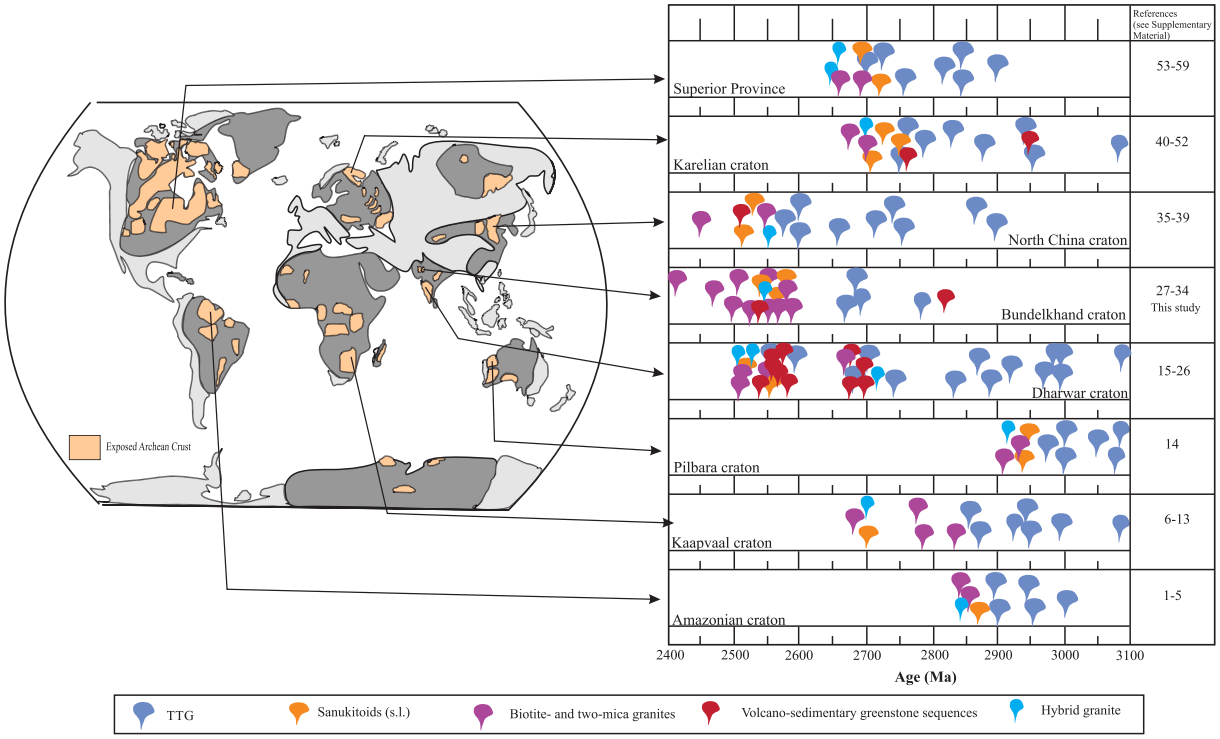

Fig. 17. Left: exposed Archean cratons (modified after Bleeker, 2003), selected cratons of curiosity, where the late-Archean magmatic events are well recognized. Right: late-Archean geologic events distribution of various cratonic terrains (modified and updated after Heilimo et al., 2011; Laurent et al., 2014).

Buendelkhand sanukitoids range from −1.0 to −3.0 indicating the involvement of a crustal component (Fig. 12, Table 4), whereas the Dharwar sanukitoids show ε_{Nd} (T = 2540 Ma) values of +1 to −3, which favor the slightly depleted to enriched juvenile sources with variable crustal contamination (Jayananda et al., 2000). Therefore, the degree of interaction between mantle-derived sanukitoid magmas with pre-existing crust is reduced in the Bundelkhand Craton and higher in the Dharwar Craton, which can be compared to sanukitoids from the North China Craton (Wang et al., 2009).

Geochronological features of Archean cratons have been illustrated in the simplified map in Fig. 17, where age distribution of crust formation and sanukitoids (s.l.) magmatism in Meso-Neoarchean blocks are mentioned. All cratons have their unique type and volume of magmatism. The age distribution bars show volumes TTG-type plutonism with minor sanukitoids (s.l.) magmatism and coeval with anatectic granites (complete or partially). These sanukitoids (s.l.) magmatism can be correlated to other Archean cratons in order to understand the geodynamic evolution and will probably indicate the last stage of plate dynamic processes, somehow related to subduction characteristics. For example, geochronological data for sanukitoids (s.l.) from the Bundelkhand, Dharwar, and North China cratons might be part of the same “supercontinent” whose magmatism occur ca. 2.5 Ga (Fig. 17). However, these findings are based on geochemistry and geochronology, and should be considered carefully because similar magmatic processes could have occurred simultaneously in different places around the Earth. In summary, the planetary scale of late Archean crust forming events is highlighted by the coeval formation of sanukitoids (s.l.) and anatectic granites as well TTG in most cratons (Fig. 17, Laurent et al., 2014; Kaur et al., 2016; Halla et al., 2017; Jayananda et al., 2018).

7. Conclusions

This contribution provides bulk-rock Sm–Nd results for the first time, and new geochronology and geochemistry of sanukitoids (s.l.) as well as the geochemistry of high-K anatectic granites from the northern and central parts of the Bundelkhand Craton. This study also provides new important constraints to understanding the formation of the Bundelkhand Craton by expanding the observed compositional heterogeneity and the temporal overlap of the different late Archean granitoid suites. The results lead to the following conclusions:

1. The age of the Bundelkhand sanukitoids (s.l.) (2577 ± 16 Ma) indicates that sanukitoid magmatism occurred contemporaneously with high-K anatectic granitic magmatism.
2. Major trace elements and Nd isotopes suggest that the sanukitoid plutons were produced by the mixing of metasomatized mantle melts with anatectic melts, and their homogenization occurred at shallow levels of emplacement.
3. High-K anatectic granitic plutons geochemical characteristics suggest that they were formed by the reworking (partial melting) of pre-existing TTG and were vastly emplaced during cratonic stabilization at 2.5 Ga.
4. The granitic plutons indicate a temporal evolution from TTG-dominated through sanukitoids (s.l.) to high-K anatectic leucogranites-dominated (sodic to potassic) throughout the Archean era, which is inferred as evidence for the internal reworking and diversification of the continental crust. This process of crustal differentiation towards stabilization of the continental crust coincided with voluminous pulses of anatectic granitic magmatism during ca. 2.5 Ga throughout the Bundelkhand Craton.
5. Sanukitoids (s.l.) originated from subduction-related setting and high-K anatectic granites formed in collision environments.

Conflict of interest

All authors agree that this is an original contribution, all have contributed to its development, and there is no conflict of interest.

Acknowledgements

This research was funded by the IPICYT internal grant to the first author (PKS), whose doctoral thesis is in preparation under the

guidance of the second author (SKV). First author also thanks to the National Council of Science and Technology (CONACYT), Mexico for his doctoral fellowship [grant # 612752]. PKS also thanks to Dr. Courtney Perkins for his English language editing. SKV and EPO thank to the São Paulo Research Foundation (FAPESP) for the grants [# 2012/07243-3 and 2012/15824-6], which were used in the analytical purpose. SKV is grateful to Newton Advance Fellowship award–The Royal Society, UK for the grant [NA160116]. VKS thanks to Department of Science and Technology, Govt. of India for grant [# INT/RUS/RFBR/P-279]. VKS and SKV thank to the Bundelkhand University, Jhansi, India and IPICYT for collaboration agreement for this work. We appreciate Erica, Margrates, Bia, Paola, and Mauricio for their assistance in zircon U–Pb dating and whole-rock analyses. We express our sincere gratitude to Dr. Carmen Galindo Francisco and Dr. Jose Manuel Fuenlabrada Perez for isotopic analyses at CAI de Ciencias de la Tierra y Arqueometría, Universidad Complutense de Madrid, Spain. We also thank to anonymous reviewer, and associate editor Prof. Manoj Pandit for their critical comments and efficient editorial handling, whose suggestions help to enhance the quality of revised version of the manuscript.

Appendix A. Supplementary material

Supplementary data to this article can be found online at https://doi.org/10.1016/j.jseaes.2018.12.013.

References

Absar, N., Raza, M., Roy, M., Naqvi, S.M., Roy, A.K., 2009. Composition and weathering conditions of Paleoproterozoic upper crust of Bundelkhand Craton, Central India: records from geochemistry of clastic sediments of 1.9 Ga Gwalior Group. Precambr. Res. 168, 313–329.
Aitchison, J., 1986. The Statistical Analysis of Compositional Data. Chapman and Hall, London, UK, pp. 416.
Almeida, J.D.A.C., Dall'Agnol, R., da Silva Leite, A.A., 2013. Geochemistry and zircon geochronology of the Archean granite suites of the Rio Maria granite-greenstone terrane, Carajás Provincem Brazil. J. South Amer. Earth Sci. 42, 103–126.
Barbarin, B., 1999. A review of the relationships between granitoid types, their origins and their geodynamic environments. Lithos 46, 605–626.
Basu, A.K., 1986. Geology of parts of the Bundelkhand granite massif central India. Rec. Geol. Surv. India (Ed.) 117, 61–124.
Bea, F., Montero, P., González-Lodeiro, F., Talavera, C., 2007. Zircon inheritance reveals exceptionally fast crustal magma generation processes in Central Iberia during the Cambro-Ordovician. J. Petrol. 48, 2327–2339.
Bibikova, E.V., Samsonov, A.V., Petrova, A.Y., Kirnozova, T.I., 2005. The Archean geochronology of western Karelia. Stratigr Geol Correl. 13, 459–475.
Bleeker, W., 2003. The late Archean record: a puzzle in ca. 35 pieces. Lithos 71, 99–134.
Cotta, A.J.B., Enzweiler, J., 2009. Quantification of major and trace elements in water samples by ICP-MS and collision cell to attenuate Ar and Cl-based polyatomic ions. J. Anal. At. Spectrom. 24, 1406–1413.
Dall'Agnol, R., da Cunha, I.R.V., Guimarães, F.V., de Oliveira, D.C., Teixeira, M.F.B., Feio, G.R.L., Lamarão, C.N., 2017. Mineralogy, geochemistry, and petrology of Neoarchean ferroan to magnesian granites of Carajás Province, Amazonian Craton: the origin of hydrated granites associated with charnockites. Lithos 277, 3–32.
Dey, S., Pandey, U.K., Rai, A.K., Chaki, A., 2012. Geochemical and Nd isotope constraints on petrogenesis of granitoids from NW part of the eastern Dharwar craton: possible implications for late Archaean crustal accretion. J. Asian Earth Sci. 45, 40–56.
Dey, S., Nandy, J., Choudhary, A.K., Liu, Y., Zong, K., 2014. Origin and evolution of granitoids associated with the Kadiri greenstone belt, eastern Dharwar craton: a history of orogenic to anorogenic magmatism. Precambr. Res. 246, 64–90.
Dey, S., Halla, J., Kurhila, M., Nandy, J., Heilimo, E., Pal, S., 2016. Geochronology of Neoarchaean granitoids of the NW eastern Dharwar craton: implications for crust formation. Geol. Soc. London Spec. Publ. 449 SP449–9.
Dickinson, W.R., Gehrels, G.E., 2003. U-Pb ages of detrital zircons from Permian and Jurassic eolian sandstones of the Colorado Plateau, USA: paleogeographic implications. Sediment. Geol. 163, 29–66.
Farina, F., Albert, C., Lana, C., 2015. The Neoarchean transition between medium-and high-K granitoids: clues from the Southern São Francisco Craton Brazil. Precambr. Res. 266, 375–394.
Farooqui, S.A., Singh, A.K., 2006. Platinum mineralization in Ikauna Area, Lalitpur District, Uttar Pradesh. J. Geol. Soc. India 68, 582–584.
Foley, S.F., Barth, M.G., Jenner, G.A., 2000. Rutile/melt partition coefficients for trace elements and an assessment of the influence of rutile on the trace element characteristics of subduction zone magmas. Geochim. Cosmochim. Acta 64, 933–938.
Foley, S., Tiepolo, M., Vannucci, R., 2002. Growth of early continental crust controlled by melting of amphibolite in subduction zones. Nature 417, 837.
Frost, B.R., Barnes, C.G., Collins, W.J., Arculus, R.J., Ellis, D.J., Frost, C.D., 2001. A geochemical classification for granitic rocks. J. Petrol. 42, 2033–2048.
Frost, B.R., Frost, C.D., 2008. A geochemical classification for feldspathic igneous rocks. J. Petrol. 49, 1955–1969.
Green, T.H., 1995. Significance of Nb/Ta as an indicator of geochemical processes in the crust-mantle system. Chem. Geol. 120, 347–359.
Halla, J., 2005. Late Archean high-Mg granitoids sanukitoids in the southern Karelian domain, eastern Finland: Pb and Nd isotopic constraints on crust – mantle interactions. Lithos 79, 161–178.
Halla, J., van Hunen, J., Heilimo, E., Hölttä, P., 2009. Geochemical and numerical constraints on Neoarchean plate tectonics. Precambr. Res. 174, 155–162.
Halla, J., Whitehouse, M.J., Ahmad, T., Bagai, Z., 2017. Archaean granitoids: an overview and significance from a tectonic perspective. Geol. Soc. London Spec. Publ. 449, 1–18.
Hawkesworth, C., Cawood, P., Dhuime, B., 2013. Continental growth and the crustal record. Tectonophysics 609, 651–660.
Hawkesworth, C., Cawood, P.A., Dhuime, B., 2018. Rates of generation and growth of the continental crust. Geosci. Front. https://doi.org/10.1016/j.gsf.2018.02.004.
Heilimo, E., Halla, J., Hölttä, P., 2010. Discrimination and origin of the sanukitoid series: geochemical constraints from the Neoarchean western Karelian Province Finland. Lithos 115, 27–39.
Heilimo, E., Halla, J., Huhma, H., 2011. Single-grain zircon U-Pb age constraints of the western and eastern sanukitoid zones in the Finnish part of the Karelian Province. Lithos 12, 87–99.
Jahn, B.M., Auvray, B., Shen, Q.H., Liu, D.Y., Zhang, Z.Q., Dong, Y.J., Mace, J., 1988. Archean crustal evolution in China: the Taishan complex, and evidence for juvenile crustal addition from long-term depleted mantle. Precambr. Res. 38, 381–403.
Jayananda, M., Martin, H., Peucat, J.J., Mahabaleswar, B., 1995. Late Archaean crust-mantle interactions: geochemistry of LREE-enriched mantle derived magmas. Example of the Closepet batholith, southern India. Contrib. Mineral. Petrol. 119, 314–329.
Jayananda, M., Moyen, J.F., Martin, H., Peucat, J.J., Auvray, B., Mahabaleswar, B., 2000. Late Archaean 2550–2520 Ma juvenile magmatism in the Eastern Dharwar craton, southern India: constraints from geochronology, Nd–Sr isotopes and whole rock geochemistry. Precambr. Res. 99, 225–254.
Jayananda, M., Chardon, D., Peucat, J.J., Capdevila, R., 2006. 2.61 Ga potassic granites and crustal reworking in the western Dharwar craton, southern India: tectonic, geochronologic and geochemical constraints. Precambr. Res. 150, 1–26.
Jayananda, M., Santosh, M., Aadhiseshan, K.R., 2018. Formation of Archean 3600–2500 Ma continental crust in the Dharwar Craton, southern India. Earth Sci. Rev. 181, 12–42.
Jiang, N., Guo, J., Fan, W., Hu, J., Zong, K., Zhang, S., 2016. Archean TTGs and sanukitoids from the Jiaobei terrain, North China craton: insights into crustal growth and mantle metasomatism. Precambr. Res. 281, 656–672.
Joshi, K.B., Bhattacharjee, J., Rai, G., Halla, J., Ahmad, T., Kurhila, M., Choudhary, A.K., 2017. The diversification of granitoids and plate tectonic implications at the Archaean-Proterozoic boundary in the Bundelkhand Craton, Central India. Geol. Soc. London Spec. Publ. 449, 123–157.
Käpyaho, A., Mänttäri, I., Huhma, H., 2006. Growth of Archaean crust in the Kuhmo district, eastern Finland: U-Pb and Sm–Nd isotope constraints on plutonic rocks. Precambr. Res. 146, 95–119.
Kaur, P., Zeh, A., Chaudhri, N., 2014. Characterisation and U-Pb–Hf isotope record of the 3.55 Ga felsic crust from the Bundelkhand Craton, northern India. Precambr. Res. 255, 236–244.
Kaur, P., Zeh, A., Chaudhri, N., Eliyas, N., 2016. Unravelling the record of Archaean crustal evolution of the Bundelkhand Craton, northern India using U-Pb zircon–monazite ages, Lu–Hf isotope systematics, and whole-rock geochemistry of granitoids. Precambr. Res. 281, 384–413.
Keller, C.B., Schoene, B., 2012. Statistical geochemistry reveals disruption in secular lithospheric evolution about 2.5 Gyr ago. Nature 485, 490.
Kovalenko, A., Clemens, J.D., Savatenkov, V., 2005. Petrogenetic constraints for the genesis of Archaean sanukitoid suites: geochemistry and isotopic evidence from Karelia, Baltic Shield. Lithos 79, 147–160.
Kudryashov, N.M., Petrovsky, M.N., Mokrushin, A.V., Elizarov, D.V., 2013. Neoarchean sanukitoid magmatism in the Kola region: geological, petrochemical, geochronological, and isotopic-geochemical data. Petrology 21, 351–374.
Larionova, Y.O., Samsonov, A.V., Shatagin, K.N., 2007. Sources of Archean sanukitoids High-Mg subalkaline granitoids in the Karelian craton: Sm-Nd and Rb-Sr isotopic-geochemical evidence. Petrology 15, 530–550.
Laurent, O., Martin, H., Doucelance, R., Moyen, J.F., Paquette, J.L., 2011. Geochemistry and petrogenesis of high-K "sanukitoids" from the Bulai pluton, Central Limpopo Belt, South Africa: implications for geodynamic changes at the Archaean-Proterozoic boundary. Lithos 123, 73–91.
Laurent, O., Martin, H., Moyen, J.F., Doucelance, R., 2014. The diversity and evolution of late-Archean granitoids: evidence for the onset of "modern-style" plate tectonics between 3.0 and 2.5 Ga. Lithos 205, 208–235.
Laurent, O., Zeh, A., 2015. A linear Hf isotope-age array despite different granitoid sources and complex Archean geodynamics: example from the Pietersburg block (South Africa). Earth Planet. Sci. Lett. 430, 326–338.
Le Bas, T.M., Maitre, R.L., Streckeisen, A., Zanettin, B., 1986. A chemical classification of volcanic rocks based on the total alkali-silica diagram. J. Petrol. 27, 745–750.
Liang, Q., Jing, H., Gregoire, D.C., 2000. Determination of trace elements in granites by inductively coupled plasma mass spectrometry. Talanta 51, 507–513.
Lobach-Zhuchenko, S.B., Rollinson, H., Chekulaev, V.P., Savatenkov, V.M., Kovalenko, A.V., Martin, H., Guseva, N.S., Arestova, N.A., 2008. Petrology of a Late Archaean, highly potassic, sanukitoid pluton from the Baltic Shield: insights into Late Archaean mantle metasomatism. J. Petrol. 49, 393–420.
Ludwig, K.R., 2012. User's Manual for Isoplot 3.75: A Geochronological Toolkit for Microsoft Excel. Berkeley Geochronology Center, Speical Publication No. 5.
Ma, X., Guo, J., Liu, F., Qian, Q., Fan, H., 2013. Zircon U-Pb ages, trace elements and Nd–Hf isotopic geochemistry of Guyang sanukitoids and related rocks: implications for the Archean crustal evolution of the Yinshan Block, North China Craton. Precambr. Res. 230, 61–78.
Malviya, V.P., Arima, M., Pati, J.K., Kaneko, Y., 2006. Petrology and geochemistry of

metamorphosed basaltic pillow lava and basaltic komatiite in the Mauranipur area: subduction related volcanism in the Archean Bundelkhand craton, Central India. J. Miner. Petrolo. Sci. 101, 199–217.
Martin, H., Smithies, R.H., Rapp, R., Moyen, J.F., Champion, D., 2005. An overview of adakite, tonalite–trondhjemite–granodiorite TTG, and sanukitoid: relationships and some implications for crustal evolution. Lithos 79, 1–24.
Martin, H., Moyen, J.-F., Rapp, R., 2010. The sanukitoid series: magmatism at the Archean-Proterozoic transition. Trans. Roy. Soc. Edinburgh 100, 15–33.
McDonough, W.F., Sun, S.S., 1995. The composition of the Earth. Chem. Geol. 120, 223–253.
Meert, J.G., Pandit, M.K., Pradhan, V.R., Banks, J., Sirianni, R., Stroud, M., Newstead, B., Gifford, J., 2010. Precambrian crustal evolution of Peninsular India: a 3.0 billion year odyssey. J. Asian Earth Sci. 39, 483–515.
Middlemost, E.A., 1989. Iron oxidation ratios, norms and the classification of volcanic rocks. Chem. Geol. 77, 19–26.
Mohan, M.R., Singh, S.P., Santosh, M., Siddiqui, M.A., Balaram, V., 2012. TTG suite from the Bundelkhand Craton, Central India: geochemistry, petrogenesis and implications for Archean crustal evolution. J. Asian Earth Sci. 58, 38–50.
Mondal, M.E.A., Sharma, K.K., Rahman, A., Goswami, J.N., 1998. Ion microprobe 207 Pb/206 Pb zircon ages for gneiss-granitoid rocks from Bundelkhand massif: evidence for Archaean components. Curr. Sci. 70–75.
Mondal, M.E.A., Goswami, J.N., Deomurari, M.P., Sharma, K.K., 2002. Ion microprobe 207Pb/206Pb ages of zircons from the Bundelkhand massif, northern India: implications for crustal evolution of the Bundelkhand-Aravalli protocontinent. Precambr. Res. 117, 85–100.
Moreno, J.A., Molina, J.F., Montero, P., Anbar, M.A., Scarrow, J.H., Cambeses, A., Bea, F., 2014. Unraveling sources of A-type magmas in juvenile continental crust: constraints from compositionally diverse Ediacaran post-collisional granitoids in the Katerina Ring Complex, southern Sinai, Egypt. Lithos 192, 56–85.
Moreno, J.A., Molina, J.F., Bea, F., Anbar, M.A., Montero, P., 2016. Th-REE-and Nb-Ta-accessory minerals in post-collisional Ediacaran felsic rocks from the Katerina Ring Complex S. Sinai, Egypt: an assessment for the fractionation of Y/Nb, Th/Nb, La/Nb and Ce/Pb in highly evolved A-type granites. Lithos 258, 173–196.
Moreno, J.A., Baldim, M.R., Semprich, J., Oliveira, E.P., Verma, S.K., Teixeira, W., 2017. Geochronological and geochemical evidences for extension-related Neoarchean granitoids in the southern São Francisco Craton, Brazil. Precambr. Res. 294, 322–343.
Moyen, J.F., Martin, H., Jayananda, M., Auvray, B., 2003. Late Archaean granites: a typology based on the Dharwar Craton India. Precambr. Res. 127, 103–123.
Moyen, J.F., Laurent, O., 2018. Archaean tectonic systems: a view from igneous rocks. Lithos 302–303, 99–125.
Naqvi, S.M., Rogers, J.J.W., 1987. Precambrian Geology of India: Oxford Monographs on Geology and Geophysics, no. 6. Oxford University Press, Oxford, pp. 223.
O'Brien, H., Huhma, H., Sorjonen-Ward, P., 1993. Petrogenesis of the late Archean Hattu schist belt, Ilomantsi, eastern Finland: geochemistry and Sr, Nd isotopic composition. Geol. Surv. Finland Sp. Paper 17, 147–184.
Oliveira, M.A., Dall'Agnol, R., Althoff, F.J., da Silva Leite, A.A., 2009. Mesoarchean sanukitoid rocks of the Rio Maria granite-greenstone terrane, Amazonian Craton Brazil. J. S. Am. Earth Sci. 27, 146–160.
Oliveira, M.A., Dall'Agnol, R., Scaillet, B., 2010. Petrological constraints on crystallization conditions of Mesoarchean Sanukitoid Rocks, southeastern Amazonian craton Brazil. J. Petrol. 51, 2121–2148.
Oliveira, M.A., Dall'Agnol, R., de Almeida, J.D.A.C., 2011. Petrology of the Mesoarchean Rio Maria suite and the discrimination of sanukitoid series. Lithos 12, 192–209.
Pandey, U.K., Bhattacharya, D., Sastry, D.V.L.N., Pandey, B.K., 2011. Geochronology Rb-Sr, Sm-Nd and Pb-Pb, isotope geochemisty and evolution of the granites and andesites hosting Mohar Cauldron, Bundelkhand Granite Complex, Shivpuri district, Central India. Explo. Res. Atom. Min. 21, 103–116.
Pati, J.K., Patel, S.C., Pruseth, K.L., Malviya, V.P., Arima, M., Raju, S., Prakash, K., 2007. Geology and geochemistry of giant quartz veins from the Bundelkhand Craton, central India and their implications. J. Earth. Syst. Sci. 116, 497–510.
Paton, C., Woodhead, J.D., Hellstrom, J.C., Hergt, J.M., Greig, A., Maas, R., 2010. Improved laser ablation U-Pb zircon geochronology through robust downhole fractionation correction. Geochem. Geophys. Geosyst. 11.
Prabhakar, B.C., Jayananda, M., Shareef, M., Kano, T., 2009. Synplutonic mafic injections into crystallizing granite pluton from Gurgunta area, northern part of eastern Dharwar Craton: implications for magma chamber processes. J. Geol. Soc. India 74, 171–188.
Pradhan, V.R., Meert, J.G., Pandit, M.K., Kamenov, G., Mondal, M.E.A., 2012. Paleomagnetic and geochronological studies of the mafic dyke swarms of Bundelkhand craton, central India: implications for the tectonic evolution and paleogeographic reconstructions. Precambr. Res. 198, 51–76.
Qian, Q., Hermann, J., 2010. Formation of high-Mg diorites through assimilation of peridotite by monzodiorite magma at crustal depths. J. Petrol. 51, 1381–1416.
Radhakrishna, T., Chandra, R., Srivastava, A.K., Balasubramonian, G., 2013. Central/Eastern Indian Bundelkhand and Bastar cratons in the Palaeoproterozoic supercontinental reconstructions: a palaeomagnetic perspective. Precambr. Res. 226, 91–104.
Ramakrishnan, M., Vaidyanadhan, R., 2010. Geology of India. J. Geol. Soc. India 556.
Rao, J.M., Rao, G.P., Widdowson, M., Kelley, S.P., 2005. Evolution of Proterozoic mafic dyke swarms of the Bundelkhand Granite Massif, central India. Curr. Sci. 502–506.
Rapp, R.P., Norman, M.D., Laporte, D., Yaxley, G.M., Martin, H., Foley, S.F., 2010. Continent formation in the Archean and chemical evolution of the cratonic lithosphere: melt–rock reaction experiments at 3–4 GPa and petrogenesis of Archean Mg-diorites sanukitoids. J. Petrol. 51, 1237–1266.
Saha, L., Pant, N.C., Pati, J.K., Upadhyay, D., Berndt, J., Bhattacharya, A., Satynarayanan, M., 2011. Neoarchean high-pressure margarite–phengitic muscovite–chlorite corona mantled corundum in quartz-free high-Mg, Al phlogopite–chlorite schists from the Bundelkhand craton, north central India. Contrib. Mineral. Petrol. 161, 511–530.
Saha, L., Frei, D., Gerdes, A., Pati, J.K., Sarkar, S., Patole, V., Nasipuri, P., 2016. Crustal geodynamics from the Archaean Bundelkhand Craton, India: constraints from zircon U-Pb–Hf isotope studies. Geol. Mag. 153, 179–192.
Santos, M.N.S., Oliveira, D.C., 2016. Rio Maria granodiorite and associated rocks of Ourilândia do Norte-Carajás province: petrography, geochemistry and implications for sanukitoid petrogenesis. J. S. Am. Earth Sci. 72, 279–301.
Sarkar, A., Paul, D.K., Potts, P.J., 1996. Geochronology and geochemistry of Mid Archaean Trondhjemitic gneisses from Bundelkhand craton, Central India. Recent Res. Geol. 16, 76–92.
Sarvothaman, H., 2001. Archaean high-Mg granitoids of mantle origin in the Eastern Dharwar Craton of Andhra Pradesh. J. Geol. Soc. India 583, 261–268.
Shand, S.J., 1943. Eruptive rocks: their genesis, composition, classification, and their relation to ore deposits with a chaper on meteorites No. 552.1 S43 1943.
Schmidt, M.W., Dardon, A., Chazot, G., Vannucci, R., 2004. The dependence of Nb and Ta rutile–melt partitioning on melt composition and Nb/Ta fractionation during subduction processes. Earth Planet. Sci. Lett. 226, 415–432.
Semprich, J., Moreno, J.A., Oliveira, E.P., 2015. Phase equilibria and trace element modeling of Archean sanukitoid melts. Precambr. Res. 269, 122–138.
Shirey, S.B., Hanson, G.N., 1984. Mantle-derived Archaean monzodiorites and trachyandesites. Nature 310, 222–224.
Singh, V.K., Slabunov, A., 2015a. The central Bundelkhand Archaean greenstone complex, Bundelkhand craton, central India: geology, composition, and geochronology of supracrustal rocks. Int. Geol. Rev. 57, 1349–1364.
Singh, V.K., Slabunov, A., 2015b. Geochemical characteristics of Banded Iron Formation and Metavolcanics of Babina greenstone belt of the Bundelkhand Craton, Central India. J. Econ. Geol. Georesource Manage 10, 63–74.
Singh, V.K., Slabunov, A., 2016. Two types of Archaean supracrustal belts in the Bundelkhand craton, India: geology, geochemistry, age and implication for craton crustal evolution. J. Geol. Soc. India 88, 539–548.
Slabunov, A., Singh, V.K., Kumar, B., Xiaoli, L., 2017a. Paleoarchean zircons from quartzite of South Bundelkhand Supracrustal Complex: origin and implications for crustal evolution in Bundelkhand Craton, Central India. Curr. Sci. 112, 794–801.
Slabunov, A.I., Singh, V.K., Shchiptsov, V.V., Lepekhina E. N., Kevlich V.I., 2017b. A new Paleoproterozoic 1.9–1.8 Ga event in the crustal evolution of the Bundelkhand Craton, India: the results of SHRIMP Dating of zircons from giant quartz veins. In: Slabunov, A.I., Svetov, S.A., Baltibaev, Sh.K. (Eds.), Early Precambrian vs Modern Geodynamics. Extended Abstracts and Field Trips Guide. Petrozavodsk: KarRC RAS, pp. 239–241.
Slabunov, A., Singh, V.K., 2018. Meso-Neoarchean crustal evolution of the Bundelkhand Craton, Indian Shield: new data from greenstone belts. Int. Geol. Rev. https://doi.org/10.1080/00206814.2018.1512906. ID: 1512906.
Smithies, R.H., Champion, D.C., 2000. The Archaean high-Mg diorite suite: links to tonalite–trondhjemite–granodiorite magmatism and implications for early Archaean crustal growth. J. Petrol. 41, 1653–1671.
Stern, R.A., Hanson, G.N., 1991. Archean high-Mg granodiorite: a derivative of light rare earth element-enriched monzodiorite of mantle origin. J. Petrol. 32, 201–238.
Stevenson, R., Henry, P., Gariépy, C., 1999. Assimilation–fractional crystallization origin of Archean sanukitoid suites: western Superior Province, Canada. Precambr. Res. 96, 83–99.
Tanaka, T., Togashi, S., Kamioka, H., Amakawa, H., Kagami, H., Hamamoto, T., Kunimaru, T., 2000. JNdi-1: a neodymium isotopic reference in consistency with LaJolla neodymium. Chem. Geol. 168, 279–281.
Turner, C.C., Meert, J.G., Pandit, M.K., Kamenov, G.D., 2014. A detrital zircon U-Pb and Hf isotopic transect across the Son Valley sector of the Vindhyan Basin, India: implications for basin evolution and paleogeography. Gondwana Res. 26, 348–364.
Vendemiatto, M.A., Enzweiler, J., 2001. Routine control of accuracy in silicate rock analysis by X-ray fluorescence spectrometry. Geostand. Geoanalytical Res. 25, 283–291.
Verma, S.P., Rivera-Gomez, M.A., 2013. Computer programs for the classification and nomenclature of igneous rocks. Episodes 36, 115–124.
Verma, S.K., Pandarinath, K., Verma, S.P., 2012. Statistical evaluation of tectonomagmatic discrimination diagrams for granitic rocks and proposal of new discriminante function based multi-dimensional diagrams for acid rocks. Int. Geol. Rev. 54, 325–347.
Verma, S.P., Pandarinath, K., Verma, S.K., Agrawal, S., 2013. Fifteen new discriminant-function-based multi-dimensional robust diagrams for acid rocks and their application to Precambrian rocks. Lithos 168–169, 113–123.
Verma, S.K., Verma, S.P., Oliveira, E.P., Singh, V.K., Moreno, J.A., 2016. LA-SF-ICP-MS zircon U-Pb geochronology of granitic rocks from the central Bundelkhand greenstone complex, Bundelkhand craton, India. J. Asian Earth Sci. 118, 125–137.
Wang, Y., Zhang, Y., Zhao, G., Fan, W., Xia, X., Zhang, F., Zhang, A., 2009. Zircon U-Pb geochronological and geochemical constraints on the petrogenesis of the Taishan sanukitoids Shandong: implications for Neoarchean subduction in the Eastern Block, North China Craton. Precambr. Res. 174, 273–286.
Watkins, J.M., Clemens, J.D., Treloar, P.J., 2007. Archaean TTGs as sources of younger granitic magmas: melting of sodic metatonalites at 0.6–1.2 GPa. Contrib. Mineral. Petrol. 154, 91–110.
Wiedenbeck, M.A.P.C., Alle, P., Corfu, F., Griffin, W.L., Meier, M., Oberli, F.V., Spiegel, W., 1995. Three natural zircon standards for U-Th-Pb, Lu-Hf, trace element and REE analyses. Geostandards Newslett. 19, 1–23.

CHAPTER 4

Zircon geochronology, geochemistry and petrogenesis of the TTG gneisses and high-K granitoids from the central Bundelkhand granite–greenstone terrane in the Bundelkhand Craton, India: Implications for Archean crustal evolution

A presentation of the submitted research paper

This research manuscript is submitted in *Lithos*, in which the author of this thesis actively participated. I am the first author, and Dr. Sanjeet K. Verma, Prof. Vinod K. Singh, Dr. Juan A. Moreno and Prof. Elson P. Oliveira are the co-authors of the paper.

My Contribution in this research work can be summarized as follows:

1. Field work and sample collection
2. Sample preparation
3. Data acquisitions
4. Data calculation and diagram preparation
5. Data interpretation and write-up of the work

Abstract

The central Bundelkhand granite–greenstone terrane, located in the central part of the Bundelkhand Craton, preserves one of the oldest crustal fragments on the Indian shield and has a complex evolutionary history with multi-stage crustal growth (~3.59–2.50 Ga). The Tonalites-Trondhjemites-Granodiorites (TTGs) gneisses and high-K granitoids are the most voluminous rocks with volcano-sedimentary assemblage in this terrane. To enhance understanding of the crust-mantle evolution, continental generation and reworking throughout the entire Archean, we report field geology, U–Pb zircon geochronology, whole-rock Sm–Nd isotopes and geochemistry on felsic plutonic rocks, including TTG gneisses and high-K granitoids, from this terrane. This study reports ca. 3.51 Ga xenocrystic zircon of TTG gneiss from the Mauranipur, which resemble the earliest felsic crust (3.59–3.55 Ga) in the study area. Two discrete episodes of Neoarchean TTG magmatism (~2.71–2.67 Ga) from the Babina and Mauranipur areas were reported for the first time. This study finds that first major crustal formation events occurred between ~3.41 and 3.20 Ga, which is recorded in TTG gneisses. Further, magmatic zircon ages of the high-K granitoids reveal synchronous emplacement ages from ~2.57–2.50 Ga with xenocrystic zircons in the study area, comprising sanukitoids, granodiorites and anatectic granites. These granitoids commonly represent the last Archean magmatic event with large scale crustal melting appearing to be related to final stabilization of the craton. In addition, this study also identifies a TTG gneiss significantly older than thus far assumed in the eastern part of the study area, which reveals the existence of TTG gneiss ~3.34 Ga around the Charkhari area. Also, but very important, research findings between Paleoarchean TTG emplacements and ultramafic–mafic

volcanism that suggest a coeval felsic plutonism and mafic volcanism occurred at ca. 3.40 Ga in the Babina and Mauranipur terranes. The studied Paleoarchean TTG gneisses contain minor inherited zircons aged ~3.51–3.29 Ga. However, studied Neoarchean TTG gneisses include few inherited zircons of 3.39–2.97 Ga. This inclusion suggests that involvement of ancient crustal rocks in their genesis. Moreover, combined zircon CL images and U–Pb data unravel metamorphic events/overprint at ~3.31–3.10 Ga and 2.64 Ga that may have formed mainly by recrystallization.

Whole-rock geochemistry and Sm–Nd isotopic compositions of Paleoarchean TTG gneisses suggest that they are low-HREE and high-HREE character. The values of εNd(t) ranging from +4.3 to +0.3 (excepting one sample showing –0.5) along with their whole-rock geochemical nature indicate that the low-HREE type TTGs were produced through melting of subducted oceanic arc crust at different depths which probably interacted variably with felsic crustal melts in a stability fields of garnet and ilmenite, probably plagioclase-free source. On the other hand, high-HREE type TTG suggest a likely origin in a plagioclase and garnet-amphibolite at low pressure. Further, a Neoarchean TTG gneiss shows εNd(t) values of +4.5 belonging to the low-HREE group and was formed by the partial melting of deep-seated mafic crust in the garnet stability field with trivial involvement of ancient crustal material.

The juvenile magmatic rocks (sanukitoids) reveal that they were produced by the mingling of mantle melts with crustal generated granitic melt (anatectic melt) and were followed by homogenization at lower levels of intrusion in the subduction setting. The high-K granitoids show $\varepsilon_{Nd}(t)$ ranging from −3.6 to −1.6, containing sanukitoids and anatectic granites. These results also support similar petrogenesis.

Lastly, the amalgamation of diverse micro-blocks occurred by the arc-continent collision and repeated slab break-off between north and south terranes of the BC during late Archean. This event shows evidence that the BC did not merge together until ~2.50 Ga. The voluminous anatectic granites were generated by intensive partial melting of the continental crust in an arc-continent collision, representing the final stabilization of the BC. The Paleo- and Neoarchean crust-mantle evolution, continental growth and reworking processes of the BC are similar to Earth's main Archean geological events.

Key words: Bundelkhand Craton, granite-greenstone terrane, Archean TTG, Granitoids, Zircon geochronology, Sm–Nd isotopes, Geochemistry, Juvenile and reworked crust.

1. Introduction

The Archean era is one of the most significant periods in the formation of the felsic continental crust in the Earth's history (Belousova et al., 2010; Hawkesworth et al., 2010, 2013, 2019; Dhuime et al., 2012; Moyen and Martin, 2012; Laurent et al., 2014; Jayananda et al., 2018). Archean felsic plutonic crust comprises large parts of granitoids that mainly consist of TTG gneiss and high-K granitic rocks all generated between 4.0 and 2.5 Ga (Windley, 1995; Smithies and Champion, 2000; Moyen et al., 2003a, b; Martin et al., 2005; Moyen, 2011; Laurent et al., 2014; Jayananda et al., 2018; Hawkesworth et al., 2019). The occurrence of early felsic plutonic crust is an important clue to understanding the mechanisms of continental growth and emphasizes crustal reworking as a pertinent process of magma genesis. However, the understanding of the formation and evolution of Archean felsic continental crust remains debated (Martin and Moyen, 2002; Kamber, 2015; Spencer et al., 2017; Moyen and Laurent, 2018; Terentiev and Santosh, 2018).

Differentiation of the Archean felsic plutonic crust from mantle, and the subsequent reworking processes of this felsic crust reflect the interaction of thermal and tectonic processes in the evolving earth (Taylor and McLennan, 1995; Zhai., 2014; Tang et al., 2016; Hawkesworth et al., 2019). Accordingly, understanding the changes in composition of "juvenile" magmatic rocks in the continental crust through time is important for advancing insights into petrogenetic processes as well as into the thermal and chemical evolution of mantle. Hypotheses regarding the origin of the Archean felsic plutonic crust include (a) progressive differentiation of mantle-derived magma over a long-lived mantle plume (Smithies, 2000; Smithies and Champion, 2000; Van Kranendonk, 2010), and (b) formation through operational subduction-

collision tectonics (Martin et al., 2005; Condie and Kroner, 2008; Laurent et al., 2014; Dall'Agnol et al., 2017; Singh et al., 2019b). Geochemical and petrological studies of felsic plutonic crust display dramatic changes in their composition of TTG to sanukitoids rocks, and an increased crustal reworking process of the latter (that is, of the TTG and sanukitoids) formed voluminous anatectic granites towards the end of the Archean. This, therefore, suggests a fundamental change in the petrogenetic and geodynamic processes of the crustal growth (Belousova et al., 2010; Condie and O'Neill, 2010; Dhuime et al., 2011; Guitreau et al., 2012; Keller and Schoene, 2012; Laurent et al., 2014; Jayananda et al. 2018; Moyen and Laurent, 2018; Hawkesworth et al., 2019). Further, TTG suites and high-K granitic rocks provide wide windows of time (3500–2500 Ma) thus allowing investigation of the Archean continental growth and differentiation in the Earth's history.

The Bundelkhand Craton (BC) is one of the oldest cratonic blocks situated in the north–central part of the Indian shield. The BC exposes a large section of Archean continental crust that has a diverse evolutionary history (Fig. 1a&b; Mondal et al., 2002; Mohan et al., 2012; Kaur et al., 2014, 2016; Singh and Slabunov, 2015a, b; Verma et al., 2016; Joshi et al., 2017; Singh et al., 2019a, b). The central part of the BC and mainly consists of volcano-sedimentary sequences, TTG gneiss and high-K granitoid rocks called central Bundelkhand granite-greenstone terrane (CBGGT) (Mondal et al., 2002; Kaur et al., 2014, 2016; Singh and Slabunov, 2015a, b; Saha et al., 2016; Verma et al., 2016; Joshi et al., 2017; Singh et al., 2018; Singh et al., 2019a, b).

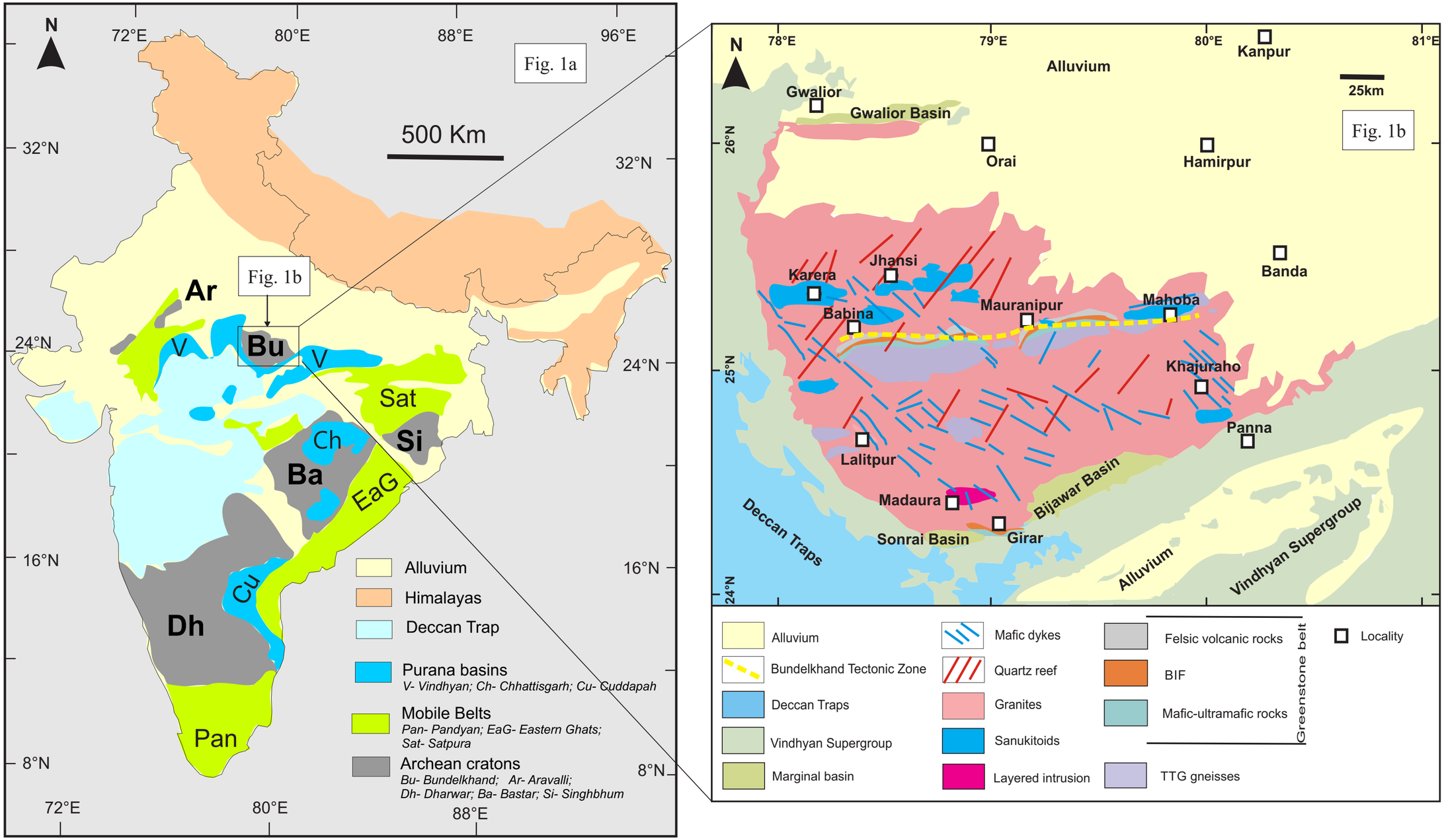

Fig. 1. (a) Schematic geological map of the Indian shield showing major Precambrian cratons and Phanerozoic outcrops (modified after: Ramakrishnan and Vaidyanadhan, 2010; Verma et al., 2016).
(b) Geological outline map of the Bundelkhand Craton (after Basu, 1986; Malviya et al., 2006; Absar et al., 2009; Singh and Slabunov, 2015a; Verma et al., 2016; Joshi et al., 2017).

The CBGGT bears important evidence of crust-mantle coupling in an accretionary setting (Fig. 2; Mondal et al., 2002; Singh and Slabunov, 2015a; Kaur et al., 2016; Saha et al., 2016; Joshi et al., 2017; Singh et al., 2018; Singh et al., 2019a, b), and has attracted wide attention from geoscientists in past decades. However, the Archean continental growth mechanism and tectonic evolution of the CBGGT have not been clearly understood by researchers. Although published research on TTG geochronology have been reported between 3.59 and 3.20 Ga. magmatism in the CBGGT suggest four phases of Paleoarchean TTG magmatism. However, Verma et al. (2016), reported one Neoarchean (~2.67 Ga) TTG rock from the Babina belt. To date, this is the youngest TTG rock in the BC. But as these authors did not provide geochemistry, it is difficult to determine whether it is a TTG *sensu stricto* or a granodiorite gneiss. Therefore, further geochronological and geochemical studies are required for the identification of TTG and for understanding how many TTG magmatic phases occurred in the BC. Additionally, research on high-Mg granitoids (sanukitoids) and their petrogenetic link between high-K anatectic granites is scarce (Joshi et al., 2017; Singh et al., 2019b). Thus, there is a paucity of information of emplacement age and petrogenetic link between these granitoids. The foregoing demonstrates that the CBGGT had a complicated evolutionary history with multi-stage crustal growth, recording nearly all important geological events in the early geotectonic history of the Earth.

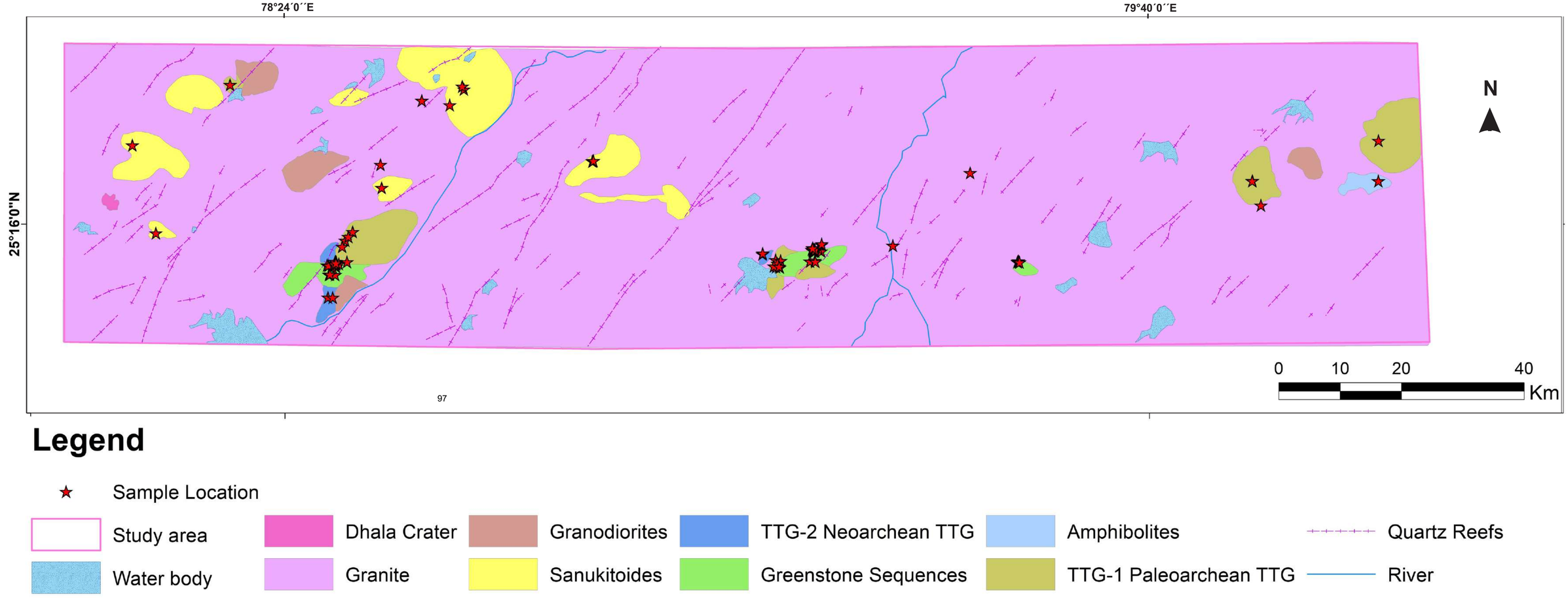

Fig. 2. Geological map of the CBGGT, central part of the BC showing the sample locations.

In this contribution, we report a systematic study for whole-rock major, trace elements and Sm–Nd isotopes, and U–Pb zircon geochronology on TTG gneisses and on the high-K granitoids. Besides, these granitoid samples are representative of all different types of felsic plutonic rocks identified in the CBGGT. The Sm–Nd isotopic data on basement unit TTG gneisses, and high-K granites (anatectic granites) of the CBGGT were never reported thus furthering the lack of understanding about crust-mantle interaction during the generation of granitoids. The main purposes of the study are as follows: (1) to determine the magmatic phases of TTG gneisses and other granitoids; (2) to constrain petrogenesis of TTG gneisses and high-K granitoids; and (3) to discuss the interaction of mantle melts and anatectic melts in magma generation and crustal evolution. Thus, the results of the present research provide insights into crust formation ages, secular changes in granitoid compositions, crustal reworking, cratonization and the Archean crustal evolution of the Bundelkhand Craton.

2. Geological background

The Indian shield has five main cratons; they are composite, consolidated and rigid blocks that evolved during the Archean Eon. The ENE–WSW trending Central Indian Tectonic Zone (Fig. 1a) broadly divides the Indian Shield into two cratonic blocks (see, for example, Acharyya (2003)): the southern cratonic block consisting of Dharwar, Bastar, and Singhbhum cratons, and the northern cratonic block comprising Aravalli and Bundelkhand cratons (Fig. 1a; Naqvi and Rogers, 1987; Yedekar et al., 1990; Ramakrishnan and Vaidyanadhan, 2010; Valdiya, 2010).

The BC is located in the north–central part of the Indian shield and delimited to the west by the Great Boundary Fault, to the northeast by the Indo-Gangetic alluvial plains and to the south and southeast by the Narmada–Son lineament (Ahmad and Tarney, 1994; Ramakrishnan and Vaidyanadhan, 2010). The BC is also bounded by marginal sedimentary basins of the Paleoproterozoic (2.0–1.8 Ga). These are Gwalior (Northwest), Sonrai (South) and Bijawar (Southeast) (Fig. 1b), all of which are homotaxial and characterized by clastic sedimentary rocks at their base and by topmost units composed of carbonates with banded iron formations (BIFs) (Absar et al., 2009). Rocks of the Vindhyan Supergroup (Mesoproterozoic: 1.1–1.0 Ga) overlay these marginal basins (Meert et al., 2010; Turner et al., 2014). The northern side of the craton is covered by Gangetic alluvial plains (Fig. 1b; Manglik et al., 2015).

The BC is a composite mosaic of Archean crustal nuclei, exposed in semicircular shape, occupying about 26,000 sq. km, and mainly comprising TTG gneisses, volcanic-sedimentary greenstone sequences and voluminous high-K granitoids (granodiorites, sanukitoids and anatectic granites) (Mondal et al., 2002; Kaur et al., 2014, 2016; Singh and Slabunov, 2015a, b; Joshi et al., 2017; Singh et al., 2018; Singh et al., 2019a, b). The BC was formed largely in the Paleo- to Neoarchean with multi-stage crustal growth (Figs. 1a and 2; Basu, 1986; Mondal et al., 2002; Malviya et al., 2006; Kaur et al., 2014, 2016; Singh and Slabunov, 2015a, 2016; Saha et al., 2016; Verma et al., 2016; Joshi et al., 2017; Slabunov et al., 2017a; Nasipuri et al., 2019; Singh et al., 2019a, b). The TTG gneisses are the most widespread basement lithology spatially associated with supracrustals (greenstone belts), exposed mainly in central part of the Craton. They are polyphase deformed and sporadic

occurrences in linear E–W trending belt in central part, whereas patchy basement outcrop around Rungaon area in the southern part of the BC (Mondal et al., 2002; Kaur et al., 2014, 2016; Saha et al., 2016; Joshi et al., 2017; Nasipuri et al., 2019). This basement rock is distinguished from undeformed later episode high-K granitoids except for the some granitoids that locally show shear zone. TTGs comprise the oldest rocks in the BC, and reported geochronological data show four distinct episodes of TTG magmatism of Paleoarchean (3.59–3.20 Ga) (Mondal et al., 2002; Kaur et al., 2014, 2016; Saha et al., 2016; Joshi et al., 2017) and one Neoarchean (~2.67 Ga) TTG plutons reported from the Babina belt (Verma et al., 2016).

The BC has two distinct Archean granite–greenstone terranes: (i) the central Bundelkhand granite–greenstone terrane (CBGGT) and (ii) the southern Bundelkhand granite–greenstone terrane (SBGGT), have been recognized based on detailed field and stratigraphic relationships in the craton (Malviya et al., 2006; Singh and Slabunov, 2015a, b, 2016; Slabunov et al., 2017a; Singh et al., 2018; Singh et al., 2019a). The SBGGT located in the southern part of the craton. It occurs around Rungaon and Girar areas, comprises mostly thick metasedimentary units (variety of quartzite and BIF) and ultramafic–mafic volcanic rocks (Farooqui and Singh, 2006; Singh and Slabunov, 2016; Slabunov et al., 2017a). Recently, Slabunov et al. (2017a) reported detrital zircons from the quartzite that yield 3.4–3.3 Ga age, which indicates the existence of an Archean crustal block. The layered igneous complex outcrops also occur around Madawara–Ikauna and Lalitpur areas in the SBGGT of the BC. It is considered that layered igneous complexes (*age?*) are older than the high-K granitoids of the BC on basis of field relationships (Figs. 1a; Farooqui and Singh, 2006; Satyanarayanan et al., 2014; Slabunov et al., 2017a,

2018; Mohanty et al., 2018; Ramiz et al., 2018; Slabunov and Singh, 2019;). The Madawara–Ikauna layered ultramafic–mafic complex comprises two types of lithostratigraphic unit: (i) undeformed ultramafic-mafic plutonic rocks (gabbro, harzburgite, lherzolite, and olivine websterite) and (ii) high-Mg ultrabasic–basic rocks (serpentinites, schists and spinel-bearing schists). The former one has experienced low-grade metamorphism (Farooqui and Singh, 2006; Satyanarayanan et al., 2014; Mohanty et al., 2018; Ramiz et al., 2018; Slabunov et al., 2018; Slabunov and Singh, 2019). Detailed Petrological and mineralogical studies suggest that high-Mg ultrabasic/basic rocks are generated the partial melting of metasomatized mantle at shallow depth, whereas the undeformed ultramafic–mafic plutonic rocks were originated as a consequence of asthenospheric upwelling from a greater depth that induced the melting in the overlying lithosphere (Mohanty et al., 2018; Ramiz et al., 2018; Slabunov et al., 2018; Slabunov and Singh, 2019).

The CBGGT is mostly comprised of Archean TTG gneisses, volcano-sedimentary sequences, sanukitoids, granodiorites, anatectic granites, which are intruded by quartz reefs and mafic dykes during Paleoproterozoic (Fig. 2) (Mondal et al., 1998, 2002; Malviya et al., 2006; Kaur et al., 2014, 2016; Singh and Slabunov, 2015a, b; 2016; Verma et al., 2016; Joshi et al., 2017; Singh et al., 2019a, b). The outcrops of the CBGGT terrane exposes in the central part of the BC, which ranges from the Mahoba to Jhansi, passing through Mauranipur and Babina, covering a horizontal length of approximately 200 km (Malviya et al., 2006; Singh and Slabunov, 2015a, 2016; Verma et al., 2016; Singh et al., 2018; Singh et al., 2019a, b). The TTG oldest gneisses are exposed as basement rock around Mauranipur and Babina areas. The previous studies conclude four discrete episodes of the TTG magmatism at ~3.59–

3.51 Ga, 3.44–3.39 Ga, 3.36–3.30, Ga 3.28–3.20 Ga (Mondal et al., 2002; Kaur et al., 2014, 2016; Saha et al., 2016; Joshi et al., 2017; Nasipuri et al., 2019). Additionally, a new phase TTG magmatism reported at 2.67 Ga from Babina belt by Verma et al. (2016) which is youngest TTG phase in the BC. The volcano-sedimentary sequences comprise mainly ultramafic–mafic volcanics, BIFs and felsic volcanics. Recently, Singh et al. (2019a) dated ~3.44 Ga ultramafic–mafic volcanic rocks from Babina and Mauranipur belts which suggest Paleoarchean age for ultramafic–mafic volcanism in the CBGGT. This volcanism age could probably be syn- to post of the basement rock (~3.55–3.20 Ga). Further, these authors also proposed that the ultramafic–mafic rocks were originated in subduction environment with depleted mantle composition. Whereas, Slabunov and Singh (2015) and Slabunov and Singh (2019) have reported felsic volcanic rock ages in Babina (~2.54 Ga) and Mauranipur (2.81 Ga and 2.56 Ga) respectively. A comparable rhyolite age (2.52 Ga) reported by Mondal et al. (2002) from Bansi south of the Babina belt. To date, there is no BIFs age reporting from the BC whereas field relationship suggest that they are older than felsic volcanics and younger than ultramafic–mafic rocks. On the other hand, scarce research metamorphic history of this terrane. Saha et al. (2011) provide an insight on metamorphism and suggest that a high-pressure metamorphism at ~2.78 Ga documented in a corundum-bearing white schist from the Babina belt.

The voluminous undeformed plutons of the high-K granitoid (granodiorites, sanukitoids, anatectic granites) rocks are occupied largest part of the CBGGT in the BC and intruded in the TTG-greenstone assemblage during Neoarchean (2.58–2.50 Ga) (Figs. 1b and 2; Mondal et al., 2002; Kaur et al., 2016; Saha et al., 2016; Joshi

et al., 2017; Singh et al., 2019b). They locally display intrusive relationship with TTG gneisses and/or greenstone sequences. Most high-K granitoids plutons are undeformed to weakly foliated, but some of them show a moderate to well-developed foliation (Fig. 3c and o in Singh et al., 2019b). The entire craton is dissected by E–W, NE–SW, NW–SE, and N–S trending shear fractures/joints. These granitoids show multiple episodes of magmatism and crustal reworking in the subduction related setting mostly during Neoarchean (2.58–2.50 Ga) throughout craton. Recently, Joshi et al. (2017) and Singh et al. (2019b) published research on sanukitoids (high-Mg granitoids) and suggest synchronous emplacement with anatectic granites (2.57–2.50 Ga). Singh et al., (2019b) proposed that they were formed by the mixing of mantle melts with anatectic melt (crustal generated granitic melt) and were followed by homogenization at lower levels of emplacement in the subduction environment. On the other hand, anatectic granitic plutons suggest that they were originated by the reworking (partial melting) of earlier continental crust and were enormously emplaced during the collision of distinct blocks. This conform that they cratonization of the BC happened at ca. 2.5 Ga (Mondal et al., 2002; Kaur et al., 2016; Joshi et al., 2017; Singh et al., 2019b). Additionally, mafic magmatic enclaves recognized in the high-K granitoids, which also suggesting mantle involvement in the formation of high-K granitic plutons especially high-Mg granitoids in the BC (Mondal and Zainuddin, 1995, 1996; Joshi et al. 2017; Ramiz and Mondal, 2017; Singh et al., 2019b).

The mafic dyke warms and giant quartz reefs are important post-Archean magmatic events in the BC, which are emplaced into the granite–greenstone terrane which make complexities to determine field relations (Pati et al. 1997, 2007; Mondal and

Ahmad 2001; Rao et al., 2005; Pradhan et al., 2012; Radhakrishna et al., 2013; Slabunov et al., 2017a). The mafic dyke swarms show variable orientations. In general, mafic dykes and quartz reef are more commonly aligned along NW–SE and NE–SW directions, respectively.

Table 1. Sample locations, description and summary of U-Pb zircon results obtained from TTG gneisses and high-K granitoids in the CBGGT. ([c]Concordia age; [#]upper intercept age).

Sample no.	Rock type	Locality and GPS co-ordinates	Field geology: lithology description and stratigraphic unit	Crystallization age (Ma)
BC.16	TTG gneiss	Baragaon village 79°10'10"E 25°12'44"N	TTG sample coarse grained, heterogeneous comprising of alternating quartzo-felspathic and mafic bands (typical gneissic banding). Occur as basement unit and emplaced by quartz reef (NNE–SSW preferred orientation) which demarcates the boundary between TTG and greenstone sequences located 1 Km south of Baragaon village.	3410.5 ± 9.1[c]
BC.19	TTG gneiss	Roni village 79°07'35"E 25°12'48"N	TTG gneiss outcrop show E–W trend and exposure occur in low laying area in front of Indian oil petrol pump (before Roni circle: Mauranipur–Jatara road); light grey, strongly deformed, medium- to coarse-grained TTG gneiss, sharp contact with mafic unit of Mauranipur terrane. TTG gneiss exposure displays intrusion of pink/grey granites. This exposure has similar trend of sample BC.16 and continuous, but sporadic exposures.	3343 ± 85[#]
BC.41	TTG gneiss	Roni village 79°07'11"E 25°12'14"N	The sample outcrop situated eastern side of the Mauranipur–Jatara road and intruded by anatectic granites and sanukitoids and locally emplaced by pegmatite veins and display sings of later deformation. Sample generally whitish to deep grey in color, leucocratic to mesocratic, medium- to coarse-grained and gneissic appearance.	3391 ± 39[c]
BC.45	TTG gneiss	Roni village 79°07'31"E 25°12'12"N	Strongly deformed, light grey, coarse-grained gneissic TTG is exposed in the eastern side of the Mauranipur–Jatara road near Roni village, Mauranipur. At places the TTG gneiss shows alternate light and dark (biotite-rich) magmatic bands. Sharp contact with fine grained anatectic granite observed.	3364.2 ± 9.9[c]
BC.60	TTG gneiss	Charkhari, Mahoba 79°49'03"E 25°19'48"N	This sample show gneissic layering which consist of alternate quartzo-feldspathic and mafic bands that are folded. TTG gneiss outcrop intruded by anatectic granites, collected southern side of the Muskara–Mahoba–Charkhari road (about 10 km before Charkhari city). Highly deformed, medium- to coarse-grained and grey to light pink in color. They consist of alternate quartzo feldspathic and mafic bands that are folded.	3278 ± 20[#]
BC.61	TTG gneiss	Charkhari, Mahoba 79°49'04.7"E 25°19'48.9"N	Amphibolite-banded TTG from the Charkhari, Mahoba, typically polyphased highly deformed and metamorphosed outcrop. Heterogeneous bodies consisting biotite rich and quartzo-feldspathic bands. This outcrop exposed as basement rock in the eastern side of the Bundelkhand Craton. Tectonic interlayering of older (3.34 Ga; dark grey) and younger (3.27 Ga; light grey) TTG gneisses in a high-strain zone of the CBGGT terrane.	3346.3 ± 10[c]
BC.27	TTG gneiss	Babina 78°27'42"E 25°12'23"N	Weakly deformed and compositional banding of trondhjemitic to granodioritic TTG gneiss outcrop. TTG gneiss show weakly foliated, light grey to whitish in color, medium- to coarse-grained and occur sporadic exposures in Babina granite-greenstone terrane. TTG gneiss display parallel alignment of elongated mafic mineral-rich streaks.	2669 ± 11[c]
BC.31	TTG gneiss	Babina 78°27'52"E 25°11'34"N	Sample medium- to coarse-grained and shows strong gneissic fabric including of alternating quartzo-felspathic and mafic bands and locally intruded by pegmatite. High-strain zone observed and revealed by tectonic interlayering of dark grey and light grey at gneissic TTG outcrop in the Babina terrane.	2706.3 ± 11[c]

Table 1 Continue.

BC.50	TTG gneiss	Kuraicha, Mauranipur 79°05'59"E 25°13'22"N	Sample BC.50 from Kuraicha, Mauranipur belt are exposed in abundance along the Saprar river section and around Kuraicha village. They show medium gneissic banding to massive structures, grayish medium- to fine-grained, and having sharp contact with anatectic granites. They intrude into and are co-folded with mafic-ultamafic units and banded iron formation in the Mauranipur belt.	2712 ± 16[#]
BC.23	High-K granitoids	Babina 78°29'57"E 25°15'20"N	Granodiorite strongly sheared and occur in ductile shear zone near BHEL plant, east side of the highway, and coarse grained, gray to light gray in color, moderate to crude foliated and locally contain mafic minerals in patches and locally emplaced by pegmatite and quartz veins, mainly intrusive into TTG and/ or greenstone belts, showing sharp contact with these rocks.	2556 ± 23[#]
BC.33	High-K granitoids	Baghora, Babina 78°28'12"E 25°09'33"N	Massive high-K anatectic granites exposed around the Baghora village, Babina terrane and are light colored, medium- to fine-grained rocks showing weak deformation and locally containing xenoliths of TTG and granodiorites. High-K anatectic granites crop out 80 part of the Babina terrane.	2557 ± 16[#]
BC.35	High-K granitoids	Jhansi 78°39'35"E 25°28'07"N	Large sanukitoids outcrop from the Kochhabhanwar, Jhansi terrane vastly intruded by anatectic granites. Fabric intensity beads off away from the enclave margin and is absent in the body of the host granites, suggesting a synmagmatic origin of sanukitoids and anatectic granites.	2568 ± 12[c]

The mafic dyke warms are nonfoliated and cross-cut the TTG–greenstone assemblage and high-K granitoids (Pradhan et al., 2012). Rao et al. (2005) and Pradhan et al. (2012) recommended that two episodes of mafic magmatic (NW–SE trending ~2.0 Ga and NE–SW oriented ca. 1.10 Ga.) occurred in the BC. The giant quartz reefs were intruded at ca. 1.9–1.8 Ga (Pati et al., 2007; Slabunov et al., 2017b). They have preferred NE–SW and N–S alignment and emplaced into the TTG–greenstone assemblage and high-K granitoids. Researchers suggest that they were formed in the tectonically controlled hydrothermal activity along vertical to subvertical shear zones that generated in reaction to extensional tectonics (Pati et al., 2007; Slabunov et al., 2017b).

3. Sample description and petrography

This study investigated 9 TTG gneisses and 3 high-K granitoids from the CBGGT (Fig. 2). Sample locality and field characteristics are summarized in Table 1, and field occurrences shown in the figure 3a–l and microscopic features in the figure.

4a–h. All the studied samples that are representative of all different types of felsic plutonic rocks identified in the CBGGT. The studied samples are classified and described in three groups: Paleo- and Neoarchean TTG gneisses and high-K granitoids (Fig. 3a–l and Table 1).

3.1. Paleoarchean TTG gneiss

In this study, six samples were collected from the CBGGT, including four samples from Mauranipur (BC.16, BC.19, BC.41 and BC.45) and two samples Charkhari (BC.60 and BC.61) (Table 1). Paleoarchean TTG gneisses represent basement unit and occur around the Mauranipur, Baragaon, Roni and Charkhari (Fig. 2 and Fig. 3a–f). They are generally whitish to greyish in color varying generally between leucocratic to mesocratic, medium- to coarse-grained and locally show banded structures. Baragaon TTG pluton (BC.16; Fig. 3a) provided a basement for greenstone sequences and intruded by quartz reef. The field relationship suggests that TTG and ultramafic–mafic volcanic rocks were sub-contemporaneous ~3.44 Ga (Singh et al., 2019a). Similarly, Sample BC.19 outcrop has sharp contact with mafic rocks, and it show E–W trend long exposure of similar lithology from Baragaon village to Roni village, about 3 km (Fig. 3b). The south of the BC.19 sample location, there is large TTG plutons and show sharp contact with anatectic granites whereas grey granite plutons also observed (Fig. 3c–d). At places, high-K granitoids are intrusive in the Paleoarchean TTG gneisses, and having sharp contact (Fig. 3c–d). The eastern part of the CBGGT also has TTG plutons around Charkhari area which show multiple phase deformation and metamorphism (Fig. 3e–f). They are mainly tonalitic type TTG gneiss and showing 2–5 cm wide paleosome and neosome banding at outcrop (Fig. 3f).


a
Quartz reef
TTG outcrop
Baragaon greenstone belt exposures
BC.16
Paleoarchean TTG
b
High-K granitoids
BIF's exposures
Mafic rock exposures
BC.19
Paleoarchean TTG
c
BC.41
Paleoarchean TTG
d
Grey granitoids
High-K anatectic granites
BC.45
Paleoarchean TTG
e
Paleoarchean TTG
BC.60
f
Paleoarchean TTG
107
BC.61
g
Neoarchean TTG
BC.27
h
Neoarchean TTG
BC.31
ii
Neoarchean TTG
BC.50
j
high-K granitoids
BC.23
k
high-K granitoids
BC.35
l
high-K granitoids
BC.33

Fig. 3.

Fig. 3. Demonstrative field photos of the TTG gneisses and high-K granitoids of the CBGGT. (a) Paleoarchean TTG gneiss from Baragaon belt and comprising of alternating quartzo-felspathic and mafic bands (typical gneissic banding) (length of the pen 14 cm). (b) Contact between TTG gneiss and mafic rocks of the Mauranipur belt near the Roni village. (c) and (d) Highly deformed Paleoarchean TTG gneiss outcrop located eastern side of the Mauranipur–Jatara road and intruded by anatectic granites as well as locally emplaced by pegmatite veins (pen is 14-cm long). (e) Outcrop show gneissic layering which consist of alternate light and dark bands that are folded, collected the Charkhari area in the eastern part of the CBGGT. (f) Polyphase deformed Paleoarchean TTG gneiss outcrop near to the Charkhari and shows alternate light and dark (biotite-rich) magmatic bands. About 10 km before Charkhari city (length of the pen 14 cm). (g) Outcrop and close-up view of the Babina Neoarchean TTG gneiss and display feebly deformation. Gneissic banding displays parallel alignment of elongated mafic mineral-rich streaks. (h) Strongly deformed banded TTG gneiss and show alternate banding of quartzo-felspathic and mafic bands as well as intruded by pegmatite in the Babina belt. (i) Deformed TTG gneiss outcrop from Kuraicha area in the Mauranipur belt and show medium gneissic banding to massive structures. It shows sharp contact with anatectic granites (length of the pen 13 cm). (j) Outcrop of the Babina granodiorite with deformed structure showing mafic minerals in patches and locally pegmatite and quartz veins. (k) Massive outcrop of anatectic granite from the Baghora village in the Babina belt. (l) Sanukitoids outcrop highly intruded by anatectic granite in the Jhansi terrain (length of the hammer 70 cm).

These samples contain the main minerals that are plagioclase, quartz, hornblende, biotite, and K-feldspar (Fig. 4a–d), whereas some samples have abundant biotite mineral (Fig. 4d). Plagioclase is generally anhedral to subhedral in shape with multiple (polysynthetic) twinning. Furthermore, the antiperthite lamellae are also common, and some plagioclase crystals are partially altered to sericite. Microcline exhibits characteristic cross-hatched twinning. Ilmenite, titanite, zircon and apatite are accessory minerals (Fig. 4a–d).

3.2. Neoarchean TTG gneiss

Two Neoarchean TTG samples from Babina and one sample from Kuraicha, Mauranipur were collected (Fig. 2). These TTG gneisses show medium- to coarse-grained granoblastic textures and locally intruded by pegmatite and quartz vein (Fig. 3g–i). Sample BC.31 shows strong gneissic fabric (Fig. 3h), the sample BC.27 has weak gneissic bands and generally display massive structures (Fig. 3g). Similarly, sample BC.50 in the Mauranipur belt shows medium gneissic banding to massive structures, and having sharp contact with anatectic granites (Fig. 3i).

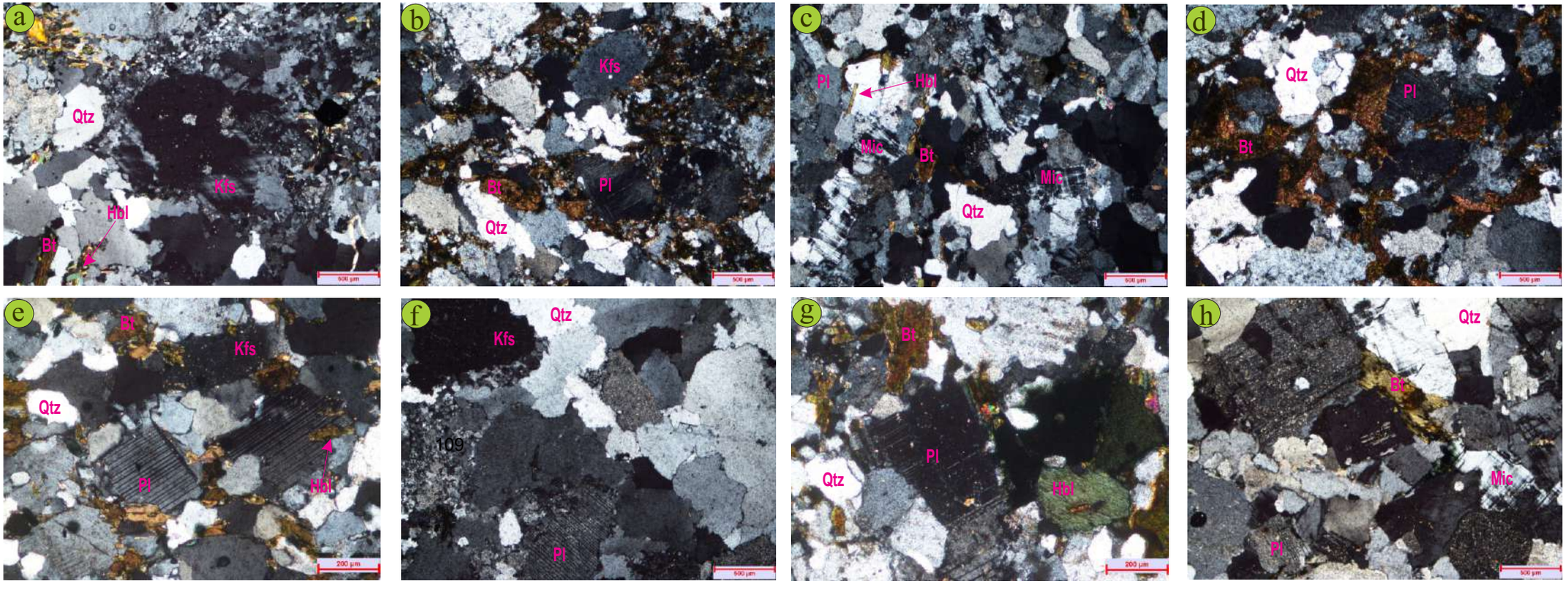

Fig. 4. Representative photomicrographs of mineral assemblages: (a–d) Paleoarchean TTG gneisses are comprise the minerals that are plagioclase, quartz, hornblende, biotite, and K-feldspar; (e–f) Neoarchean TTG gneisses are contained primarily of plagioclase, quartz, hornblende, biotite, and K-feldspar, and plagioclase are altered into sericite and (g–h) high-K granites include K-feldspar, bimodal quartz, minor plagioclase, hornblende and biotite and zircon, titanite and apatite in accessory minerals. *Abbreviations:* Qtz-quartz, Pl-plagioclase, Hbl-hornblenbe, Ms-muscovite, Kfs-K-feldspar and Bt-biotite. All photomicrographs with crossed nicols

These TTG gneisses are composed primarily of plagioclase, quartz, hornblende, biotite, and K-feldspar (Fig. 4e–f). Plagioclase are altered into sericite (Fig. 4f). These gneisses carry accessory minerals of zircon, apatite, titanite, allanite, and magnetite.

3.3. High-K granitoids

High-K granitoids are well exposed throughout BC. Three samples were collected from around Babina (BC.23), Baghora (BC.33) in the CBGGT whereas sample BC.35 from the Jhansi area (Fig. 2). They are intrusive into TTG-greenstone belts, showing sharp contact with these rocks. These granitoids are coarse-grained, gray to light gray in color, moderate to crude foliated and locally containing mafic minerals in patches (Fig. 3j–l). They are locally emplaced by pegmatite and quartz vein (Fig. 3k). Common mineral assemblages include K-feldspar, quartz, minor plagioclase, hornblende and biotite in the high-K granitoids. Accessory minerals represented by zircon, titanite and apatite (Fig. 4g–h). K-feldspar phenocrysts belong to microcline with cross-hatched (“tartan”) multiple twinning and perthite (exsolution texture), with pervasive secondary sericite generated by deuteric alteration (Fig. 4h). Biotite presents numerous radiogenic haloes, probably of zircon inclusion.

4. Analytical techniques

4.1. Zircon CL imaging and LA–ICP–MS U–Pb dating

Twelve samples were selected for zircon U–Pb dating (Table 1). Approximately 6 kg of each of the 12 samples were treated for zircon separation using conventional jaw crusher, milling, panning, magnetic separation and heavy liquids methods. The zircons were hand-picked, were selected, according to size, color, and shape under

a binocular microscope and mounted on 25 mm epoxy mounts. The final process consisted in the polish of their surfaces. In order to observe the morphological features and recognize the zonation patterns in the zircon grains and to have a guide for the geochronological analysis, backscattered electron (BSE) and cathodoluminescence (CL) images of individual representative grains were obtained for this study. The zircon separation and imaging were done at the Institute of Geosciences, University of Campinas (IG-UNICAMP), SP, Brazil.

Zircon U–Pb isotopic analysis were performed using an LA–ICP–MS Element XR (Thermo Scientific) at the IG-UNICAMP, Brazil. U–Th–Pb ratios and absolute abundances were determined relative to the standard zircon 91,500 (Wiedenbeck et al., 1995). Obtained data were reduced off-line using *Iolite software (version 2.5)* subsequent the method described by Paton et al. (2010). The Peixe zircon standard (ID–TIMS age of 564 ± 4 Ma; cf. Dickinson and Gehrels, 2003) was used to monitor the quality of the reduction procedures (further details are given in Moreno et al., 2017). All data are reported with 2 sigma uncertainties. The LA–ICP–MS data were used for ages calculation and plotting on Concordia diagrams using the software *ISOPLOT 3.75* (Ludwig, 2012).

4.2. Whole-rock elements

Twelve rock samples were analyzed for the whole rock geochemistry. Major oxides and selected trace elements were analyzed using X-ray fluorescence spectrometer (XRF). For this procedure, 1.2 g-powdered sample were mixed with 6 g lithium borate flux (consisting of 35.3% tetraborate and 64.7% metaborate). Further, the fusion bead method was used to prepare the glass bead at 1000 °C for ≈8 min in Pt–Au crucible for only major elements analyses. For selected trace element

analyses, 9 g of sample was pressed into a pellet using 1.2 g Wax binding agent. Both, glass bead and pressed pellet were analyzed at the IG-UNICAMP, Brazil. The analytical precision for major oxides and trace elements, based on certified standards (W-2 and BHVO for major elements, and RGM-1 and WSE for trace elements), and accuracy was considered less than 5% for major oxides and up to 10% for trace elements (Vendemiatto and Enzweiler, 2001). Fe-oxidation adjustment followed the procedure of Middlemost (1989) on an anhydrous basis to 100%. This was easily achieved using the computer program, *IgRoCS_M1* (Verma and Rivera-Gómez, 2013).

The remaining rare earth and other trace elements were analyzed on a quadrupole Thermo (Xseries2) ICP-MS at the IG-UNICAMP, Brazil (Liang et al., 2000). Cotta and Enzweiler (2009) described details of the instrument and sample preparation. The standards used for this work, were BRP-1, RGM-1 and GSP-2, with a 10% standard deviation.

4.3. TIMS Sm–Nd isotope bulk-rock analyses

Seven samples were selected for Sm–Nd isotopic analyses. Sm–Nd isotopic ratios were determined at the Centro de Geocronología y Geoquímica Isotópica from the Universidad Complutense de Madrid, Spain using thermal ionization mass spectrometry (TIMS-Phoenix®). These analyses were performed in whole-rock powders using a ^{150}Nd-^{149}Sm tracer by Isotope Dilution-TIMS (for detail see Singh et al., 2019a, b).

5. Results

5.1. Zircon CL images and U–Th–Pb systematics

Twelve representative TTG gneiss and high-K granitoid samples were chosen for *in situ* zircon U–Pb dating (see Table 1). The CL and BSE images of representative zircons are shown in Fig. 5a–l. The analytical results for the zircon U–Th–Pb isotopes and calculated ages are provided in the online Supplementary Table S1, and zircon Pb–Pb Concordia plotted in Figs. 6a–f and 7a–f. The combined CL images and the U–Pb data were used to discriminate different zircon growth and/or metamorphic events. As presented in CL images (Fig. 5a–l), many grains display typical oscillatory or linear magmatic zoning patterns. However, sample grains show complex core-rim zoning. A number of inherited/xenocrystic zircon grains were identified. Generally, samples can be classified in three groups: Paleoarchean TTG gneiss, Neoarchean TTG gneiss and high-K granitoids.

5.1.1. Paleoarchean TTG gneiss

The sample, **BC.16**, was collected from the Baragaon village, Mauranipur (Table 1). This sample contains magmatic zircon grains. They are pink, euhedral, prismatic to stubby, and simple oscillatory zoning is common. No inherited cores were observed (Fig. 5a). Thirteen spot analyses on thirty-one zircons show U (94–662 ppm) and Th (38–863 ppm) with Th/U in the range of 0.22–2.06 (Table S1). Two zircon spot analyses yield a Concordia age of 3410 ± 9.1 Ma (MSWD = 0.21) (Fig. 6a). This age is identical, within error, to the Sm-Nd isochron ages 3435 ± 160 Ma ultramafic–mafic unit of Baragaon belt (Singh et al., 2019a). The **BC.19** sample was taken from Roni village (west of BC.16 sample location). The sample comprises magmatic and inherited zircons (Fig. 5b). Fourteen spot analyses on twelve grains show variable U

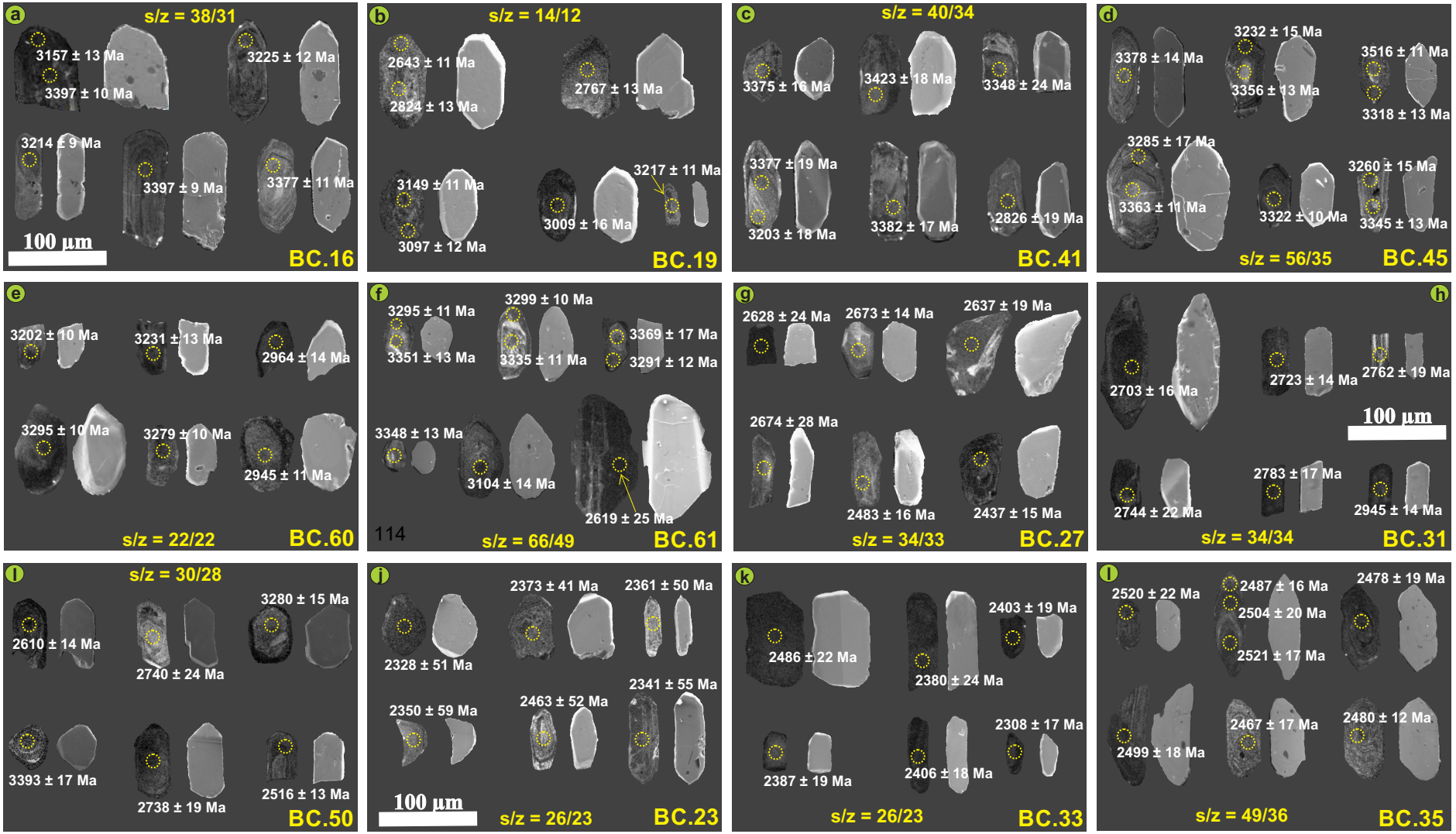

Fig. 5. Representative CL and BSE images of zircons for TTG gneisses and high-K granitoids of the CBGGT. Yellow doted circles (25µm) indicate position of laser spots. s/z; s: number of spot analyses per samples; z: number of zircon gains analyzed per sample.

(mostly 308–1021 ppm) and Th (30–560 ppm) with Th/U ranging from 0.14 to 1.66. The analyses are highly discordant and suggest lead loss (Table S1). Six discordant analyses yield an upper intercept age of 3343 ± 85 Ma (MSWD = 7.8) (Fig. 6b).

The zircon grains of the **BC.41** sample are magmatic and mostly long-prismatic and euhedral to subhedral in nature. A few elongated prismatic zircon grains exhibit broad-banded zoning and one grain displays a convoluted zone (Fig. 5c), suggesting a magmatic origin (Corfu et al., 2003). A total of 40 U–Pb isotopic spot analyses were performed on 34 zircon grains and show variable U (mostly 92–317 ppm) and Th (13–358 ppm) with Th/U ranging from 0.14 to 1.49, which are typical of magmatic zircons (Table S1). Ten spot analyses yield an upper intercept of 3422 ± 39 Ma, and two concordant grains give a Concordia age of 3391 ± 39 Ma (MSWD = 9.6) (Fig. 6c). One concordant zircon core reveals an older age of 3425 ± 16 Ma (Fig. 5c). One zircon grain reveals the youngest apparent $^{207}Pb/^{206}Pb$ age of 2826 ± 19 Ma (Fig. 5c). The zircon grains from the sample, **BC.45**, are euhedral and prismatic and the majority of grains are transparent and light rose in color. As shown in Fig. 5d, simple internal oscillatory zoning is common, and inherited cores were observed. Fifty-six U–Pb analyses on 35 zircon grains were performed (Table S1). Most of the spot analyses show U (106–325 ppm) and Th (59–365 ppm) with Th/U in the range of 0.28–1.26, thus reflecting their magmatic origin (Table S1). Some of the measuring spots reveal relatively high Th and U concentrations. These phenomena may be attributed to later tectothermal events. Three concordant analyses yield a Concordia age of 3364.2 ± 9.9 Ma (Fig. 6d) while the upper intercept age of 3389.6 ± 9.7 Ma (MSWD = 5.5; n = 49) (Fig. 6d). Two zircon grains show core ages of 3356 ± 13 Ma and 3363 ± 11 Ma with rims of younger ages of 3232 ± 15 Ma and 3285 ± 17 Ma,

respectively (Fig. 5d). These younger ages may represent metamorphic events. One xenocrystic zircon grain reveals a concordant age of 3515 ± 11 Ma in core with a rim that shows 3318 ± 13 Ma (Fig. 5d).

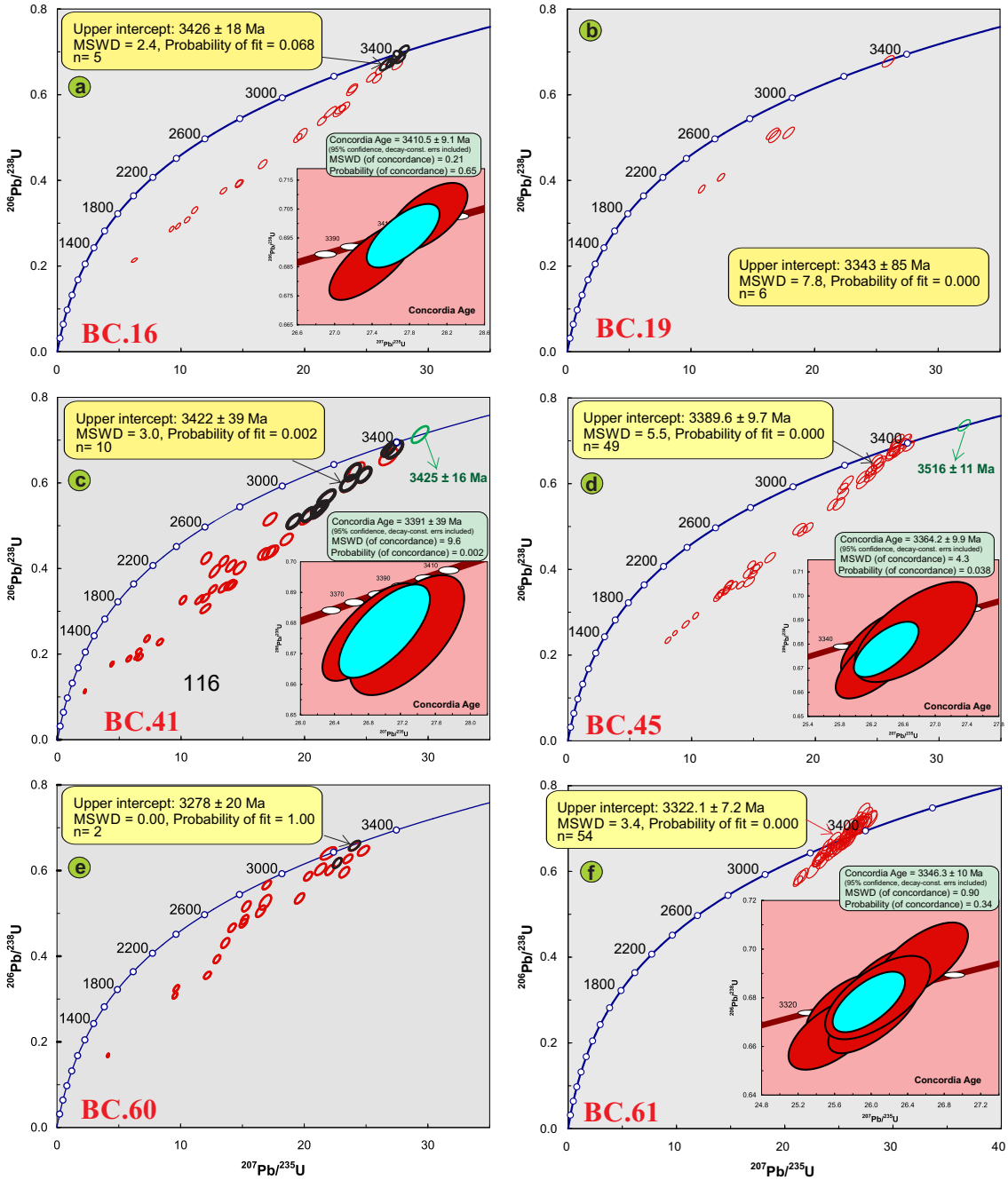

Fig. 6(a–f). Zircon U–Pb Concordia diagrams for TTG gneisses from the CBGGT.

The zircons in the sample, **BC.60**, are colorless, transparent, and mainly subhedral to euhedral and prismatic in form (Fig. 5e). Nearly all grains show a typical magmatic nature, and have high content of U (61–655 ppm) and Th (26–266 ppm) with high Th/U ratios of 0.13–1.03, except two grains that show low Th/U ratios of 0.01(Table S1). The U–Pb data are sub-concordant to variably discordant, indicating lead loss from the zircon grains (Fig. 6e). Two analyses define an upper intercept age of 3278 ± 20 Ma (MSWD = 0.00) (Fig. 6e). Two concordant grains show younger ages of 3202 ± 10 Ma and 2945 ± 11 Ma (Fig. 5e).

BC.61 sample zircons are light yellow to rose in color, transparent, and mainly euhedral and prismatic in form. As presented in Fig. 5f, simple internal oscillatory zoning is frequent, and inherited cores were observed. Few grains are elongated prismatic and display broad-banded zoning (Fig. 5f), suggesting a magmatic origin (Corfu et al., 2003). Sixty-six U–Pb isotopic spot analyses were conducted on 49 grains and display variable U (mostly 54–364 ppm) and Th (mostly 13–272 ppm), except one very high Th 646 ppm with Th/U ranging from mostly 0.11 to 2.69, which are typical of magmatic zircons (Table S1). Fifty-four spot analyses yield an upper intercept age of 3322.1 ± 7.2 Ma (MSWD = 3.4) (Fig. 6f). This age is identical to the Concordia age of 3346.3 ± 10 Ma (MSWD = 0.90) (Fig. 6f). Most of the zircon gains show that the cores with poorly developed oscillatory zoning are surrounded by structureless rims or bright blurred domains (Fig. 5f). Mostly, grain cores display older ages of 3351 ± 13 Ma, 3335 ± 11 Ma and 3396 ± 17 Ma, and the rims show younger ages of 3295 ± 11 Ma, 3299 ± 10 Ma and 3291 ± 12 Ma, respectively (Fig. 5f). These younger ages of the rims may represent metamorphic events (Kaur et al.,

2016). One large zircon grain reveals younger ages of 2619 ± 25 Ma, and one structureless grain shows an age of 3104 ± 14 Ma.

5.1.2. Neoarchean TTG gneiss

The sample, **BC.27**, was taken from the Babina area (Table 1). Zircon grains of this sample are translucent, colorless and structureless, and euhedral to subhedral with simple oscillatory zoning, and no inherited cores were observed (Fig. 5g). Thirty-four U–Pb analyses were conducted on 33 zircons, showing U (53–546 ppm) and Th (mostly 24–469 ppm) with Th/U mostly in the range from 0.13–1.49 (Table S1). Many analyses are discordant, with Pb-loss distribution suggesting multiple episodes of relatively recent losses (Fig. 7a). Two zircon spot analyses reveal a Concordia age of 2669 ± 11 Ma (MSWD = 8.7), and eight sub-discordant grains yield an upper intercept age of 2681 ± 10 Ma (MSWD = 1.4) (Fig. 7a). Few grains display younger ages of 2483 ± 16 Ma and 2437 ± 15 Ma (Fig. 5g). The **BC.31** sample was collected from 3 km south of BC.27 sample in the Babina area (Table 1). The zircon grains of this sample are colorless, transparent, largely euhedral and prismatic (Fig. 5h). Zircon grains are homogeneous and unzoned. Few cores surrounded by a thin structureless or patchy zoned rim, and inherited cores were observed (Fig. 5h). Thirty-four zircon U–Pb analyses were performed on 34 grains, displaying U and Th contents of 26–231 ppm and 9–153 ppm, respectively, with high Th/U ratio ranging from 0.28–0.86 (Table S1). Six concordant zircon grains reveal a Concordia age of 2706.3 ± 11 Ma (MSWD = 0.69) (Fig. 7b). Twenty-six spot analyses yield an upper intercept age of 2706 ± 9.2 Ma (MSWD = 2.1) (Fig. 7b). One concordant zircon grain shows an older age of 2975 ± 12 Ma (Fig. 5h).

The zircon grains in the sample, **BC.50** from Kuraicha in the Mauranipur belt, are colorless, transparent, mainly subhedral to euhedral and prismatic in form (Fig. 5i).

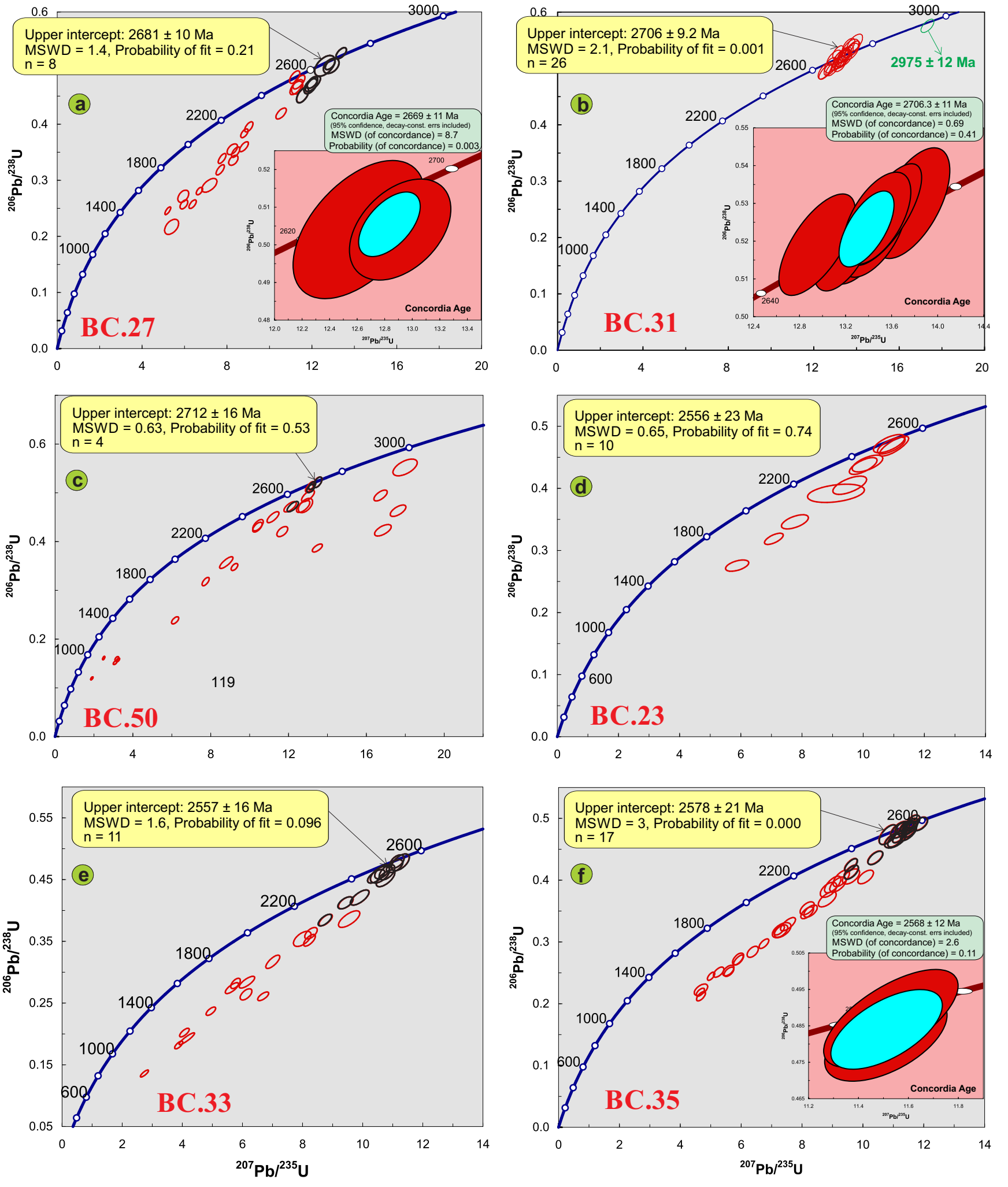

Fig. 7(a–f). Zircon U–Pb Concordia diagrams for TTG gneisses and high-K granitoids from the CBGGT in the BC.

This sample of zircon grains have an oscillatory zoned core surrounded by a thin structureless or patchy zoned rim, and inherited cores were identified (Fig. 5i). Thirty spot analyses were performed on 28 grains and have a high content of U (mostly 184–883 ppm) and Th (55–337 ppm) mostly with Th/U ratios ranging from 0.10–0.82 (Table S1). The U–Pb data are sub-concordant to variably discordant, indicating lead loss from the zircon grains (Fig. 7c). Four discordant grains yield an upper intercept age of 2712 ± 16 Ma (MSWD = 0.63) (Fig. 7c). As presented in Fig. 5i, older zircon grains of ages of 3393 ± 17 Ma and 3280 ± 15 Ma, and younger ones of ages of 2516 ± 13 Ma were observed.

5.1.3. Neoarchean High-K granitoids

The sample, **BC.23**, was taken from the Babina area (Table 1). Zircon grains generally show stubby to prismatic shapes that they have inner cores with oscillatory or structureless zoning that are surrounded by blurred zoned rims, signifying an inherited or captured origin (Fig. 5j). U–Pb isotopic analysis of thirty-three zircon grains and mostly highly discordant. Ten isotopic analysis yielded an upper intercept age of 2556 ± 23 Ma (MSWD = 0.65) (Fig. 7d); the Th/U ratios of these grains are 0.58–2.21, which are revealing of a magmatic origin (Table S1). The sample, **BC.33**, was collected around Baghora village in the Babina area (Table 1). Zircons of this sample are translucent, colorless and euhedral to subhedral with no pronounced oscillatory zoning, and no inherited cores were observed (Fig. 5k). Twenty-six U–Pb analyses were performed on 23 zircons, showing a U content (mostly 113–515 ppm) and Th (mostly 69–557 ppm) mostly with Th/U ratios ranging from 0.13–1.69 (Table S1). Eleven U–Pb spot analyses yield an upper intercept age of 2557 ± 16 Ma

(MSWD = 1.6) (Fig. 7e). Few zircon grains show younger ages of 2308 ± 17 Ma (Fig. 5k).

The sample, **BC.35**, was taken from Jhansi area (Table 1). The zircon grains of this sample are colorless, transparent, mainly euhedral to subhedral and prismatic (Fig. 5l). As shown in Fig. 5l, simple internal oscillatory zoning is common, and inherited cores were observed in a single grain (Fig. 5l). One large grain (~150 μm) shows a core, a middle rim and an outer rim, and they reveal different ages (Fig. 5l). Forty-nine U–Pb isotopes spot analyses were conducted on 36 grains and show U and Th contents are 78–610 ppm and 55–325 ppm but mostly in the latter, respectively, with variable Th/U ratios ranging from 0.14–1.21 (Table S1). Seventeen spot analyses yield an upper intercept age of 2578 ± 21 Ma (MSWD = 3) (Fig. 7f) whereas two spot analyses produce a Concordia age of 2568 ± 12 Ma (MSWD = 2.6) (Fig. 7f). One zircon grain shows three different phases of evolution concluded by three different ages of 2521 ± 17 Ma (core), 2504 ± 20 Ma (middle rim) and 2487 ± 16 Ma (outer rim) (Fig. 5l). These rim ages possibly represent metamorphic events.

5.2. Whole-rock geochemistry

Whole-rock major and trace elements data and calculated parameters for the nine TTG gneiss and three high-K granitoid rock samples from the CBGGT are listed in Table S2 and plotted in Figs. 8–11. Based on their petrological and geochemical characteristics and the geochronological data, these samples can be divided into three groups: (i) Paleoarchean TTG gneisses, (ii) Neoarchean TTG gneisses (granodioritic), and (iii) Neoarchean high-K granitoids.

5.2.1. Major elements

The studied Paleoarchean TTG gneisses show SiO_2 (64.84–73.73 wt%) and plotted in the fields of granodiorite and granites with characteristics of sub-alkaline range in the total alkali versus silica (TAS) diagram (Fig. 8a, after Le Bas et al., 1986). Neoarchean TTG gneisses display SiO_2 (66.47–74.37 wt%) and plotted in the fields of granite and granodiorite, whereas high-K granitoids show high content of SiO_2 (72.57–78.33 wt%) and plotted in the granite field (Fig. 8a). In the normative Ab–An–Or triangular diagram of Barker (1979), all the studied samples were plotted in the tonalite, trondhjemite, granodiorite and granite fields (Fig. 8b). Paleo- and Neoarchean TTG gneiss samples were plotted in the global typical Archean TTG field in the Na_2O/K_2O–2A/CNK–2FMSB diagram, and high-K granitoids were plotted in biotite- two mica granite field, whereas one sample was plotted in a sanukitoid field (Fig. 8c, after Laurent et al., 2014). Paleo- and Neoarchean TTG gneisses and high-K granitoids display geochemical features ranging from calcic to alkali, mostly magnesian and metaluminous to peraluminous (Fig. 9a–c). In figure SiO_2 *vs.* K_2O, samples were mostly identified as medium-K, with few samples extending into high-K or low-K fields (Fig. 9d). Paleoarchean TTG gneisses are characterized by low K_2O contents (1.34–3.08 wt%) but high Na_2O contents (3.73–5.57 wt%). This leads to low K_2O/Na_2O ratios (0.25–0.71), alkali (K_2O + Na_2O) (6.29–7.78 wt%), MgO (0.43–2.42 wt%), Fe_2O_3 (0.47–1.59 wt%), and Al_2O_3 (14.53–16.35 wt%) contents. However, they have relatively low contents of TiO_2 (0.16–0.55 wt %) and P_2O_5 (0.05–0.23 wt%) (Table S2). Neoarchean TTG gneisses show variable contents of K_2O (0.93–3.48 wt%) and MgO (0.46–1.26 wt%), and moderate contents of Fe_2O_3 (0.53–1.57 wt%), and Al_2O_3 (13.72–15.57 wt%). But, they possess comparatively low contents of TiO_2 (0.18–0.66 wt %), and P_2O_5 (0.08–0.25 wt%) (Table S2). High-K

granitoid samples display high contents of K_2O (1.74–5.94 wt%), and variable contents of MgO (0.30–3.00 wt%), moderate contents of Fe_2O_3 (0.46–1.63 wt%). However, they possess relatively low contents of Al_2O_3 (9.76–12.99 wt%), TiO_2 (0.15–0.87 wt %), and P_2O_5 (0.025–0.096 wt%) (Table S2). There is an inverse relation in which a general increase in MgO, Al_2O_3, Na_2O, CaO, and P_2O_5 generates a complimentary decrease in SiO_2 from Paleo- and Neoarchean TTG gneisses to high-K granitoids (Fig. 10).

5.2.2. Trace elements

The Paleo- and Neoarchean TTG gneisses and high-K granitoids exhibit large variations in trace element contents. On Harker's binary diagrams, trace elements for individual groups show a positive trend of La, Eu, Nb, Ni, Rb, and Yb, and constant trend by Zr and Cr against SiO_2 (figure not shown here). Paleoarchean TTG gneisses, Neoarchean TTG gneisses and high-K granitoids display large variations in total REE contents (78.16 to 319.10 ppm) and show distinct REE patterns (Table S2). Among the TTG gneisses, the Paleoarchean TTG type is characterized by moderate to high total REE (78.16–319.10 ppm) and moderately fractionated REE patterns [$(La/Yb)_{CN}$=3.88–41.12] with variable negative Eu anomalies, except two samples not showing anomalies (Table S2; Fig. 11a, after McDonough and Sun, 1995). These features can be endorsed to magma derivation from heterogeneous mafic sources without any residual garnet in the source but with significant residual plagioclase. In contrast, Neoarchean TTG gneisses contain moderate total REE (107.20–142.68 ppm) and strongly fractionated REE patterns [$(La/Yb)_{CN}$ = 9.83–26.44] without any significant Eu anomalies (Fig. 11a) signifying the role of garnet in

source residue. Additionally, high-K granitoids comprise high total REE (144.70–159.96 ppm) and moderately fractionated REE patterns [$(La/Yb)_{CN}$ = 11.38–18.34] without any significant Eu anomalies, except one sample showing negative Eu anomalies (Table S2 and Fig. 11a).

On the Primitive Mantle (PM) normalized incompatible elements diagram (Fig. 11b; McDonough and Sun, 1995), Paleoarchean TTG gneiss samples show enrichment in Ba, U, K and Pb and slightly elevated values for Sr, and Zr, with large negative Nb and Ti anomalies and weak negative Ce, P and Ta anomalies (Fig. 11b). A similar pattern also recognized in Neoarchean TTG gneisses and high-K granitoids (except few high-K granitoid samples) show highly elevated values for Th, and U (Fig. 11b). Negative Nb–Ta and positive Pb anomalies are typical features of TTG suites, and are generally interpreted as subduction-related magma generation (Martin, 1999; Foley et al., 2000; Moyen et al., 2001; Schmidt et al., 2004; Condie, 2005a, b; Martin et al., 2005; Moyen and Martin, 2012; Guice et al., 2019).

5.3. Whole-rock Sm–Nd systematics

The whole-rock Sm–Nd isotopic compositions of the Paleo- and Neoarchean TTG gneisses and high-K granitoids are presented in Fig. 12a–c and listed in Table 2. Furthermore, collected Sm–Nd isotopic data from published works are plotted in Fig. 12 (Pandey et al., 2011; Singh et al., 2019b). Hence, based on the zircon U–Pb formation ages of the TTG gneisses and granitoids, the $\varepsilon_{Nd}(t)$ values were calculated (Table 2). The four samples of Paleoarchean TTG gneisses (BC.16, BC.45, BC.60 and BC.61) are characterized by variable contents of Sm (1.63–9.78 ppm) and of Nd

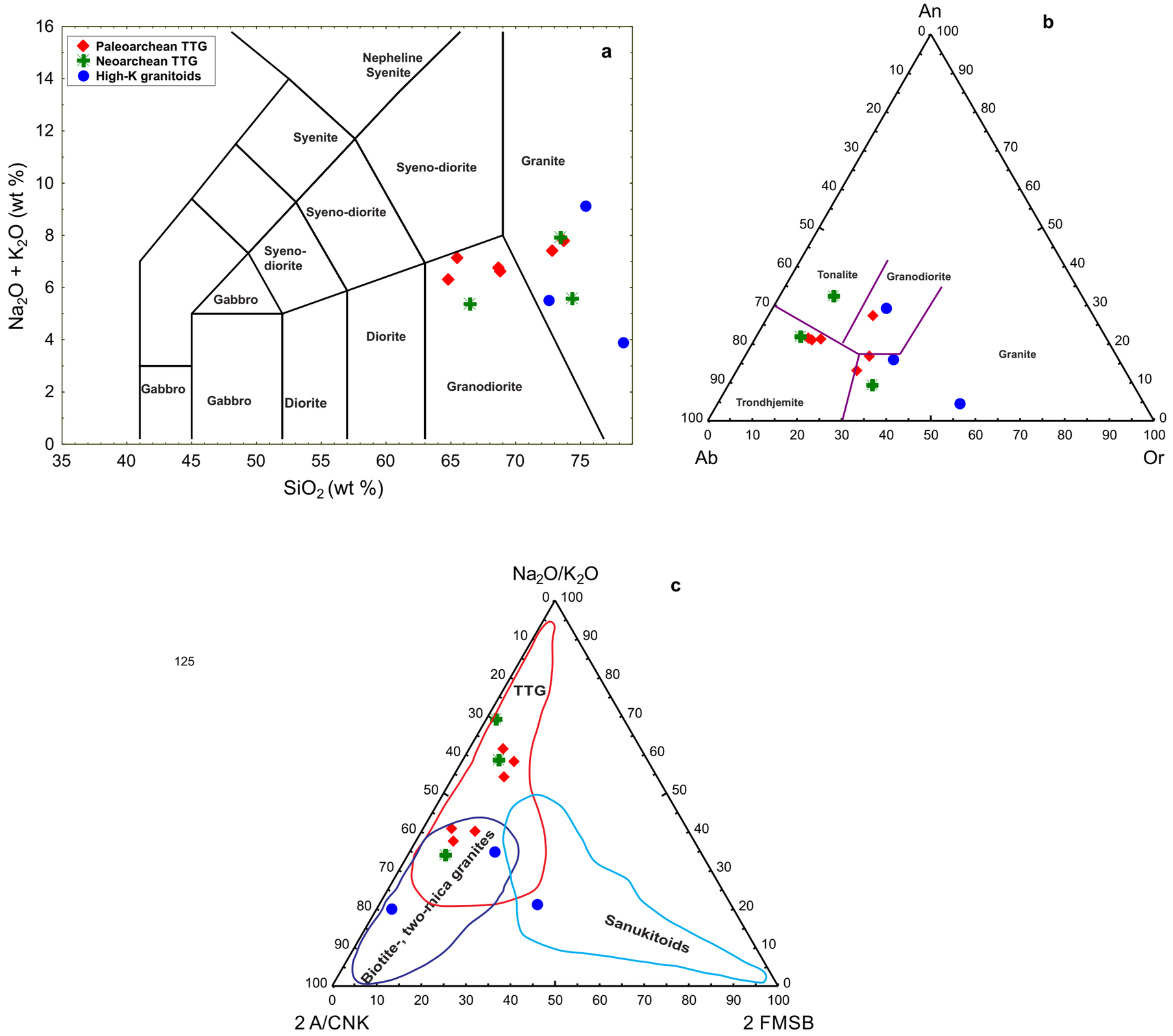

Fig. 8. (a) TAS (total alkalis *vs.* SiO2) diagram of Le Bas et al. (1986) obtained from the *IgRoCS* computer program (Verma and Rivera-Goméz, 2013). (b) Normative Ab-An-Or triangular diagram (after O'Connors, 1965) with fields from Barker (1979). (c) A ternary diagram ((Na2O/K2O)–2*A/CNK (molar Al2O3/ [CaO + Na2O+K2O])–2* [(FeOt + MgO) wt.% * (Sr + Ba) wt.%] = FMSB)) of Laurent et al., 2014) for TTGs and high-K granitoids.

(12.60–44.45 ppm) with 143Nd/144Nd (0.510328–0.511257) and 147Sm/144Nd (0.078–0.133) values. The εNd(t) values of samples, BC.60, BC.16, BC.61 and BC.45 are **+4.3**, **+0.6**, **+0.3** and **–0.5**, respectively. Their TDM values vary from 3.06 to 3.55 Ga (Table 2). Sample BC.27 from Neoarchean TTG gneisses shows an εNd(t) value of **+4.5** and has contents of Sm (3.4 ppm) and of Nd (16.86 ppm) with 143Nd/144Nd (0.511548), and 147Sm/144Nd (0.122) values. Furthermore, two samples of high-K

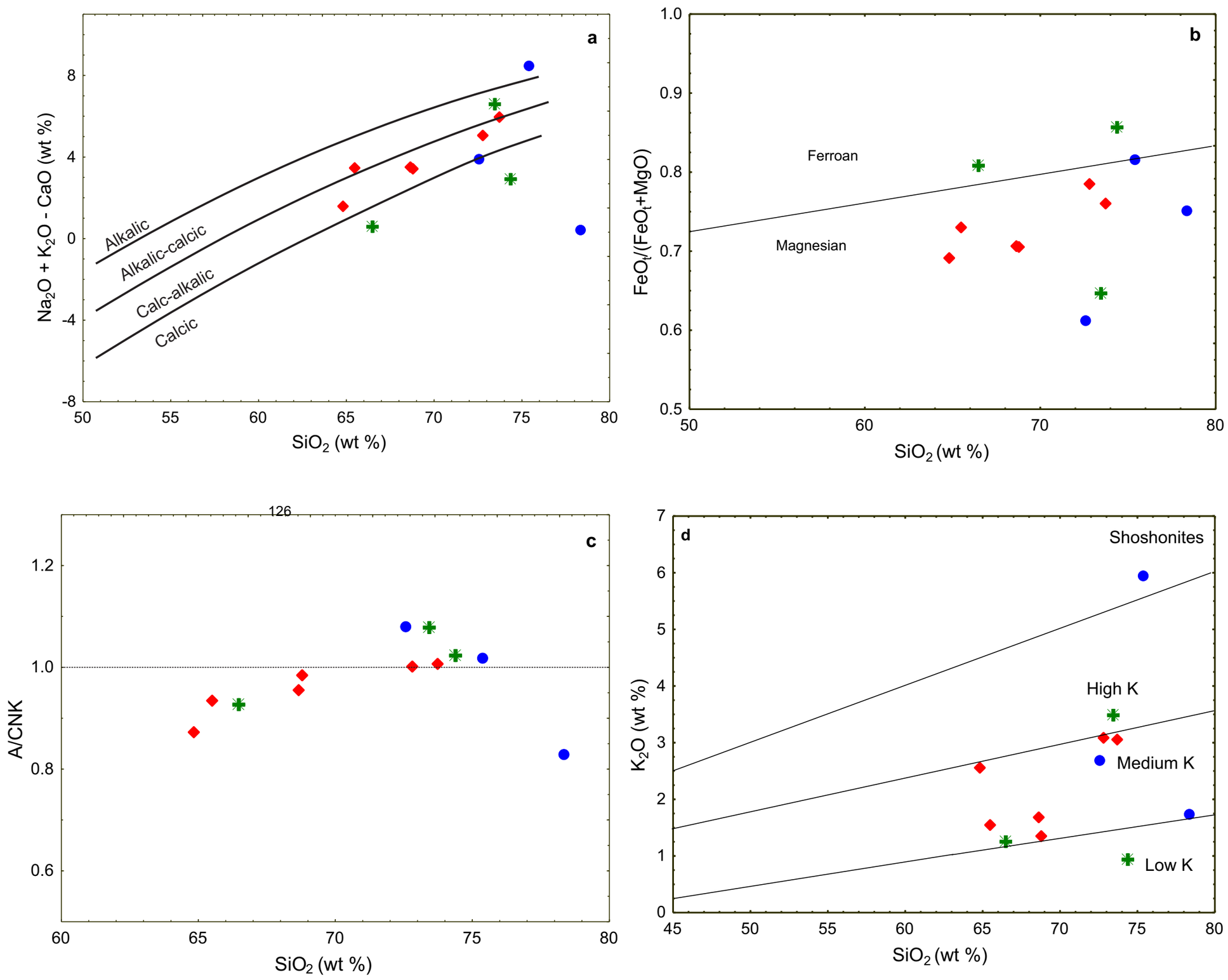

Fig. 9. (a) SiO_2 *vs.* MALI-index diagram (after Frost et al., 2001). (b) SiO_2 *vs.* (FeOt/(FeOt+MgO) diagram, line separating ferroan and magnesian fields (after Frost et al., 2001). (c) A/CNK [Al_2O_3/ (CaO + Na_2O + K_2O)] *vs.* SiO_2 diagram (after Shand, 1943). (d) K_2O *vs.* SiO_2 diagram (after Laurent et al., 2011).

granitoids (BC.33 and BC.35) show a constant range of T_{DM} (2.91–2.97 Ga) with $\varepsilon_{Nd}(t)$ ranging from **−3.4** to **−1.7** (Table 2).

Table 2. ID-TIMS whole-rock Sm–Nd isotopic data for TTG gneisses and high-K granitoids from the CBGGT.

Sample	Rock type	Sm (ppm)	Nd (ppm)	$^{147}Sm/^{144}Nd$	$^{143}Nd/^{144}Nd$	$^{143}Nd/^{144}Nd_t$	t (Ma)	$\varepsilon_{Nd}(t)$	±2σ	T_{DM}
BC.16	Paleoarchean TTG	2.35	13.94	0.102	0.510532	0.508233	3410	0.63	$1*10^{-6}$	3451
BC.45	Paleoarchean TTG	7.54	34.99	0.13	0.511126	0.508212	3364	-0.53	$1*10^{-6}$	3556
BC.60	Paleoarchean TTG	1.63	12.6	0.078	0.510328	0.508658	3278	4.33	$1*10^{-6}$	3060
BC.61	Paleoarchean TTG	9.78	44.45	0.133	0.511257	0.508332	3446	0.38	$1*10^{-6}$	3420
BC.27	Neoarchean TTG	3.4	16.86	0.122	0.511548	0.509394	2669	4.54	$1*10^{-6}$	2480
BC.33	High-K granitoids	6.42	38.45	0.101	0.510848	0.509146	2557	-3.44	$1*10^{-6}$	2975
BC.35	High-K granitoids	3.78	20.08	0.114	0.511141	0.509204	2568	-1.7	$1*10^{-6}$	2911

6. Discussion

6.1. Geochronology, zircon inheritance and metamorphic events

The CBGGT is exposed in the central part of the BC where they occupy an area extending from the Mahoba to Jhansi through Mauranipur and Babina areas. They include variably deformed volcano-sedimentary sequences, TTG suites and the latter phase of high-K granitoid rock emplacements (Mondal et al., 2002; Kaur et al., 2014, 2016; Singh and Slabunov, 2015a; Saha et al., 2016; Verma et al., 2016; Joshi et al., 2017; Singh et al., 2018; Singh et al., 2019a, b). Studied high-precision LA-ICP-MS data on zircons of granitoids suggest five major periods of felsic crust formation at ca. 3550 Ma, 3440–3300 Ma, 3285–3200 Ma, 2712–2669 Ma, and 2568–2500 Ma, which are sub-contemporaneous with the episodes of greenstone volcanism in the BC (Tables 1 and S3; Figs. 6 and7). The Archean felsic crust formation events of the BC could probably be correlated with the common pattern of global Archean crustal evolution and reworking at 3.5–3.2 Ga, 2.8–2.7 Ga, and 2.6–2.5 Ga (Condie and Aster, 2010).

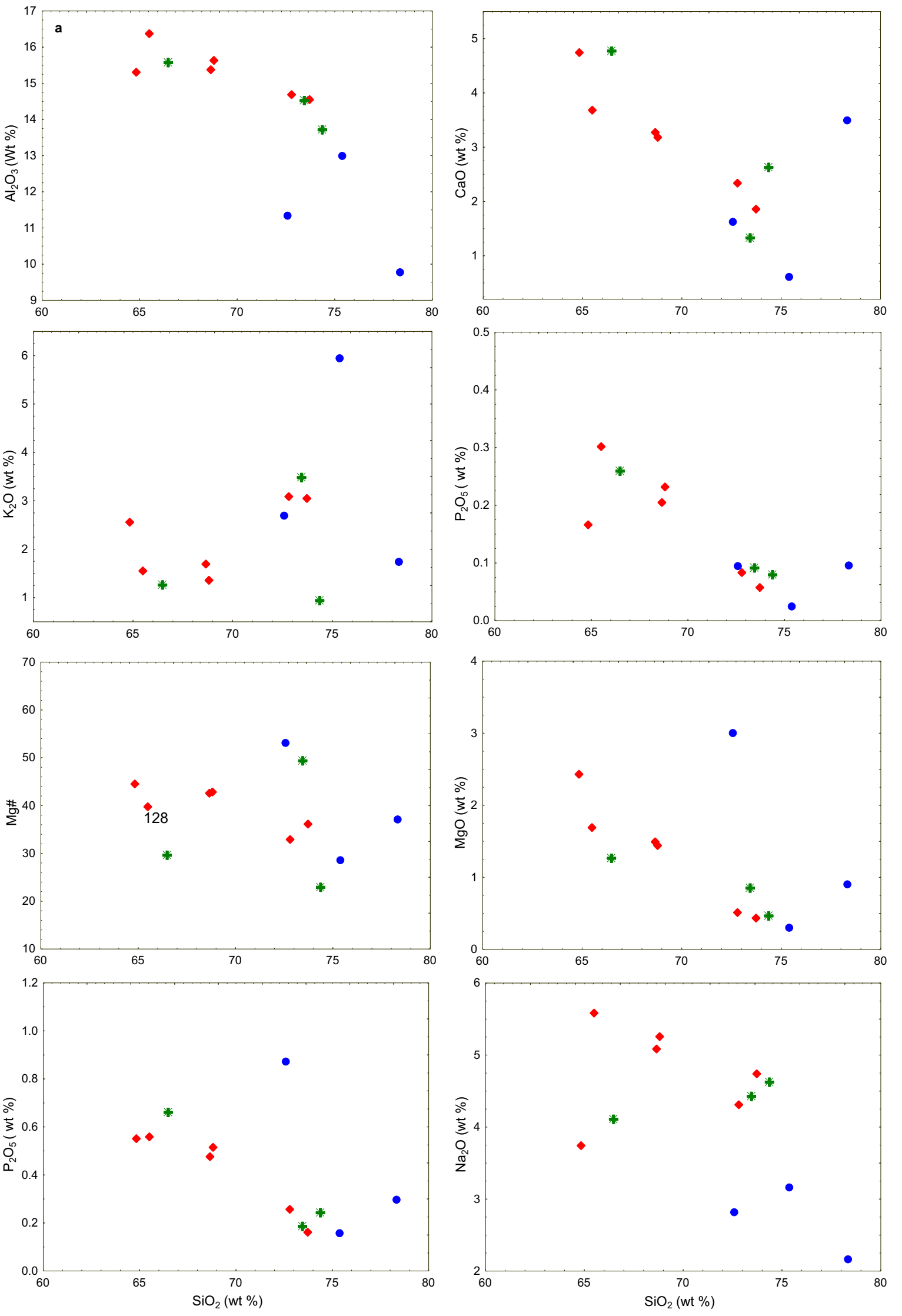

Fig. 10. Hacker's binary plots for selected major elements for TTG and high-K granitoids.

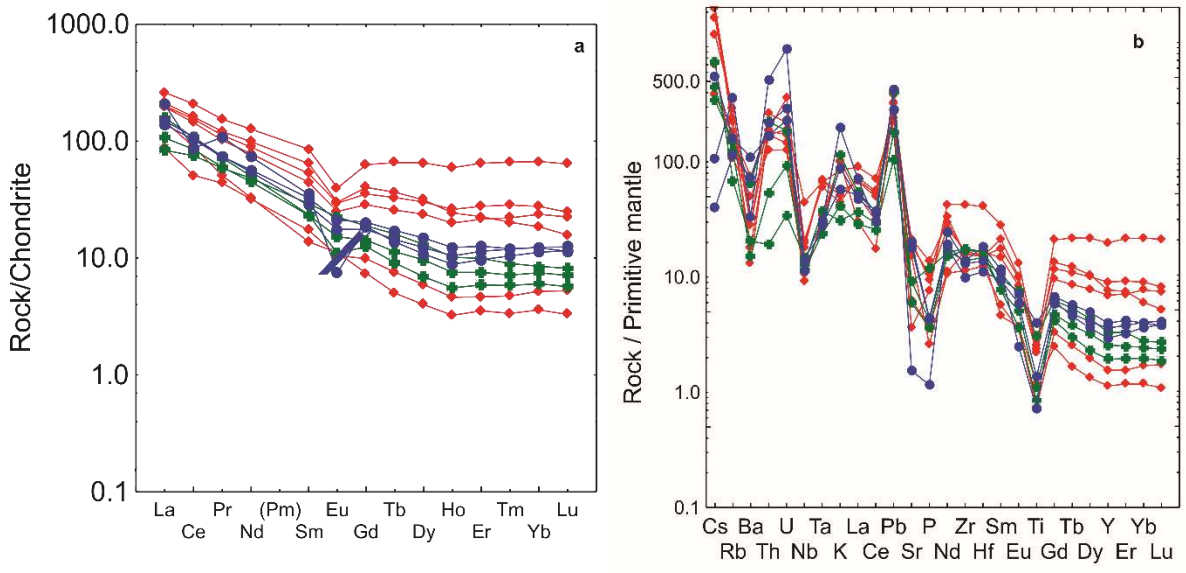

Fig. 11. (a) Chondrite-normalized REE patterns (after McDonough and Sun, 1995). (b) Primitive mantle-normalized multi element plots (after McDonough and Sun, 1995).

U–Pb geochronological studies have suggested that the oldest rocks (basement unit) formed between 3.33 and 3.59 Ga ago, but some ages of ~3.20 Ga were also reported (Mondal et al., 2002; Kaur et al., 2014, 2016; Saha et al., 2016; Joshi et al., 2017). The oldest rock of the BC is identified as a TTG gneiss (3.55 Ga) in the Mauranipur belt (Kaur et al., 2016) and 3.44 Ga TTG with xenocrystic zircons 3.59 Ga years old are reported from the Babina belt (Saha et al., 2016; Nasipuri et al., 2019). The present study also reports a xenocrystic zircon of 3.51 Ga from a TTG pluton of 3.36 Ga (BC.45) near Roni village, Mauranipur belt (Figs. 5d and 6d). The TTG gneiss sample, BC.16 (Baragaon belt), provides a Concordia age of 3.41 Ga and few zircon grains reveal a metamorphic event at 3.15 Ga. This Concordia age of TTG gneiss could probably be correlated with the age of ultramafic-mafic volcanics (3.43 Ga; Singh et al., 2019a) from Baragaon. This would then suggest a highly interesting magmatic event because it is both felsic plutonism and mafic

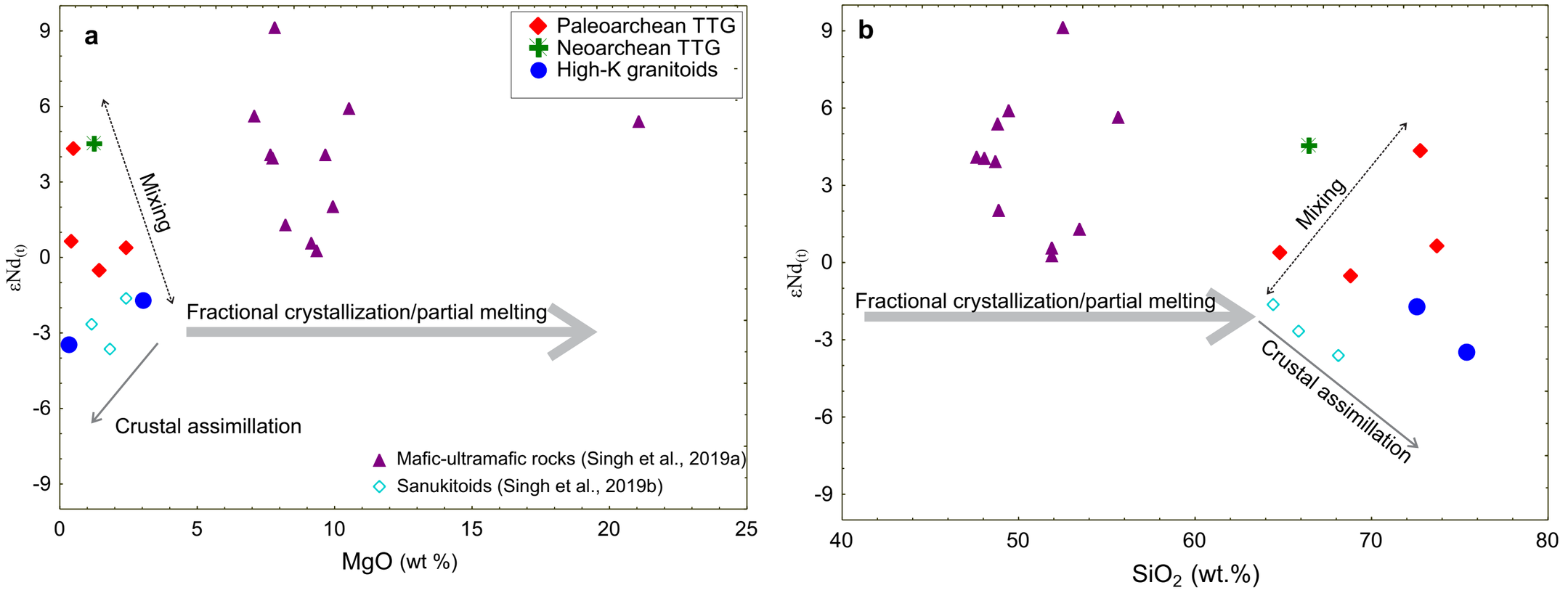

Fig. 12. (a) εNd(t) *vs.* MgO. (b) εNd(t) *vs.* SiO2. (c) εNd(t) *vs.* formation age (Ma).

volcanism that may have occurred synchronously in the Baragaon, Mauranipur belt (Singh et al., 2019a). The present study also reports three more ages within the Mauranipur belt. They are 3.34 (BC.19), 3.39 (BC.41) and 3.36 (BC.45). These ages support synchronous magmatic events in the Mauranipur terrane (Mondal et al., 2002; Kaur et al., 2016; Singh et al., 2019a). Furthermore, Saha et al. (2016) and Nasipuri et al. (2019) have reported TTG plutonism of ca. 3.44 Ga from the Babina belt, which is similar in age to the ultramafic-mafic volcanism of this belt as reported by Singh et al. (2019a), thus suggesting a synchronous event similar to that of the Mauranipur belt. Two zircon grain rims of the sample, BC.19, suggest a metamorphic overprint at ca. 3.09 Ga and 2.64 Ga (Figs. 5b; Table S3). Additionally, one zircon grain of BC.41 advocates a metamorphic event at ca. 3.20 Ga (Figs. 5c), and two grains of sample, BC.45, reveal a similar metamorphic overprint at ca. 3.31 and 3.23 Ga (Figs. 5d; Table S3).

This study reports tonalitic TTG (BC.61) and granodioritic TTG samples (BC.60) from the eastern part of the CBGGT around the Charkhari, Mahoba, which show two distinct phases of TTG magmatism. This study also identifies a TTG gneiss significantly older than thus far assumed in the eastern part of the study area, which reveals the existence of TTG gneiss 3.34 Ga (BC.61) around the Charkhari area (Fig. 6f). This sample also reveals a metamorphic event/overgrowth at ca. 3.29 Ga, which is concluded from the rim ages of zircons (Fig. 5f). This metamorphic age is similar to the youngest TTG plutonism (~3.27 Ga) reported in this study and by Mondal et al. (2002) and Kaur et al. (2016) from the similar exposure. This metamorphic event is similar to that of the Mauranipur belt (Table S3). Kaur et al. (2016) have reported a metamorphic age of ~3.18 Ga from Charkhari area whereas

Mondal et al. (2002) documented a ~3.24 Ga metamorphic event from metabasic enclave within the TTG gneiss in the Mahoba area, which is similar to the metamorphic overgrowth of the sample BC.45 of the Mauranipur belt. These metamorphic ages suggest a metamorphic event/overgrowth in between ~3.29 and 3.18 Ga in the Mahoba area (the eastern part of the BC), which is comparable to the metamorphic overgrowths of the Mauranipur terrane (Fig. 5f and Table S3). Dispersed TTG gneissic plutons occur in the southern part of the BC where Kaur et al. (2016) have reported a 3.20 Ga TTG pluton with ~3.53 Ga and ~3.33 Ga xenocrystic zircons from Rungaon area. This age shows the oldest TTG magmatism age in the southern part of the BC. Furthermore, Slabunov et al. (2017a) reported a quartzite (~3.43 Ga) from the south granite-greenstone terrane in the BC, which suggests a Paleoarchean crustal material for its provenance. All these findings confirm that the predominance of basement rock unit was generated during a time span from ~3.44–3.30 Ga, and mostly in the CBGGT (Table S3).

This study provides, for the first time, unequivocal evidence for the presence of Neoarchean TTG gneisses in the CBGGT from the Babina and Mauranipur terranes (Fig. 2 and Table 1). We dated two samples (BC.27 and BC.31) from the Babina belt and one sample (BC.50) from the Mauranipur belt all of which provide the ages of 2.67 Ga, 2.70 Ga and 2.71 Ga, respectively (Table S3; Figs. 7a, c and b). Sample BC.27 is undeformed granodioritic TTG rock (Fig. 3g) that shows a transitional TTG nature as documented in various cratons globally (Dey et al., 2009; Laurent et al., 2014; Jayananda et al., 2018). This sample provides a Concordia age of 2669 ± 11 Ma without any xenocrystic zircon ages, which reveals this for juvenile origin (Figs. 7a and 5g). This TTG age is similar to the TTG age, 2669 ± 7 Ma, as reported by

Verma et al. (2016) from the same location. Up to the time of my study, these authors had not provided any geochemical or petrological evidence that this sample came from TTG rock, whereas in the present study, we then studied two samples from different locations in the Babina belt. Hence we have provided here geochemical and petrological evidence confirming that they are Neoarchean TTG plutons. The second sample, BC.31, is highly deformed and shows gneissic banding (Fig. 3h). The Pb–Pb results of this sample yielded a Concordia age of 2706.3 ± 11 Ma and included a zircon xenocryst of 2.97 Ga (Fig. 7b). This age is similar to ion microprobe ages of granodiorite reported by Mondal et al. (1998) with zircon xenocrystic ages of 2.91 Ga and 2.81 Ga. Additionally, Saha et al. (2011) reported a metamorphic event at ~2.78 Ga from the white schist in the Babina belt.

To date, the magmatic ages similar to the abovementioned xenocrystic ages have not yet been reported from the BC (Tables 1 and S3). Additionally, this study also reports for the first time, Neoarchean TTG magmatism (sample BC.50) around the Kuraicha village in the Mauranipur belt. The TTG outcrop shows medium gneissic banding to massive structures, and has sharp contact with anatectic granites (Fig. 3i). The magmatic zircon grains of this sample provides a very similar emplacement age of 2712 ± 16 Ma as reported in the Babina belt. This sample includes xenocrystic zircons with ages of 3.39 and 3.28 Ga (Fig. 5i), which are a very similar emplacement ages to the late Paleoarchean TTG gneisses of this terrane (BC.16, BC.19, BC.41, and BC.45) (Fig. 7c). This suggests that older crustal blocks contributed to their genesis. Similar crustal recycling is reported in the Babina belt. Furthermore, Slabunov and Singh (2019) dated a felsic volcanic rock of ~2.81 Ga from Baragaon village in the Mauranipur belt. This age represents the earliest episode of the felsic

volcanism in the study area. This study confirms that the episodic Neoarchean TTG magmatism occurred between 2.71 and 2.67 Ga in the Babina and Mauranipur terranes of the CBGGT. The occurrence of Paleoarchean xenocrystic zircons in the Neoarchean TTG gneisses reveal that the earlier crust was involved in their generation. The identified new TTG phases in this study are similar to the cases of the adjacent Aravalli Craton (Kaur et al., 2019) and other major Archean cratons worldwide (e.g., the Dharwar, North China, São Francisco, Slave and Kaapvaal cratons) (Davis and Hegner, 1992; Almeida et al., 2011; Laurent et al., 2013, 2014; Ma et al., 2013; Zhai, 2014; Jayananda et al., 2018; Zhou et al., 2018).

The voluminous undeformed plutons of the high-K granitoid rocks (granodiorites, sanukitoids, anatectic granites) occupy most of the BC and intrude into the TTG-greenstone assemblage of the CBGGT. They show emplacement ages between 2577–2482 Ma (typically >2520 Ma), except one granitic pluton of the age 2583 ± 10 Ma from the Kalothara area (Tables 1 and S3; Mondal et al., 2002; Kaur et al., 2016; Joshi et al., 2017; Singh et al., 2019b). The present study dated three samples of high-K granitoids from the CBGGT, comprising two samples from the Babina belt (BC.23 and BC.33) and one sample from the Jhansi terrain (BC.35) north of the Babina belt. In the granodiorite sample, BC.23, zircon analyses are highly discordant and yield an upper intercept age of 2556 ± 23 Ma (Figs. 5j and 7d). This granodiorite occurs in large plutons around the city of Babina. It is typically medium- to coarse-grained, undeformed to slightly deformed, and with moderate- to crude-foliated and locally containing mafic minerals (biotite and amphiboles) in aggregates or clots (Figs. 3j). On the other hand, magmatic zircons of the sample, BC.35, yielded a Concordia age of 2568 ± 12 (Figs. 5l and 7f), of which a sample is collected from the

Jhansi terrain. This age is very similar to the ages of sanukitoids and granodiorites described by Joshi et al. (2017) and Kaur et al. (2016) from the Jhansi terrain (Table S3). The zircon cores of the sanukitoids (2.56 Ga) display older xenocrystic ages of 2.91 and 2.84 Ga from the Orccha sanukitoids pluton as reported in the Joshi et al. (2017) study. Moreover, Kaur et al. (2016) documented similar zircon xenocrystic ages (3.11 Ga, 2.82 Ga, and 2.64 Ga) from the Panchora granodiorite gneiss in the study area. However, the present study did not report any xenocrystic zircon from the sanukitoids. In this study, one large zircon grain shows two distinct rim ages of 2.50 Ga (middle rim) and 2.48 Ga (outer rim) with a core age of 2.52 Ga (Fig. 5l and Table S3). These rim ages could probably be related to the metamorphic events/overgrowths. A similar metamorphic overprint was reported by Kaur et al. (2016) from the Panchora granodiorite gneiss (Table S3). These metamorphic ages possibly signify a minimum age due to zircon alteration. Additionally, anatectic granite sample, BC.33, provide an upper intercept age of 2557 ± 16 Ma. This sample age is older than that reported by Kaur et al. (2016) from the similar exposure (2525 ± 25 Ma). However, Verma et al. (2016) documented anatectic granite from Babina belt which is younger than the studied rock (BC.33).

It is noteworthy here that high-K granitoids (granodiorites, sanukitoids, anatectic granites) show emplacement ages between 2.58 and 2.48 Ga (typically >2.52 Ga) (Tables 1 and S3; Mondal et al., 2002; Kaur et al., 2016; Verma et al., 2016; Joshi et al., 2017; Singh et al., 2019b). The field relationship between the granodiorite and sanukitoid with anatectic granites indicate that the earlier ones (i.e. granodiorite and sanukitoid) are older. However, A few granodiorite and sanukitoid plutons as well as anatectic granites reveal a synchronous magmatism of the late Archean (Table S3;

Kaur et al., 2016; Joshi et al., 2017; Singh et al., 2019b). These high-K granitoids show multiple episodes of magmatism and crustal reworking mostly during late Neoarchean (2.58–2.50 Ga) throughout the craton, which are aligned with the cratonization of the BC during Neoarchean (ca. 2.50 Ga). Further, zircons show xenocrystic ages (2.91Ga, 2.84 Ga, 2.64 Ga, and 2.61 Ga), which suggest that the anatectic granites were generated by the partial melting of ancient crustal rocks (Kaur et al., 2016; Joshi et al., 2017; Singh et al., 2019b). These ages of the high-K granitoids (2.58–2.50 Ga) could possibly be correlated with the age of felsic volcanic rocks of the Babina and Mauranipur belts as described by Mondal et al. (2002), Singh and Slabunov (2015), and Slabunov and Singh (2019) (Table S3). These ages suggest a synchronous felsic plutonism and felsic volcanism ca. 2.55–2.51 Ga in the CBGGT.

Finally, the incorporation of varied micro-blocks occurred by the arc-continent collision mechanism and common slab break-off between north and south blocks of the BC during late Archean. This event shows that the BC did not amalgamate together until ~2.50 Ga. The voluminous anatectic granitic rocks were produced by intense partial melting of the older crustal blocks in an arc-continent collision, demonstrating the final cratonization of the BC.

6.2. Petrogenesis

6.2.1. TTG gneiss

Numerous researchers have proposed two distinct petrogenetic models as accounting for the generation of TTG magmas: (i) hydrous melting of subducted basaltic crust and (ii) melting at the base of a mafic crust (Drummond and Defant, 1990; Smithies, 2000; Martin and Moyen, 2002; Condie, 2005a, b; Martin et al.,

2005, 2014; Hoffmann et al., 2011; Moyen, 2011; Guitreau et al., 2012; Moyen and Martin, 2012; Nagel et al., 2012; Polat, 2012; Laurent et al., 2014; Jayananda et al., 2018).

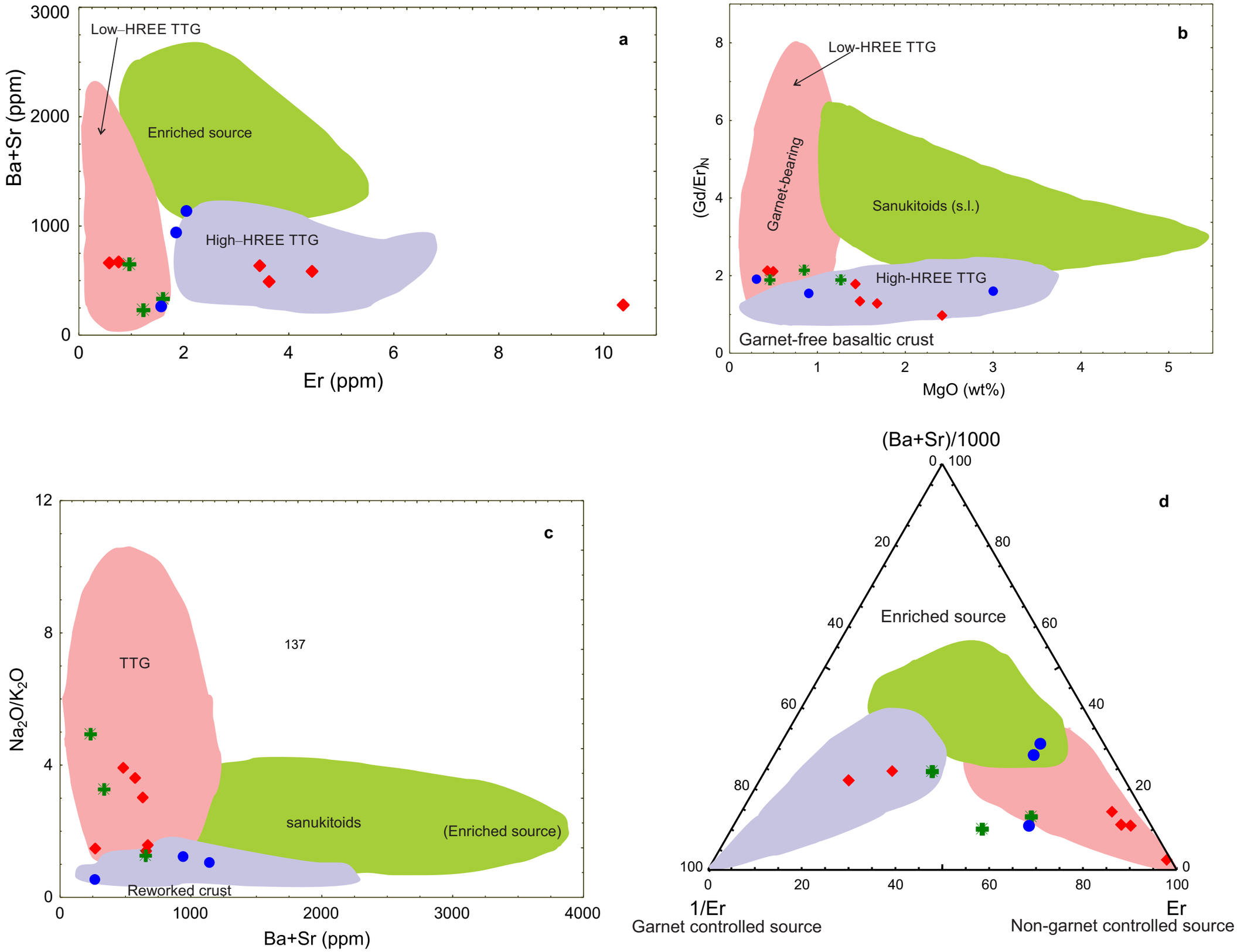

Fig. 13. Classification diagrams for TTG gneisses and high-K granitoids. (a). Ba+Sr *vs.* Er binary plot (after Heilimo et al., 2010). (b) (Gd/Er) *vs.* MgO (Halla et al., 2009). (c) Na2O/K2O *vs.* Ba+Sr (after Halla et al., 2009). (d) (Ba+Sr/1000)−1/Er−Er triangular plot for distinguishing sources and role of garnet in residue (after Heilimo et al., 2010).

The most accepted petrogenetic model is proposed on the basis of integrated petrological and geochemical investigations of TTG suites from different cratons. This model suggests that melting of thickened oceanic arc crust at different depths can produce Archean TTG compositions (Hoffmann et al., 2011; Moyen, 2011; Polat, 2012; Huang et al., 2013; Moyen and Laurent, 2018; Liou and Guo, 2019).

The oldest felsic crust (TTG gneiss of 3.55 Ga) has been reported near Kuraicha village, Mauranipur in the CBGGT (Kaur et al., 2014). Additionally, others reported are 3.44 Ga old, a TTG gneiss containing xenocrystic zircons 3.58 Ga old, which are from the Babina belt in the CBGGT (Saha et al., 2016; Nasipuri et al., 2019). Furthermore, the present study reports that there is also a 3.51-Ga xenocrystic zircon found in the 3.36 Ga TTG pluton (sample, BC.45) near Roni village, Mauranipur belt (Table 1; Figs. 5d and 6d). These findings attest to the presence of old continental crust at least from two localities (Mauranipur and Babina) in the CBGGT. To date, this crust represents the oldest one in the northern part of the Indian shield (Fig. 2). These oldest TTG gneisses are a heterogeneous assemblage of highly deformed plutons, tectonically interleaved on a centimeter scale with amphibolite, ultramafic rocks and anatectic granites. Geochemical and isotopic compositions suggest that they were originated by reworking of Eoarchean mafic and/or felsic crust which include partial melting of deep-seated mafic crust in the garnet stability field (Kaur et al., 2014, 2016; Saha et al., 2016; Nasipuri et al., 2019). The studied samples display low Sr (76.35–452.50 ppm) and Ba (92.20–525.39 ppm) contents as well as negative Eu anomalies (Eu/Eu*0.538–1.05) (Fig. 11a; Table S2), indicating that plagioclase may have existed as a residual or fractionated phase. Combined major and trace element data have been plotted in various bivariate and ternary diagrams for characterization of their sources, i.e., (Er *vs.* Ba+Sr), (MgO *vs.* $(Gd/Er)_N$), (Ba+Sr *vs.* Na_2O/K_2O), and [1/Er–Er–(Ba+Sr)/1000] (Fig. 13a–d). On the other hand, the variable amounts of HREEs (0.581–10.95 ppm Yb) and Sr/Y ratios (0.84–25.70), except one sample 45.48 ppm and relatively high La_N/Yb_N (3.88–16.75) (Fig. 14a–b; Table S2).

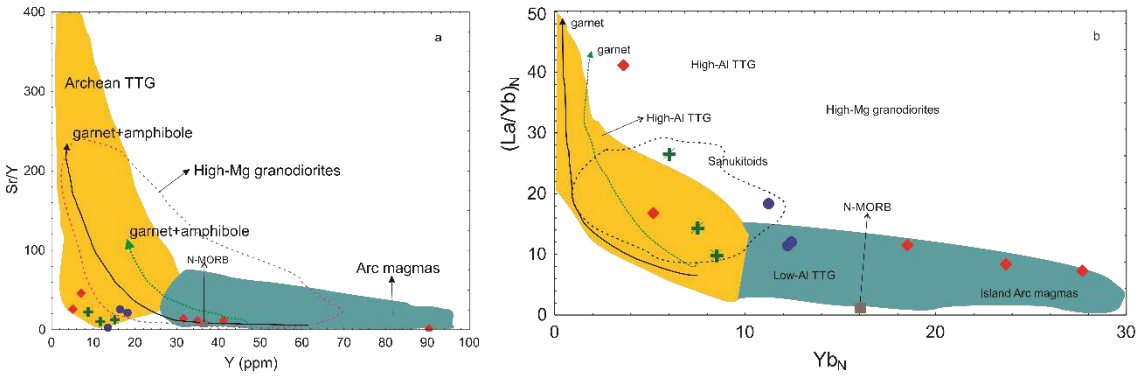

Fig. 14. (a) Sr/Y *vs.* Y diagram (after Defant and Drummond, 1986) for distinguishing role of mineral phase in source residue. (b) $(La/Yb)_N$ *vs.* versus $(Yb)_N$ diagram (Martin, 1986) for characterizing the residual garnet and or amphibole.

To assess residual mineralogy and depth of melting of TTGs the binary diagrams of the Y vs. Sr/Y (Fig. 14a) and $(Yb)_N$ vs. $(La/Yb)_N$ (Fig. 14b) are used, indicative of modern adakites, which are commonly endorsed to high pressure partial melting of hydrous basaltic rocks with a garnet bearing amphibolite/eclogite as residuum (Martin et al., 2005; Moyen and Martin, 2012), or fractional crystallization with accumulation phases such as pyroxene + garnet/amphibolite (Kleinhanns et al., 2003) (Fig. 14a–b; Table S2). The coexistence of garnet and plagioclase indicate a garnet amphibolite-facies source with pressures over 10 kbar (>30 km deep) (Moyen, 2011). The $\varepsilon_{Nd}(t)$ values show from +0.38 to +4.33, except one sample reveal –0.53 an T_{DM} (3.55–3.06 Ga) supporting the similar type of petrogenetic process. In addition, Kaur et al. (2016) have been reported $\varepsilon_{Hf}(t)$ data and show complex and CHUR parallel range suggest that this source crust might be long lived (>0.4 Ga), it was derived from a depleted mantle source. The depleted mantle signatures of the mafic-ultramafic rocks also support this petrogenetic mechanism (Singh et al., 2019a). There are two common tectonic scenarios to produce TTG

magmatism: (1) melting of subducted oceanic crust and (2) melting at the base of a mafic crust (Drummond and Defant, 1990; Smithies, 2000; Martin and Moyen,2002; Condie, 2005a, b; Martin et al., 2005, 2014; Hoffmann et al., 2011; Moyen, 2011; Moyen and Martin, 2012). Subduction-related TTG magmas tend to own higher Mg#, Cr and Ni contents, due to interactions between the TTG melts and the mantle wedge (Smithies, 2000; Martin and Moyen, 2002; Martin et al., 2005; Moyen and Martin, 2012). However, the 3.41–3.20 Ga TTG gneisses have low Cr (3.33–19.03 ppm), Ni (1.73–11.40 ppm) and Mg# (32.90–44.41) contents and positive to negative εNd(t) values, signifying limited, interactions of the older TTG melt with the mantle melts (Tables 2; Fig. 12). The 3.41–3.20 Ga TTG gneisses predominantly occurrences in the CBGGT and few plutons recognized in the southern part of the BC. Integrated geochemical and isotopic results suggest that they were formed by mixing between juvenile mafic melts and reworked oldest felsic crust (TTGs) at different times and depth (Mohan et al., 2012; Kaur et al., 2016; Saha et al., 2016; Joshi et al., 2017). This petrogenetic mechanism can be reveal from the depleted mantle signatures of the mafic-ultramafic rocks in the CBGGT reported by Singh et al. (2019a). Additionally, occurrences of inherited zircon grains in these TTG gneisses also support reworking of oldest felsic crust (TTGs) and involvement of juvenile mafic melts in their petrogenesis (Table S3).

The *in-situ* dating of magmatic zircon grains of the TTG gneisses provided emplacement ages (2.71, 2.70 and 2.67 Ga) of the three Neoarchean TTG gneisses (BC.50, BC.31 and BC.27) in this study approve the existence of Neoarchean (2.67–2.7 Ga) TTG magmatism in the CBGGT in the BC. These finding are consistent with the previous documented Neoarchean TTG magmatic events (2.67 Ga) by Verma

et al. (2016). The studied gneisses from Babina and Mauranipur plutons have relatively high Na_2O/K_2O ratios (1.27–4.93) but low ferromagnesian elements (Fe_2O_{3t}+MgO+MnO+TiO_2) (1.61–3.59 wt%). They also display negative Nb-Ta and Ti anomalies (Fig. 11b), and fractionated REE patterns with low HREE contents (0.97–1.37 ppm Yb). These geochemical signatures are comparable to the Neoarchean TTGs (Figs. 8c and 13a–d). In the Y vs. Sr/Y and $(Yb)_N$ vs. $(La/Yb)_N$ binary diagrams, the samples dominantly fall into the fields of typical high-Al TTG rocks (Fig. 14a–b). On the other hand, chondrite-normalized REE and primitive mantle normalized trace element diagrams (Fig. 11a–b), indicate flat REE pattern and no negative Eu anomaly, which indicate there are no fractional crystallization of plagioclase. The samples BC.27 show whole-rock $\varepsilon_{Nd}(t)$ value of +4.53 (Table 2 and Fig. 12), indicating a juvenile crustal source. They are enhanced in LILEs such as Th, Ba and K, with negative Sr, Ti and Ba anomalies (Fig. 11b). The geochemical characters point out that their parental melts generated from partial melting of basaltic rocks (hydrated) at high-pressures, with garnet without plagioclase, in the residue (Rapp et al., 1991; Sen and Dunn, 1994) (Fig. 13a–d). The Neoarchean TTG gneisses also have high content of MgO, Mg#, Cr and Ni (Table S2). Rapp et al. (1999) and Rapp and Watson, (1995) experimentally concluded that the pure partial melting of hydrous basaltic rocks formed some magmas with low Mg# (<45), irrespective of the pressure conditions. Further, magmas that generate natural adakitic rocks with low Mg# values and low Cr and Ni contents can be formed by the partial melting of mafic magmas that form an underplate within the lower crust (Atherton and Petford, 1993; Petford and Atherton, 1996). So, these evidences point out that that TTG gneisses (granodioritic) experienced the accumulation of mantle

material. The occurrences of older inherited zircons (3.39 Ga, 3.28 Ga, 2.97 Ga, 2.91 Ga, 2.81 Ga and 2.80 Ga) (Table S3). demonstrate that reworking of older felsic crust and ca. 2.78 Ga metamorphism and also intercrustal re-melting (anataxis) in the CBGGT. In conclusion, these geochemical signatures endorse that they were originated from the partial melting of a juvenile crustal source and intermingled with the mantle material and the widespread Neoarchean formation by tectono-thermal events.

6.2.2. High-K granitoids

Ample plutons of the high-K granitoid (granodiorites, sanukitoids, anatectic granites) show emplacement ages between 2577–2482 Ma (typically >2520 Ma), intrusive in TTG-greenstone association of the CBGGT and occupied major part of the BC (Tables S3; Mondal et al., 2002; Kaur et al., 2016; Joshi et al., 2017; Singh et al., 2019b). They contain the dominant Al-rich minerals of magmatic biotite and minor muscovite (Fig. 4g–h) and display high K_2O, Rb and Th contents, and low TiO_2, P_2O_5, Ga and A/CNK values (Table S2). Moderate CaO concentrations (0.615–3.49 wt.%) and moderate Al_2O_3 contents. Conversely, the moderate amounts of HREEs (1.80–1.99 ppm Yb) and Sr/Y ratios (21.0–25.87), except one sample show low 2.42 ppm and high La_N/Yb_N (11.38–18.34) but no Eu anomalies except one sample display significant negative Eu anomalies (Figs. 11a and 14a–b; Table S2). Their primitive mantle normalized patterns are similar to those of TTG gneisses, except for higher contents in highly incompatible elements (Table S2) and negative Ba, Nb, Ti and Sr anomalies and higher concentrations in Y–HREE (Fig. 11b). Their whole-rock $\varepsilon_{Nd}(t)$ (–1.7 to –3.44) (Table 2), indicating produced by the partial melting of the older continental crust whereas few plutons (BC.35) suggest mingling of crustal magmas

and mantle melts and their homogenization at the lower crust level (Fig. 12). The late-Archean high-K granitoids are generally formed slightly later than the typical Neoarchean TTGs (transitional TTG) and they share similar geochemical features (Champion and Smithies, 2007; Smithies et al., 2009). These granitoids were concluded as formed in an extensional or late- to post-orogenic setting, marking the maturity and consolidation of the Archean cratonic terrains. Additionally, given the anataxis of older felsic crust in the lower crust, Watkins et al. (2007) discussed that merely partial melting of single TTGs linking the breakdown of biotite and hornblende is unable to generate late Archean voluminous K-rich magmatism but relatively sodic melts.

Integrated with field and other geological evidences, Bundelkhand high-K granitoids are proposed to have been produced by partial melting of the older continental crust in a post-collision extensional environment after an arc-continent collision. Therefore, the Bundelkhand Craton did not merge together until ca. 2.5 Ga. Compiled zircon U-Pb ages, Hf and Nd isotopes suggest that the ca. 2.5 Ga ample magmatism signifies reworking of the continental crust. In conclusion, they were formed by the partial melting of the older crust (TTG gneissic and metasediments) while few plutons suggest intermingling of crustal magmas and mantle melts and their homogenization at the shallow crust level (Kaur et al., 2016; Joshi et al., 2017; Singh et al., 2019b). Through their way to higher crustal levels, the magmas experienced fractional crystallization and crustal contamination leading to the wide range in silica percentage.

6.3. Implications for crustal evolution and reworking

Published geochronological and petrological studies from the CBGGT in the BC suggest three major Archean continental growth and reworking events, including five major periods of felsic crust formation at ca. 3.55 Ga, 3.44–3.30 Ga, 3.29–3.20 Ga, 2.70–2.67 Ga, and 2.58–2.50 Ga. which are sub-contemporaneous (3.44-2.70 Ga) with the episodes of greenstone volcanism in the BC (Tables S3; Mondal et al., 2002; Kaur et al., 2014, 2016; Singh and Slabunov, 2015a; Saha et al., 2016; Joshi et al., 2017; Slabunov and Singh, 2019; Singh et al., 2019a, b). Further, the earliest continental crust of the BC was formed as early as ~3.55 Ga and Hf isotope data provide evidence for earliest crust accretion during 3.85–3.60 Ga (Kaur et al., 2014 and Saha et al., 2016).

Archean TTG gneisses display secular changes in composition signifying transformation in geodynamic setting of their formation (Smithies, 2000; Martin and Moyen, 2002). Younger TTG gneisses (<3.0 Ga) show enhanced MgO, Mg#, Cr and Ni compared to their older counterparts (Martin and Moyen, 2002; Hoffmann et al., 2014). It is worthy to note that majority of the <3.0 Ga TTGs are low-HREE type with dissimilar enrichment of Sr (Laurent et al., 2014). This enrichment is probably connected to the growing role of subduction-like processes in the origin of TTG towards the end of the Archean (Laurent et al., 2014). The subsequent TTG melt intermingled with the overlying mantle segment, thus enhancing their mantle element (MgO, Ba, Cr and Ni) contents. On the other hand, Paleoarchean TTG gneisses commonly display little indication of interaction with mantle melts (Smithies, 2000; Martin and Moyen, 2002; Moyen and Martin, 2012). In many Archean terrains reveal synchronous high-HREE and low-HREE TTG gneisses occurrences, thus implying an intracrustal genesis unrelated to subduction which is recorded in the

Kaapvaal and Pilbara cratons (Champion and Smithies, 2007; Moyen and Martin, 2012; Van Kranendonk et al., 2015). Partial melting of mafic crust at variable depth can elucidate incidence of synchronous TTGs of both the types.

The oldest TTG (3.55 Ga) from the Kuraicha, Mauranipur belt in the CBGGT have mainly high-Al, low-HREE trondhjemite character and was generated by reworking of older crust (Hf model ages of 3.80–3.95 Ga) (Kaur et al., 2014). In this study we recognized synchronous high-HREE and low-HREE Paleoarchean TTG gneisses (3.44–3.20 Ga) in the CBGGT (Fig. 13a–d), thus implying an intracrustal genesis unrelated to subduction (Champion and Smithies, 2007; Van Kranendonk et al., 2015). The formation of synchronous TTGs of both the types can be possible by partial melting of mafic crust at variable depth.

On the other hand, studied TTG samples (BC.19, BC.41, BC.45 and BC.61) in this contribution display high MgO, Mg#, Cr and Ni that would be probable in case of melts produced from subducted oceanic crust which should have pass over the overlying mantle melts (Smithies, 2000; López et al., 2006). Consequently, the presence of two distinct Paleoarchean TTG types in the CBGGT can at best be elucidated by melting of mafic crust at different depths within an oceanic plateau and interacted with mantle melts (Smithies, 2000; Martin and Moyen, 2002; Champion and Smithies, 2007; Halla et al., 2009; Moyen and Martin, 2012) foremost to the evolution of early cratonic nucleus in the Bundelkhand Craton. Additionally, Martin et al. (2014) proposed that formation of Archean TTGs required a LILE-enriched basaltic source similar to oceanic plateau basalts, and subduction of oceanic plateau, before melting at its base, was the main mechanism for TTG production during Archean.

The record of the Paleoarchean mafic-ultramafic volcanic rocks identified in the Babina and Mauranipur belts which age of intrusion is poorly constrained. Recently, Singh et al. (2019a) have first time reported a bulk-rock Sm–Nd isochron age of 3.43 ± .16 Ga from the Babina and Mauranipur belts in the CBGGT and are similar to the age of common TTG gneisses in the CBGGT which suggest that felsic plutonism and mafic volcanism were synchronous in the Mauranipur and Babina belts. These mafic-ultramafic volcanics were produced from a depleted mantle source and evolved through fractional crystallization associated with crustal assimilation (Singh et al., 2019a). On the other hand, Singh et al. (2018) suggested that they were formed in plume-arc related geodynamic environment and represent plausible remnants of oceanic crust.

The 2.70–2.50 Ga granitoids plutonism is globally documented as a major crust-forming event in early Earth (Condie et al., 2005). This study also provides unequivocal evidence for the extensive crust-forming episode during late Archean (~2.55 Ga). The Neoarchean crustal evolution of the CBGGT recorded in TTG gneisses, granodiorites, sanukitoids, felsic volcanics, and anatectic granites, and were took place during 2810–2500 Ma (Tables S3) in the BC which is similar to global crust-forming event. The Neoarchean granitoids constitute ~85% in volume of the CBGGT whereas ~75% of the whole cratonic part of the BC, among granitoids rocks, anatectic granites predominate (Figs. 1b and 2; Tables S3; Mondal et al., 2002; Kaur et al., 2016; Singh and Slabunov, 2015a; Joshi et al., 2017; Slabunov and Singh, 2019; Singh et al., 2019b). The new zircon chronological data presented in this study conform that the TTG magmatic were emplaced at ~2701–2669 Ma (Verma et al., 2016), and voluminous high-K granitoids were intruded during 2585–

2500 Ma (Tables S3; Mondal et al., 2002; Kaur et al., 2016; Verma et al., 2016; Joshi et al., 2017; Singh et al., 2019b). Neoarchean TTG magmatic event was started after ~488 Ma magmatic cessation subsequent to Paleoarchean TTG magmatism. After this magmatic event again magmatic shutdown for at least 93–115 Ma and after that after sanukitoid magmatism were began at ca. 2.57 Ga (Tables S3).

The Neoarchean (2.71–2.67 Ga) TTG gneisses in the CBGGT are show high-HREE (BC.27) and low-HREE (BC.31 and BC.50) both type of characters which is a very similar geochemical character and petrogenesis with Paleoarchean TTG gneisses of the CBGGT in the BC (Fig. 13a–d). The high angle subduction of oceanic slab and interaction of subsequent slab melts with mantle segment during their ascent could be linked to elevated content of compatible elements in the high-HREE TTG gneisses, which is very similar to well described transitional TTGs (Martin and Moyen, 2002; Foley et al., 2002; Dey et al., 2009; Laurent et al., 2014; Jayananda et al., 2018). Nevertheless, interaction of slab melts with superimposing mantle segment (peridotitic) can enhance MgO, Ni and Cr contents (compatible elements) in the earlier but fail to explanation for recognized elevated contents of Rb, Ba, Sr, LREE. Consecutively, the production of enriched arc crust and its succeeding melting with significant mantle material input can be measured (Smithies, 2000; Martin and Moyen, 2002; Champion and Smithies, 2007; Dey et al., 2009; Halla et al., 2009; Moyen and Martin, 2012; Polat, 2012; Jayananda et al., 2018). The studied Neoarchean high-HREE TTG gneisses were formed by high-degree melting of thickened enriched arc slab and interaction with mantle segment during their ascent at around 2.71–2.67 Ga in the CBGGT. On the other hand, Neoarchean low-HREE TTG gneiss (BC.31 and BC.50) reveal that they were formed by reworking of older

mafic and/or felsic crust which comprise partial melting of deep-seated mafic crust in the garnet stability field (Kaur et al., 2014, 2016; Saha et al., 2016; Nasipuri et al., 2019). These observations elucidate similar petrogenetic and geodynamic processes during Paleoarchean to Neoarchean eras.

Recently, Joshi et al. (2017) and Singh et al. (2019b) identified sanukitoids plutons in the BC, mainly in the CBGGT, and they were emplaced at ~2.57–2.56 Ga (Tables S3). These plutons represent late Archean juvenile magmatic growth events which are important evidence for the change in the geodynamic and petrogenetic processes in the BC. Bundelkhand sanukitoids display evolved nature (variable range of SiO_2, elevated Ba, Sr, K, LREE with higher to moderate Mg#, Ni, Cr, and negative $\varepsilon_{Nd}(t)$) (Joshi et al., 2017 and Singh et al.,2019b). Integrated geochemical and isotopic studies advocate that the sanukitoid rocks formed by the mixing of mantle melts with crustal generated granitic melt (anatectic melt) and were followed by homogenization at lower levels of intrusion (Joshi et al., 2017; Singh et al., 2019b). The existence of older inherited zircon (2.91 Ga, 2.84 Ga, 2.64 Ga and 2.61 Ga) in sanukitoids also support this geodynamic model (Tables S3). The tectonic settings of sanukitoids magma production and intrusion have been proposed to subduction zone related tectonics (Joshi et al., 2017; Singh et al.,2019b). Similar petrogenetic and geodynamic process have been described in various cratonic bodies (Halla, 2005; Jayananda et al., 2000; Moyen et al., 2003a, b; Heilimo et al., 2010; Ma et al., 2013; Dey et al., 2017; Jayananda et al., 2018; Terentiev and Santosh, 2018). Sanukitoid magmatism relates to the terminal event of major Archean juvenile growth in the BC and they were emplaced at least 93–115 Ma after the closure of the Neoarchean TTG accretion (Tables S3). The U–Pb zircon dating

of sanukitoid, granodiorite and anatectic granite rocks of the CBGGT suggest synchronous emplacement in between 2.58– 2.54 Ga (Tables S3).

A number of studies on anatectic granite suggest that the they were formed by the intense partial melting of crustal rocks (mainly felsic rocks) by collision mechanism through the cratonic stabilization ca. 2.5 Ga (Mondal et al., 2002; Kaur et al., 2016; Joshi et al., 2017; Singh et al., 2019b). The felsic volcanism of the Babina belt (Singh and Slabunov, 2015a) and felsic plutonism (voluminous anatectic granites) were coeval in the CBGGT (Mondal et al., 2002; Kaur et al., 2016; Joshi et al., 2017; Singh et al., 2019b). We proposed the BC shaped by the amalgamation of several micro-continents which were fused together along Neoarchean greenstone sequences at ca. 2.5 Ga (Mondal et al., 2002; Singh and Slabunov, 2015a; Singh et al., 2019b). The voluminous high-K granitoids may have been produced during the incorporation micro-continents which were happened by subduction and collision mechanism, and they are similar to those of modern plate tectonic systems, but in much trivial scale (Singh et al., 2019b). The entire Archean continental crust participated in the final cratonization through slow cooling up to 2.48 Ga followed by injection of quartz reefs and mafic dyke swarms at ca. 2.10–1.10 Ga (Pati et al., 2007; Pradhan et al., 2012). These geological events indicate a secular change in their composition from Paleoarchean TTG-domination through Neoarchean sanukitoids (s.l.) to anatectic granites by reworking of the pre-existing continental crust by including various geodynamic environments in the BC during Paleoarchean to Neoarchean eras (Mondal et al., 2002; Mohan et al., 2012; Saha et al., 2011, 2016; Kaur et al., 2014, 2016; Singh and Slabunov, 2015a, b; Verma et al., 2016; Joshi et al., 2017; Singh et al., 2018, Singh et al., 2019a, b).

6.4. Comparison with Archean cratons globally

The Archean granite–greenstone terranes record oldest crustal fragments on the Earth, allows an understanding of the development of the early Earth. The Archean geological events of the CBGGT in the BC be able to compared with other Archean terranes globally (e.g. Singhbhum and Dharwar cratons in the Indian shield, North China Craton (NCC), Pilbara and Yilgarn cratons in the western Australia, and Kaapvaal and Tanzania Cratons in southern Africa). These Archean cratons comprise TTG gneisses, greenstone belts, high-K granitoids and anatectic granites ranging in age from ~3.5 to 2.5 Ga (Laurent et al., 2014; Nelson et al., 2014; Kaur et al., 2016; Jayananda et al., 2018). A great number of geochronological studies from various cratons have suggested that four main peaks of igneous magmatic events (e.g. 3300 Ga, 2700 Ga, 2680 Ga and 2500 Ga) (Condie et al., 2009; Condie and Aster, 2010).

The early (3.55–3.59 Ga) geological growth of the BC (Kaur et al., 2014; Saha et al., 2016) has identical age to that of TTG gneisses and granites (3.58–3.56 Ga) from Singhbhum Craton in the Indian shield (Ghosh, 2004; Rajesh et al., 2009). In addition, ca. 3.50 Ga greenstone sequence from Singhbhum Craton represent oldest greenstone sequence in the Indian shield (Mukhopadhyay et al., 2008; Upadhyay et al., 2014). Whereas ~3.34 Ga mafic-ultramafic rocks also identified in the same craton (Sharma et al., 1994; Mondal, 2009; Chaudhuri et al., 2017) which is identical to 3.44 Ga mafic-ultramafic units of the Babina greenstone belt in the BC (Singh et al., 2019a). The Dharwar Craton show five major periods of Archean continental crustal growth during ~3.45–3.30 Ga, 3.23–3.15 Ga, 3.00–2.96 Ga, 2.70–2.60 Ga, 2.56–2.50 Ga (Jayananda et al., 2000, 2018; Chardon et al., 2002, 2011; Moyen et

al., 2003a, b; Peucat et al., 2013). Similar Archean crustal growth events recognized in the BC which represent five major felsic magmatic episodes of ~3.55 Ga, 3.45–3.30 Ga, 3.28–3.20 Ga, 2.73–2.67 Ga, and 2.58–2.50 Ga. These felsic magmatic are sub-contemporaneous with the episodes of greenstone volcanism in the CBGGT (Mondal et al., 2002; Saha et al., 2011, 2016; Kaur et al., 2014, 2016; Singh and Slabunov, 2015a; Verma et al., 2016; Joshi et al., 2017; Slabunov and Singh, 2019; Singh et al., 2019a, b). In addition, Bundelkhand TTGs zircons show Hf-model ages of about 3.95 Ga. Similar Hf-model ages identified in the Dharwar Craton which proposed that prolonged reworking of Eoarchean mafic crust (Santosh et al., 2016) and Laurent and Zeh (2015) suggested that this trend possibly due to product from the reworking of crustal rocks in light of crust–mantle interaction in the subduction zone related setting.

The North China Craton (NCC) records 3.8 Ga old earliest continental crust (Liu et al., 1992, 2007, 2008; Wan et al., 2005, 2013; Lui, 2008) which is so for older than Bundelkhand earliest continental crust (Kaur et al., 2014; Saha et al., 2016). On the other hand, major Archean crustal-growth episodes of the NCC during ~3.3 Ga, 3.0–2.9 Ga, 2.72–2.60 Ga and 2.55–2.50 Ga and assembly of micro-continents have been documented in this craton (Wan et al., 2012; Yang et al., 2008; 2016a, b, Zhai and Santosh, 2011; Yang and Santosh, 2017). These magmatic events of the NCC indicate a similar crustal growth history with the BC, predominantly with respect to Neoarchean TTGs, juvenile (sanukitoids) and high-K granitoids magmatism and crustal reworking (Zhai and Santosh, 2011; Ma et al., 2013; Jihang et al., 2016). In conclusion, the NCC Neoarchean (2.70–2.50 Ma) crustal growth events (Ma et al.,

2013; Jiang et al., 2016) synchronous with the crustal growth of the BC during Neoarchean (2.70–2.50 Ma).

The Paleoarchean crustal growth history of the BC has various events shared with that of the Pilbara Craton in the Western Australia. The Pilbara Craton documents emplacement of ample ~3.50–3.22 Ga TTG gneisses and granitoids with a traces of Hadean rocks (~3.80–3.60 Ga) (Smithies and Champion, 2009; Hickman and Van Kranendonk, 2012) which is similar with the 3.55–3.20 Ga TTG gneisses of the BC (Mondal et al., 2002; Kaur et al., 2014, 2016; Saha et al., 2016; Joshi et al., 2017). While rocks of ~3.55 Ga have a very limited record (Kaur et al., 2014; Saha et al., 2016) and zircons have Hf-model ages of about 3.95 Ga that advocate possible involvement older crusts (>3.6 Ga) in their origin (Kaur et al., 2014; Saha et al., 2016; Joshi et al., 2017). Such type of older crust possibly has been derived from ancient cratonic terrains (e.g. Pilbara or Kaapvaal Cratons). The Bundelkhand Neoarchean TTG gneisses have a are very similar magmatic ages with that of the Yilgarn Craton transitional TTG which emplaced at ca. 2.70–2.63 Ga with remnants of 3.70–3.01 Ga rocks (Champion and Smithies, 2003; Cassidy et al., 2006).

Geochronological studies in the Kaapvaal Craton suggest Paleoarchean TTGs and greenstone sequences were formed between 3.46 and 3.18 Ga with remnants as old as 3.66 Ga and a predominant Meso- to Neoarchean episode between 3.11 and 2.67 Ga which is recorded in the gneisses, greenstones and the granitoids (de Wit et al. 1992; Kröner et al., 1996, 2014, 2016; Zeh et al., 2007, 2009, 2011; Schoene et al., 2009; Laurent and Zeh, 2015). The Paleoarchean (3.46–3.18 Ga) TTG gneisses and mafic sequences in the Pietersburg and Giyani greenstone belts are coeval which suggest that a coeval felsic plutonism and mafic volcanism in the

Kaapvaal Craton (de Wit et al. 1992; Laurent and Zeh 2015). The Similar coeval felsic plutonism (TTGs) and mafic volcanism (mafic-ultramafic sequences) magmatic event identified from the CBGGT in the BC (Kaur et al., 2016; Saha et al., 2016; Nasipuri et al., 2019; Singh et al., 2019a, this study). The ca. 2.61–2.59 sanukitoid rocks of the Limpopo belt are comparable with that of 2.70–2.67 Ga TTGs in the CBGGT of the BC (Verma et al., 2016; Singh et al., 2019b, this study). Even similar juvenile magmatism (transitional TTGs and sanukitoids) are documented in the Dharwar Craton (Jayananda et al., 1995, 2018; Chardon et al., 2011; Guitreau et al., 2017). The Tanzania Craton has preserves Mesoarchean crustal growth events which is recorded in the orthogneisses show ages of ~3.23–3.14 Ga with >3.60 Ga old zircon xenocryst. These ages comparable with few TTG gneiss plutons of the CBGGT in the BC (Tables S3; Mondal et al., 2002; Kaur et al., 2016; this study). The Neoarchean TTG gneiss ages of the BC display equivalent ages with that of the hornblende granitoids of the Tanzania Craton were emplace in between ca. 2.72 Ga and 2.64 Ga. In addition, ca. 2.81 Ga and 2.51 Ga old greenstone sequences have been reported in the Tanzania Craton (Kabete et al., 2012b) which are comparable with the felsic volcanics of the Mauranipur (2.81 Ga and 2.55 Ga) and Babina (2.54 Ga) belts in the CBGGT (Singh and Slabunov, 2015a; Slabunov and Singh, 2019).

In conclusion, the geochronological studies of the Archean rocks in the BC suggest seven major crustal growth and reworking episodes of ~3.59–3.51 Ga, 3.44–3.39 Ga, 3.36–3.30, Ga 3.28–3.20 Ga, 2.73–2.70 Ga, 2.69–2.67, and 2.58–2.50 Ga and zircons reveal metamorphic events at ~3.30 Ga, 3.29 Ga, 3.20 Ga, 2.78 Ga, 2.55 Ga, 2.48 Ga and ~2.13 Ga (Mondal et al., 2002; Saha et al., 2011, 2016; Kaur et al., 2014, 2016; Singh and Slabunov, 2015a; Verma et al., 2016; Joshi et al., 2017;

Slabunov and Singh, 2019; Nasipuri et al., 2019; Singh et al., 2019a, b). The Archean magmatic and metamorphic histories in the BC are synchronous with the common pattern of global Archean crustal growth and reworking at 3.5–3.2 Ga, 2.8–2.7 Ga, and 2.6–2.5 Ga (Condie and Aster, 2010).

7. Conclusions

In this contribution, we report zircon U–Pb geochronology, whole-rock geochemistry and Sm–Nd isotopes on TTG gneisses and high-K granitoids that are representative of all different type of felsic plutonic rocks identified from the CBGGT in the CB. This study constraint to understanding of the crust–mantle evolution, continental growth and reworking throughout the entire Archean to comprehend continental forming events of the Earth. The following main conclusions are obtained:

(1) The CBGGT has a complex evolutionary history with multi-stage crustal growth, recording nearly all important Archean geological events of the Earth.

(2) Geochronology of felsic plutonic rocks of the BC that propose seven major periods of felsic crust formation at ca. 3.51 Ga, 3.44–3.39 Ga, 3.36–3.30, Ga 3.28–3.20 Ga, ~2.71 Ga, ~2.67 Ga, and 2.57–2.50 Ga which are synchronous with the common pattern of global Archean felsic crustal growth and reworking at ca. 3.5–3.2 Ga, 2.8–2.7 Ga, and 2.6–2.5 Ga.

(3) TTG gneisses represent basement unit and the oldest rocks in the BC. The reported zircon U–Pb ages show four distinct episodes of Paleoarchean TTG magmatism happened between ~3.51 Ga and 3.20 Ga and two discrete phases of Neoarchean TTG magmatism generated between ~2.73 Ga and 2.67 Ga in the CBGGT.

(4) The major continental growth occurred between 2.58 Ga and 2.50 Ga that documented in the sanukitoid, granodiorite and anatectic granite rocks and are occupied largest part of the BC. These granitoids reveal a synchronous magmatism.

(5) The Paleoarchean TTG gneiss and mafic–ultramafic volcanic rocks endorsed that a coeval felsic plutonism and mafic volcanism occurred at ~3.44 Ga in this terrane.

(6) The $\varepsilon_{Nd}(t)$ values ranging between +4.3 and –0.5 for Paleoarchean TTG gneisses, +4.5 for Neoarchean TTG gneiss, and ranging from −3.6 to −1.6, for high-K granitoids.

(7) Whole-rock element and Nd isotopic compositions suggest that Paleoarchean TTG gneisses are low-HREE and high-HREE nature and generated by the partial melting of mafic crust at different depths within an oceanic plateau and interacted with the mantle melts. Further, a Neoarchean TTG gneiss are the low-HREE nature and was formed by the partial melting of deep-seated mafic crust in the garnet stability field with trivial involvement of ancient crustal material.

(8) Juvenile magmatic rocks unveil that they were generated by the mixing of the mantle melts with crustal originated melt (anatectic melt) and were followed by homogenization at lower levels of intrusion in the subduction zone setting.

(9) Lastly, the amalgamation of varied micro-blocks happened by the arc-continent collision mechanism and frequent slab break-off between north and south blocks of the BC during late Archean. This event displays evidence that the BC did not merge together until ~2.50 Ga. The ample anatectic granites were generated by intensive

partial melting of the continental crust in an arc-continent collision, representing the final cratonization of the BC.

Acknowledgements

PKS gratefully acknowledge the doctoral scholarship [grant #612752] from the National Council of Science and Technology (CONACYT), Mexico, and funding source from IPICYT (internal grant). PKS is also grateful to Dr. Courtney Parkins-Ferron for the language editing. SKV and EPO thank to the São Paulo Research Foundation (FAPESP) for the grants [# 2012/07243-3 and 2012/15824-6], which were used in the analytical purpose. SKV is grateful to Newton Advance Fellowship award–The Royal Society, UK for the grant [NA160116]. We appreciate Dr. Erica, Margrates, Bia, Paola, and Mauricio for their assistance during analysis at UNICAMP. We are grateful to Dr. Carmen Galindo Francisco and Dr. Jose Manuel Fuenlabrada Perez for ID-TIMS isotopic analyses.

References:

Absar, N., Raza, M., Roy, M., Naqvi, S. M., Roy, A. K., 2009. Composition and weathering conditions of Paleoproterozoic upper crust of Bundelkhand craton, Central India: records from geochemistry of clastic sediments of 1.9 Ga Gwalior Group. Precambrian Research 168, 313–329.

Acharyya, S.K., 2003. The nature of Mesoproterozoic Central Indian Tectonic Zone with exhumed and reworked older granulites. Gondwana Research 6, 197–214.

Ahmad, T., Tarney, J., 1994. North Indian Proterozoic volcanic products of lithosphere extension: geochemical studies bearing on lithosphere derivation rather than crustal contamination. Rifted basin and aulocogens 130–147.

Almeida, JDAC, Dall'Agnol, R., de Oliveira, MA, Macambira, MJB, Pimentel, MM, Rämö, OT, da Silva Leite, AA, 2011. Zircon geochronology, geochemistry and origin of the TTG suites of the Rio Maria granite-greenstone terrane: Implications for the growth of the Archean crust of Carajás province, Brazil. Precambrian Research 187, 201–221.

Atherton, M. P., Petford, N., 1993. Generation of sodium-rich magmas from newly underplated basaltic crust. Nature 362, 144.

Bas, M. L., Maitre, R. L., Streckeisen, A., Zanettin, B., IUGS Subcommission on the Systematics of Igneous Rocks., 1986. A chemical classification of volcanic rocks based on the total alkali-silica diagram. Journal of Petrology 27, 745–750.

Basu, A. K., 1986. Geology of parts of the Bundelkhand granite massif central India. In: Records, Geological Survey of India (Ed.) 117, 61–124.

Belousova, E. A., Kostitsyn, Y. A., Griffin, W. L., Begg, G. C., O'Reilly, S. Y., Pearson, N. J., 2010. The growth of the continental crust: constraints from zircon Hf-isotope data. Lithos 119, 457–466.

Cassidy, K.F., Champion, D.C., Krapez, B., Barley, M.E., Brown, S.J.A., Blewett, R.S., Groenewald, P.B., Tyler, I.M., 2006. A Revised Geological Framework for the Yilgarn Craton: Geological Survey of Western Australia. (Record 2006/8, 8p).

Cawood, P. A., Hawkesworth, C. J., Dhuime, B., 2013. The continental record and the generation of continental crust. Bulletin 125, 14–32.

Champion, D. C., Smithies, R. H., 2007. .3 Geochemistry of Paleoarchean Granites of the East Pilbara Terrane, Pilbara Craton, Western Australia: Implications for Early Archean Crustal Growth. Developments in Precambrian Geology 15, 369–409.

Chardon, D., Jayananda, M., Peucat, J. J., 2011. Lateral constrictional flow of hot orogenic crust: Insights from the Neoarchean of south India, geological and geophysical implications for orogenic plateaux. Geochemistry, Geophysics, Geosystems 12.

Chardon, D., Peucat, J. J., Jayananda, M., Choukroune, P., Fanning, C. M., 2002. Archean granite-greenstone tectonics at Kolar (south India): Interplay of diapirism and bulk inhomogeneous contraction during juvenile magmatic accretion. Tectonics 21, 7–1.

Chaudhuri, T., Satish-Kumar, M., Mazumder, R., Biswas, S., 2017. Geochemistry and Sm-Nd isotopic characteristics of the Paleoarchean Komatiites from Singhbhum Craton, Eastern India and their implications. Precambrian Research 298, 385–402.

Condie, K. C., 2005a. High field strength element ratios in Archean basalts: a window to evolving sources of mantle plumes?. Lithos 79, 491–504.

Condie, K. C., 2005b. TTGs and adakites: are they both slab melts?. Lithos 80, 33–44.

Condie, K. C., Aster, R. C., 2010. Episodic zircon age spectra of orogenic granitoids: the supercontinent connection and continental growth. Precambrian Research, 180, 227–236.

Condie, K. C., Kröner, A., 2008. When did plate tectonics begin? Evidence from the geologic record. In When did plate tectonics begin on planet Earth. Geological Society of America Special Papers 440, 281–294.

Condie, K. C., O'Neill, C., 2010. The Archean-Proterozoic boundary: 500 My of tectonic transition in Earth history. American Journal of Science 310, 775–790.
Corfu, F., Hanchar, JM, Hoskin, PW and Kinny, P., 2003. Atlas of zircon textures. Reviews in mineralogy and geochemistry 53, 469–500.
Cotta, A. J. B., Enzweiler, J., 2009. Quantification of major and trace elements in water samples by ICP-MS and collision cell to attenuate Ar and Cl-based polyatomic ions. Journal of Analytical Atomic Spectrometry 24, 1406–1413.
Dall'Agnol, R., da Cunha, IRV, Guimarães, FV, de Oliveira, DC, Teixeira, MFB, Feio, GRL, Lamarão, CN, 2017. Mineralogy, geochemistry, and petrology of Neoarchean ferroan to magnesian granites of Carajás Province, Amazonian Craton: The origin of hydrated granites associated with charnockites. Lithos 277, 3–32.
Davis, W. J., Hegner, E., 1992. Neodymium isotopic evidence for the tectonic assembly of Late Archean crust in the Slave Province, northwest Canada. Contributions to Mineralogy and Petrology 111, 493–504.
de Wit, M.J., Roering, C., Hart, R.J., Armstrong, R.A., de Ronde, R.E.J., Green, R.W., Tredoux, M., et al., 1992. Formation of an Archaean continent. Nature 357, 553–562.
Dey, S., Halla, J., Kurhila, M., Nandy, J., Heilimo, E., Pal, S., 2017. Geochronology of Neoarchaean granitoids of the NW eastern Dharwar craton: implications for crust formation. Geological Society, London, Special Publications 449, 89–121.
Dey, S., Rai, AK, Chaki, A., 2009. Geochemistry of granitoids of Bilgi area, northern part of eastern Dharwar craton, southern India-Example of transitional TTGs derived from depleted source. Journal of the Geological Society of India 73, 854.
Dhuime, B., Hawkesworth, C. J., Cawood, P. A., Storey, C. D., 2012. A change in the geodynamics of continental growth 3 billion years ago. Science 335, 1334–1336.
Dhuime, B., Hawkesworth, C., Cawood, P. 2011. When continents formed. Science 331, 154–155.
Dickinson, W.R., Gehrels, G.E., 2003. U-Pb ages of detrital zircons from Permian and Jurassic eolian sandstones of the Colorado Plateau, USA: paleogeographic implications. Sedimentary Geology 163, 29–66.
Drummond, M. S., Defant, M. J., 1990. A model for trondhjemite-tonalite-dacite genesis and crustal growth via slab melting: Archean to modern comparisons. Journal of Geophysical Research: Solid Earth 95, 21503–21521.
Farooqui, S. A., Singh, A. K., 2006. Platinum mineralization in Ikauna Area, Lalitpur District, Uttar Pradesh. Journal Geological Society of India 68, 582–584.
Foley, S., Tiepolo, M., Vannucci, R., 2002. Growth of early continental crust controlled by melting of amphibolite in subduction zones. Nature 417, 837.
Ghosh, J. G., 2004. 3.56 Ga tonalite in the central part of the Bastar craton, India: oldest Indian date. Journal of Asian Earth Sciences 23, 359–364.
Gokarn, S. G., Rao, C. K., Selvaraj, C., Gupta, G., Singh, B. P., 2013. Crustal evolution and tectonics of the Archean Bundelkhand craton, Central India. Journal of the Geological Society of India 82, 455–460.
Guice, G. L., McDonald, I., Hughes, H. S. and Anhaeusser, C. R., 2019. An evaluation of element mobility in the Modderfontein ultramafic complex, Johannesburg: Origin as an Archaean ophiolite fragment or greenstone belt remnant?. Lithos 332–333, 99-119.
Guitreau, M., Blichert-Toft, J., Martin, H., Mojzsis, S. J., Albarède, F., 2012. Hafnium isotope evidence from Archean granitic rocks for deep-mantle origin of continental crust. Earth and Planetary Science Letters 337, 211–223.
Halla, J., 2005. Late Archean high-Mg granitoids (sanukitoids) in the southern Karelian domain, eastern Finland: Pb and Nd isotopic constraints on crust− mantle interactions. Lithos 79, 161–178.

Halla, J., van Hunen, J., Heilimo, E., Hölttä, P., 2009. Geochemical and numerical constraints on Neoarchean plate tectonics. Precambrian Research 174, 155–162.
Hawkesworth, C. J., Dhuime, B., Pietranik, A. B., Cawood, P. A., Kemp, A. I. S., Storey, C. D., 2010. The generation and evolution of the continental crust. Journal of the Geological Society 167, 229–248.
Hawkesworth, C., Cawood, P. A., Dhuime, B., 2019. Rates of generation and growth of the continental crust. Geoscience Frontiers 10, 165–173.
Hawkesworth, C., Cawood, P., Dhuime, B., 2013. Continental growth and the crustal record. Tectonophysics 609, 651–660.
Hawkesworth, C., Cawood, P.A., Dhuime, B., 2018. Rates of generation and growth of the continental crust. Geoscience Frontiers 10, 165–173.
Heilimo, E., Halla, J., Hölttä, P., 2010. Discrimination and origin of the sanukitoid series: geochemical constraints from the Neoarchean western Karelian Province Finland. Lithos 115, 27–39.
Hickman, A. H., Van Kranendonk, M. J., 2012. Early Earth evolution: evidence from the 3.5-1.8 Ga geological history of the Pilbara region of Western Australia. Episodes 35, 283–297.
Hoffmann, J. E., Münker, C., Næraa, T., Rosing, M. T., Herwartz, D., Garbe-Schönberg, D., Svahnberg, H., 2011. Mechanisms of Archean crust formation inferred from high-precision HFSE systematics in TTGs. Geochimica et Cosmochimica Acta 75, 4157–4178.
Hoffmann, J. E., Nagel, T. J., Muenker, C., Næraa, T., Rosing, M. T., 2014. Constraining the process of Eoarchean TTG formation in the Itsaq Gneiss Complex, southern West Greenland. Earth and Planetary Science Letters 388, 374–386.
Huang, H., Polat, A., Fryer, B. J., 2013. Origin of Archean tonalite–trondhjemite–granodiorite (TTG) suites and granites in the Fiskenæsset region, southern West Greenland: implications for continental growth. Gondwana Research 23, 452–470.
Jayananda, M., Moyen, J. F., Martin, H., Peucat, J. J., Auvray, B., Mahabaleswar, B., 2000. Late Archaean (2550–2520 Ma) juvenile magmatism in the Eastern Dharwar craton, southern India: constraints from geochronology, Nd–Sr isotopes and whole rock geochemistry. Precambrian Research 99, 225–254.
Jayananda, M., Santosh, M., Aadhiseshan, K. R., 2018. Formation of Archean (3600–2500 Ma) continental crust in the Dharwar Craton, southern India. Earth-Science Reviews 181, 12–42.
Jiang, N., Guo, J., Fan, W., Hu, J., Zong, K., Zhang, S., 2016. Archean TTGs and sanukitoids from the Jiaobei terrain, North China craton: Insights into crustal growth and mantle metasomatism. Precambrian Research 281, 656–672.
Joshi, K. B., Bhattacharjee, J., Rai, G., Halla, J., Ahmad, T., Kurhila, M., Choudhary, A. K., 2017. The diversification of granitoids and plate tectonic implications at the Archaean–Proterozoic boundary in the Bundelkhand Craton, Central India. Geological Society, London, Special Publications 449, 123–157.
Kabete, J.M., McNaughton, N.J., Groves, D.I., Mruma, A.H., 2012. Reconnaissance SHRIMP 851 U-Pb zircon geochronology of the Tanzania Craton: evidence for Neoarchean granitoid-greenstone belts in the Central Tanzania Region and the Southern East Africa Orogen. Precambrian Research 216−219, 232–266.
Kaur, P., Zeh, A., Chaudhri, N., 2014. Characterisation and U–Pb–Hf isotope record of the 3.55 Ga felsic crust from the Bundelkhand Craton, northern India. Precambrian Research 255, 236–244.
Kaur, P., Zeh, A., Chaudhri, N., 2019. Archean crustal evolution of the Aravalli Banded Gneissic Complex, NW India: Constraints from zircon U-Pb ages, Lu-Hf isotope

systematics, and whole-rock geochemistry of granitoids. Precambrian Research 327, 81–102.
Kaur, P., Zeh, A., Chaudhri, N., Eliyas, N., 2016. Unravelling the record of Archaean crustal evolution of the Bundelkhand Craton, northern India using U–Pb zircon–monazite ages, Lu–Hf isotope systematics, and whole-rock geochemistry of granitoids. Precambrian Research 281, 384–413.
Keller, C.B., Schoene, B., 2012. Statistical geochemistry reveals disruption in secular lithospheric evolution about 2.5 Gyr ago. Nature 485, 490.
Kleinhanns, I. C., Kramers, J. D., Kamber, B. S., 2003. Importance of water for Archaean granitoid petrology: a comparative study of TTG and potassic granitoids from Barberton Mountain Land, South Africa. Contributions to Mineralogy and Petrology 145, 377–389.
Kröner, A., Anhaeusser, C. R., Hoffmann, J. E., Wong, J., Geng, H., Hegner, E., Liu, D., 2016. Chronology of the oldest supracrustal sequences in the Palaeoarchaean Barberton Greenstone Belt, South Africa and Swaziland. Precambrian Research 279, 123–143.
Kröner, A., Hegner, E., Wendt, J. I., Byerly, G. R. 1996. The oldest part of the Barberton granitoid-greenstone terrain, South Africa: evidence for crust formation between 3.5 and 3.7 Ga. Precambrian Research 78, 105–124.
Kröner, A., Hoffmann, J. E., Xie, H., Münker, C., Hegner, E., Wan, Y., Yang, J., 2014. Generation of early Archaean grey gneisses through melting of older crust in the eastern Kaapvaal craton, southern Africa. Precambrian Research 255, 823–846.
Laurent, O., Martin, H., Doucelance, R., Moyen, J. F., Paquette, J. L., 2011. Geochemistry and petrogenesis of high-K “sanukitoids” from the Bulai pluton, Central Limpopo Belt, South Africa: Implications for geodynamic changes at the Archaean–Proterozoic boundary. Lithos 123, 73–91.
Laurent, O., Martin, H., Moyen, J. F., Doucelance, R., 2014. The diversity and evolution of late-Archean granitoids: Evidence for the onset of “modern-style” plate tectonics between 3.0 and 2.5 Ga. Lithos 205, 208–235.
Laurent, O., Paquette, J. L., Martin, H., Doucelance, R., Moyen, J. F., 2013. LA-ICP-MS dating of zircons from Meso-and Neoarchean granitoids of the Pietersburg block (South Africa): crustal evolution at the northern margin of the Kaapvaal craton. Precambrian Research 230, 209–226.
Laurent, O., Zeh, A., 2015. A linear Hf isotope-age array despite different granitoid sources and complex Archean geodynamics: example from the Pietersburg block (South Africa). Earth and Planetary Science Letters 430, 326–338.
Liang, Q., Jing, H. and Gregoire, D. C., 2000. Determination of trace elements in granites by inductively coupled plasma mass spectrometry. Talanta 51, 507–513.
Liou, P., Guo, J., 2019. Generation of Archaean TTG Gneisses Through Amphibole-Dominated Fractionation. Journal of Geophysical Research: Solid Earth 124, 3605–3619.
Liu, D. Y., Wan, Y. S., Wu, J. S., Wilde, S. A., Zhou, H. Y., Dong, C. Y., Yin, X. Y., 2007. Eoarchean rocks and zircons in the North China Craton. Developments in Precambrian Geology 15, 251–273.
Liu, D.Y., Nutman, A.P., Compston, W., Wu, J.S., Shen, Q.H., 1992. Remnants of ≥3800 Ma crust in the Chinese part of the Sino-Korean craton. Geology 20,339–342.
Liu, Y., Gao, S., Kelemen, PB, Xu, W., 2008. Recycled crust controls contrasting source compositions of Mesozoic and Cenozoic basalts in the North China Craton. Geochimica et Cosmochimica Acta 72, 2349–2376.
López, S., Fernández, C., Castro, A., 2006. Evolution of the Archaean continental crust: Insights from the experimental study of Archaean granitoids. Current Science 607–621.

Ludwig, K.R., 2012. User's Manual for Isoplot 3.75: A Geochronological Toolkit for Microsoft Excel. Berkeley Geochronology Center, Speical Publication No. 5.
Ma, X., Guo, J., Liu, F., Qian, Q., Fan, H., 2013. Zircon U-Pb ages, trace elements and Nd-Hf isotopic geochemistry of Guyang sanukitoids and related rocks: Implications for the Archean crustal evolution of the Yinshan Block, North China Craton. Precambrian Research 230, 61–78.
Malviya, V. P., Arima, M., Pati, J. K., Kaneko, Y., 2006. Petrology and geochemistry of metamorphosed basaltic pillow lava and basaltic komatiite in the Mauranipur area: subduction related volcanism in the Archean Bundelkhand craton, Central India. Journal of Mineralogical and Petrological Sciences 101, 199–217.
Martin, H., 1999. Adakitic magmas: modern analogues of Archaean granitoids. Lithos 46, 411–429.
Martin, H., Moyen, J. F., 2002. Secular changes in tonalite-trondhjemite-granodiorite composition as markers of the progressive cooling of Earth. Geology 30, 319–322.
Martin, H., Moyen, J. F., Guitreau, M., Blichert-Toft, J., Le Pennec, J. L., 2014. Why Archaean TTG cannot be generated by MORB melting in subduction zones. Lithos 198, 1–13.
Martin, H., Moyen, J.-F., Rapp, R., 2010. The sanukitoid series: magmatism at the Archean–Proterozoic transition. Transactions of the Royal Society of Edinburgh 100, 15–33.
Martin, H., Smithies, R. H., Rapp, R., Moyen, J. F., Champion, D., 2005. An overview of adakite, tonalite–trondhjemite–granodiorite TTG, and sanukitoid: relationships and some implications for crustal evolution. Lithos 79, 1–24.
McDonough, W. F., Sun, S. S., 1995. The composition of the Earth. Chemical geology 120, 223–253.
Middlemost, E. A., 1989. Iron oxidation ratios, norms and the classification of volcanic rocks. Chemical geology 77, 19–26.
Mohan, M. R., Singh, S. P., Santosh, M., Siddiqui, M. A., Balaram, V., 2012. TTG suite from the Bundelkhand Craton, Central India: geochemistry, petrogenesis and implications for Archean crustal evolution. Journal of Asian Earth Sciences 58, 38–50.
Mondal, M. E. A., Goswami, J. N., Deomurari, M. P., Sharma, K. K., 2002. Ion microprobe $^{207}Pb/^{206}Pb$ ages of zircons from the Bundelkhand massif, northern India: implications for crustal evolution of the Bundelkhand–Aravalli protocontinent. Precambrian Research 117, 85–100.
Mondal, M. E. A., Sharma, K. K., Rahman, A., Goswami, J. N., 1998. Ion microprobe 207 Pb/206 Pb zircon ages for gneiss-granitoid rocks from Bundelkhand massif: Evidence for Archaean components. Current Scinece 70–75.
Mondal, S. K., 2009. Chromite and PGE deposits of Mesoarchaean ultramafic-mafic suites within the greenstone belts of the Singhbhum Craton, India: Implications for mantle heterogeneity and tectonic setting. Journal of the Geological Society of India 73, 36–51.
Moyen, J. F. and Martin, H., 2012. Forty years of TTG research. Lithos 148, 312–336.
Moyen, J. F., 2011. The composite Archaean grey gneisses: petrological significance, and evidence for a non-unique tectonic setting for Archaean crustal growth. Lithos 123, 21–36.
Moyen, J. F., Laurent, O., 2018. Archaean tectonic systems: a view from igneous rocks. Lithos 302, 99–125.
Moyen, J. F., Martin, H., Jayananda, M., 2001. Multi-element geochemical modelling of crust–mantle interactions during late-Archaean crustal growth: the Closepet granite (South India). Precambrian Research 112, 87–105.
Moyen, J. F., Martin, H., Jayananda, M., Auvray, B., 2003a. Late Archaean granites: a typology based on the Dharwar Craton India. Precambrian Research 127, 103–123.

Moyen, J. F., Nédélec, A., Martin, H., Jayananda, M., 2003b. Syntectonic granite emplacement at different structural levels: the Closepet granite, South India. Journal of Structural Geology 25, 611–631.
Mukhopadhyay, J., Beukes, N. J., Armstrong, R. A., Zimmermann, U., Ghosh, G., Medda, R. A., 2008. Dating the oldest greenstone in India: a 3.51-Ga precise U-Pb SHRIMP zircon age for dacitic lava of the southern Iron Ore Group, Singhbhum craton. The Journal of Geology 116, 449–461.
Nagel, T. J., Hoffmann, J. E., Münker, C., 2012. Generation of Eoarchean tonalite-trondhjemite-granodiorite series from thickened mafic arc crust. Geology 40, 375–378.
Naqvi, S.M., Rogers, J.J.W., 1987, Precambrian Geology of India: Oxford monographs on geology and geophysics, no. 6, Oxford, Oxford University Press 223.
Nasipuri, P., Saha, L., Hangqiang, X., Pati, J.K, Satyanaryanan, M., Sarkar, S., Bhandari, A., Gaur, Y., 2019. Paleoarchean Crustal Evolution of the Bundelkhand Craton, North Central India. Earth's Oldest Rocks, Chapter 31, 793–817.
Nelson, D. R., Bhattacharya, H. N., Thern, E. R. and Altermann, W., 2014. Geochemical and ion-microprobe U–Pb zircon constraints on the Archaean evolution of Singhbhum Craton, eastern India. Precambrian Research 255, 412–432.
Pandey, U. K., Bhattacharya, D., Sastry, D. V. L. N., Pandey, B. K., 2011. Geochronology Rb-Sr, Sm-Nd and Pb-Pb, isotope geochemisty and evolution of the granites and andesites hosting Mohar Cauldron, Bundelkhand Granite Complex, Shivpuri district, Central India. Explo. Res. Atom. Min. 21, 103–116.
Pati, J. K., Patel, S. C., Pruseth, K. L., Malviya, V. P., Arima, M., Raju, S., Prakash, K., 2007. Geology and geochemistry of giant quartz veins from the Bundelkhand Craton, central India and their implications. Journal of Earth System Science 116, 497.
Paton, C., Woodhead, J. D., Hellstrom, J. C., Hergt, J. M., Greig, A., Maas, R., 2010. Improved laser ablation U-Pb zircon geochronology through robust downhole fractionation correction. Geochemistry, Geophysics, Geosystems 11.
Petford, N. and Atherton, M., 1996. Na-rich partial melts from newly underplated basaltic crust: the Cordillera Blanca Batholith, Peru. Journal of Petrology 37, 1491–1521.
Peucat, JJ, Jayananda, M., Chardon, D., Capdevila, R., Fanning, CM, Paquette, JL, 2013. The lower crust of the Dharwar Craton, Southern India: Patchwork of Archean granulitic domains. Precambrian Research 227, 4–28.
Polat, A., 2012. Growth of Archean continental crust in oceanic island arcs. Geology 40, 383–384.
Pradhan, V. R., Meert, J. G., Pandit, M. K., Kamenov, G., Mondal, M. E. A., 2012. Paleomagnetic and geochronological studies of the mafic dyke swarms of Bundelkhand craton, central India: implications for the tectonic evolution and paleogeographic reconstructions. Precambrian Research 198, 51–76.
Pradhan, V. R., Meert, J. G., Pandit, M. K., Kamenov, G., Mondal, M. E. A., 2012. Paleomagnetic and geochronological studies of the mafic dyke swarms of Bundelkhand craton, central India: implications for the tectonic evolution and paleogeographic reconstructions. Precambrian Research 198, 51–76.
Rajesh, H. M., Mukhopadhyay, J., Beukes, N. J., Gutzmer, J., Belyanin, G. A., Armstrong, R. A., 2009. Evidence for an early Archaean granite from Bastar craton, India. Journal of the Geological Society 166, 193–196.
Ramakrishnan, M., Vaidyanadhan, R., 2010. Geology of India (Vol. 1 & 2). GSI Publications, 2.
Ramakrishnan, M., Vaidyanadhan, R., 2010. Geology of India. J. Geol. Soc. India 556.
Rao, J. M., Rao, G. P., Widdowson, M., Kelley, S. P., 2005. Evolution of Proterozoic mafic dyke swarms of the Bundelkhand Granite Massif, central India. Current Science 502–506.

Rapp, R. P., Norman, M. D., Laporte, D., Yaxley, G. M., Martin, H., Foley, S. F., 2010. Continent formation in the Archean and chemical evolution of the cratonic lithosphere: melt–rock reaction experiments at 3–4 GPa and petrogenesis of Archean Mg-diorites sanukitoids. Journal of Petrology 51, 1237–1266.

Rapp, R. P., Shimizu, N., Norman, M. D., Applegate, G. S., 1999. Reaction between slab-derived melts and peridotite in the mantle wedge: experimental constraints at 3.8 GPa. Chemical Geology 160, 335–356.

Rapp, R. P., Watson, E. B., 1995. Dehydration melting of metabasalt at 8–32 kbar: implications for continental growth and crust-mantle recycling. Journal of Petrology 36, 891–931.

Rapp, R. P., Watson, E. B., Miller, C. F., 1991. Partial melting of amphibolite/eclogite and the origin of Archean trondhjemites and tonalites. Precambrian Research 51, 1–25.

Saha, L., Frei, D., Gerdes, A., Pati, J. K., Sarkar, S., Patole, V., Nasipuri, P., 2016. Crustal geodynamics from the Archaean Bundelkhand Craton, India: constraints from zircon U–Pb–Hf isotope studies. Geological Magazine 153, 179–192.

Saha, L., Pant, N. C., Pati, J. K., Upadhyay, D., Berndt, J., Bhattacharya, A., Satynarayanan, M., 2011. Neoarchean high-pressure margarite–phengitic muscovite–chlorite corona mantled corundum in quartz-free high-Mg, Al phlogopite–chlorite schists from the Bundelkhand craton, north central India. Contributions to Mineralogy and Petrology 161, 511–530.

Santosh, M., Yang, Q. Y., Shaji, E., Mohan, M. R., Tsunogae, T., Satyanarayanan, M., 2016. Oldest rocks from Peninsular India: evidence for Hadean to Neoarchean crustal evolution. Gondwana Research 29, 105–135.

Sarkar, A., 1996. Geochronology and Geochemistry of Mid Archaean Trondhjemitic gneisses from Bundelkhand craton, Central India. Recent Res. Geol. 16, 76–92.

Schmidt, MW, Dardon, A., Chazot, G. Vannucci, R., 2004. The dependence of Nb and Ta rutile-melt partitioning on melt composition and Nb / Ta fractionation during subduction processes. Earth and Planetary Science Letters 226, 415–432.

Schoene, B., Dudas, F. O., Bowring, S. A., De Wit, M., 2009. Sm–Nd isotopic mapping of lithospheric growth and stabilization in the eastern Kaapvaal craton. Terra Nova 21, 219–228.

Sen, C., Dunn, T., 1994. Dehydration melting of a basaltic composition amphibolite at 1.5 and 2.0 GPa: implications for the origin of adakites. Contributions to Mineralogy and Petrology 117, 394–409.

Shand, S. J., 1943. Eruptive rocks: their genesis, composition, classification, and their relation to ore deposits with a chaper on meteorites No. 552.1 S43 1943.

Sharma, M., Basu, A. R., Ray, S. L., 1994. Sm-Nd isotopic and geochemical study of the Archean tonalite-amphibolite association from the eastern Indian Craton. Contributions to Mineralogy and Petrology 117, 45–55.

Singh, P.K., Verma, S.K., Moreno, J.A., Singh, V.K., Malviya, V.P., Oliveira, E.P., Mishra, M., Arima, M., 2019a. Geochemistry and Sm–Nd isotope systematics of mafic-ultramafic rocks from the Babina and Mauranipur greenstone belts, Bundelkhand Craton, India: Implications for tectonic setting and Paleoarchean mantle evolution. Lithos 330, 90–107.

Singh, P.K., Verma, S.K., Singh, V.K., Moreno, J.A., Oliveira, E.P., Mehta, P., 2019b. Geochemistry and petrogenesis of sanukitoids and high-K anatectic granites from the Bundelkhand Craton, India: Implications for late-Archean crustal evolution. Journal of Asian Earth Sciences 174, 263–282.

Singh, S. P., Subramanyam, K. S. V., Manikyamba, C., Santosh, M., Singh, M. R., Kumar, B. C., 2018. Geochemical systematics of the Mauranipur-Babina greenstone belt,

Bundelkhand Craton, Central India: Insights on Neoarchean mantle plume-arc accretion and crustal evolution. Geoscience Frontiers 9, 769–788.
Singh, V. K., Slabunov, A., 2016. Two types of Archaean supracrustal belts in the Bundelkhand craton, India: Geology, geochemistry, age and implication for craton crustal evolution. Journal of Geological Society of India 88, 339–348.
Singh, V.K., Slabunov, A., 2015a. The central Bundelkhand Archaean greenstone complex, Bundelkhand craton, central India: geology, composition, and geochronology of supracrustal rocks. International Geology Review 57, 1347–1362.
Singh, V.K., Slabunov, A., 2015b. Geochemical characteristics of banded iron formation and metavolcanics of Babina greenstone belt of the Bundelkhand Craton, Central India. Journal of Economic Geology & Geo Resource Management 10, 63–74.
Slabunov, A., Singh, V.K., Kumar, B., Xiaoli, L., 2017a. Paleoarchean zircons from quartzite of South Bundelkhand Supracrustal Complex: origin and implications for crustal evolution in Bundelkhand Craton, Central India. Current Science 112, 794-801.
Slabunov, A.I., Singh, V.K., Shchiptsov, V.V., Lepekhina E. N., Kevlich V.I., 2017b. A new Paleoproterozoic 1.9–1.8 Ga event in the crustal evolution of the Bundelkhand Craton, India: the results of SHRIMP Dating of zircons from giant quartz veins. In: Slabunov, A.I., Svetov, S.A., Baltibaev, Sh.K. eds., Early Precambrian vs Modern Geodynamics. Extended Abstracts and Field Trips Guide. Petrozavodsk: KarRC RAS 239–241.
Slabunov, A. I., Singh, V. K., 2019. Meso–Neoarchaean crustal evolution of the Bundelkhand Craton, Indian Shield: new data from greenstone belts. International Geology Review 1409-14281.
Smithies, R. H., 2000. The Archaean tonalite–trondhjemite–granodiorite (TTG) series is not an analogue of Cenozoic adakite. Earth and Planetary Science Letters 182, 115–125.
Smithies, R. H., Champion, D. C., Cassidy, K. F., 2003. Formation of Earth's early Archaean continental crust. Precambrian Research 127, 89–101.
Smithies, R. H., Champion, D. C., Van Kranendonk, M. J., 2009. Formation of Paleoarchean continental crust through infracrustal melting of enriched basalt. Earth and Planetary Science Letters 281, 298–306.
Smithies, R. H., Champion, D. C., Van Kranendonk, M. J., 2009. Formation of Paleoarchean continental crust through infracrustal melting of enriched basalt. Earth and Planetary Science Letters 281, 298–306.
Smithies, R.H., Champion, D.C., 2000. The Archaean high-Mg diorite suite: links to tonalite–trondhjemite–granodiorite magmatism and implications for early Archaean crustal growth. Journal of Petrology 41, 1653–1671.
Stern, R. A., Hanson, G. N., 1991. Archean high-Mg granodiorite: a derivative of light rare earth element-enriched monzodiorite of mantle origin. Journal of Petrology 32, 201–238.
Stevens, G., Moyen, J. F., 2007. Metamorphism in the Barberton Granite Greenstone Terrain: A Record of Paleoarchean Accretion. Developments in Precambrian geology 15, 669–698.
Stevenson, R., Henry, P., Gariépy, C., 1999. Assimilation–fractional crystallization origin of Archean sanukitoid suites: western Superior Province, Canada. Precambrian Research 96, 83–99.
Sutcliffe, R. H., Smith, A. R., Doherty, W., Barnett, R. L., 1990. Mantle derivation of Archean amphibole-bearing granitoid and associated mafic rocks: evidence from the southern Superior Province, Canada. Contributions to Mineralogy and Petrology 105, 255–274.
Tang, M., Chen, K., Rudnick, R. L., 2016. Archean upper crust transition from mafic to felsic marks the onset of plate tectonics. Science 351, 372–375.
Taylor, S. R., McLennan, S. M., 1995. The geochemical evolution of the continental crust. Reviews of geophysics 33, 241–265.

Terentiev, R. A., Santosh, M., 2018. High magnesian granitoids in the Precambrian continental crust: Implication for the continuum between ferro–potassic and magnesio–potassic rock suites. Lithos 314, 669–682.
Turner, C. C., Meert, J. G., Pandit, M. K., Kamenov, G. D., 2014. A detrital zircon U–Pb and Hf isotopic transect across the Son Valley sector of the Vindhyan Basin, India: implications for basin evolution and paleogeography. Gondwana Research 26, 348–364.
Upadhyay, D., Chattopadhyay, S., Kooijman, E., Mezger, K., Berndt, J., 2014. Magmatic and metamorphic history of Paleoarchean tonalite–trondhjemite–granodiorite (TTG) suite from the Singhbhum craton, eastern India. Precambrian Research 252, 180–190.
Valdiya, K. S., 2015. The making of India: geodynamic evolution. Springer.
Van Kranendonk, M. J., 2010. Two types of Archean continental crust: Plume and plate tectonics on early Earth. American Journal of Science 310, 1187–1209.
Van Kranendonk, M. J., Smithies, R. H., Griffin, W. L., Huston, D. L., Hickman, A. H., Champion, D. C., Pirajno, F., 2015. Making it thick: a volcanic plateau origin of Palaeoarchean continental lithosphere of the Pilbara and Kaapvaal cratons. Geological Society, London, Special Publications 389, 83–111.
Vendemiatto, M. A., Enzweiler, J., 2001. Routine Control of Accuracy in Silicate Rock Analysis by X-Ray Fluorescence Spectrometry. Geostandards Newsletter 25, 283–291.
Verma, S. K., Verma, S. P., Oliveira, E. P., Singh, V. K., Moreno, J. A., 2016. LA-SF-ICP-MS zircon U–Pb geochronology of granitic rocks from the central Bundelkhand greenstone complex, Bundelkhand craton, India. Journal of Asian Earth Sciences 118, 125–137.
Verma, S. P., Rivera-Gomez, M. A., 2013. Computer programs for the classification and nomenclature of igneous rocks. Episodes, 36, 115–124.
Wan, Y.S., Dong, C.Y., Liu, D.Y., Kröner, A., Yang, C.H., Wang,W., Du, L.L., Xie, H.Q., Ma, M.Z., 2012. Zircon ages and geochemistry of late Neoarchean syenogranites in the North China Craton: a review. Precambrian Research 222-223, 265–289.
Wan, Y.S., Liu, D.Y., Nutman, A., Zhou, H.Y., Dong, C.Y., Yin, X.Y., Ma, M.Z., 2013. Multiple 3.8–3.1 Ga Tectono-magmatic Events in a Newly Discovered Area of Ancient Rocks (The Shengousi Complex), Anshan, North China Craton.
Wan, Y.S., Liu, D.Y., Song, B., 2005. Geochemical and Nd isotopic composition of 3.8 Ga meta-quartz dioritic and trondhjemitic rocks from the Archean area and their geological significance. Journal of Asian Earth Sciences 24, 563–575.
Watkins, J. M., Clemens, J. D., Treloar, P. J., 2007. Archaean TTGs as sources of younger granitic magmas: melting of sodic metatonalites at 0.6–1.2 GPa. Contributions to Mineralogy and Petrology 154, 91–110.
Wiedenbeck, M. A. P. C., Alle, P., Corfu, F., Griffin, W. L., Meier, M., Oberli, F. V., Spiegel, W., 1995. Three natural zircon standards for U-Th-Pb, Lu-Hf, trace element and REE analyses. Geostandards newsletter 19, 1–23.
Windley, B.F., 1995. The Evolving Continents, 3rd ed. Chichester, John Wiley 526.
Yang, Q.Y., Santosh, M., 2017. The building of an Archean microcontinent: evidence from the North China Craton. Gondwana Research 50, 3–37.
Yang, Q.Y., Santosh, M., Collins, A.S., Teng, X.M., 2016a. Microblock amalgamation in the North China Craton: evidence from Neoarchaean magmatic suite in the western margin of the Jiaoliao Block. Gondwana Research 31, 96–123.
Yang, Q.Y., Santosh, M., Tsunogae, T., 2016b. High-grade metamorphism during Archean–Paleoproterozoic transition associated with microblock amalgamation in the North China Craton: mineral phase equilibria and zircon geochronology. Lithos 263, 101–121.
Yedekar, DB, 1990. The central Indian collision suture. Geological Survey of India, Special Publication 28, 1–43.

Zeh, A., Gerdes, A., Barton, J.M., 2009. Archean accretion and crustal evolution of the Kalahari Craton-the zircon age and Hf isotope record of granitic rocks from Barberton/Swaziland to the Francistown arc. Journal of Petrology 50, 933–966.
Zeh, A., Gerdes, A., Klem, J., Barton Jr., J.M., 2007. Archean to Proterozoic crustal evolution in the Central zone of Limapo belt (S.Africa and Botswana: Constraints from combined U-Pb and Lu-Hf isotopic analysis of zircon). Journal of Petrology 48, 1605–1639.
Zeh, A., Gerdes, A., Millonig, L., 2011. Hafnium Isotope Record of the Ancient Gneiss Complex, Swaziland, Southern Africa: Evidence for Archaean Crust–Mantle Formation and Crust Reworking Between 3.66 And 2.73 Ga. vol. 168. Geological Society of London 953–963.
Zhai, M., 2014. Multi-stage crustal growth and cratonization of the North China Craton. Geoscience Frontiers 5, 457–469.
Zhai, M.G., Santosh, M., 2011. The early Precambrian odyssey of the North China Craton: a synoptic overview. Gondwana Research 20, 6–25.
Zhou, G., Wu, Y., Li, L., Zhang, W., Zheng, J., Wang, H., Yang, S., 2018. Identification of ca. 2.65 Ga TTGs in the Yudongzi complex and its implications for the early evolution of the Yangtze Block. Precambrian Research 314, 240–263.

CHAPTER 5

Conclusions

In this thesis, geology, petrography, geochemistry, mineralogy, zircon geochronology and Sm–Nd isotopes geochemistry of ultramafic-mafic volcanic rocks, TTG gneisses, sanukitoids and anatectic granites were used to decode the crust formation ages, secular changes in crustal compositions, crustal reworking, and cratonization that happened between ~3.59 and 2.50 Ga in the Central Bundelkhand Greenstone Complex (CBGC), Bundelkhand Craton (BC). The results lead to the following conclusions:

1. ID-TIMS whole-rock Sm-Nd isochron yield an age of ~3.44 Ga for ultramafic-mafic volcanic rocks for the first time.
2. Trace element compositions indicate that the fractionation of clinopyroxene and minor olivine were the most likely process involved in the formation of the ultramafic-mafic volcanic rocks.
3. Integrated whole-rock geochemical and $\varepsilon_{Nd}t$ (+0.2 to +9.0) results unravel that mafic magma was produced from a depleted mantle source and evolved through fractional crystallization linked with crustal assimilation.
4. The mafic–ultramafic volcanic rocks and associated metasedimentary rocks are remnants of oceanic crust and were probably emplaced in a subduction related setting during Paleoarchean Era.

5. LA-SF-ICP-MS zircon dating results suggest that TTG magmatic events mainly happened around 3.51–3.20 Ga at regular intervals of 100 Myr. It has also showed and evidence of younger Neoarchean TTG magmatism at 2.71–2.67 Ga. Additionally, study find a contemporary felsic plutonism and mafic volcanism at ~3.44 Ga.
6. Zircon dating of sanukitoid and anatectic granite rocks reveal two discrete episodes of magmatism during Neoarchean between ~2.58 and 2.50 Ga and suggest a synchronous magmatism between these rocks, which linked to the final cratonization of the BC.
7. Paleoarchean TTG gneisses show $\varepsilon_{Nd}(t)$ values between +4.3 and –0.5 whereas Neoarchean TTG gneiss display +4.5. On the other hand, sanukitoids show $\varepsilon_{Nd}(t)$ values between −3.6 to −1.6 and anatectic granites display high negative $\varepsilon_{Nd}(t)$ values between −3.4 to −8.7.
8. TTG gneisses are characterized by low-HREE and high-HREE. Low-HREE type TTGs were produced through melting of subducted oceanic arc crust at different depths which probably interacted variably with felsic crustal melts in stable fields of garnet and ilmenite, probably plagioclase-free source. On the other hand, a high-HREE type of TTG suggests a likely origin in a plagioclase and garnet-amphibolite at low pressure. In contrast, Neoarchean TTG gneisses display low-HREE and originated by the partial melting of deep-seated mafic crust in the garnet-stable field with minor involvement of ancient felsic crustal material in a subduction setting.

9. Sanukitoid plutons were generated by the mingling of metasomatized mantle melts with anatectic melts and were followed by homogenization at shallow levels of emplacement in a subduction-related setting.
10. Anatectic granitic plutons were originated purely by partial melting of ancient crusts (anatexis) and were voluminously emplaced during cratonic stabilization at ~2.50 Ga in an arc-collisional environment.
11. Finally, the incorporation of diverse micro-blocks occurred by the arc-continent collision mechanism and frequent slab break-off between the north and south blocks of the BC during late Archean. This evidence shows that the BC did not merge together until ~2.50 Ga. The ample anatectic granites emplacements were connected to the final cratonization and stabilization of the BC.

APPENDIX I:

CHAPTER 2

SUPPLEMENTARY MATERIAL

This contains Tables S1-S2, Figure S1, and References SR1-SR2.

Analytical method

Mineralogy

Eight samples were powdered at ~10 μm (or 300-mesh) using agate mortar pestle. X-ray diffraction (XRD) analysis was carried out by Smartlab Rigaku (Cu Ka X-ray tube; 40 kV 44 mA) at Instituto Potosino de Investigación Científica y Tecnológica, IPICYT, San Luis Potosi, Mexico. Diffraction data is acquired by exposing powder samples to Cu-Kα X ray radiation, which has a characteristic wavelength of 1.5418Å. X ray were generated from Cu anode supplied with 40 kV and 35 mA current. Diffractogram were processed and mineral identification is carried out by using ICDD (pdf-2 and pdf-4) database.

Table S1. X-ray diffraction (XRD) semi-quantitative analysis of mafic-ultramafic minerals (%) in whole rock from the Babina and Mauranipur greenstone belts, BC, India

Sample	Rock unit	Amp	Pl	Chl	Srp/Tlc	Px	Cr-Spl/Mag	Ol	Ill/Mica	Qtz
	Babina									
BCB-01	Mafic	62	15	12	3	6	-	-	2	-
BCB-05	Mafic	63	14	15	4	4	-	-	-	-
BCB-13	Mafic	65	18	9	5	3	-	-	-	-
BCB-17	Ultramafic	27	-	56	17	-	-	-	-	-
	Mauranipur									
BCB-20	Ultramafic	28	-	53	18	-	1	-	-	-
BCB-27	Mafic	70	25	-	-	2	-	-	-	3
BCB-29	Mafic	60	30	-	-	3	1	-	-	6
BG-1708	Ultramafic cumulate	26	-	16	48	-	2	8	-	-

Amp = amphibole, Pl = plagioclase, Chl = chlorite, Srp = serpentine, Tlc = talc, Px = pyroxene, Spl = spinel, Mag = magnetite, Ol = olivine, Ill = illite, Qtz = quartz

Table S2. Representative whole rock compositions of mafic-ultramafic rocks from the Babina and Mauranipur greenstone belts, BC, India. Major elements in weight percent and trace elements in ppm.

Sample	BCB-01	BCB-02	BCB-03	BCB-04	BCB-05	BCB-06	BCB-07	BCB-08	BCB-09	BCB-10	BCB-11
Rock unit	Mafic	Mafic	Mafic	Mafic	Mafic	Mafic	Mafic	Mafic	Mafic	Mafic	Mafic
Rock (TAS)	Basic	Basic	Inter	Basic	Basic	Basic	Basic	Basic	Basic	Basic	Basic
Locality	Babina	Babina	Babina	Babina	Babina	Babina	Babina	Babina	Babina	Babina	Babina
Long. (°E)	78.4639	78.4751	78.4745	78.4743	78.4738	78.4730	78.4754	78.4737	78.4909	78.4736	78.4736
Lat. (°N)	25.2061	25.2114	25.2116	25.2116	25.2117	25.2081	25.2083	25.2117	25.2114	25.1926	25.2117
SiO_2	43.9	51.13	52.09	51.29	47.66	48.72	49.47	47.988	48.92	47.65	47.946
TiO_2	0.71	0.61	0.56	0.61	0.53	0.82	0.31	0.649	0.71	0.62	0.602
Al_2O_3	12.74	14.14	13.32	15.32	16.1	15.2	16.69	14.56	13.55	13.36	14.366
Fe_2O_3	11.8	11.52	11.16	10.88	11.52	12.92	7.49	13.591	13.8	18.23	12.853
MnO	0.28	0.2	0.2	0.19	0.17	0.19	0.14	0.197	0.23	0.72	0.184
MgO	11	7.77	8.17	7.38	9.69	7.75	10.55	10.156	9.94	8.09	10.436
CaO	14.35	10.9	10.95	10.2	10.75	9.69	9.46	10.411	10.35	11.12	10.334
Na_2O	0.21	2.66	2.68	2.95	1.86	2.3	1.9	1.6	1.78	0.19	1.547
K_2O	2	0.46	0.27	0.66	0.39	1.62	2.3	0.454	0.67	0.25	0.481
P_2O_5	0.37	0.05	0.04	0.05	0.05	0.07	0.03	0.052	0.06	0.01	0.061
LOI	3.07	0.76	0.7	0.86	1.13	1.52	2.43	0.4	0.1	0.2	1.19
Total	100.43	100.2	100.14	100.39	99.85	100.8	100.77	99.658	100.01	100.24	100
Ba	254	67.9	56.1	83.2	21.7	96	101	58.44	49.40	531.15	67.00
Co	51	45	47	41	57	50	36	51.05	55.27	34.89	62.58
Cr	700	370	490	350	170	230	680	128.37	312.13	146.59	216.00
Cs	14.75	0.6	0.14	0.6	0.63	1.03	4.87	1.12	1.50	0.13	0.93
Cu	1	22	25	29	191	76	2	95.80	124.26	0.89	303.49
Ga	14	13.6	11.4	13.3	14.3	15.4	11.4	12.46	12.47	14.66	12.82
Hf	2.3	1	1	1.1	1	1.4	0.6	0.96	1.16	2.87	1.19
Nb	10.1	1.5	1.4	1.5	1.3	1.8	0.8	1.81	3.61	10.65	1.55
Ni	235	105	142	90	262	131	99	232.81	214.23	22.64	325.00
Pb	5	10	9	10	9	11	12	6.62	6.94		8.47
Rb	205	19.2	8.9	31	25.2	93.8	175.5	24.54	43.35	9.18	29.96
Sc	23	40	37	37	23	32	32	40.00	34.00	31.00	26.93
Sr	318	126.5	149.5	153.5	100	162.5	226	95.56	99.67	76.45	74.75
Ta	0.4	0.1	0.1	0.1	0.1	0.1		0.10	0.29	2.39	0.16
Th	2.4	0.4	0.36	0.39	0.36	0.31	0.19	0.48	0.78	4.39	0.53
U	0.5	0.09	0.08	0.08	0.08	0.18	0.1	0.08	0.31	2.06	0.25
V	200	274	236	267	200	291	170	244.65	304.80	131.45	189.20
Y	18.9	15.2	13.4	15.5	13.4	19.2	8.2	17.65	36.55	38.00	13.83
Zn	241	111	115	93	83	90	68	111.33	111.87	53.23	114.00
Zr	107	37	35	39	34	50	22	37.89	55.45	124.11	37.33
La	32.4	2.6	2.3	2.6	2.4	2.8	1.6	2.55	3.94	11.59	2.69
Ce	63.3	6.3	5.6	6.2	5.7	7.2	3.5	6.04	9.92	22.35	6.58
Pr	7.78	1.02	0.92	1	0.91	1.21	0.53	0.84	1.37	2.45	0.94
Nd	28.9	4.9	4.4	5	4.3	5.9	2.3	4.19	6.59	11.25	4.94
Sm	5.09	1.59	1.39	1.49	1.35	1.92	0.66	1.36	1.90	3.33	1.50
Eu	1.54	0.64	0.47	0.64	0.53	0.75	0.28	0.59	0.57	1.02	0.59
Gd	4.35	2.17	1.94	2.25	1.84	2.67	1.02	1.77	2.37	4.19	1.93
Tb	0.66	0.43	0.36	0.41	0.36	0.52	0.2	0.35	0.45	0.75	0.37
Dy	3.49	2.65	2.25	2.6	2.2	3.27	1.29	2.24	2.83	4.37	2.64
Ho	0.71	0.57	0.5	0.57	0.47	0.7	0.3	0.48	0.62	0.86	0.53
Er	1.85	1.76	1.49	1.69	1.47	2.12	0.93	1.54	1.90	2.57	1.64
Tm	0.27	0.25	0.22	0.25	0.21	0.31	0.14	0.24	0.29	0.37	0.25
Yb	1.72	1.69	1.47	1.75	1.46	2.18	1	1.51	1.91	2.28	1.69
Lu	0.23	0.24	0.22	0.25	0.21	0.32	0.15	0.22	0.27	0.34	0.24
Bi	0.27	0.17	0.13	0.13	0.12	0.09	0.15	0.39	0.12	1.22	0.40
Sn	4	2	1	2		1	1	2.88	3.38	7.07	0.48
Mg#	68.5	61.1	64.8	63.0	66.2	58.3	76.7	63.5	62.7	50.9	65.4
ΣREE	148.80	24.16	21.28	24.10	21.21	28.60	12.61	21.67	32.10	63.36	23.89
$(La/Yb)_{PM}$	12.80	1.05	1.06	1.01	1.12	0.87	1.09	1.15	1.40	3.45	1.08
$(La/Sm)_{PM}$	3.99	1.02	1.04	1.09	1.11	0.91	1.52	1.17	1.30	2.18	1.12
$(Gd/Yb)_{PM}$	2.05	1.04	1.07	1.04	1.02	0.99	0.83	0.95	1.01	1.49	0.92
$(La/Yb)_{CN}$	12.80	1.05	1.06	1.01	1.12	0.87	1.09	1.15	1.40	3.45	1.08
$(La/Sm)_{CN}$	3.98	1.02	1.03	1.09	1.11	0.91	1.51	1.17	1.29	2.17	1.12
$(Gd/Yb)_{CN}$	2.05	1.04	1.07	1.04	1.02	0.99	0.83	0.95	1.01	1.49	0.92
(Nb/Nb*)	0.33	0.31	0.34	0.26	0.54	0.28	0.13	0.41	0.78	0.32	0.32
(Ta/Ta*)	0.24	0.38	0.45	0.33	0.77	0.29		0.44	1.15	1.31	0.60
(Ti/Ti*)	0.47	0.74	0.85	0.73	0.76	0.83	0.79	0.77	0.54	0.38	0.80
(Eu/Eu*)	0.97	1.05	0.87	1.06	1.03	1.01	1.04	1.15	0.82	0.83	1.06
(Ce/Ce*)	0.94	0.94	0.93	0.93	0.93	0.95	0.92	1.00	1.03	0.97	1.00

Table S2 continue.

Sample	BCB-12	BCB-13	BCB-14	BCB-15	BCB-16	BCB-17	BCB-18	BCB-19	BCB-20	BG-1708*
Rock unit	Mafic	Mafic	Mafic	ultramafic	ultramafic	ultramafic	ultramafic	ultramafic	ultramafic	Cumulate
Rock (TAS)	Basic	Basic	Basic	Basic	Basic	Basic	Basic	Inter	Basic	Basic
Locality	Babina	Babina	Babina	Babina	Babina	Babina	Babina	Babina	Mauranipur	Mauranipur
Long. (°E)	78.4747	78.4758	78.4764	78.4751	78.4788	78.4736	78.4722	78.4745	79.1858	
Lat. (°N)	25.2125	25.2114	25.2108	25.2042	25.2085	25.2070	25.2082	25.2095	25.2269	
SiO_2	48.089	48.224	50.493	48.42	47.78	48.83	49.68	50.3	46.93	44.5
TiO_2	0.964	0.579	1.147	0.41	0.45	0.46	0.42	0.39	0.33	0.11
Al_2O_3	16.441	14.803	12.448	4.71	5.01	4.95	4.34	4.37	6.41	1.32
Fe_2O_3	14.112	12.619	16.463	11.5	12.97	12.36	11.82	11.02	9.15	14.36
MnO	0.435	0.187	0.211	0.18	0.17	0.17	0.18	0.15	0.28	0.33
MgO	7.701	10.337	5.465	21.01	20.2	21.1	20.51	21.12	20.7	34.27
CaO	11.931	10.615	10.251	7.28	8.25	8.3	9.14	7.51	8.78	1.73
Na_2O	2.879	1.681	2.057	0.5	0.41	0.67	0.43	0.39	0.07	0.2
K_2O	0.458	0.22	0.442	0.04	0.01	0.13	0.02	0.01	0.02	0.02
P_2O_5	0.14	0.054	0.103	0.04	0.05	0.03	0.04	0.03	0.04	0.01
LOI	0.85	0.68	0.92	5.01	4.21	2.02	3.06	4.32	6.39	
Total	104	99.999	100	99.1	99.51	99.02	99.64	99.61	99.1	
Ba	69.88	78.00	48.01	12.8	13.4	15.9	18.5	15	28.7	21.02
Co	32.46	64.48	48.93	75	65	78	52	81	68	92.01
Cr	377.00	286.00	58.00	2652	2275	2930	2328	2657	2070	3829
Cs	0.23	0.49	0.13	0.52	0.47	0.64	0.38	0.24	0.09	1
Cu	23.11	235.92	81.78	6	59	122	79	15	24	
Ga	17.91	12.19	16.09	5.9	6.8	7.9	8.5	9.1	7.7	
Hf	4.20	1.18	2.23	0.7	0.5	0.9	0.8	0.6	1.4	0.2
Nb	10.24	1.30	3.24	1.6	1.5	1.5	1.7	1.4	2.9	2.9
Ni	131.00	316.00	45.00	1058	852	971	1135	1201	1590	957.1
Pb	14.35	7.86	8.17			5				
Rb	11.03	9.95	6.23	3.9	4.7	4.2	4.3	3.4	1.4	4.7
Sc	21.64	25.82	36.70	15	18	18	21	19	14	
Sr	162.58	68.26	114.32	59	61	70	47	66	7.7	10.2
Ta	1.37	0.13	0.35	0.15	0.18	0.1	0.13	0.1	0.2	0.03
Th	8.63	0.47	1.36	0.35	0.2	0.41	0.25	0.31	2.51	0.31
U	1.41	0.09	0.29	0.11	0.17	0.12	0.21	0.18	0.44	0.09
V	133.21	182.36	324.33	84	132	142	158	148	97	93.3
Y	26.94	11.86	22.31	7	6	9	8	9	9.9	6.0
Zn	123.00	92.00	132.00			90			68	84.9
Zr	107.00	34.52	42.00	21	15	31	25	16	53	13.5
La	21.46	2.40	4.45	2.89	3.81	3.2	2.97	2.58	10.7	0.88
Ce	38.51	5.75	12.22	6.58	7.85	7.2	6.98	5.83	17.3	1.95
Pr	4.76	0.81	1.79	0.95	1.08	1.05	1.07	0.84	2.03	0.23
Nd	19.34	4.15	9.15	3.54	4.9	4.5	4.02	3.41	7.2	0.98
Sm	4.32	1.29	2.67	1.1	1.31	1.21	1.17	1.03	1.36	0.26
Eu	1.17	0.51	0.99	0.29	0.32	0.31	0.27	0.25	0.24	0.08
Gd	4.42	1.65	3.18	1.48	1.72	1.52	1.41	1.35	1.55	0.26
Tb	0.81	0.34	0.64	0.24	0.31	0.28	0.21	0.19	0.26	0.05
Dy	5.29	2.24	4.40	1.46	1.78	1.63	1.24	1.14	1.56	0.32
Ho	1.00	0.46	0.88	0.31	0.38	0.35	0.27	0.24	0.34	0.07
Er	3.00	1.43	2.74	0.91	1.08	0.99	0.81	0.72	0.96	0.23
Tm	0.45	0.21	0.41	0.13	0.15	0.14	0.12	0.101	0.15	0.04
Yb	2.90	1.41	2.64	0.85	1.03	0.94	0.69	0.76	0.95	0.25
Lu	0.42	0.22	0.40	0.13	0.15	0.12	0.101	0.11	0.14	0.04
Bi	0.86	0.36	0.19			0.63			0.43	
Sn	3.68	0.35	0.93			2				
Mg#	56.0	65.6	43.6	80.7	77.6	79.9	79.4	78.8	82.8	84.7
ΣREE	102.55	20.63	42.16	19.40	24.09	21.81	20.09	17.41	43.18	5.53
$(La/Yb)_{PM}$	5.03	1.15	1.15	2.31	2.52	2.32	2.93	2.31	7.67	2.40
$(La/Sm)_{PM}$	3.11	1.16	1.05	1.65	1.82	1.66	1.59	1.57	4.93	2.12
$(Gd/Yb)_{PM}$	1.24	0.95	0.98	1.41	1.35	1.31	1.66	1.44	1.32	0.84
$(La/Yb)_{CN}$	5.03	1.16	1.15	2.31	2.51	2.31	2.92	2.31	7.65	2.39
$(La/Sm)_{CN}$	3.10	1.16	1.04	1.64	1.82	1.65	1.59	1.56	4.91	2.11
$(Gd/Yb)_{CN}$	1.23	0.94	0.98	1.41	1.35	1.31	1.65	1.44	1.32	0.84
(Nb/Nb*)	0.68	0.24	0.67	0.73	0.55	0.60	0.67	0.65	0.41	0.44
(Ta/Ta*)	1.69	0.44	1.34	1.27	1.23	0.74	0.95	0.86	0.52	0.35
(Ti/Ti*)	0.63	0.90	0.93	1.16	1.27	1.08	1.12	1.03	0.86	0.55
(Eu/Eu*)	0.81	1.07	1.04	0.69	0.65	0.70	0.64	0.65	0.50	0.93
(Ce/Ce*)	0.89	0.99	1.05	0.96	0.93	0.95	0.95	0.96	0.84	1.03

*taken from Malviya et al. (2006)

Table S2 continue.

Sample	BCB-21	BCB-22	BCB-23	BCB-24	BCB-25	BCB-26	BCB-27	BCB-28	BCB-29
Rock unit	Mafic	Mafic	Mafic	Mafic	Mafic	Mafic	Mafic	Mafic	Mafic
Rock (TAS)	Inter	Inter	Inter	Inter	Inter	Inter	Inter	Inter	Inter
Locality	Mauranipur	Mauranipur	Mauranipur	Mauranipur	Mauranipur	Mauranipur	Mauranipur	Mauranipur	Mauranipur
Long. (°E)	79.1819	79.1733	79.1756	79.1264	79.1767	79.1745	79.1742	79.1739	79.1731
Lat. (°N)	25.2308	25.2319	25.2275	25.2131	25.2272	25.2273	25.2274	25.2274	25.2279
SiO_2	53.29	54.54	54.06	52.81	55.69	53.39	53.13	52.33	52.08
TiO_2	0.67	0.61	0.65	0.85	0.64	0.65	0.66	0.65	0.66
Al_2O_3	13.91	12.24	13.63	9.3	13.38	13.13	13.69	13.68	13.76
Fe_2O_3	10.54	7.67	9.61	14.08	8.04	9.31	10.17	9.73	9.85
MnO	0.21	0.47	0.15	0.44	0.16	0.16	0.17	0.16	0.17
MgO	7.84	6.91	7.97	8.34	7.1	7.68	8.51	8.72	8.44
CaO	9.64	13.55	10.9	9.85	13.25	12.55	11.75	11.2	11.15
Na_2O	1.71	2.26	2.67	2.71	1.62	2.18	1.99	2.9	2.87
K_2O	0.97	1.36	0.13	1.18	0.07	0.09	0.14	0.09	0.18
P_2O_5	0.07	0.1	0.06	0.11	0.06	0.07	0.06	0.06	0.06
LOI	1.35	0.91	0.5	0.58	0.66	1.02	0.56	0.64	0.82
Total	100.2	100.62	100.33	100.25	100.67	100.23	100.83	100.16	100.04
Ba	98.2	121	71.3	44.1	44.3	35.2	44.7	69.4	77.6
Co	75	32	41	56	36	43	42	42	43
Cr	150	590	520	540	510	550	640	510	520
Cs	1.28	1.31	0.19	1.46	0.23	0.48	0.23	0.09	0.39
Cu	88	1	69	7	63	164	79	81	91
Ga	13.7	14.8	13.6	22.2	13.8	14.3	13.8	14.7	14.6
Hf	1.6	3.6	1.5	2.6	1.4	1.4	1.4	1.4	1.4
Nb	2.3	8.7	2	12.8	1.8	1.8	1.7	1.8	1.7
Ni	65	200	129	137	123	140	131	133	134
Pb	3	6	8	5	4	9		4	4
Rb	47.8	64.7	2.8	79.6	2.2	3.2	2.8	1.7	5.1
Sc	41	19	37	31	36	36	38	37	38
Sr	88.7	116.5	106.5	146	87.3	76.7	122	133.5	98.4
Ta	0.2	0.7	0.2	1.2	0.1	0.1	0.1	0.1	0.1
Th	1.5	7.99	1.48	2.35	1.01	1.11	0.98	0.96	0.96
U	0.38	1.88	0.31	2.06	0.28	0.29	0.27	0.26	0.27
V	315	146	288	231	290	293	301	315	309
Y	19.8	24.4	17	51.1	16.8	16.6	17.2	17.3	17.4
Zn	67	229	63	189	56	58	65	63	63
Zr	57	138	54	94	50	50	50	51	51
La	5.6	24.8	4.4	11	4.1	4	3.9	3.4	4
Ce	11.6	46.4	9.4	28.6	8.9	8.7	8.3	8	8.5
Pr	1.48	5.33	1.29	4.49	1.25	1.24	1.21	1.14	1.2
Nd	6.3	19	5.6	19.9	5.5	5.4	5.5	5.3	5.5
Sm	1.73	3.99	1.61	6.02	1.65	1.63	1.71	1.67	1.66
Eu	0.66	0.94	0.59	1.11	0.62	0.64	0.67	1.11	0.67
Gd	2.64	4.15	2.36	7.19	2.47	2.36	2.42	2.45	2.53
Tb	0.51	0.74	0.46	1.37	0.48	0.47	0.48	0.48	0.49
Dy	3.3	4.24	2.82	8.33	2.85	2.85	3	3	2.98
Ho	0.74	0.88	0.62	1.74	0.62	0.62	0.65	0.64	0.65
Er	2.27	2.51	1.82	5.31	1.85	1.83	1.9	1.88	1.96
Tm	0.34	0.36	0.26	0.83	0.27	0.28	0.28	0.28	0.27
Yb	2.26	2.34	1.74	5.83	1.73	1.79	1.85	1.83	1.86
Lu	0.33	0.34	0.25	0.84	0.25	0.26	0.27	0.26	0.26
Bi	0.02	0.02	0.01	0.68	0.02	0.02	0.01	0.02	0.02
Sn	1	2	1	12		1	1	1	1
Mg#	65.1	69.3	67.6	59.8	68.9	67.4	67.7	69.2	68.3
ΣREE	36.46	35.5	30.40	94.23	29.69	29.22	29.14	28.44	29.55
$(La/Yb)_{PM}$	1.69	7.21	1.72	1.28	1.28	1.61	1.52	1.43	1.26
$(La/Sm)_{PM}$	2.03	3.89	1.71	1.14	1.14	1.56	1.54	1.43	1.28
$(Gd/Yb)_{PM}$	0.95	1.44	1.10	1.00	1.00	1.16	1.07	1.06	1.09
$(La/Yb)_{CN}$	1.68	7.20	1.72	1.28	1.28	1.61	1.52	1.43	1.26
$(La/Sm)_{CN}$	2.02	3.88	1.71	1.14	1.14	1.55	1.53	1.42	1.27
$(Gd/Yb)_{CN}$	0.95	1.43	1.10	1.00	1.00	1.16	1.07	1.06	1.08
(Nb/Nb*)	0.29	0.45	0.33	1.58	0.40	0.46	0.39	0.33	0.28
(Ta/Ta*)	0.46	0.67	0.61	2.74	0.41	0.47	0.42	0.34	0.30
(Ti/Ti*)	0.71	0.48	0.78	0.42	0.75	0.76	0.73	0.54	0.74
(Eu/Eu*)	0.94	0.70	0.92	0.51	0.94	1.00	1.00	1.67	1.00
(Ce/Ce*)	0.96	0.93	0.95	0.99	0.94	0.94	0.92	0.98	0.93

Table S2 continue.

Sample	BCB-30	BCB-31	BCB-32	BCB-33	BCB-34	BCB-35	BCB-36
Rock unit	Mafic	Mafic	Mafic	Mafic	Mafic	Mafic	Mafic
Rock (TAS)	Inter	Inter	Inter	Inter	Inter	Inter	Inter
Locality	Mauranipur	Mauranipur	Mauranipur	Mauranipur	Mauranipur	Mauranipur	Mauranipur
Long. (°E)	79.1753	79.1720	79.1750	79.1752	79.1754	79.1762	79.1766
Lat. (°N)	25.2279	25.2292	25.2295	25.2296	25.2294	25.2293	25.2289
SiO_2	53.05	52.52	53.58	52.02	52.48	54.65	53.44
TiO_2	0.68	0.72	0.66	0.68	0.72	0.63	0.64
Al_2O_3	13.59	15.26	13.64	13.98	14.78	12.96	13.49
Fe_2O_3	9.61	9.89	9.62	10.46	9.06	9.17	10.3
MnO	0.16	0.18	0.15	0.18	0.16	0.15	0.17
MgO	8.62	7.82	8.08	8.96	8.46	8.24	9.52
CaO	11.15	10.7	12.9	11.7	12.3	12.05	9.53
Na_2O	3.05	3.2	1.22	2.17	2.22	1.68	2.99
K_2O	0.21	0.09	0.03	0.11	0.15	0.03	0.11
P_2O_5	0.06	0.08	0.06	0.07	0.07	0.06	0.06
LOI	0.73	0.58	0.56	0.64	0.6	0.62	0.61
Total	100.91	101.04	100.5	100.97	101	100.24	100.86
Ba	69.2	38.6	31.1	27.7	61	38.2	60.2
Co	40	41	44	44	44	40	40
Cr	530	190	510	490	480	530	470
Cs	0.61	0.12	0.02	0.23	0.66	0.08	0.34
Cu	84	92	85	84	22	72	100
Ga	11.9	14.1	15.1	14.1	14.8	14.5	13.4
Hf	1.5	1.6	1.4	1.5	1.6	1.4	1.4
Nb	1.8	2.3	1.7	1.7	1.9	1.7	1.6
Ni	130	72	126	127	133	128	122
Pb			4	2	2	3	
Rb	8.4	1.9	0.4	2.3	4.3	0.6	3.1
Sc	38	42	38	38	40	36	35
Sr	88.5	93.6	120.5	105	126	88	62.6
Ta	0.1	0.1	0.1	0.1	0.1	0.1	0.1
Th	0.99	1.28	0.92	0.96	1.02	0.92	0.88
U	0.72	0.34	0.25	0.26	0.28	0.26	0.25
V	313	343	299	312	320	300	304
Y	17.6	21.2	17.3	17.9	17.1	16.9	17.6
Zn	64	69	65	72	79	60	69
Zr	52	60	51	51	55	50	49
La	3.6	4.2	3.8	3.8	3.9	3.7	3.6
Ce	8.1	9.9	8.1	8.4	8.8	8	8
Pr	1.19	1.39	1.2	1.22	1.32	1.18	1.15
Nd	5.3	6.1	5.4	5.6	5.8	5.4	5.2
Sm	1.71	1.66	1.67	1.7	1.83	1.6	1.63
Eu	0.65	0.58	0.7	0.6	0.71	0.66	0.66
Gd	2.52	2.65	2.46	2.46	2.64	2.35	2.41
Tb	0.49	0.54	0.47	0.48	0.49	0.45	0.49
Dy	3.05	3.4	2.92	3.03	3.05	2.94	2.94
Ho	0.64	0.78	0.64	0.65	0.66	0.65	0.63
Er	1.98	2.46	1.96	1.97	1.96	1.85	1.85
Tm	0.28	0.36	0.28	0.29	0.27	0.28	0.28
Yb	1.9	2.5	1.85	1.87	1.78	1.81	1.84
Lu	0.28	0.35	0.27	0.26	0.25	0.25	0.26
Bi	0.01	0.02	0.02	0.01	0.01	0.01	
Sn		1	1		1	1	
Mg#	69.2	66.5	67.8	68.3	70.1	69.3	69.9
ΣREE	28.64	33.47	28.80	29.30	30.41	28.18	28.00
$(La/Yb)_{PM}$	1.46	1.29	1.14	1.40	1.38	1.49	1.33
$(La/Sm)_{PM}$	1.51	1.32	1.59	1.43	1.40	1.34	1.38
$(Gd/Yb)_{PM}$	1.10	1.08	0.86	1.08	1.07	1.20	1.06
$(La/Yb)_{CN}$	1.46	1.29	1.14	1.40	1.38	1.28	1.33
$(La/Sm)_{CN}$	1.50	1.31	1.58	1.42	1.40	1.14	1.38
$(Gd/Yb)_{CN}$	1.10	1.07	0.86	1.08	1.06	1.00	1.06
(Nb/Nb*)	0.33	0.54	0.47	0.49	0.36	0.43	0.32
(Ta/Ta*)	0.34	0.44	0.51	0.54	0.35	0.47	0.37
(Ti/Ti*)	0.76	0.77	0.72	0.78	0.78	0.72	0.71
(Eu/Eu*)	0.95	0.84	1.05	0.89	0.99	1.04	1.01
(Ce/Ce*)	0.94	0.99	0.91	0.94	0.94	0.92	0.95

Table S2 continue.

Sample	BCB-37	BCB-38	BCB-39	BCB-40	BCB-41	BCB-42	BCB-43
Rock unit	Mafic	Mafic	Mafic	Mafic	Mafic	Mafic	Mafic
Rock (TAS)	Inter	Inter	Inter	Inter	Inter	Inter	Inter
Locality	Mauranipur	Mauranipur	Mauranipur	Mauranipur	Mauranipur	Mauranipur	Mauranipur
Long. (°E)	79.1768	79.1765	79.1766	79.1861	79.1766	79.1771	79.1732
Lat. (°N)	25.2278	25.2274	25.2289	25.2362	25.2132	25.2118	25.2314
SiO_2	55.24	52.16	51.9	53.51	51.89	52.09	53.06
TiO_2	0.64	0.68	0.7	0.68	0.65	0.73	0.74
Al_2O_3	13.44	14.3	13.23	13.6	12.56	14.72	14.3
Fe_2O_3	8.53	10.33	10.87	9.75	10.42	9.4	10.81
MnO	0.14	0.17	0.17	0.16	0.19	0.16	0.19
MgO	8.11	8.69	9.37	8.22	9.16	8.04	7.57
CaO	11.6	11.65	10.29	10.98	13.14	12.16	10.75
Na_2O	1.82	2.09	2.79	2.85	1.83	2.22	1.99
K_2O	0.04	0.19	0.1	0.11	0.36	0.31	0.19
P_2O_5	0.06	0.07	0.07	0.06	0.06	0.07	0.08
LOI	0.64	0.64					
Total	100.26	100.97	99.49	99.92	100.26	99.9	99.68
Ba	41.4	41.7	46.49	96.71	86.85	71.07	37.2
Co	37	42	36.53	38	37.8	38.17	40.17
Cr	570	660	373.73	462.55	403.48	413.87	186.77
Cs	0.08	0.41	0.3	0.11	0.79	1.06	0.3
Cu	79	93	111.7	69.32	36.34	117.66	102.08
Ga	14.3	15.1	11.93	12.23	10.6	13.12	12.39
Hf	1.4	1.5	1.46	1.41	1.27	1.38	1.85
Nb	1.7	1.8	1.95	1.9	2.25	2.17	2.59
Ni	125	136	99.46	95.2	95.35	100.54	50.62
Pb		6					
Rb	0.6	5.6	3.5	4.9	19.33	16.81	8.12
Sc	35	38					
Sr	89.6	110	62.84	96.07	80.13	126.46	103.35
Ta	0.1	0.1	0.11	0.11	0.11	0.11	0.18
Th	0.94	1.01	1.18	1.19	1.1	1.12	1.97
U	0.26	0.28	0.29	0.28	0.27	0.27	0.45
V	302	319	313.2	369.33	351.15	399.61	377.81
Y	17.3	18.3	22.08	25.28	24.84	27.19	33.5
Zn	54	68	73.75	66.37	73.43	68.05	71.55
Zr	52	54	56.16	54.95	52.74	58	72.11
La	3.9	3.9	3.46	3.86	3.39	3.49	5.92
Ce	8.2	8.5	7.69	8.16	7.46	7.61	12.66
Pr	1.21	1.25	1.01	1.05	0.96	0.94	1.56
Nd	5.3	5.7	4.89	5.33	4.89	4.73	7.41
Sm	1.66	1.75	1.55	1.66	1.56	1.59	2.22
Eu	0.66	0.71	0.59	0.61	0.52	0.66	0.74
Gd	2.45	2.64	2.26	2.31	2.11	2.21	2.94
Tb	0.47	0.51	0.44	0.44	0.42	0.43	0.57
Dy	2.92	3.16	2.88	2.93	2.82	2.81	3.83
Ho	0.65	0.69	0.63	0.63	0.61	0.59	0.83
Er	1.93	1.99	1.9	1.91	1.86	1.79	2.61
Tm	0.27	0.28	0.27	0.28	0.28	0.27	0.39
Yb	1.8	1.9	1.7	1.74	1.7	1.7	2.52
Lu	0.26	0.29	0.25	0.26	0.25	0.25	0.38
Bi	0.01	0.01					
Sn	1	1	2.66	2.86	2.6	2.22	2.42
Mg#	70.5	67.9	68.4	67.9	68.8	68.2	63.7
ΣREE	28.76	30.11	26.64	28.24	26.01	26.26	40.75
$(La/Yb)_{PM}$	1.47	1.40	1.39	1.51	1.36	1.40	1.60
$(La/Sm)_{PM}$	1.47	1.40	1.40	1.46	1.36	1.38	1.67
$(Gd/Yb)_{PM}$	1.10	1.13	1.08	1.08	1.01	1.05	0.95
$(La/Yb)_{CN}$	1.47	1.39	1.38	1.51	1.35	1.39	1.60
$(La/Sm)_{CN}$	1.47	1.39	1.39	1.45	1.36	1.37	1.67
$(Gd/Yb)_{CN}$	1.10	1.12	1.08	1.07	1.00	1.05	0.94
(Nb/Nb*)	0.40	0.43	0.46	0.27	0.36	0.39	0.51
(Ta/Ta*)	0.44	0.44	0.48	0.29	0.32	0.37	0.66
(Ti/Ti*)	0.72	0.71	0.73	0.64	0.66	0.64	0.55
(Eu/Eu*)	1.00	1.01	0.96	0.95	0.87	1.07	0.88
(Ce/Ce*)	0.91	0.93	0.99	0.97	0.99	1.00	0.99

$Nb/Nb^* = 2*Nb_{PM} / (Ba+La)_{PM}$
$Ta/Ta^* = 2*Ta_{PM} / (Ba+La)_{PM}$
$Ti/Ti^* = Ti_{PM} / ((EU+Y)/2)_{PM}$
$Eu/Eu^* = 2*Eu_{PM} / (Sm+Gd)_{PM}$
$Ce/Ce^* = 2*Ce_{PM} / (La+Pr)_{PM}$
$_{PM}$= Primitive mantle normalized value (taken from McDonough and Sun, 1995)
$_{CN}$= Chondrite-normalized (taken from McDonough and Sun, 1995).

Figure S1. Bivariate ratio between Zr *vs* Nb, Th, U, and Hf.

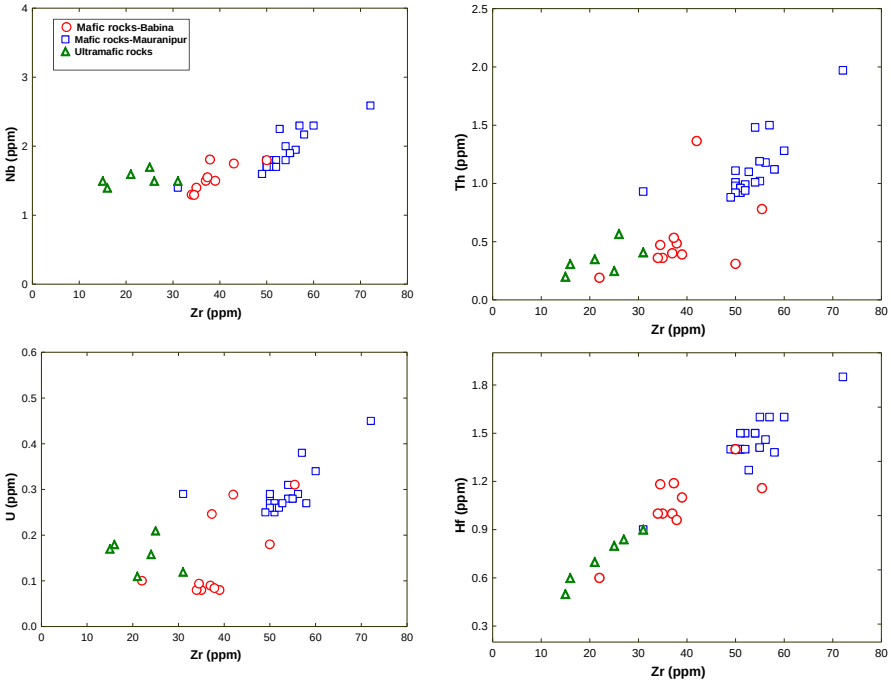

References SR1.

1. Joshi, K. B., Bhattacharjee, J., Rai, G., Halla, J., Ahmad, T., Kurhila, M., Heilimo, E., Choudhary, A. K., 2017. The diversification of granitoids and plate tectonic implications at the Archean–Proterozoic boundary in the Bundelkhand craton, Central India. In: Halla, J., Whitehouse, M.J., Ahmad, T., Bagai, Z. (eds) Crust–Mantle Interactions and Granitoid Diversification: Insights from Archean Cratons. Geological Society, London, Special Publications 449, 123–157.
2. Kaur, P., Zeh, A., Chaudhri, N., 2014. Characterisation and U–Pb–Hf record of the 3.55 Ga felsic crust from the Bundelkhand Craton, northern India. Precambrian Research 255, 236–244.
3. Kaur, P., Zeh, A., Chaudhri, N., Eliyas, N., 2016. Unravelling the record of Archean crustal evolution of the Bundelkhand Craton, northern India using U–Pb zircon–monazite ages, Lu–Hf isotope systematics, and whole-rock geochemistry of granitoids. Precambrian Research 281, 384–413.
4. Mohan, M.R., Singh, S.P., Santosh, M., Siddiqui, M.A., Balaram, V., 2012. TTG suite from the Bundelkhand Craton, Central India: geochemistry, petrogenesis and implications for Archean crustal evolution. Journal of Asian Earth Sciences 58, 38–50.
5. Mondal, M.E.A., Goswami, J.N., Deomurari, M.P., Sharma, K.K., 2002. Ion microprobe 207Pb/206Pb ages of zircons from the Bundelkhand massif, northern India: implications for crustal evolution of the Bundelkhand–Aravalli protocontinent. Precambrian Research 117, 85–100.
6. Saha, L., Frei, D., Gerdes, A., Pati, J.K., Sarkar, S., Patoke, V., Bhandari, A., Nasipur, P., 2016. Crustal geodynamics from the Archean Bundelkhand Craton, India:constraints from zircon U–Pb–Hf isotope studies. Geological Magazine 153, 179–192.
7. Saha, L., Pant, N.C., Pati, J.K., Berndt, J., Bhattacharya, A., Satynarayanan, M., 2011. Neoarchean high-pressure margarite-phengitic muscovite-chlorite corona mantled corundum in quartz-free high-Mg, Al phlogopite-chlorite schists from the Bundelkhand craton, north central India. Contributions to Mineralogy and Petrology 161, 511–530.
8. Sarkar, G., Corfu, F., Paul, D. K., McNaughton, N. J., Gupta, S. N., Bishui, P. K. 1993. Early Archean crust in Bastar Craton, Central India—a geochemical and isotopic study. Precambrian Research 62, 127-137.
9. Malviya, V. P., Arima, M., Pati, J. K., Kaneko, Y., 2004. First report of metamorphosed pillow lava in central part of Bundelkhand craton–an island arc setting of possible late Archean age. Gondwana Research 7, 1338–1340.
10. Malviya, V.P., Arima, M., Pati, J.K., Kaneko, Y., 2006. Petrology and geochemistry of metamorphosed basaltic pillow lava and basaltic komatiite in the Mauranipur area: subduction related volcanism in the Archean Bundelkhand craton, Central India. Journal of Mineralogical and Petrological Sciences 101, 199–217.
11. Singh, S. P., Subramanyam, K. S. V., Manikyamba, C., Santosh, M., Singh, M. R., Kumar, B. C. 2018. Geochemical systematics of the Mauranipur-Babina greenstone belt, Bundelkhand Craton, Central India: Insights on Neoarchean mantle plume-arc accretion and crustal evolution. Geoscience Frontiers 9, 769–788.
12. Singh, V.K., Slabunov, A., 2015a. The central Bundelkhand Archean greenstone complex, Bundelkhand craton, central India: geology, composition, and geochronology of supracrustal rocks. International Geology Review 57, 1349–1364.
13. Singh, V.K., Slabunov, A., 2015b. Geochemical characteristics of Banded Iron Formation and Metavolcanics of Babina greenstone belt of the Bundelkhand Craton, Central India. Journal of Economic Geology & Geo Resource Management 10, 63–74.
14. Singh, V.K., Slabunov, A., 2016. Two types of Archean supracrustal belts in the Bundelkhand craton, India: Geology, geochemistry, age and implication for craton crustal evolution. Journal of Geological Society of India 88, 339–348.
15. Malviya, V.P., Arima, M. and Pati, J.K. 2013. Petrochemical and geochemical study of Banded Iron Formation (BIF) from Archean greenstone belt of Bundelkhand craton. 3rd Precambrian Continental Growth and Tectonism (PCGT 2013) 23-26 November 2013, Jhansi, India Abstract Volume IAGR Conference Series No. 16, pp. 99-10.
16. Slabunov, A., Singh, V.K., Kumar, B., Xiaoli, L., 2017. Paleoarchean zircons from quartzite of South Bundelkhand Supracrustal Complex: origin and implications for crustal evolution in Bundelkhand Craton, Central India. Current Science 112, 794–801.
17. Slabunov, A., Singh, V.K., 2018. Meso–Neoarchaean crustal evolution of the Bundelkhand Craton, Indian Shield: new data from greenstone belts. International Geology Review, in press, https://doi.org/10.1080/00206814.2018.1512906.
18. Verma, S.K., Verma, S.P., Oliveira, E.P., Singh, V.K., Moreno, J.A., 2016. LA-SF-ICP-MS zircon U–Pb geochronology of granitic rocks from the central Bundelkhand greenstone complex, Bundelkhand craton, India. Journal of Asian Earth Sciences 118, 125–137.
19. Pati, J.K., Patel, S.C., Pruseth, K.L., Malviya, V.P., Arima, M., Raju, S., Pati, P., Prakash, K., 2007. Geology and geochemistry of giant quartz veins from the Bundelkhand Craton, central India and their implications. Journal of Earth System Science 116, 497–510.
20. Rao, J.M., Rao, G.V.S.P., Widdowson, M., Kelley, S.P., 2005. Evolution of Proterozoic mafic dyke swarms of the Bundelkhand Granite Massif, Central India. Current Science 88, 502–506.
21. Pradhan, V.R., Meert, J.G., Pandit, M., Kamenov, G., Mondal, M.E.A., 2012. Paleomagnetic and geochronological studies of the mafic dyke swarms of Bundelkhand craton, central India: implications for the tectonic evolution and paleogeographic reconstructions. Precambrian Research 198–199, 51–76.
22. Absar, N., Raza, M., Roy, M., Naqvi, S.M., Roy, A.K., 2009. Composition and weathering conditions of Paleoproterozoic upper crust of Bundelkhand craton, Central India: records from geochemistry of clastic sediments of 1.9 Ga Gwalior Group. Precambrian Research 168, 313–329.
23. Gregory, L.C., Meert, J.G., Bingen, B., Pandit, M.K., Torsvik, T.H., 2009.Paleomagnetism and geochronology of the Malani Igneous Suite, northwestIndia: implications for the configuration of Rodinia and the assembly of Gondwana. Precambrian Research 170, 13–26.
24. Turner, C.C., Meert, J.G., Pandit, M.K., Kamenov, G.D., 2014. A detrital zircon U–Pb and Hf isotopic transect across the Son Valley sector of the Vindhyan Basin, India: implication for basin evolution and paleogeography. Gondwana Research 26, 348–364.

References SR2.

1. Jayananda, M., Kano, T., Peucat, J.-J., Channabasappa, S., 2008. 3.35 Ga komatiitevolcanism in the western Dharwar craton, southern India: constraints from Ndisotopes and whole-rock geochemistry. Precambrian Research 162, 160–179.
2. Maya, M., Bhutani, R., Balakrishnan, S., Sandhya, S.R., 2017. Petrogenesis of 3.15 Ga old Banasandra komatiites from the Dharwar craton, India: Implications for early mantle heterogeneity. Geoscience Frontiers 8, 467–481.
3. Chaudhuri, T., Satish-Kumar, M.,Mazumder, R., Biswas, S., 2017. Geochemistry and Sm-Nd isotopic characteristics of the Paleoarchean Komatiites from Singhbhum Craton, Eastern India and their implications. Precambrian Research 298, 385–402.
4. Sharma, M., Basu, A. R., Ray, S. L. 1994. Sm-Nd isotopic and geochemical study of the Archean tonalite-amphibolite association from the eastern Indian Craton. Contributions to Mineralogy and Petrology 117, 45-55.
5. Chakraborti, T.M., Ray, A., Deb, G.K., Chakrabarti, R., Banerjee, A., 2017. Evidence of enriched mantle in the Archaean beneath eastern Indian Singhbhum Craton: constraints from geochemistry and Sr-Nd isotopic studies of mafic-ultramafic rocks from Bangriposi, Orissa, India. Geophysical Research Abstracts, Vol. 19, EGU2017-273, 2017.

APPENDIX II:

CHAPTER 3

SUPPLEMENTARY MATERIAL

This supplement contains 2 Tables (Tables S1-S2) and references.

Table S1. Representative Major (anhydrous calculated oxide) (wt.%) and trace (ppm) element concentrations for the sanukitoid suites (s.l.) and high-K anatectic granites in the BC.

Sample	BC-16-01	BC-16-02	BC-16-03	BC-16-04	BC-16-05	BC-16-06	BC-16-07	BC-16-08	BC-16-09
Rock unit	Sanukitoids	Sanukitoids	Sanukitoids	Sanukitoids	Sanukitoids	Sanukitoids	Sanukitoids	Sanukitoids	Sanukitoids
SiO_2	68.148	65.870	64.462	64.317	63.983	71.141	65.178	66.102	64.208
TiO_2	0.468	0.429	0.586	0.585	0.315	0.480	0.529	0.510	0.598
Al_2O_3	14.858	13.885	15.196	15.384	13.632	14.054	15.409	14.866	15.391
Fe_2O_3	1.199	1.651	1.575	1.647	2.995	1.110	1.462	1.473	1.621
FeO	2.999	4.127	3.937	4.117	7.487	2.219	3.656	3.682	4.053
MnO	0.080	0.132	0.102	0.102	0.161	0.050	0.096	0.112	0.093
MgO	1.857	3.122	2.444	2.705	0.883	0.679	2.620	2.705	2.650
CaO	3.622	4.991	5.401	4.912	3.918	1.933	3.731	3.896	4.432
Na_2O	3.818	3.705	3.502	3.444	3.735	3.267	3.538	3.712	3.552
K_2O	2.825	1.974	2.637	2.628	2.697	4.955	3.633	2.793	3.239
P_2O_5	0.126	0.114	0.157	0.161	0.194	0.113	0.148	0.148	0.161
Total	100.0	100.0	100.0	100.0	100.0	100.0	100.0	100.0	100.0
LOI	0.62	0.29	1.10	1.13	0.50	0.73	1.49	1.22	1.10
Ba	715.40	508.40	690.52	816.06	502.71	784.95	1003.73	836.69	967.43
Co	15.39	15.51	18.86	18.45	69.35	14.42	15.03	17.52	18.10
Cr	49.03	46.15	87.35	92.43	13.67	12.71	79.46	65.79	68.58
Cs	17.49	6.66	0.80	3.08	4.71	1.92	1.25	2.10	3.35
Cu	8.70	8.99	22.41	10.22	11.08	6.19	15.73	3.71	13.92
Hf	5.20	4.76	3.75	4.28	4.78	9.43	4.98	4.39	4.70
Nb	10.33	9.96	9.08	9.15	34.40	23.57	9.72	9.14	9.39
Ni	12.40	15.05	18.89	16.00	15.32	4.69	16.36	12.96	15.52
Pb	15.98	15.80	19.03	19.44	17.89	28.57	23.28	20.60	17.11
Rb	141.15	84.97	67.72	87.11	140.13	190.55	115.69	154.46	99.42
Sb	0.95	0.92	0.26	0.18	0.13	0.06	0.32	0.03	0.24
Sc	5.57	7.43	18.51	14.73	32.38	19.80	12.09	12.85	20.03
Sr	303.36	248.53	392.14	412.29	352.91	184.54	343.28	266.65	353.92
Ta	1.57	0.70	0.89	0.85	7.80	3.40	0.90	1.03	0.85
Th	8.09	13.05	14.12	13.95	22.02	43.21	17.94	17.54	12.18
U	1.38	1.76	2.57	3.08	13.36	11.19	5.01	6.11	4.20
V	84.94	86.42	82.14	104.32	37.54	32.41	79.27	78.69	97.25
Y	8.92	24.13	28.40	22.95	97.36	60.71	22.82	19.30	24.32
Zn	45.04	59.13	56.56	68.60	67.01	31.34	63.74	62.59	62.28
Zr	192.23	162.26	137.84	150.57	129.45	337.72	182.10	150.66	166.41
La	36.09	52.76	41.85	41.92	111.52	113.60	49.18	42.43	37.60
Ce	78.62	99.29	64.86	71.82	205.67	195.97	84.11	73.71	69.47
Pr	6.76	10.91	8.74	7.92	21.88	22.52	8.93	7.83	7.58
Nd	23.98	40.53	32.82	28.50	26.78	27.89	31.28	27.24	27.30
Sm	4.24	8.38	6.90	5.57	16.26	14.66	5.90	5.10	5.63
Eu	1.23	1.39	1.71	1.64	2.03	1.75	1.86	1.48	1.75
Gd	4.71	8.52	7.85	6.48	19.16	17.39	7.30	6.20	6.77
Tb	0.55	1.18	1.03	0.79	2.69	2.22	0.84	0.70	0.84
Dy	2.65	6.39	5.25	4.03	15.01	11.07	4.02	3.37	4.24
Ho	0.53	1.26	1.04	0.80	3.18	2.19	0.82	0.68	0.88
Er	1.53	3.53	3.01	2.42	9.71	6.35	2.41	2.04	2.58
Tm	0.20	0.49	0.41	0.33	1.44	0.84	0.32	0.27	0.35
Yb	1.43	3.18	2.69	2.25	9.98	5.30	2.18	1.91	2.42
Lu	0.22	0.47	0.41	0.35	1.54	0.76	0.34	0.30	0.39
Mo	0.36	0.30	1.10	0.47	0.46	0.57	1.18	0.30	1.37
Sn	4.41	6.38	2.24	2.57	13.83	3.67	2.10	2.35	2.11
Ba+Sr	1018	757	1082	1228	855	969	1347	1103	1321
K_2O/Na_2O	0.740	0.533	0.753	0.763	0.722	1.517	1.027	0.753	0.912
Mg#	44.809	49.785	44.866	46.272	13.385	27.328	48.43	49.057	46.147
A/CNK	0.933	0.802	0.824	0.882	0.842	0.986	0.932	0.917	0.884
ANK	1.575	1.683	1.736	1.779	1.467	1.295	1.549	1.601	1.620
$\frac{FeO_t}{(FeO_t+MgO)}$	0.687	0.643	0.687	0.674	0.920	0.826	0.655	0.649	0.675
ASI	0.951	0.815	0.841	0.902	0.867	1.005	0.952	0.937	0.904
ΣREE	160.084	231.901	173.323	170.797	481.840	461.434	195.461	169.895	163.555
$(La/Yb)_{CN}$	17.200	11.281	10.570	12.672	7.593	14.573	15.360	15.080	10.547
$(La/Lu)_{CN}$	16.848	11.556	10.640	12.440	7.499	15.483	15.085	14.800	10.073
$(La/Sm)_{CN}$	5.312	3.930	3.788	4.702	4.283	4.838	5.206	5.200	4.169
$(Gd/Yb)_{CN}$	2.673	2.171	2.361	2.333	1.554	2.657	2.716	2.626	2.262
Nb/Nb*	0.187	0.187	0.159	0.144	0.412	0.238	0.127	0.141	0.136
Ta/Ta*	0.496	0.229	0.272	0.234	1.625	0.597	0.204	0.277	0.216
Ti/Ti*	0.466	0.292	0.329	0.364	0.087	0.186	0.303	0.361	0.351
Eu/Eu*	0.833	0.495	0.708	0.832	0.350	0.333	0.863	0.801	0.860
Gd/Er	2.2	1.74	1.87	1.92	1.42	1.97	2.17	2.17	1.88
Sr/Y	34.01	10.23	13.8	17.97	3.63	3.04	15.05	13.82	14.55
Nb/Th	0.152	0.091	0.077	0.078	0.186	0.065	0.065	0.062	0.092
La/Yb	25.319	16.606	15.560	18.654	11.178	35.452	22.610	22.198	15.526

Table S1 continue.

Sample	BC-16-10	BC-16-11	BC-16-12	BC-16-13	BC-16-14	BC-16-15	BC-16-16	BC-16-17	BC-16-18
Rock unit	Sanukitoids	Sanukitoids	Sanukitoids	Sanukitoids	Sanukitoids	Sanukitoids	Sanukitoids	Sanukitoids	Sanukitoids
SiO_2	68.284	71.074	61.813	63.919	69.712	66.467	66.406	66.671	65.894
TiO_2	0.402	0.427	0.778	0.575	0.437	0.497	0.833	0.763	0.832
Al_2O_3	15.138	12.991	16.131	15.722	14.315	15.967	15.322	15.071	15.242
Fe_2O_3	0.948	1.149	1.644	1.590	1.092	1.354	1.648	1.583	1.771
FeO	2.371	2.873	4.697	3.974	2.184	2.707	3.297	3.167	3.543
MnO	0.076	0.130	0.110	0.108	0.154	0.070	0.106	0.103	0.115
MgO	0.769	1.527	2.850	2.757	1.262	1.532	1.640	1.054	1.159
CaO	4.223	3.976	5.090	4.613	2.832	3.235	2.014	2.981	3.276
Na_2O	3.931	3.510	3.874	3.673	3.620	3.487	3.990	3.767	3.937
K_2O	3.734	2.224	2.748	2.924	4.243	4.553	4.465	4.590	3.927
P_2O_5	0.123	0.120	0.267	0.145	0.150	0.131	0.278	0.250	0.303
Total	100.0	100.0	100.0	100.0	100.0	100.0	100.0	100.0	100
LOI	1.03	0.49	1.23	1.05	1.04	1.35	1.55	0.65	0.96
Ba	705.91	906.53	1278.88	697.03	1293.31	1523.76	2516.74	2107.19	2334
Co	11.50	17.75	19.96	15.71	19.14	18.41	8.75	13.13	9.9
Cr	22.65	62.24	70.52	60.96	34.03	43.62	8.72	10.69	5.40
Cs	2.26	6.63	2.69	1.04	1.15	0.87	0.81	2.78	1.90
Cu	4.17	3.85	19.52	18.21	7.03	8.89	5.36	9.63	3.82
Hf	4.36	4.43	5.59	4.17	4.14	7.29	6.12	6.89	5.67
Nb	12.01	10.75	11.47	9.98	13.49	8.75	12.33	13.52	10.7
Ni	10.03	15.90	21.64	18.97	12.03	11.21	2.41	3.89	1.17
Pb	36.26	24.56	16.77	18.95	88.17	22.72	8.05	27.26	23.3
Rb	175.75	114.18	102.47	85.16	159.46	116.19	193.08	168.82	121
Sb	0.04	0.15	0.08	0.18	0.04	0.18	0.04	0.10	0.06
Sc	4.14	6.17	8.32	23.69	4.44	10.71	11.61	12.19	10.2
Sr	693.14	529.65	622.38	319.13	526.08	353.25	277.50	357.26	410
Ta	0.99	0.92	0.76	0.86	1.16	0.47	0.97	1.05	1.15
Th	18.03	13.84	11.72	17.59	18.06	13.02	19.93	25.03	19.4
U	4.98	4.68	2.78	3.99	6.34	1.82	3.93	5.79	4.08
V	111.11	124.40	169.00	80.56	99.52	59.31	35.46	34.03	39.0
Y	16.59	17.20	13.31	25.11	14.55	21.56	27.21	27.85	21.4
Zn	50.36	82.13	87.27	58.59	172.49	58.40	62.54	72.47	76.1
Zr	172.87	184.97	250.92	160.66	157.39	271.28	224.33	245.55	213
La	49.72	44.72	65.73	46.09	45.98	65.64	69.45	71.08	55.2
Ce	91.86	82.96	136.30	72.57	87.63	102.20	119.24	127.41	106
Pr	9.71	8.38	11.34	8.72	8.42	11.41	13.10	13.90	11.2
Nd	33.69	29.65	38.42	30.94	28.77	39.54	46.74	48.98	41.9
Sm	6.26	5.69	6.35	6.10	5.21	6.82	8.43	8.67	7.02
Eu	1.43	1.50	1.79	1.58	1.56	2.27	4.02	3.35	2.98
Gd	7.62	7.07	8.38	6.98	6.65	7.76	9.42	9.33	5.61
Tb	0.86	0.82	0.83	0.88	0.73	0.88	1.06	1.06	0.81
Dy	4.05	4.09	3.62	4.53	3.40	4.03	4.99	5.08	4.41
Ho	0.82	0.82	0.71	0.92	0.69	0.80	0.99	1.00	0.80
Er	2.50	2.48	2.15	2.64	2.13	2.25	2.88	2.93	2.36
Tm	0.35	0.34	0.27	0.36	0.31	0.29	0.38	0.39	0.34
Yb	2.46	2.33	1.79	2.35	2.16	1.94	2.54	2.63	2.13
Lu	0.38	0.36	0.28	0.36	0.35	0.31	0.40	0.41	0.32
Mo	0.14	0.12	0.46	0.73	0.19	0.35	1.18	1.89	2.19
Sn	3.48	3.68	2.19	1.88	2.42	1.30	1.88	2.38	1.76
Ba+Sr	1399	1436	1901	1016	1819	1877	2794	2464	2743
K_2O/Na_2O	0.950	0.634	0.709	0.796	1.172	1.306	1.119	1.218	0.997
Mg#	29.835	41.055	45.131	47.624	41.532	41.023	37.946	29.035	28.702
A/CNK	0.832	0.843	0.867	0.894	0.912	0.965	1.017	0.909	0.913
ANK	1.421	1.575	1.695	1.682	1.339	1.472	1.318	1.336	1.42
$\frac{FeO_t}{(FeO_t+MgO)}$	0.807	0.719	0.684	0.662	0.715	0.719	0.745	0.813	0.815
ASI	0.846	0.859	0.898	0.912	0.933	0.984	1.065	0.943	0.955
ΣREE	207.649	187.144	274.338	180.485	190.583	242.089	278.651	291.144	237.165
$(La/Yb)_{CN}$	13.708	13.049	24.942	13.345	14.440	19.993	18.589	18.364	17.589
$(La/Lu)_{CN}$	13.639	13.018	24.670	13.231	13.741	22.237	17.985	17.984	18.210
$(La/Sm)_{CN}$	4.961	4.905	6.466	4.722	5.506	6.010	5.146	5.121	4.920
$(Gd/Yb)_{CN}$	2.503	2.458	3.786	2.406	2.489	3.236	3.002	2.872	2.127
Nb/Nb*	0.194	0.155	0.115	0.168	0.150	0.078	0.075	0.094	0.823
Ta/Ta*	0.279	0.230	0.133	0.252	0.225	0.074	0.103	0.126	0.135
Ti/Ti*	0.306	0.309	0.528	0.355	0.323	0.251	0.257	0.270	0.342
Eu/Eu*	0.628	0.721	0.749	0.737	0.805	0.949	1.369	1.128	1.402
Gd/Er	2.18	2.04	2.79	1.89	2.25	2.47	2.35	2.28	1.71
Sr/Y	41.78	30.8	46.75	12.71	36.16	16.39	10.2	12.83	0.25
Nb/Th	0.079	0.093	0.117	0.068	0.089	0.080	0.074	0.064	0.744
La/Yb	20.179	19.208	36.716	19.644	21.256	33.847	27.364	27.032	25.893

Table S1 continue.

Sample	BC-16-19	BC-16-20	BC-16-21	BC-16-22	BC-16-23	BC-16-24	BC-16-25
Rock unit	Sanukitoids	Anatectic granites	Anatectic granites	Anatectic granites	Anatectic granites	Anatectic granites	Anatectic granites
SiO_2	70.306	72.385	70.594	70.203	75.430	76.048	75.815
TiO_2	0.193	0.301	0.275	0.407	0.185	0.096	0.151
Al_2O_3	14.164	14.005	15.749	13.745	13.096	13.486	12.679
Fe_2O_3	1.029	0.702	0.705	1.000	0.429	0.329	0.419
FeO	2.058	1.403	1.410	2.000	0.858	0.658	0.838
MnO	0.074	0.034	0.034	0.090	0.032	0.016	0.014
MgO	1.065	0.395	0.511	0.866	0.632	0.220	0.166
CaO	2.811	1.390	2.625	2.412	0.467	1.388	0.990
Na_2O	5.866	2.930	3.680	4.176	3.147	4.102	3.361
K_2O	2.296	6.391	4.360	4.961	5.684	3.621	5.544
P_2O_5	0.138	0.065	0.056	0.140	0.038	0.035	0.023
Total	100.0	100.0	100.0	100.0	100.0	100.0	100.0
LOI	0.52	0.64	0.54	0.67	0.80	0.45	0.59
Ba	399.80	1011.63	1193.97	1437.34	498.11	417.71	275.89
Co	14.62	16.47	11.06	12.59	27.88	19.25	26.76
Cr	0.22	13.58	17.42	22.90	16.32		2.50
Cs	3.86	28.15	3.35	2.07	3.84	0.75	1.06
Cu	10.59	3.02	2.67	3.67	4.07	1.08	1.31
Hf	3.28	7.49	5.33	4.52	4.27	2.02	4.56
Nb	3.72	15.86	10.93	12.80	15.51	6.92	15.48
Ni	6.27	2.66	5.26	4.84	2.21	2.69	1.56
Pb	71.52	47.27	28.25	30.40	19.16	33.07	44.79
Rb	111.96	324.60	154.78	166.30	264.81	80.20	241.67
Sb	0.08	0.18	0.18	0.05	0.03	0.03	0.01
Sc	11.99	2.72	11.60	2.28	2.02	14.34	18.29
Sr	298.49	174.01	343.35	399.13	82.59	110.15	112.36
Ta	0.51	1.57	0.98	1.04	2.40	1.31	2.33
Th	11.22	40.28	20.24	9.50	36.95	9.87	67.04
U	1.99	5.57	3.04	4.07	6.81	3.25	20.21
V	37.96	85.96	22.05	81.88	67.32	8.57	9.28
Y	10.47	17.34	23.24	5.04	13.98	39.00	30.18
Zn	84.47	27.57	33.35	59.07	22.26	10.34	14.01
Zr	125.04	264.27	181.04	173.91	136.04	58.17	127.44
La	41.30	97.33	59.28	25.97	28.64	17.54	57.02
Ce	71.78	224.46	98.21	68.75	49.80	32.33	103.92
Pr	8.01	17.95	10.41	4.12	6.19	3.53	11.54
Nd	28.97	57.97	34.95	13.60	20.97	12.50	38.54
Sm	5.62	8.96	6.19	2.33	4.24	3.26	7.38
Eu	1.22	1.24	1.86	1.15	0.67	0.66	0.70
Gd	6.65	10.52	7.66	3.35	4.94	4.06	8.38
Tb	0.68	1.03	0.84	0.32	0.68	0.77	1.04
Dy	2.47	4.29	3.99	1.37	3.77	5.38	5.14
Ho	0.42	0.85	0.81	0.27	0.77	1.22	1.05
Er	1.23	2.66	2.45	0.86	2.37	3.81	3.21
Tm	0.12	0.36	0.34	0.11	0.35	0.62	0.47
Yb	0.86	2.47	2.31	0.84	2.47	4.32	3.29
Lu	0.13	0.39	0.36	0.13	0.38	0.66	0.52
Mo	0.10	0.54	1.15	0.15	0.41	0.22	0.28
Sn	5.87	10.31	2.40	3.79	4.97	1.41	2.33
Ba+Sr	698	1185	1537	1836	580	527	388
K_2O/Na_2O	0.391	2.182	1.185	1.188	1.806	0.883	1.649
Mg#	38.891	25.725	30.814	34.739	47.511	29.139	19.609
A/CNK	0.821	0.982	1.013	0.827	1.075	1.022	0.951
ANK	1.158	1.183	1.451	1.113	1.145	1.257	1.092
$\frac{FeO_t}{(FeO_t+MgO)}$	0.737	0.837	0.800	0.770	0.663	0.813	0.880
ASI	0.837	0.993	1.022	0.844	1.083	1.029	0.955
ΣREE	166.992	426.197	225.671	121.795	122.470	85.290	237.068
$(La/Yb)_{CN}$	32.523	19.741	17.398	19.914	7.886	2.756	11.768
$(La/Lu)_{CN}$	32.454	25.614	17.029	20.167	7.782	2.748	11.309
$(La/Sm)_{CN}$	4.591	6.780	5.977	6.970	4.218	3.362	4.824
$(Gd/Yb)_{CN}$	6.234	3.442	2.677	3.243	1.620	0.759	2.059
Nb/Nb*	0.089	0.155	0.119	0.147	0.385	0.227	0.354
Ta/Ta*	0.212	0.267	0.185	0.208	1.035	0.751	0.929
Ti/Ti*	0.185	0.247	0.157	0.470	0.241	0.070	0.129
Eu/Eu*	0.609	0.390	0.822	1.259	0.447	0.555	0.268
Gd/Er	3.88	2.84	2.25	2.79	1.49	0.77	1.88
Sr/Y	28.52	10.04	14.78	79.2	5.9	2.83	3.73
Nb/Th	0.040	0.047	0.064	0.161	0.050	0.083	0.028
La/Yb	37.875	39.364	25.611	31.081	11.608	4.057	17.323

Table S1 continue.

Sample	BC-16-26	BC-16-27	BC-16-28	BC-16-29	BC-16-30	BC-16-31	BC-16-32	BC-16-33
Rock unit	Anatectic granites	Anatectic granites	Anatectic granites	Anatectic granites	Anatectic granites	Anatectic granites	Anatectic granites	Anatectic granites
SiO_2	75.732	74.585	77.075	77.193	77.132	75.081	75.489	76.477
TiO_2	0.161	0.210	0.111	0.120	0.085	0.188	0.060	0.109
Al_2O_3	13.034	13.512	12.583	12.460	12.444	13.117	13.638	12.687
Fe_2O_3	0.461	0.505	0.402	0.253	0.327	0.513	0.145	0.391
FeO	0.922	1.010	0.803	0.505	0.655	1.027	0.291	0.782
MnO	0.035	0.041	0.021	0.013	0.018	0.034	0.012	0.024
MgO	0.297	0.410	0.098	0.264	0.180	0.366	0.092	0.101
CaO	0.926	1.114	0.740	0.286	0.462	0.695	0.451	0.819
Na_2O	3.704	3.570	3.859	3.051	3.439	3.398	3.584	3.166
K_2O	4.695	4.996	4.292	5.837	5.240	5.547	6.208	5.425
P_2O_5	0.033	0.048	0.016	0.017	0.017	0.033	0.030	0.019
Total	100.0	100.0	100.0	100.0	100.0	100.0	100.0	100.0
LOI	0.71	1.13	0.53	0.46	0.62	0.73	0.54	0.45
Ba	246.04	51.66	1289.53	89.39	933.66	235.90	145.74	145.28
Co	14.15	48.04	12.74	23.59	20.35	22.58	13.16	36.72
Cr	10.65	6.52		8.81	8.66	10.54	9.21	9.25
Cs	3.46	2.88	5.87	1.96	3.56	2.16	5.27	4.29
Cu	2.23	9.32	16.59	3.98	4.69	2.75	6.85	1.65
Hf	3.96	0.67	3.67	4.05	4.39	7.39	1.12	6.96
Nb	43.03	2.12	10.39	3.13	10.64	37.74	64.27	16.74
Ni	2.12	143.84	1.90	0.92	0.79	1.71	0.78	1.62
Pb	7.90	14.14	29.91	28.70	36.98	53.28	45.56	76.82
Rb	202.69	48.37	177.68	188.73	298.51	412.71	383.27	343.57
Sb	0.02	0.18	0.10	0.01	0.01	0.02		0.02
Sc	0.86	52.55	21.61	9.48	9.12	13.78	14.21	17.06
Sr	19.68	119.40	83.01	32.39	73.88	58.75	84.64	68.38
Ta	7.22	0.19	1.32	0.73	1.39	3.65	11.50	2.18
Th	4.30	0.85	22.27	38.73	27.42	81.28	10.79	45.60
U	0.31	0.71	7.11	6.42	8.43	20.87	10.48	30.68
V	32.20	186.83	5.12			2.79	7.54	1.17
Y	7.16	18.20	25.88	5.91	27.62	68.09	36.53	29.31
Zn	11.79	79.45	11.79	9.31	16.17	26.55	5.46	16.22
Zr	141.74	173.20	104.95	93.13	108.01	182.93	10.73	152.83
La	7.87	4.22	38.07	34.13	41.20	89.97	11.23	29.11
Ce	10.28	8.84	67.63	51.49	72.00	170.81	27.65	59.47
Pr	1.89	1.27	7.48	4.75	7.56	17.99	3.60	6.48
Nd	6.88	5.62	26.33	14.40	25.89	58.05	13.17	22.10
Sm	1.38	1.80	5.52	2.23	5.34	11.69	4.05	4.72
Eu	0.19	0.63	2.08	0.24	0.98	0.65	0.21	0.50
Gd	1.48	2.31	8.32	2.76	6.13	13.71	4.10	5.56
Tb	0.22	0.44	0.97	0.24	0.81	1.91	0.74	0.79
Dy	1.42	2.84	4.52	0.94	4.45	10.67	4.57	4.49
Ho	0.35	0.65	0.95	0.19	0.92	2.28	0.96	1.00
Er	1.20	1.95	2.98	0.61	2.75	6.93	3.06	3.13
Tm	0.22	0.29	0.41	0.09	0.40	1.04	0.57	0.49
Yb	1.78	1.97	2.85	0.71	2.73	6.98	4.74	3.59
Lu	0.30	0.30	0.43	0.13	0.43	1.08	0.80	0.58
Mo	0.18	0.30	1.18	0.29	3.91	0.23	3.44	0.21
Sn	7.65	4.90	2.64	1.32	3.27	8.52	7.17	2.78
Ba+Sr	265	171	1372	121	1007	294	230	213
K_2O/Na_2O	1.268	1.400	1.112	1.913	1.524	1.632	1.732	1.713
Mg#	28.335	33.313	12.999	39.143	25.299	30.481	27.893	13.651
A/CNK	1.014	1.015	1.020	1.051	1.022	1.020	1.015	1.009
ANK	1.156	1.182	1.137	1.093	1.090	1.121	1.074	1.138
$\frac{FeO_t}{(FeO_t+MgO)}$	0.818	0.781	0.923	0.735	0.840	0.803	0.822	0.919
ASI	1.020	1.024	1.023	1.055	1.026	1.026	1.021	1.013
ΣREE	34.021	30.276	164.020	111.950	167.159	383.079	74.877	137.530
$(La/Yb)_{CN}$	11.009	11.459	9.069	32.460	10.268	8.759	1.609	5.512
$(La/Lu)_{CN}$	2.714	1.457	9.155	27.139	9.880	8.629	1.463	5.216
$(La/Sm)_{CN}$	3.571	1.464	4.306	9.573	4.816	4.805	1.734	3.850
$(Gd/Yb)_{CN}$	0.672	0.950	2.361	3.122	1.819	1.590	0.699	1.255
Nb/Nb*	2.587	0.439	0.121	0.141	0.154	0.643	4.845	0.743
Ta/Ta*	7.549	0.678	0.269	0.567	0.352	1.081	15.078	1.683
Ti/Ti*	0.553	0.250	0.057	0.409	0.065	0.092	0.060	0.106
Eu/Eu*	0.400	0.937	0.932	0.289	0.523	0.155	0.156	0.296
Gd/Er	0.88	0.85	1.99	3.25	1.59	1.42	0.96	1.23
Sr/Y	2.75	6.56	3.2	5.48	2.68	0.87	2.32	2.34
Nb/Th	1.193	0.298	0.056	0.010	0.046	0.055	0.710	0.044
La/Yb	4.429	2.147	13.350	30.782	15.114	30.894	2.369	8.115

$Nb/Nb^* = 2^*Nb_{PM} / (Ba+La)_{PM}$
$Ta/Ta^* = 2^*Ta_{PM} / (Ba+La)_{PM}$
$Ti/Ti^* = Ti_{PM} / ((EU+Y)/2)_{PM}$;
$Eu/Eu^* = 2^*Eu_{PM} / (Sm+Gd)_{PM}$
$Mg\# = 100 \times (Mg^{2+} /(Mg^{2+} + Fe^{2+}))$
$_{PM}$= Primitive mantle normalized value (taken from McDonough and Sun, 1995),
$_{CN}$= Chondrite-normalized (taken from McDonough and Sun, 1995).

Table S2. Compilation of age data of late-Archean rocks from BC.

Terrain	Locality	Sample No.	Rock type	Formation age (Ma)	Method	Reference (s)
Northern Bundelkhand terrain	Karera	BETG 119	Sanukitoid	2563 ± 2	SIMS (zr)	Joshi et al. (2017)
	Raksa	BETG 120	Sanukitoid	2559 ± 7	SIMS (zr)	Joshi et al. (2017)
	Orccha	BCTG 129	Closepate granite	2560 ± 7	SIMS (zr)	Joshi et al. (2017)
	Bedaura	2BK-30	Granodiorite	2551 ± 7	LA-ICP-MS (zr)	Kaur et al. (2016)
	Raksa	BLHM 118	Monzogranite	2557 ± 19	SIMS (zr)	Joshi et al. (2017)
	Garhmau	BLHM 127	Monzogranite	2569 ± 19	SIMS (zr)	Joshi et al. (2017)
	Garhmau	BLHM 128	Monzogranite	2571 ± 16	SIMS (zr)	Joshi et al. (2017)
	Karera	BM-567	Granodiorite	2561 ± 6	Ion microprobe (zr)	Mondal et al. (2002)
	Jhansi	BK-2	Granites	2529 ± 8	LA-ICP-MS (zr)	Kaur et al. (2016)
	Jhansi	BK-3	Granites	2566 ± 14	LA-ICP-MS (zr)	Kaur et al. (2016)
	Dhala	SK-27	Granites	2553 ± 6	SHRIMP (zr)	Pati et al. (2010)
	Dhala	MCB-10	Granites	2563 ± 7	SHRIMP (zr)	Pati et al. (2010)
	Mohar		Granites	3035 - 3170	ID-TIMS (Rb-Sr, WR)	Pandey et al. (2011)
	Mohar		Andesites	2510 ± 280 2622 ± 300	ID-TIMS (Rb-Sr, WR) ID-TIMS (Pb-Pb, WR)	Pandey et al. (2011)
	Datia	MB-549	Biotite granite	2515 ± 5	Ion microprobe (zr)	Mondal et al. (2002)
	Kalothara	BK-1	Granites	2583 ± 10	LA-ICP-MS (zr)	Kaur et al. (2016)
	Patha Bharthari	2BK-25	Leucogranites	2543 ± 10	LA-ICP-MS (zr)	Kaur et al. (2016)
	Vijaipur	2BK-26	Leucogranites	2537 ± 8 2134 ± 19*	LA-ICP-MS (zr)	Kaur et al. (2016)
	Utwaha	2BK-57	Leucogranites	2554 ± 5	LA-ICP-MS (zr)	Kaur et al. (2016)
Central Bundelkhand terrain	Babina	BC-04	TTG gneiss	2669 ± 7	LA-ICP-MS (zr)	Verma et al. (2016)
	Babina	MB-245	Granodiorite	2703 ± 3	Ion microprobe (zr)	Mondal et al. (1998)
	Baghora	MB-110	Granodiorite	2697 ± 3	Ion microprobe (zr)	Mondal et al. (2002)
	Babina	WS2	White schist	2785 ± 49*	LA-ICP-MS (zr)	Saha et al. (2011)
	Babina	WS5	White schist	2733 ± 30	LA-ICP-MS (zr)	Saha et al. (2011)
	Babina	BLEM 124	Monzogranite	2546 ± 3	SIMS (zr)	Joshi et al. (2017)
	Talbehat	BLEM 109	Monzogranite	2544 ± 3	SIMS (zr)	Joshi et al. (2017)
	Bijoli	BMG 130	Granites	2562 ± 6	SIMS (zr)	Joshi et al. (2017)
	Bijoli	BC-01	Pink granites	2531 ± 21	LA-ICP-MS (zr)	Verma et al. (2016)
	Bijoli	BC-02	Pink granites	2516 ± 38	LA-ICP-MS (zr)	Verma et al. (2016)
	Babina	BC-03	Pink granites	2514 ± 13	LA-ICP-MS (zr)	Verma et al. (2016)
	Baghora	2BK-29	Granites	2525 ± 25	LA-ICP-MS (zr)	Kaur et al. (2016)
	Babina	Ba-17/4	Felsic volcanics	2542 ± 17	SHRIMP (zr)	Singh and Slubanov, (2015a)
	Dinara	BK-12	Granodiorite	2561 ± 11	LA-ICP-MS (zr)	Kaur et al. (2016)
	Dinara	BK-13	Granites	2563 ± 10	LA-ICP-MS (zr)	Kaur et al. (2016)
	Sakrar	BC-16-18	Sanukitoids	2577 ± 16	LA-ICP-MS (zr)	**In this study**
	Mauranipur	M-8/2	Metasomatic (Ep-Q-Pl)	2687 ± 17*	SHRIMP (zr)	Slubanov and Singh, (2018)
	Mauranipur	BLEM 103	Monzogranite	2578 ± 22	SIMS (zr)	Joshi et al. (2017)
	Kuraichha	BK-9	Leucogranites	2545 ± 10	LA-ICP-MS (zr)	Kaur et al. (2016)
	Roni	2BK-33	Leucogranites	2548 ± 8	LA-ICP-MS (zr)	Kaur et al. (2016)
	Charkhari	2BK-40	Leucogranites	2549 ± 13	LA-ICP-MS (zr)	Kaur et al. (2016)
	Mahoba	MB-657	Leucogranites	2482 ± 7	Ion microprobe (zr)	Mondal et al. (2002)
	Bilbai	BK-19	Granodiorite	2566 ± 11	LA-ICP-MS (zr)	Kaur et al. (2016)
Southern Bundelkhand terrain	Panchora	2BK-53	Granodiorite	2546 ± 6 2002 ± 42*	LA-ICP-MS (zr)	Kaur et al. (2016)
	Khajuraho	BSTM 104	Sanukitoid	2544 ± 6	SIMS (zr)	Joshi et al. (2017)
	Lalitpur	BK-6	Granites	2564 ± 42	LA-ICP-MS (zr)	Kaur et al. (2016)
	Lalitpur	M-154	Granites	2521 ± 7	Ion microprobe (zr)	Mondal et al. (2002)
	Lalitpur	M-136	Granites	2492 ± 10	Ion microprobe (zr)	Mondal et al. (2002)
	Panchwara	M-151A	Granites	2522 ± 22	Ion microprobe (zr)	Mondal et al. (1998)
	Khajuraho	BMG 105	Monzogranite	2565 ± 8	SIMS (zr)	Joshi et al. (2017)
	Chhayan	2BK-49	Leucogranites	2491 ± 17	LA-ICP-MS (zr)	Kaur et al. (2016)
	Chhatarpur	2BK-44	Leucogranites	2516 ± 35	LA-ICP-MS (zr)	Kaur et al. (2016)
	Panchora	2BK-54	Leucogranites	2539 ± 7	LA-ICP-MS (zr)	Kaur et al. (2016)
	Jakhuara	M-46	Leucogranites	2516 ± 4	Ion microprobe (zr)	Mondal et al. (2002)
	Bansi	MB-518	Rhyolite	2517 ± 7	Ion microprobe (zr)	Mondal et al. (2002)

*Metatmorphic age

References of Figure 17.

(1-5) Althoff et al. (2000); Oliveira et al. (2009); Almeida et al. (2010, 2011, 2013); (6-13) Kröner et al. (1991, 2000); Henderson et al. (2000); Zeh et al. (2009); Laurent et al. (2011, 2013a, b, 2014); (14) Smithies and Champion, (2000); (15-26) Jayananda et al. (1995, 2006, 2013a, b, 2015); Moyen et al. (2003); Vijaya Kumar et al. (2011); Chardon et al. (2011); Dey et al. (2012, 2014, 2016); Maibam et al. (2016); (27-34) Mondal et al. (1998, 2002); Pati et al. (2010); Pandey et al. (2011); Singh and Slabunov, (2015a); Kaur et al. (2016); Verma et al. (2016); Joshi et al. (2017); (35-39) Liu et al. (2004); Yang et al. (2008); Wang et al. (2009); Ma et al. (2013); Jiang et al. (2016); (40-52) Bibikova et al. (2005); Halla, (2005, 2009); Kovalenko et al. (2005); Lobach-Zhuchenko et al. (2005, 2008); Käpyaho et al. (2006); Heilimo et al. (2007, 2010, 2011); Mikkola et al. (2011a, b, 2014); (53-59) Stern et al. (1989); Sutcliffe et al. (1990); Stern and Hanson, (1991); Breaks and Moore, (1992); Feng and Kerrich, (1992); Sage et al. (1996); Whalen et al. (2004).

Almeida, J. D. A. C., Dall'Agnol, R., de Oliveira, M. A., Macambira, M. J. B., Pimentel, M. M., Rämö, O. T., da Silva Leite, A. A., 2011. Zircon geochronology, geochemistry and origin of the TTG suites of the Rio Maria granite-greenstone terrane: Implications for the growth of the Archean crust of the Carajás province, Brazil. Precambr. Res. 187, 201–221.

Almeida, J. D. A. C., Dall'Agnol, R., da Silva Leite, A. A., 2013. Geochemistry and zircon geochronology of the Archean granite suites of the Rio Maria granite-greenstone terrane, Carajás Province, Brazil. J. South Amer. Earth Sci. 42, 103–126

Almeida, J. D. A. C., Dall'Agnol, R., Dias, S. B., Althoff, F. J., 2010. Origin of the Archean leucogranodiorite–granite suites: evidence from the Rio Maria terrane and implications for granite magmatism in the Archean. Lithos 120, 235–257.

Althoff, F., Barbey, P., Boullier, A. M., 2000. 2.8–3.0 Ga plutonism and deformation in the SE Amazonian craton: The Archaean granitoids of Marajoara Carajás Mineral Province, Brazil. Precambr. Res. 104, 187–206.

Bibikova, E. V., Samsonov, A. V., Petrova, A. Y., Kirnozova, T. I., 2005. The Archean geochronology of western Karelia. Stratigr Geol Correl. 13, 459–475.

Breaks, F. W., Moore, J. M., 1992. The Ghost Lake Batholith, Superior Province of northwestern Ontario; a fertile, S-type, peraluminous granite-rare-element pegmatite system. Can. Mineral. 30, 835–875.

Chardon, D., Jayananda, M., Peucat, J.J., 2011. Lateral constrictional flow of hot orogenic crust: Insights from the Neoarchean of south India, geological and geophysical implications for orogenic plateaux. Geochem. Geophys. Geosyst. 12 (http://dx.doi.org/10.1029/2010GC003398).

Dey, S., Halla, J., Kurhila, M., Nandy, J., Heilimo, E., Pal, S., 2016. Geochronology of Neoarchaean granitoids of the NW eastern Dharwar craton: implications for crust formation. Geol. Soc. London Spec. Publ. 449, SP449–9.

Dey, S., Nandy, J., Choudhary, A.K., Liu, Y., Zong, K., 2014. Origin and evolution of granitoids associated with the Kadiri greenstone belt, eastern Dharwar craton: A history of orogenic to anorogenic magmatism. Precambr. Res. 246, 64–90.

Dey, S., Pandey, U. K., Rai, A. K., Chaki, A., 2012. Geochemical and Nd isotope constraints on petrogenesis of granitoids from NW part of the eastern Dharwar craton: possible implications for late Archaean crustal accretion. J. Asian Earth Sci. 45, 40–56.

Feng, R., Kerrich, R., 1992. Geochemical evolution of granitoids from the Archean Abitibi Southern Volcanic Zone and the Pontiac subprovince, Superior Province, Canada: implications for tectonic history and source regions. Chem. Geol. 98, 23–70.

Halla, J., 2005. Late Archean high-Mg granitoids sanukitoids in the southern Karelian domain, eastern Finland: Pb and Nd isotopic constraints on crust−mantle interactions. Lithos 79, 161–178.

Halla, J., van Hunen, J., Heilimo, E., and Hölttä, P., 2009. Geochemical and numerical constraints on Neoarchean plate tectonics. Precambr. Res. 174, 155–162.

Heilimo, E., Halla, J., and Huhma, H., 2011. Single-grain zircon U–Pb age constraints of the western and eastern sanukitoid zones in the Finnish part of the Karelian Province. Lithos 12, 87–99.

Heilimo, E., Halla, J., Hölttä, P., 2010. Discrimination and origin of the sanukitoid series: geochemical constraints from the Neoarchean western Karelian Province Finland. Lithos 115, 27–39.

Heilimo, E., Mikkola, P., Halla, J., 2007. Age and petrology of the Kaapinsalmi sanukitoid intrusion in Suomussalmi, eastern Finland. Bull. Geol. Soc. Finland 79, 117.

Henderson, D. R., Long, L. E., Barton Jr, J. M., 2000. Isotopic ages and chemical and isotopic composition of the Archaean Turfloop Batholith, Pietersburg granite—greenstone terrane, Kaapvaal Craton, South Africa. S. Afr. J. Geol. 103, 38–46.

Jayananda, M., Chardon, D., Peucat, J.J., Capdevila, R., 2006. 2.61 Ga potassic granites and crustal reworking in the western Dharwar craton, southern India: tectonic, geochronologic and geochemical constraints. Precambr. Res. 150, 1-26.

Jayananda, M., Chardon, D., Peucat, J.J., Fanning, C.M., 2015. Paleo-to Mesoarchean TTG accretion and continental growth in the western Dharwar craton, Southern India: Constraints from SHRIMP U–Pb zircon geochronology, whole-rock geochemistry and Nd–Sr isotopes. Precambr. Res. 268, 295–322.

Jayananda, M., Martin, H., Peucat, J. J., Mahabaleswar, B., 1995. Late Archaean crust-mantle interactions: geochemistry of LREE-enriched mantle derived magmas. Example of the Closepet batholith, southern India. Contrib. Mineral. Petrol. 119, 314–329.

Jayananda, M., Peucat, J.J., Chardon, D., Rao, B.K., Fanning, C.M., Corfu, F., 2013a. Neoarchean greenstone volcanism and continental growth, Dharwar craton, southern India: constraints from SIMS U–Pb zircon geochronology and Nd isotopes. Precambr. Res. 227, 55–76.

Jayananda, M., Tsutsumi, Y., Miyazaki, T., Gireesh, R.V., Kapfo, K.U., Hidaka, H., Kano, T., 2013b. Geochronological constraints on Meso-and Neoarchean regional metamorphism and magmatism in the Dharwar craton, southern India. J. Asian Earth Sci. 78, 18–38.

Jiang, N., Guo, J., Fan, W., Hu, J., Zong, K., Zhang, S., 2016. Archean TTGs and sanukitoids from the Jiaobei terrain, North China craton: Insights into crustal growth and mantle metasomatism. Precambr. Res. 281, 656–672.

Joshi, K. B., Bhattacharjee, J., Rai, G., Halla, J., Ahmad, T., Kurhila, M., Choudhary, A. K., 2017. The diversification of granitoids and plate tectonic implications at the Archaean–Proterozoic boundary in the Bundelkhand Craton, Central India. Geol. Soc. London Spec. Publ. 449, 123–157.

Käpyaho, A., Mänttäri, I. and Huhma, H., 2006. Growth of Archaean crust in the Kuhmo district, eastern Finland: U–Pb and Sm–Nd isotope constraints on plutonic rocks. Precambr. Res. 146, 95–119.

Kaur, P., Zeh, A., Chaudhri, N., Eliyas, N., 2016. Unravelling the record of Archaean crustal evolution of the Bundelkhand Craton, northern India using U–Pb zircon–monazite ages, Lu–Hf isotope systematics, and whole-rock geochemistry of granitoids. Precambr. Res. 281, 384–413.

Kovalenko, A., Clemens, J. D., Savatenkov, V., 2005. Petrogenetic constraints for the genesis of Archaean sanukitoid suites: geochemistry and isotopic evidence from Karelia, Baltic Shield. Lithos 79, 147–160.

Kröner, A., Byerly, G. R., Lowe, D. R., 1991. Chronology of early Archaean granite-greenstone evolution in the Barberton Mountain Land, South Africa, based on precise dating by single zircon evaporation. Earth Planet. Sci. Lett. 103, 41–54.

Kröner, A., Jaeckel, P., Brandl, G., 2000. Single zircon ages for felsic to intermediate rocks from the Pietersburg and Giyani greenstone belts and bordering granitoid orthogneisses, northern Kaapvaal Craton, South Africa. J. Afr. Earth Sci. 30, 773–793.

Laurent, O., Doucelance, R., Martin, H., Moyen, J. F., 2013 a. Differentiation of the late-Archaean sanukitoid series and some implications for crustal growth: insights from geochemical modelling on the Bulai pluton, Central Limpopo Belt, South Africa. Precambr. Res. 227, 186–203.

Laurent, O., Martin, H., Doucelance, R., Moyen, J. F., Paquette, J. L., 2011. Geochemistry and petrogenesis of high-K “sanukitoids” from the Bulai pluton, Central Limpopo Belt, South Africa: Implications for geodynamic changes at the Archaean–Proterozoic boundary. Lithos 123, 73–91.

Laurent, O., Martin, H., Moyen, J. F., Doucelance, R., 2014. The diversity and evolution of late-Archean granitoids: Evidence for the onset of “modern-style” plate tectonics between 3.0 and 2.5 Ga. Lithos 205, 208–235.

Laurent, O., Paquette, J. L., Martin, H., Doucelance, R., Moyen, J. F., 2013 b. LA-ICP-MS dating of zircons from Meso- and Neoarchean granitoids of the Pietersburg block South Africa: crustal evolution at the northern margin of the Kaapvaal craton. Precambr. Res. 230, 209–226.

Liu, S., Pan, Y., Xie, Q., Zhang, J., Li, Q., 2004. Archean geodynamics in the Central Zone, North China Craton: constraints from geochemistry of two contrasting series of granitoids in the Fuping and Wutai complexes. Precambr. Res. 130, 229–249.

Lobach-Zhuchenko, S. B., Rollinson, H. R., Chekulaev, V. P., Arestova, N. A., Kovalenko, A. V., Ivanikov, V. V., Jarvis, K. E., 2005. The Archaean sanukitoid series of the Baltic Shield: geological setting, geochemical characteristics and implications for their origin. Lithos 79, 107–128.

Lobach-Zhuchenko, S.B., Rollinson, H., Chekulaev, V.P., Savatenkov, V.M., Kovalenko, A.V., Martin, H., Guseva, N.S., Arestova, N.A., 2008. Petrology of a Late Archaean, highly potassic, sanukitoid pluton from the Baltic Shield: insights into Late Archaean mantle metasomatism. J. Petrol. 49, 393–420.

Ma, X., Guo, J., Liu, F., Qian, Q., Fan, H., 2013. Zircon U–Pb ages, trace elements and Nd–Hf isotopic geochemistry of Guyang sanukitoids and related rocks: Implications for the Archean crustal evolution of the Yinshan Block, North China Craton. Precambr. Res. 230, 61–78.

Maibam, B., Gerdes, A., Goswami, J.N., 2016. U–Pb and Hf isotope records in detrital and magmatic zircon from eastern and western Dharwar craton, southern India: Evidence for coeval Archaean crustal evolution. Precambr. Res. 275, 496–512.

Mikkola, P., Heilimo, E., Huhma, H., 2014. Relationships between sanukitoids and crust-derived melts and their implications for the diversity of Neoarchaean granitoids: a case study from Surmansuo and nearby areas, Eastern Finland. Bull. Geol. Soc. Finland 86.

Mikkola, P., Huhma, H., Heilimo, E., Whitehouse, M., 2011a. Archean crustal evolution of the Suomussalmi district as part of the Kianta Complex, Karelia: constraints from geochemistry and isotopes of granitoids. Lithos 125, 287–307.

Mikkola, P., Salminen, P., Torppa, A., Huhma, H., 2011b. The 2.74 Ga Likamännikkö complex in Suomussalmi, East Finland: Lost between sanukitoids and truly alkaline rocks? Lithos 125, 716–728.

Mondal, M. E. A., Goswami, J. N., Deomurari, M. P., Sharma, K. K., 2002. Ion microprobe 207Pb/206Pb ages of zircons from the Bundelkhand massif, northern India: implications for crustal evolution of the Bundelkhand–Aravalli protocontinent. Precambr. Res. 117, 85–100.

Mondal, M. E. A., Sharma, K. K., Rahman, A., Goswami, J. N., 1998. Ion microprobe 207 Pb/206 Pb zircon ages for gneiss-granitoid rocks from Bundelkhand massif: Evidence for Archaean components. Curr. Sci. 70–75.

Moyen, J. F., Martin, H., Jayananda, M., Auvray, B., 2003. Late Archaean granites: a typology based on the Dharwar Craton India. Precambr. Res. 127, 103–123.

Oliveira, M. A., Dall’Agnol, R., Althoff, F. J., da Silva Leite, A. A., 2009. Mesoarchean sanukitoid rocks of the Rio Maria granite-greenstone terrane, Amazonian Craton, Brazil. J. S. Am. Earth Sci. 27, 146–160.

Pandey, U. K., Bhattacharya, D., Sastry, D. V. L. N., Pandey, B. K., 2011. Geochronology Rb-Sr, Sm-Nd and Pb-Pb, isotope geochemisty and evolution of the granites and andesites hosting Mohar Cauldron, Bundelkhand Granite Complex, Shivpuri district, Central India. Explo. Res. Atom. Min. 21, 103–116.

Pati, J.K., Jourdan, F., Armstrong, R.A., Reimold, W.U., Prakash, K., 2010. First SHRIMP U-Pb and 40Ar/39Ar chronological results from impact melt breccia from the Paleoproterozoic Dhala impact structure, India. Large Meteorite Impacts and Planetary Evolution IV. Geol. Soc. Amer. Spec. Paper 465, 571–591.

Sage, R. P., Lightfoot, P. C., Doherty, W., 1996. Geochemical characteristics of granitoid rocks from within the Archean Michipicoten Greenstone Belt, Wawa Subprovince, Superior Province, Canada: implications for source regions and tectonic evolution. Precambr. Res. 76, 155–190.

Singh, V.K., Slabunov, A., 2015a. The central Bundelkhand Archaean greenstone complex, Bundelkhand craton, central India: geology, composition, and geochronology of supracrustal rocks. Int. Geol. Rev. 57, 1347–1362.
Smithies, R.H., Champion, D.C., 2000. The Archaean high-Mg diorite suite: links to tonalite–trondhjemite–granodiorite magmatism and implications for early Archaean crustal growth. J. Petrol. 41, 1653–1671.
Stern, R. A., Hanson, G. N., 1991. Archean high-Mg granodiorite: a derivative of light rare earth element-enriched monzodiorite of mantle origin. J. Petrol. 32, 201–238.
Stern, R. A., Hanson, G. N., Shirey, S. B., 1989. Petrogenesis of mantle-derived, LILE-enriched Archean monzodiorites and trachyandesites sanukitoids in southwestern Superior Province. Can. J. Earth Sci. 26, 1688–1712.
Sutcliffe, R. H., Smith, A. R., Doherty, W., Barnett, R. L., 1990. Mantle derivation of Archean amphibole-bearing granitoid and associated mafic rocks: evidence from the southern Superior Province, Canada. Contrib. Mineral. Petrol. 105, 255–274.
Verma, S. K., Verma, S. P., Oliveira, E. P., Singh, V. K., Moreno, J. A., 2016. LA-SF-ICP-MS zircon U–Pb geochronology of granitic rocks from the central Bundelkhand greenstone complex, Bundelkhand craton, India. J. Asian Earth Sci. 118, 125–137.
Vijay Kumar, K., Ernst, W.G., Leelanandam, C., Wooden, J.L., Grove, M.J., 2011. Origin of~ 2.5 Ga potassic granite from the Nellore Schist Belt, SE India: textural, cathodoluminescence, and SHRIMP U–Pb data. Contrib. Mineral. Petrol. 162, 867–888.
Wang, Y., Zhang, Y., Zhao, G., Fan, W., Xia, X., Zhang, F., Zhang, A., 2009. Zircon U–Pb geochronological and geochemical constraints on the petrogenesis of the Taishan sanukitoids Shandong: implications for Neoarchean subduction in the Eastern Block, North China Craton. Precambr. Res. 174, 273–286.
Whalen, J. B., Percival, J. A., McNicoll, V. J., Longstaffe, F. J., 2004. Geochemical and isotopic Nd–O evidence bearing on the origin of late-to post-orogenic high-K granitoid rocks in the Western Superior Province: implications for late Archean tectonomagmatic processes. Precambr. Res. 132, 303–326.
Yang, J. H., Wu, F. Y., Wilde, S. A., Zhao, G., 2008. Petrogenesis and geodynamics of Late Archean magmatism in eastern Hebei, eastern North China Craton: geochronological, geochemical and Nd–Hf isotopic evidence. Precambr. Res. 167, 125–149.
Zeh, A., Gerdes, A., Barton Jr, J. M., 2009. Archean accretion and crustal evolution of the Kalahari Craton—the zircon age and Hf isotope record of granitic rocks from Barberton/Swaziland to the Francistown Arc. J. Petrol. 50, 933–966.

APPENDIX III:

CHAPTER 4

SUPPLEMENTARY MATERIAL

This contains 3 Tables (Tables S1, S2 and S3)

Table S1. Results of U-Pb dating of zircons on TTG gneisses and high-K granitoids.

Sample-Spot	Content (mg.g-1)								Isotopic ratios								Isotopic ages (Ma)						% conc
	f206 (%)	U	2s	Th	2s	Pb	2s	Th/U	206Pb/ 204Pb	207Pb/ 206Pb	2s	207Pb/ 235U	2s	206Pb/ 238U	2s	Rho	207Pb/ 206Pb	2s	207Pb/ 235U	2s	206Pb/ 238U	2s	
BC.16-1C	0.05	139	6	113	6	195	11	0.81	40750	0.2847	0.0031	22.070	0.410	0.5590	0.0110	0.84	3397	10	2865	47	3180	18	84
BC.16-1R	0.05	173	3	38	1	60	3	0.22	39400	0.2434	0.0034	15.330	0.270	0.4556	0.0085	0.73	3157	13	2415	37	2829	17	76
BC.16-4C	0.09	108	3	51	2	58	2	0.47	21450	0.2710	0.0040	14.720	0.260	0.3922	0.0076	0.69	3325	12	2137	35	2794	17	64
BC.16-4R	0.05	136	3	123	3	192	6	0.90	40400	0.2717	0.0034	22.390	0.380	0.5880	0.0110	0.75	3327	12	2974	44	3196	16	89
BC.16-6C	0.03	220	13	105	6	188	11	0.48	73500	0.2858	0.0031	26.150	0.350	0.6590	0.0100	0.70	3399	10	3267	39	3352	13	96
BC.16-8C	0.05	118	4	113	3	214	7	0.96	40950	0.2844	0.0030	27.410	0.380	0.6870	0.0110	0.74	3398	10	3375	40	3392	14	99
BC.16-12C	0.04	298	13	615	30	372	23	2.06	46450	0.2371	0.0037	11.110	0.200	0.3305	0.0065	0.66	3112	16	1834	32	2532	16	59
BC.16-13R	0.06	190	4	70	2	115	3	0.37	33550	0.2525	0.0032	13.440	0.220	0.3755	0.0061	0.69	3214	12	2056	28	2710	15	64
BC.16-14R	0.02	662	23	863	31	442	22	1.30	76150	0.1894	0.0017	6.560	0.100	0.2445	0.0038	0.83	2745	10	1408	20	2051	14	51
BC.16-18C	0.02	335	10	433	12	362	13	1.29	84600	0.2345	0.0026	18.950	0.290	0.5610	0.0100	0.78	3097	10	2867	42	3039	15	93
BC.16-19C	0.06	175	4	84	2	105	3	0.48	33950	0.2686	0.0038	16.610	0.280	0.4377	0.0086	0.69	3302	14	2340	38	2912	16	71
BC.16-21C	0.05	181	6	167	4	321	10	0.92	40350	0.2823	0.0033	21.400	0.300	0.5388	0.0086	0.69	3377	11	2778	36	3157	14	82
BC.16-22C	0.04	149	8	123	7	184	9	0.83	44050	0.2828	0.0034	27.990	0.350	0.7021	0.0097	0.63	3399	11	3425	37	3415	12	101
BC.16-22R	0.04	196	5	143	3	221	5	0.73	51150	0.2874	0.0032	25.370	0.360	0.6191	0.0094	0.68	3416	10	3105	37	3323	14	91
BC.16-24R	0.07	323	14	15	1	42	2	0.05	26200	0.2007	0.0038	6.230	0.190	0.2137	0.0042	0.75	2838	27	1245	22	1982	27	44
BC.16-25C	0.09	94	2	69	2	117	4	0.74	21550	0.2868	0.0041	22.810	0.410	0.5620	0.0110	0.72	3418	12	2863	47	3216	17	84
BC.16-27C	0.04	203	7	175	6	212	8	0.86	43750	0.2840	0.0035	22.870	0.350	0.5658	0.0086	0.65	3405	11	2883	35	3215	15	85
BC.16-28C	0.05	163	3	137	4	198	5	0.84	40350	0.2826	0.0028	25.860	0.300	0.6375	0.0085	0.68	3390	10	3180	34	3342	11	94
BC.16-29C	0.03	249	6	227	6	309	9	0.91	59400	0.2718	0.0032	23.820	0.350	0.6100	0.0100	0.75	3324	11	3058	40	3258	14	92
BC.16-30C	0.04	205	7	74	3	108	4	0.36	51950	0.2815	0.0026	26.950	0.270	0.6729	0.0077	0.65	3378	8	3315	30	3381	10	98
BC.16-31C	0.09	95	4	79	3	125	6	0.83	20700	0.2857	0.0037	23.220	0.350	0.5716	0.0091	0.66	3400	12	2912	37	3237	14	86
BC.16-31R	0.06	265	5	150	3	118	3	0.57	30000	0.2321	0.0030	9.760	0.170	0.2934	0.0058	0.75	3080	12	1655	29	2410	16	54
BC.16-33C	0.03	309	11	321	11	341	13	1.04	56250	0.2503	0.0031	17.950	0.290	0.4948	0.0084	0.71	3197	13	2595	35	2981	15	81
BC.16-34C	0.06	128	4	96	4	178	8	0.75	30700	0.2770	0.0031	26.590	0.400	0.6700	0.0110	0.71	3360	10	3303	41	3364	15	98
BC.16-34R	0.06	327	13	186	9	123	9	0.57	32850	0.2280	0.0033	9.250	0.160	0.2864	0.0052	0.67	3045	15	1624	26	2361	16	53
BC.16-37C	0.07	280	8	245	7	178	8	0.88	27150	0.2564	0.0038	10.110	0.180	0.2777	0.0054	0.67	3235	14	1580	27	2443	17	49
BC.16-38C	0.05	207	7	169	4	193	7	0.82	36300	0.2552	0.0038	18.040	0.310	0.4945	0.0093	0.69	3235	14	2582	40	2988	17	80
BC.16-39C	0.07	184	5	147	4	133	5	0.80	25400	0.2585	0.0035	14.670	0.210	0.3935	0.0066	0.63	3261	13	2140	30	2794	14	66
BC.16-44R	0.02	507	21	492	33	1036	51	0.97	92900	0.2552	0.0027	20.080	0.230	0.5519	0.0077	0.68	3214	9	2828	32	3095	11	88
BC.16-45C	0.06	310	5	237	4	190	4	0.77	31550	0.2370	0.0037	10.500	0.190	0.3079	0.0058	0.63	3115	15	1729	28	2476	17	56
BC.16-48C	0.05	225	3	189	3	222	5	0.84	36150	0.2725	0.0035	19.450	0.270	0.4986	0.0084	0.68	3332	12	2601	36	3059	13	78
BC.16-49C	0.09	137	4	115	3	135	4	0.84	20000	0.2735	0.0042	17.610	0.300	0.4479	0.0084	0.66	3342	15	2382	37	2964	17	71
BC.16-50C	0.05	189	10	184	9	293	14	0.98	40200	0.2855	0.0031	27.500	0.350	0.6692	0.0092	0.68	3400	10	3298	36	3401	12	97
BC.16-50R	0.08	149	3	132	3	162	4	0.89	23900	0.2873	0.0042	20.540	0.320	0.5016	0.0094	0.64	3409	12	2620	39	3113	15	77
BC.16-51C	0.11	110	3	54	1	79	3	0.49	17720	0.2717	0.0046	19.790	0.340	0.5080	0.0110	0.65	3336	15	2644	45	3077	17	79
BC.16-56C	0.06	149	5	163	6	231	9	1.09	30300	0.2817	0.0030	27.710	0.330	0.6842	0.0089	0.66	3397	9	3358	34	3406	12	99
BC.16-56R	0.06	173	8	87	4	119	6	0.51	31100	0.2720	0.0031	23.890	0.320	0.6150	0.0086	0.64	3321	10	3091	35	3262	13	93
BC.16-57C	0.04	269	14	226	12	328	17	0.84	51350	0.2764	0.0028	25.400	0.320	0.6405	0.0091	0.73	3347	9	3195	36	3322	12	95

Table S1 continue.

Sample-Spot		Content (mg.g-1)							Isotopic ratios								Isotopic ages (Ma)					% conc
	f206 (%)	U	2s	Th	2s	Pb	2s	Th/U	206Pb/ 204Pb	207Pb/ 206Pb	2s	207Pb/ 235U	2s	206Pb/ 238U	2s	Rho	207Pb/ 206Pb	2s	207Pb/ 235U	2s	206Pb/ 238U	2s	
BC.19-1C	0.12	308	11	511	20	235	10	1.66	15320	0.2226	0.0035	11.040	0.230	0.3182	0.0068	0.69	3009	16	1773	33	2524	19	59
BC.19-2C	0.05	417	24	76	4	91	8	0.18	35450	0.2425	0.0030	20.670	0.320	0.5316	0.0086	0.65	3149	11	2747	36	3116	15	87
BC.19-2R	0.04	568	19	80	3	133	5	0.14	42000	0.2352	0.0028	17.680	0.380	0.4805	0.0090	0.80	3097	12	2519	39	2969	21	81
BC.19-3C	0.03	1396	43	560	16	404	16	0.40	74450	0.1928	0.0025	9.750	0.180	0.3314	0.0057	0.70	2767	13	1844	28	2404	17	67
BC.19-4C	0.05	610	18	88	2	137	6	0.14	38700	0.1980	0.0027	12.430	0.240	0.4073	0.0074	0.71	2824	13	2201	34	2638	18	78
BC.19-4R	0.03	1021	31	30	1	129	6	0.03	55750	0.1779	0.0023	9.330	0.180	0.3399	0.0060	0.71	2643	11	1887	29	2372	18	71
BC.19-5C	0.06	642	20	155	6	157	8	0.24	30100	0.1423	0.0023	6.310	0.120	0.2880	0.0053	0.61	2279	16	1635	27	2015	16	72
BC.19-7C	0.07	397	12	79	3	266	12	0.20	25250	0.2377	0.0041	14.010	0.340	0.3971	0.0099	0.75	3123	15	2149	46	2745	23	69
BC.19-8C	0.05	312	10	51	2	145	7	0.16	37850	0.2455	0.0036	26.740	0.560	0.7360	0.0160	0.76	3159	14	3551	61	3372	21	112
BC.19-11C	0.04	457	20	96	4	142	8	0.21	47700	0.2537	0.0030	25.950	0.400	0.6780	0.0110	0.65	3217	11	3331	41	3342	15	104
BC.19-12C	0.03	767	21	70	3	271	12	0.09	61750	0.2088	0.0032	16.600	0.420	0.5090	0.0110	0.80	2901	15	2640	49	2906	24	91
BC.19-13C	0.06	400	28	133	9	193	18	0.33	30850	0.2246	0.0033	17.900	0.380	0.5110	0.0110	0.79	3021	15	2652	48	2983	20	88
BC.19-14C	0.08	544	17	80	3	61	3	0.15	24300	0.2258	0.0037	9.460	0.230	0.2812	0.0070	0.79	3048	17	1588	35	2388	23	52
BC.19-15C	0.47	54	2	32	1	31	3	0.59	4000	0.1725	0.0067	11.810	0.610	0.4590	0.0210	0.72	2617	36	2411	92	2549	49	92

Table S1 continue.

Sample-Spot	Content (mg.g-1)								Isotopic ratios								Isotopic ages (Ma)					% conc
	f206 (%)	U	2s	Th	2s	Pb	2s	Th/U	206Pb/ 204Pb	207Pb/ 206Pb	2s	207Pb/ 235U	2s	206Pb/ 238U	2s	Rho	207Pb/ 206Pb	2s	207Pb/ 235U	2s	206Pb/ 238U	2s	
BC.41-1C	0.06	278	9	336	15	279	12	1.21	32850	0.2287	0.0041	12.740	0.350	0.3940	0.0120	0.77	3077	18	2117	53	2648	26	69
BC.41-2C	0.06	246	5	358	10	321	10	1.46	30200	0.2292	0.0043	13.460	0.300	0.4170	0.0100	0.66	3073	19	2245	46	2702	21	73
BC.41-3C	0.16	92	3	70	2	132	5	0.76	11670	0.2823	0.0059	17.410	0.380	0.4400	0.0110	0.64	3396	20	2340	48	2953	21	69
BC.41-3R	0.14	375	13	13	1	46	3	0.03	13100	0.1392	0.0037	2.220	0.062	0.1129	0.0035	0.60	2236	28	688	20	1186	19	31
BC.41-4C	0.11	108	4	74	2	135	7	0.69	16700	0.2789	0.0055	20.200	0.490	0.5200	0.0140	0.70	3381	17	2683	59	3092	24	79
BC.41-4R	0.12	110	3	80	2	139	5	0.72	14970	0.2831	0.0057	18.550	0.400	0.4680	0.0110	0.60	3393	18	2464	48	3013	21	73
BC.41-6R	0.11	86	3	19	1	39	2	0.22	16400	0.2858	0.0059	26.800	0.610	0.6610	0.0160	0.61	3423	18	3267	60	3372	22	95
BC.41-7C	0.20	139	4	172	5	118	5	1.24	9275	0.2597	0.0059	8.290	0.200	0.2282	0.0060	0.58	3269	21	1322	31	2252	21	40
BC.41-12C	0.11	241	6	181	5	201	8	0.75	16700	0.2221	0.0045	7.250	0.180	0.2360	0.0064	0.61	3008	19	1363	33	2139	22	45
BC.41-13C	0.15	121	3	104	3	126	4	0.86	12835	0.2770	0.0054	14.130	0.300	0.3609	0.0086	0.70	3371	18	1978	41	2748	20	59
BC.41-14C	0.13	151	4	82	4	62	4	0.54	14350	0.2222	0.0047	10.160	0.220	0.3262	0.0079	0.62	3021	22	1819	38	2446	20	60
BC.41-15C	0.11	303	9	243	7	167	8	0.80	17800	0.2423	0.0046	6.640	0.210	0.1928	0.0062	0.61	3156	18	1126	33	2037	28	36
BC.41-16C	0.13	92	3	47	2	123	7	0.51	14600	0.2839	0.0059	21.220	0.550	0.5360	0.0160	0.84	3407	18	2742	68	3140	25	80
BC.41-17C	0.16	110	3	32	2	83	3	0.29	11435	0.2656	0.0056	13.460	0.340	0.3558	0.0095	0.72	3306	20	1947	45	2712	24	59
BC.41-20C	0.12	295	10	41	2	60	4	0.14	15000	0.1771	0.0038	4.410	0.110	0.1768	0.0046	0.69	2654	20	1043	25	1688	20	39
BC.41-22C	0.14	229	8	40	2	87	4	0.17	12960	0.2319	0.0055	6.440	0.160	0.1935	0.0050	0.78	3076	24	1138	27	2029	22	37
BC.41-22R	0.17	181	8	17	1	46	3	0.09	10730	0.2227	0.0057	6.580	0.180	0.2060	0.0056	0.54	3027	27	1204	30	2036	24	40
BC.41-23C	0.12	134	4	103	3	163	7	0.77	16230	0.2688	0.0050	16.690	0.370	0.4340	0.0110	0.57	3328	18	2308	47	2913	21	69
BC.41-24C	0.09	142	3	36	1	57	3	0.25	20900	0.2355	0.0048	17.210	0.430	0.5150	0.0120	0.68	3109	23	2665	51	2941	24	86
BC.41-24R	0.13	121	3	57	2	79	4	0.47	14900	0.2744	0.0054	17.110	0.440	0.4370	0.0130	0.69	3341	19	2331	57	2930	25	70
BC.41-25C	0.09	136	4	56	1	154	6	0.41	21300	0.2776	0.0047	21.130	0.470	0.5390	0.0130	0.77	3375	16	2771	55	3132	22	82
BC.41-26C	0.19	115	4	139	6	87	4	1.21	9745	0.2706	0.0069	11.980	0.330	0.3062	0.0086	0.74	3348	24	1721	42	2601	26	51
BC.41-27C	0.15	77	3	22	1	48	3	0.28	12650	0.2765	0.0057	23.560	0.540	0.5970	0.0150	0.59	3377	19	2998	59	3241	22	89
BC.41-27R	0.11	190	5	208	6	183	6	1.09	17550	0.2498	0.0049	11.940	0.270	0.3310	0.0079	0.66	3203	18	1838	39	2589	21	57
BC.41-33C	0.06	171	10	76	3	184	6	0.44	32500	0.2880	0.0049	29.350	0.550	0.7130	0.0160	0.67	3425	16	3463	58	3462	19	101
BC.41-37C	0.08	146	4	217	4	349	10	1.49	24000	0.2813	0.0044	24.810	0.450	0.6170	0.0140	0.62	3378	14	3082	55	3298	18	91
BC.41-39C	0.07	198	5	160	4	226	7	0.81	27600	0.2707	0.0047	20.310	0.440	0.5240	0.0130	0.65	3330	16	2708	54	3103	20	81
BC.41-40C	0.09	196	6	207	8	231	11	1.06	20750	0.2414	0.0046	14.050	0.330	0.4060	0.0110	0.72	3159	18	2190	49	2753	23	69
BC.41-41C	0.12	103	3	84	2	141	6	0.81	15450	0.2695	0.0048	21.760	0.570	0.5630	0.0150	0.73	3317	17	2871	62	3165	26	87
BC.41-42C	0.10	105	4	27	1	50	2	0.26	18000	0.2803	0.0046	26.820	0.460	0.6770	0.0130	0.72	3385	14	3316	51	3369	17	98
BC.41-44C	0.14	153	6	29	1	64	3	0.19	13150	0.2455	0.0050	11.500	0.280	0.3273	0.0084	0.77	3180	19	1816	40	2555	23	57
BC.41-45C	0.14	89	5	19	1	48	3	0.21	13600	0.2708	0.0047	24.220	0.510	0.6310	0.0140	0.64	3323	16	3148	56	3276	20	95
BC.41-46C	0.11	110	6	39	2	65	4	0.36	17500	0.2718	0.0050	23.890	0.500	0.6230	0.0160	0.66	3343	16	3096	62	3259	21	93
BC.41-47C	0.14	131	5	89	4	83	4	0.67	13500	0.2579	0.0057	14.740	0.390	0.4010	0.0120	0.68	3256	20	2170	52	2793	25	67
BC.41-47R	0.11	204	9	160	5	156	7	0.79	17100	0.2521	0.0048	12.580	0.260	0.3515	0.0078	0.70	3214	17	1937	37	2646	19	60
BC.41-48C	0.15	97	6	64	3	91	7	0.66	12150	0.2619	0.0053	19.110	0.440	0.5080	0.0130	0.67	3290	19	2632	53	3039	22	80
BC.41-49C	0.10	114	9	55	3	100	7	0.48	18700	0.2790	0.0050	27.250	0.550	0.6760	0.0160	0.62	3382	17	3326	61	3383	20	98
BC.41-50C	0.17	234	5	301	8	123	6	1.29	10900	0.2140	0.0056	5.780	0.160	0.1893	0.0055	0.66	2953	25	1112	30	1918	23	38
BC.41-51C	0.06	317	5	350	12	341	9	1.10	32750	0.1980	0.0036	12.050	0.330	0.4240	0.0110	0.64	2826	19	2264	51	2597	26	80
BC.41-52C	0.18	123	3	17	1	229	10	0.14	10570	0.2709	0.0059	13.940	0.350	0.3614	0.0099	0.73	3323	20	1978	47	2740	23	60

Table S1 continue.

Sample-Spot	Content (mg.g-1)								Isotopic ratios								Isotopic ages (Ma)					% conc
	f206 (%)	U	2s	Th	2s	Pb	2s	Th/U	206Pb/ 204Pb	207Pb/ 206Pb	2s	207Pb/ 235U	2s	206Pb/ 238U	2s	Rho	207Pb/ 206Pb	2s	207Pb/ 235U	2s	206Pb/ 238U	2s	
BC.45-1C	0.06	203	7	174	5	290	11	0.86	30050	0.2777	0.0043	23.850	0.430	0.6040	0.0130	0.71	3367	13	3043	51	3257	18	90
BC.45-1R	0.14	150	5	107	3	117	4	0.71	13500	0.2641	0.0044	13.390	0.250	0.3624	0.0075	0.62	3289	17	1988	36	2706	17	60
BC.45-2C	0.15	71	3	65	3	108	5	0.91	12550	0.2801	0.0044	28.140	0.480	0.7120	0.0140	0.68	3378	14	3458	54	3426	16	102
BC.45-2R	0.08	143	7	158	8	259	14	1.10	22250	0.2763	0.0038	24.440	0.390	0.6170	0.0110	0.69	3363	12	3098	44	3276	16	92
BC.45-3C	0.10	222	6	263	8	236	9	1.19	18800	0.2529	0.0054	12.110	0.270	0.3353	0.0084	0.66	3223	20	1856	40	2607	20	58
BC.45-3M	0.11	188	6	213	6	239	9	1.13	16900	0.2734	0.0043	13.940	0.250	0.3632	0.0072	0.65	3336	14	1988	34	2739	17	60
BC.45-3R	0.12	207	7	169	6	123	6	0.82	15055	0.2506	0.0048	10.320	0.190	0.2919	0.0062	0.59	3207	17	1653	31	2461	18	52
BC.45-5C	0.10	106	2	80	2	127	5	0.76	18310	0.2724	0.0041	26.630	0.450	0.6980	0.0140	0.70	3323	13	3414	54	3371	17	103
BC.45-5R	0.10	155	4	96	3	150	5	0.62	19100	0.2732	0.0043	19.410	0.330	0.4971	0.0095	0.62	3341	15	2598	41	3056	16	78
BC.45-6C	0.15	135	4	119	3	146	4	0.88	12820	0.2744	0.0054	14.640	0.360	0.3710	0.0096	0.69	3354	19	2027	45	2776	23	60
BC.45-6R	0.09	178	5	138	5	114	7	0.77	20100	0.2760	0.0047	17.390	0.390	0.4390	0.0110	0.74	3360	17	2340	48	2957	21	70
BC.45-8C	0.08	139	4	153	5	208	7	1.11	22700	0.2768	0.0038	26.340	0.430	0.6800	0.0120	0.64	3356	13	3349	45	3359	16	100
BC.45-8R	0.12	171	4	138	3	168	7	0.81	15480	0.2579	0.0047	12.860	0.260	0.3532	0.0077	0.67	3232	15	1947	36	2666	19	60
BC.45-10R	0.11	200	6	133	5	124	5	0.67	16650	0.2526	0.0043	12.360	0.200	0.3437	0.0066	0.56	3232	17	1899	31	2625	15	59
BC.45-11C	0.08	149	6	109	4	146	6	0.73	24350	0.2779	0.0035	26.440	0.360	0.6770	0.0100	0.63	3363	11	3324	39	3360	13	99
BC.45-11R	0.13	149	5	124	5	103	5	0.83	14510	0.2635	0.0049	15.130	0.310	0.4006	0.0088	0.65	3285	17	2162	41	2821	20	66
BC.45-12C	0.11	157	3	62	2	81	3	0.39	16665	0.2160	0.0041	13.410	0.350	0.4360	0.0100	0.70	2960	22	2327	45	2697	25	79
BC.45-12R	0.10	131	4	76	2	106	4	0.58	18800	0.2681	0.0038	22.530	0.430	0.6020	0.0130	0.78	3300	12	3016	51	3207	18	91
BC.45-13C	0.09	138	9	81	4	119	7	0.59	19950	0.2743	0.0040	23.830	0.410	0.6150	0.0120	0.67	3345	13	3082	47	3254	16	92
BC.45-13R	0.10	231	6	89	2	110	4	0.39	19050	0.2586	0.0042	12.750	0.230	0.3483	0.0069	0.64	3260	15	1923	33	2655	17	59
BC.45-14C	0.10	171	4	125	3	167	6	0.73	19085	0.2733	0.0042	18.950	0.320	0.4892	0.0097	0.67	3335	14	2563	42	3039	16	77
BC.45-16C	0.04	325	11	352	10	465	12	1.08	50200	0.2784	0.0027	26.510	0.250	0.6706	0.0076	0.60	3361	9	3303	29	3365	9	98
BC.45-17C	0.06	207	10	197	7	311	13	0.95	32500	0.2759	0.0036	25.030	0.430	0.6360	0.0120	0.74	3355	12	3164	47	3305	17	94
BC.45-18C	0.10	245	11	275	10	234	11	1.12	19500	0.2532	0.0045	12.940	0.300	0.3609	0.0089	0.72	3226	17	1984	42	2681	21	62
BC.45-18R	0.11	109	6	66	3	101	5	0.61	16550	0.2757	0.0043	25.130	0.490	0.6480	0.0130	0.71	3351	15	3206	51	3305	19	96
BC.45-19C	0.08	145	6	140	5	202	7	0.96	23850	0.3067	0.0037	31.800	0.450	0.7320	0.0120	0.69	3516	11	3530	43	3537	14	100
BC.45-19R	0.09	161	9	24	3	35	4	0.15	21750	0.2684	0.0039	22.220	0.340	0.5890	0.0100	0.63	3318	13	2981	42	3191	15	90
BC.45-20C	0.09	151	10	130	10	174	13	0.86	21850	0.2763	0.0042	24.480	0.380	0.6280	0.0120	0.63	3364	14	3134	48	3285	15	93
BC.45-20R	0.14	143	4	121	4	129	5	0.85	12965	0.2628	0.0053	14.560	0.310	0.3906	0.0091	0.59	3282	20	2117	42	2786	20	65
BC.45-22C	0.10	169	4	90	3	135	5	0.53	19650	0.2612	0.0037	19.420	0.340	0.5250	0.0100	0.69	3261	13	2720	42	3057	17	83
BC.45-22R	0.12	196	4	145	3	152	5	0.74	15790	0.2505	0.0042	13.050	0.260	0.3655	0.0075	0.66	3203	16	2006	35	2679	19	63
BC.45-23C	0.06	222	8	198	7	281	10	0.89	32700	0.2760	0.0029	27.170	0.330	0.6928	0.0092	0.65	3354	10	3388	35	3385	12	101
BC.45-23R	0.07	221	15	105	7	151	11	0.48	28450	0.2736	0.0037	22.230	0.390	0.5750	0.0110	0.72	3339	13	2920	47	3195	17	87
BC.45-25R	0.11	187	8	152	6	158	8	0.81	16700	0.2557	0.0041	14.840	0.260	0.4106	0.0075	0.62	3236	16	2214	34	2797	16	68
BC.45-26C	0.04	289	9	365	9	544	14	1.26	42550	0.2716	0.0029	26.440	0.320	0.6903	0.0099	0.67	3322	10	3377	37	3361	12	102
BC.45-27C	0.07	210	9	265	11	372	19	1.26	28500	0.2742	0.0034	25.110	0.340	0.6480	0.0100	0.64	3345	11	3219	39	3312	13	96
BC.45-27R	0.08	167	5	155	4	288	8	0.93	23250	0.2880	0.0038	26.970	0.390	0.6590	0.0110	0.64	3414	12	3260	44	3381	15	95
BC.45-28C	0.05	269	24	122	12	188	17	0.45	36900	0.2738	0.0037	24.530	0.350	0.6310	0.0100	0.63	3341	13	3147	39	3287	14	94
BC.45-29C	0.10	234	9	356	15	320	16	1.52	18550	0.2706	0.0044	14.930	0.300	0.3879	0.0079	0.67	3322	15	2106	36	2802	19	63
BC.45-29R	0.15	236	6	502	15	261	10	2.13	12105	0.2407	0.0047	8.090	0.190	0.2347	0.0061	0.68	3146	19	1359	32	2231	21	43
BC.45-30C	0.09	179	4	159	4	257	7	0.89	20650	0.2786	0.0047	21.900	0.380	0.5530	0.0120	0.63	3377	16	2844	48	3175	17	84
BC.45-33C	0.09	150	6	163	5	280	11	1.09	20750	0.2726	0.0037	26.250	0.410	0.6720	0.0120	0.68	3333	12	3318	46	3353	15	100
BC.45-34C	0.13	129	3	63	2	100	4	0.49	14885	0.2598	0.0046	20.720	0.420	0.5520	0.0120	0.64	3269	17	2816	51	3125	20	86

Table S1 continue.

BC.45-35C	0.17	108	4	82	3	115	5	0.76	11300	0.2655	0.0049	18.690	0.420	0.4940	0.0110	0.67	3293	17	2581	48	3031	22	78
BC.45-40R	0.05	263	18	144	9	198	12	0.55	35300	0.2766	0.0034	26.070	0.340	0.6647	0.0092	0.55	3348	11	3289	36	3345	13	98
BC.45-41C	0.06	211	10	92	5	244	14	0.43	31900	0.2799	0.0034	27.530	0.370	0.6878	0.0098	0.61	3378	10	3375	37	3399	13	100
BC.45-41R	0.14	155	4	86	2	131	5	0.55	13500	0.2600	0.0042	15.340	0.310	0.4065	0.0084	0.65	3269	16	2195	38	2827	19	67
BC.45-42C	0.08	148	5	114	4	201	8	0.77	22450	0.2673	0.0031	27.330	0.360	0.7020	0.0110	0.66	3303	10	3431	40	3393	13	104
BC.45-42R	0.11	177	5	149	4	165	7	0.84	16550	0.2660	0.0043	16.340	0.350	0.4273	0.0097	0.74	3294	15	2291	44	2893	21	70
BC.45-43C	0.07	193	6	183	4	266	7	0.95	27450	0.2668	0.0038	24.970	0.360	0.6540	0.0110	0.58	3300	13	3236	41	3306	14	98
BC.45-43R	0.07	269	6	75	3	124	6	0.28	25350	0.2244	0.0039	13.760	0.280	0.4269	0.0091	0.66	3028	17	2282	41	2733	19	75
BC.45-51C	0.15	82	3	59	3	111	6	0.72	12700	0.2720	0.0053	26.750	0.630	0.6850	0.0170	0.65	3338	19	3345	65	3373	23	100
BC.45-51R	0.06	229	12	140	6	204	10	0.61	28800	0.2724	0.0036	21.390	0.340	0.5510	0.0110	0.74	3331	11	2821	44	3154	16	85
BC.45-52C	0.12	252	8	150	4	136	6	0.60	15550	0.2397	0.0042	9.520	0.240	0.2718	0.0071	0.74	3148	18	1547	36	2379	23	49
BC.45-52R	0.17	143	3	99	3	109	4	0.69	11150	0.2495	0.0050	12.300	0.290	0.3425	0.0090	0.67	3204	18	1891	43	2629	22	59
BC.45-53R	0.11	280	4	159	4	149	5	0.57	16360	0.2347	0.0039	8.650	0.150	0.2514	0.0048	0.59	3107	15	1443	25	2294	16	46

Table S1 continue.

Sample-Spot	Content (mg.g-1)								Isotopic ratios							Isotopic ages (Ma)						% conc
	f206 (%)	U	2s	Th	2s	Pb	2s	Th/U	206Pb/ 204Pb	207Pb/ 206Pb	2s	207Pb/ 235U	2s	206Pb/ 238U	2s	Rho	207Pb/ 206Pb	2s	207Pb/ 235U	2s	206Pb/ 238U	2s	
BC.60-5C	0.06	153	3	99	2	108	3	0.64	30250	0.2160	0.0036	12.940	0.220	0.3931	0.0078	0.59	2961	15	2131	36	2677	16	72
BC.60-6C	0.03	202	4	103	2	180	4	0.51	64950	0.2507	0.0024	24.020	0.340	0.6567	0.0086	0.65	3197	9	3256	33	3272	14	102
BC.60-7C	0.02	268	15	175	10	283	17	0.65	82050	0.2506	0.0027	22.700	0.270	0.6189	0.0088	0.60	3202	10	3105	35	3216	12	97
BC.60-8C	0.05	184	9	61	4	72	5	0.33	41400	0.2098	0.0031	14.160	0.250	0.4664	0.0083	0.63	2922	14	2465	36	2763	17	84
BC.60-9C	0.06	200	7	26	1	49	2	0.13	33650	0.2275	0.0034	12.170	0.230	0.3554	0.0068	0.59	3052	16	1961	32	2615	18	64
BC.60-10C	0.09	145	4	52	1	54	2	0.36	21350	0.2035	0.0034	9.540	0.160	0.3080	0.0059	0.58	2875	16	1734	29	2386	15	60
BC.60-11C	0.04	156	4	108	2	185	5	0.69	44550	0.2551	0.0035	23.240	0.330	0.5960	0.0100	0.60	3231	13	3003	41	3235	14	93
BC.60-12C	0.02	290	17	194	12	312	20	0.67	86000	0.2504	0.0030	22.080	0.300	0.6014	0.0097	0.64	3196	11	3038	39	3184	13	95
BC.60-13C	0.08	98	3	41	1	63	2	0.42	23650	0.2144	0.0036	16.480	0.320	0.5050	0.0110	0.65	2952	16	2624	47	2897	18	89
BC.60-15C	0.07	122	3	64	2	111	3	0.53	28000	0.2058	0.0030	15.170	0.250	0.4854	0.0090	0.61	2891	13	2551	39	2825	15	88
BC.60-18C	0.11	67	3	36	2	60	3	0.53	17050	0.2162	0.0033	15.320	0.280	0.5166	0.0099	0.61	2964	14	2675	42	2835	17	90
BC.60-24C	0.09	258	7	266	8	111	5	1.03	20850	0.1751	0.0032	4.132	0.068	0.1684	0.0033	0.49	2616	18	1003	18	1662	13	38
BC.60-26C	0.05	655	28	246	10	105	6	0.38	39700	0.0672	0.0010	1.189	0.019	0.1250	0.0022	0.49	853	19	760	12	795	9	89
BC.60-27C	0.02	272	13	2	0	6	1	0.01	81200	0.2667	0.0031	24.790	0.370	0.6461	0.0094	0.61	3293	10	3215	36	3300	15	98
BC.60-28C	0.04	213	6	126	3	186	7	0.59	52900	0.2517	0.0035	19.620	0.310	0.5350	0.0100	0.68	3203	13	2752	43	3071	15	86
BC.60-31C	0.05	121	3	51	2	91	4	0.42	36850	0.2374	0.0036	21.950	0.510	0.6400	0.0120	0.66	3116	16	3179	48	3165	23	102
BC.60-32C	0.03	191	8	3	0	5	0	0.01	55200	0.2646	0.0027	23.540	0.300	0.6274	0.0083	0.60	3279	10	3140	32	3245	12	96
BC.60-34C	0.02	278	13	150	7	256	12	0.54	75300	0.2458	0.0026	20.320	0.270	0.5866	0.0084	0.60	3163	10	2973	34	3101	13	94
BC.60-35C	0.10	64	3	58	3	110	7	0.91	17850	0.2537	0.0038	21.320	0.370	0.6030	0.0110	0.61	3217	14	3029	45	3154	16	94
BC.60-40C	0.05	160	6	86	3	138	5	0.54	40250	0.2126	0.0024	16.970	0.280	0.5663	0.0084	0.68	2945	11	2884	35	2931	16	98
BC.60-42C	0.10	99	3	43	1	68	3	0.44	19400	0.2218	0.0040	13.610	0.270	0.4308	0.0094	0.60	3012	16	2302	41	2720	18	76
BC.60-44C	0.13	61	3	62	3	124	7	1.02	14250	0.2354	0.0049	16.850	0.390	0.5260	0.0140	0.60	3117	20	2714	59	2920	22	87

Table S1 continue.

Sample-Spot		Content (mg.g-1)							Isotopic ratios								Isotopic ages (Ma)						% conc
	f206 (%)	U	2s	Th	2s	Pb	2s	Th/U	206Pb/ 204Pb	207Pb/ 206Pb	2s	207Pb/ 235U	2s	206Pb/ 238U	2s	Rho	207Pb/ 206Pb	2s	207Pb/ 235U	2s	206Pb/ 238U	2s	
BC.61-1C	0.07	98	3	111	3	208	6	1.13	28600	0.2724	0.0033	26.720	0.440	0.6850	0.0110	0.66	3321	11	3358	42	3374	16	101
BC.61-2C	0.08	81	4	110	6	199	11	1.36	22450	0.2730	0.0039	25.750	0.440	0.6530	0.0110	0.63	3335	13	3234	44	3327	16	97
BC.61-3C	0.06	120	7	113	6	228	15	0.94	33200	0.2682	0.0037	24.360	0.370	0.6320	0.0110	0.63	3315	13	3146	45	3280	14	95
BC.61-3R	0.04	140	4	30	2	129	6	0.22	45550	0.2694	0.0042	29.470	0.540	0.7780	0.0160	0.67	3324	15	3707	60	3466	18	112
BC.61-4C	0.06	108	7	147	9	281	18	1.36	29450	0.2762	0.0040	26.080	0.430	0.6670	0.0120	0.62	3351	13	3283	49	3347	16	98
BC.61-4R	0.04	183	7	87	7	148	15	0.47	46450	0.2660	0.0034	23.310	0.350	0.6120	0.0110	0.65	3295	11	3072	45	3239	15	93
BC.61-6C	0.06	109	6	147	8	287	14	1.35	29700	0.2767	0.0040	26.700	0.450	0.6910	0.0120	0.63	3356	12	3380	47	3368	16	101
BC.61-6R	0.05	196	5	3	0	11	1	0.01	41450	0.2632	0.0043	21.100	0.370	0.5490	0.0120	0.65	3273	15	2811	48	3141	17	86
BC.61-8C	0.12	67	3	63	3	104	5	0.93	15350	0.2737	0.0051	23.840	0.470	0.6410	0.0140	0.62	3342	17	3185	55	3257	19	95
BC.61-9C	0.04	206	10	179	8	310	14	0.87	49925	0.2701	0.0044	25.870	0.490	0.7000	0.0150	0.67	3318	15	3414	58	3345	18	103
BC.61-10C	0.05	162	7	243	10	390	15	1.51	38150	0.2677	0.0036	27.240	0.450	0.7030	0.0120	0.64	3305	11	3428	45	3387	16	104
BC.61-11C	0.08	107	4	126	5	173	7	1.17	22500	0.2698	0.0039	25.760	0.450	0.6510	0.0120	0.65	3324	12	3219	45	3335	17	97
BC.61-12C	0.05	170	7	219	9	339	13	1.29	35000	0.2735	0.0034	26.550	0.420	0.6610	0.0110	0.64	3333	11	3262	43	3360	15	98
BC.61-13R	0.04	208	10	175	7	245	11	0.84	42050	0.2603	0.0045	24.420	0.460	0.6500	0.0140	0.61	3276	15	3224	55	3279	19	98
BC.61-14C	0.03	331	21	646	52	992	89	1.95	73600	0.2728	0.0033	28.260	0.440	0.6980	0.0110	0.66	3335	11	3410	43	3424	15	102
BC.61-14R	0.02	467	22	4	0	8	1	0.01	102150	0.2652	0.0029	27.610	0.420	0.7060	0.0110	0.70	3299	10	3439	41	3406	15	104
BC.61-15C	0.06	163	6	1	0	6	1	0.00	32500	0.2675	0.0038	25.130	0.380	0.6320	0.0120	0.65	3306	13	3162	49	3310	15	96
BC.61-15R	0.04	238	12	1	0	4	1	0.01	51800	0.2689	0.0033	26.760	0.370	0.6820	0.0110	0.60	3311	11	3343	43	3375	13	101
BC.61-16C	0.10	89	4	100	4	177	7	1.12	19350	0.2661	0.0044	26.680	0.490	0.6860	0.0140	0.61	3304	15	3359	53	3362	18	102
BC.61-16R	0.03	315	18	18	1	72	6	0.06	66200	0.2745	0.0041	26.230	0.420	0.6800	0.0130	0.66	3346	14	3334	51	3351	15	100
BC.61-17C	0.04	251	14	231	10	395	23	0.92	50950	0.2722	0.0050	23.900	0.460	0.6540	0.0150	0.62	3319	17	3238	60	3263	19	98
BC.61-17R	0.05	231	6	3	0	11	1	0.01	39900	0.2620	0.0039	21.100	0.320	0.5580	0.0110	0.59	3269	14	2863	45	3146	14	88
BC.61-18C	0.08	115	4	121	4	193	6	1.05	22750	0.2735	0.0041	25.210	0.410	0.6490	0.0120	0.61	3345	13	3220	46	3313	16	96
BC.61-18R	0.04	236	11	43	2	96	5	0.18	49800	0.2690	0.0034	25.990	0.380	0.6830	0.0110	0.60	3315	12	3349	41	3340	14	101
BC.61-20C	0.09	95	4	118	4	194	7	1.23	19850	0.2730	0.0039	26.330	0.470	0.6810	0.0130	0.65	3336	12	3334	49	3347	17	100
BC.61-20R	0.03	296	16	7	0	36	2	0.02	58700	0.2592	0.0031	22.810	0.340	0.6190	0.0100	0.65	3255	10	3099	41	3218	15	95
BC.61-22C	0.06	150	7	200	9	332	16	1.34	31500	0.2730	0.0037	25.420	0.400	0.6580	0.0120	0.64	3342	12	3257	47	3319	15	97
BC.61-22R	0.02	364	19	6	0	22	1	0.02	76450	0.2586	0.0031	23.930	0.340	0.6480	0.0100	0.65	3245	10	3215	41	3263	14	99
BC.61-26C	0.03	263	15	30	1	66	3	0.11	54950	0.2675	0.0037	24.100	0.350	0.6270	0.0110	0.64	3310	13	3129	46	3270	14	95
BC.61-29C	0.03	242	6	118	10	210	21	0.49	54400	0.2697	0.0034	26.790	0.380	0.7030	0.0110	0.62	3311	11	3427	42	3373	14	104
BC.61-30C	0.15	54	3	51	3	171	7	0.94	12400	0.2743	0.0048	27.790	0.590	0.7110	0.0160	0.63	3356	17	3465	59	3403	21	103
BC.61-31C	0.08	110	6	152	7	269	15	1.38	24050	0.2759	0.0042	24.810	0.430	0.6390	0.0130	0.60	3350	13	3179	50	3295	17	95
BC.61-32C	0.14	63	2	76	2	126	4	1.21	13385	0.2764	0.0047	26.400	0.520	0.6720	0.0140	0.63	3369	17	3299	53	3352	19	98
BC.61-32R	0.08	120	3	79	3	154	5	0.66	22350	0.2656	0.0037	21.450	0.340	0.5674	0.0097	0.63	3291	12	2887	40	3159	15	88
BC.61-33C	0.04	233	5	5	0	21	2	0.02	44200	0.2631	0.0045	21.930	0.490	0.5820	0.0140	0.70	3276	16	2956	58	3181	22	90
BC.61-34C	0.07	144	6	91	4	186	9	0.64	28500	0.2736	0.0053	22.290	0.490	0.6100	0.0150	0.64	3344	16	3056	61	3190	21	91
BC.61-34R	0.04	253	8	23	1	37	2	0.09	47800	0.2690	0.0038	22.230	0.350	0.5680	0.0110	0.67	3309	13	2892	45	3192	15	87
BC.61-35C	0.03	284	11	5	0	30	2	0.02	65700	0.2657	0.0037	25.250	0.420	0.6530	0.0120	0.66	3295	13	3232	46	3313	16	98

Table S1 continue.

BC.61-36C	0.06	184	7	215	7	345	19	1.17	30400	0.2704	0.0042	18.600	0.350	0.4790	0.0110	0.74	3325	14	2509	48	3011	18	75
BC.61-36R	0.05	241	7	2	0	67	3	0.01	38700	0.2542	0.0038	17.410	0.280	0.4726	0.0094	0.66	3230	14	2489	41	2958	16	77
BC.61-37C	0.09	96	5	122	5	247	15	1.26	21250	0.2671	0.0047	24.590	0.460	0.6420	0.0140	0.63	3311	15	3187	55	3289	18	96
BC.61-38C	0.04	205	6	265	8	488	16	1.30	45850	0.2707	0.0037	25.870	0.430	0.6560	0.0110	0.63	3328	13	3251	44	3340	16	98
BC.61-39C	0.04	190	6	272	9	489	17	1.43	43600	0.2659	0.0040	25.710	0.450	0.6760	0.0120	0.62	3306	12	3326	47	3332	17	101
BC.61-40C	0.06	139	6	190	9	375	18	1.37	33300	0.2694	0.0039	26.630	0.430	0.6850	0.0120	0.57	3321	13	3354	47	3371	16	101
BC.61-40R	0.08	120	4	14	1	58	3	0.12	22150	0.2607	0.0047	20.200	0.430	0.5320	0.0130	0.68	3275	16	2728	56	3101	21	83
BC.61-41C	0.08	101	5	135	6	278	14	1.34	24450	0.2712	0.0044	26.860	0.460	0.6920	0.0130	0.59	3326	14	3381	51	3370	17	102
BC.61-43C	0.07	103	5	134	6	282	12	1.31	25400	0.2683	0.0045	27.000	0.540	0.7120	0.0150	0.63	3311	16	3460	59	3377	20	105
BC.61-44R	0.07	169	3	23	1	62	3	0.14	25250	0.2458	0.0043	14.700	0.310	0.4310	0.0100	0.72	3178	16	2301	47	2794	20	72
BC.61-46C	0.11	103	4	80	3	162	9	0.77	17750	0.2674	0.0047	18.130	0.340	0.4850	0.0110	0.63	3309	16	2536	47	2995	18	77
BC.61-46R	0.04	238	6	5	0	10	1	0.02	44050	0.2548	0.0047	19.860	0.420	0.5370	0.0140	0.66	3237	17	2780	55	3088	20	86
BC.61-48C	0.05	188	5	158	4	260	9	0.84	34600	0.2605	0.0049	19.990	0.500	0.5220	0.0140	0.71	3281	16	2692	61	3090	24	82
BC.61-48R	0.05	164	4	1	0	3	0	0.01	36650	0.2616	0.0046	23.970	0.460	0.6320	0.0140	0.65	3276	16	3162	56	3266	19	97
BC.61-50C	0.14	56	2	66	3	123	6	1.17	13350	0.2723	0.0050	25.240	0.530	0.6570	0.0150	0.60	3350	17	3248	58	3314	20	97
BC.61-51C	0.09	87	4	107	5	223	10	1.23	20250	0.2803	0.0048	25.400	0.500	0.6580	0.0150	0.65	3389	15	3231	58	3316	19	95
BC.61-52C	0.06	142	6	187	10	359	17	1.32	33850	0.2766	0.0042	25.950	0.440	0.6850	0.0140	0.65	3348	13	3352	52	3343	16	100
BC.61-53C	0.04	210	8	71	5	192	11	0.34	52650	0.2761	0.0038	26.450	0.440	0.7030	0.0130	0.61	3360	12	3437	50	3360	17	102
BC.61-54C	0.07	132	3	46	2	129	4	0.35	28750	0.2795	0.0058	24.140	0.530	0.6190	0.0170	0.65	3373	19	3104	69	3273	21	92
BC.61-54R	0.05	181	5	36	1	54	3	0.20	38900	0.2759	0.0047	22.320	0.410	0.5980	0.0140	0.67	3358	16	3025	56	3198	18	90
BC.61-55C	0.19	43	2	42	2	88	4	0.99	10010	0.2753	0.0064	23.970	0.570	0.6480	0.0170	0.63	3363	22	3199	64	3268	23	95
BC.61-56C	0.09	76	4	81	5	158	9	1.07	19700	0.2796	0.0045	25.490	0.470	0.6890	0.0140	0.63	3374	14	3377	55	3320	18	100
BC.61-57C	0.17	41	2	47	2	123	6	1.14	10865	0.2796	0.0063	25.510	0.590	0.7020	0.0180	0.61	3384	22	3403	67	3325	22	101
BC.61-58R	0.08	142	5	6	0	24	2	0.04	22050	0.2426	0.0051	16.430	0.390	0.3940	0.0110	0.69	3156	18	2141	50	2898	22	68
BC.61-61C	0.06	132	4	51	2	55	3	0.39	33750	0.2362	0.0038	32.660	0.570	0.6290	0.0140	0.65	3104	14	3135	53	3565	17	101
BC.61-71R	0.16	38	2	91	4	126	5	2.42	11455	0.1997	0.0038	28.890	0.670	0.7120	0.0170	0.64	2848	18	3450	64	3436	23	121
BC.61-72R	0.18	55	2	13	1	28	2	0.24	10390	0.1743	0.0045	8.760	0.240	0.4520	0.0140	0.62	2619	25	2395	60	2298	25	91
BC.61-77C	0.07	90	5	242	12	349	22	2.69	26550	0.2273	0.0039	20.690	0.410	0.7080	0.0150	0.64	3047	15	3440	58	3117	19	113

Table S1 continue.

Sample-Spot	Content (mg.g-1)								Isotopic ratios								Isotopic ages (Ma)						% conc
	f206 (%)	U	2s	Th	2s	Pb	2s	Th/U	206Pb/ 204Pb	207Pb/ 206Pb	2s	207Pb/ 235U	2s	206Pb/ 238U	2s	Rho	207Pb/ 206Pb	2s	207Pb/ 235U	2s	206Pb/ 238U	2s	
BC.27-1C	0.14	114	5	6	0	7	1	0.05	13150	0.1747	0.0037	11.940	0.250	0.4680	0.0110	0.55	2628	24	2478	48	2598	19	94
BC.27-2C	0.13	132	5	44	3	56	4	0.33	14550	0.1709	0.0038	11.310	0.220	0.4651	0.0094	0.38	2583	21	2466	41	2548	18	95
BC.27-3C	0.04	337	7	48	2	99	7	0.14	41700	0.1743	0.0024	13.380	0.200	0.5266	0.0079	0.60	2614	13	2725	33	2705	15	104
BC.27-4C	0.09	249	9	41	1	78	4	0.16	19900	0.1729	0.0035	8.300	0.180	0.3356	0.0073	0.47	2604	19	1862	35	2265	19	72
BC.27-6C	0.08	184	5	125	4	122	5	0.68	23150	0.1812	0.0027	14.210	0.230	0.5462	0.0091	0.60	2673	14	2804	38	2760	15	105
BC.27-7C	0.09	181	6	103	2	118	3	0.57	20900	0.1756	0.0023	12.860	0.190	0.5063	0.0074	0.61	2625	12	2645	31	2666	13	101
BC.27-7R	0.24	97	6	24	1	30	2	0.25	7725	0.1620	0.0039	8.250	0.200	0.3554	0.0078	0.51	2504	24	1950	37	2248	22	78
BC.27-9C	0.18	175	6	73	2	67	3	0.42	10315	0.1605	0.0040	5.970	0.150	0.2570	0.0066	0.52	2481	25	1471	34	1967	22	59
BC.27-10C	0.10	147	6	5	0	10	1	0.04	18100	0.1718	0.0032	13.980	0.280	0.5660	0.0110	0.55	2592	19	2891	47	2743	19	112
BC.27-11C	0.04	546	17	146	5	224	9	0.27	42000	0.1555	0.0025	7.770	0.150	0.3388	0.0073	0.68	2424	16	1886	35	2203	18	78
BC.27-12C	0.05	425	16	633	43	318	14	1.49	36200	0.1589	0.0023	8.820	0.140	0.3838	0.0064	0.60	2450	14	2090	30	2317	14	85
BC.27-13C	0.07	295	8	199	5	169	6	0.68	27850	0.1712	0.0028	10.550	0.200	0.4190	0.0080	0.64	2589	15	2262	37	2479	18	87
BC.27-16C	0.03	472	13	328	17	475	23	0.69	54700	0.1712	0.0025	13.050	0.270	0.5260	0.0120	0.79	2576	14	2723	51	2683	19	106
BC.27-17C	0.06	313	10	70	5	162	15	0.22	32150	0.1773	0.0033	12.050	0.290	0.4720	0.0110	0.71	2637	19	2487	50	2609	23	94
BC.27-18C	0.32	53	4	24	2	28	2	0.44	5800	0.1768	0.0059	12.610	0.390	0.5040	0.0150	0.51	2674	28	2613	64	2643	29	98
BC.27-19C	0.08	406	9	469	14	361	11	1.16	24500	0.1656	0.0029	6.700	0.120	0.2808	0.0054	0.56	2527	17	1593	27	2072	16	63
BC.27-20C	0.38	83	6	51	4	25	2	0.61	4950	0.1649	0.0080	5.940	0.210	0.2715	0.0089	0.43	2478	37	1551	45	1972	31	63
BC.27-21C	0.13	146	7	120	4	117	5	0.82	14200	0.1712	0.0029	12.030	0.200	0.4745	0.0083	0.57	2589	16	2497	36	2600	15	96
BC.27-22C	0.10	159	4	7	0	10	1	0.04	18410	0.1727	0.0028	14.270	0.250	0.5717	0.0098	0.56	2590	15	2918	40	2765	16	113
BC.27-23C	0.10	338	14	121	5	139	9	0.36	19200	0.1699	0.0034	6.380	0.140	0.2574	0.0063	0.64	2575	21	1472	33	2028	19	57
BC.27-24C	0.11	326	12	107	4	83	5	0.33	16750	0.1459	0.0027	5.210	0.110	0.2457	0.0056	0.74	2324	19	1412	29	1844	18	61
BC.27-25C	0.09	276	5	345	12	249	8	1.25	20565	0.1634	0.0029	8.410	0.160	0.3502	0.0076	0.64	2512	17	1932	36	2273	17	77
BC.27-26C	0.80	53	2	18	2	15	2	0.34	2325	0.1808	0.0098	5.390	0.270	0.2170	0.0110	0.46	2687	51	1254	56	1871	41	47
BC.27-29C	0.12	151	9	77	4	93	6	0.51	15050	0.1577	0.0026	11.190	0.200	0.4839	0.0091	0.61	2451	16	2544	39	2531	17	104
BC.27-30C	0.11	269	10	67	2	77	3	0.25	17800	0.1655	0.0029	7.680	0.160	0.3186	0.0075	0.69	2539	18	1775	36	2187	19	70
BC.27-34C	0.19	97	4	44	2	56	4	0.46	9755	0.1757	0.0045	12.910	0.300	0.5040	0.0110	0.41	2631	24	2633	46	2670	22	100
BC.27-38C	0.06	387	10	115	3	156	6	0.30	30700	0.1561	0.0025	9.030	0.160	0.3952	0.0074	0.62	2437	15	2147	34	2343	15	88
BC.27-39C	0.08	310	8	118	4	96	4	0.38	23100	0.1653	0.0026	8.800	0.170	0.3599	0.0072	0.68	2524	16	1981	34	2315	18	78
BC.27-42C	0.04	433	14	275	7	474	18	0.64	41900	0.1636	0.0032	11.270	0.250	0.4660	0.0110	0.67	2509	16	2475	50	2538	20	99
BC.27-43C	0.19	77	3	47	3	80	4	0.61	9600	0.1637	0.0042	14.580	0.400	0.6020	0.0170	0.60	2515	24	3020	67	2777	27	120
BC.27-58C	0.09	195	9	102	3	156	5	0.52	20050	0.1619	0.0026	12.380	0.220	0.5184	0.0097	0.61	2483	16	2686	41	2634	16	108
BC.27-59C	0.51	63	2	15	1	28	2	0.23	3640	0.1720	0.0064	7.170	0.290	0.2910	0.0100	0.57	2572	40	1630	49	2110	35	63
BC.27-61C	0.08	252	6	163	4	185	6	0.65	22900	0.1742	0.0038	11.570	0.230	0.4520	0.0110	0.56	2614	19	2396	47	2567	19	92
BC.27-62C	0.09	228	6	31	2	67	4	0.13	21900	0.1648	0.0028	11.390	0.230	0.4750	0.0100	0.67	2520	18	2501	46	2552	19	99

Table S1 continue.

Sample-Spot	Content (mg.g-1)								Isotopic ratios								Isotopic ages (Ma)					% conc
	f206 (%)	U	2s	Th	2s	Pb	2s	Th/U	206Pb/ 204Pb	207Pb/ 206Pb	2s	207Pb/ 235U	2s	206Pb/ 238U	2s	Rho	207Pb/ 206Pb	2s	207Pb/ 235U	2s	206Pb/ 238U	2s	
BC.31-9C	0.10	74	4	53	3	73	4	0.71	19000	0.1827	0.0032	12.070	0.230	0.4890	0.0098	0.58	2687	15	2563	42	2606	18	95
BC.31-11C	0.06	121	6	82	5	114	7	0.68	33500	0.1828	0.0032	13.560	0.280	0.5300	0.0120	0.68	2703	16	2732	48	2711	19	101
BC.31-12C	0.06	109	4	80	2	109	4	0.73	30400	0.1824	0.0030	13.710	0.250	0.5308	0.0096	0.60	2694	15	2730	40	2725	18	101
BC.31-13C	0.08	93	4	47	2	70	3	0.51	24400	0.1836	0.0029	12.920	0.250	0.4915	0.0094	0.63	2722	15	2573	41	2670	19	95
BC.31-14C	0.07	108	7	65	5	91	8	0.60	28500	0.1829	0.0034	12.060	0.260	0.4680	0.0110	0.66	2702	16	2462	49	2602	21	91
BC.31-15C	0.03	231	9	153	4	248	8	0.66	66400	0.1841	0.0027	13.730	0.250	0.5300	0.0110	0.67	2706	14	2732	45	2727	17	101
BC.31-16C	0.05	150	7	122	5	165	7	0.81	40400	0.1838	0.0027	13.440	0.220	0.5131	0.0088	0.58	2701	13	2669	37	2706	15	99
BC.31-17C	0.07	90	3	36	1	63	2	0.40	26000	0.1844	0.0031	14.120	0.280	0.5390	0.0120	0.65	2717	16	2772	51	2754	19	102
BC.31-18C	0.08	91	4	62	3	79	4	0.68	23550	0.1842	0.0030	13.020	0.270	0.4990	0.0100	0.64	2719	14	2599	44	2674	19	96
BC.31-20C	0.11	70	5	28	2	40	3	0.39	17100	0.1810	0.0037	11.480	0.260	0.4500	0.0100	0.56	2688	20	2385	44	2557	21	89
BC.31-21C	0.07	107	4	60	2	85	4	0.56	28150	0.1873	0.0031	13.000	0.230	0.4870	0.0100	0.59	2737	15	2548	44	2683	17	93
BC.31-22C	0.08	88	5	75	4	107	7	0.85	22550	0.1888	0.0035	12.630	0.250	0.4690	0.0110	0.60	2745	18	2474	47	2641	19	90
BC.31-23C	0.09	75	4	42	1	62	2	0.56	20200	0.1797	0.0032	13.800	0.260	0.5350	0.0110	0.57	2670	17	2759	47	2734	17	103
BC.31-24C	0.07	104	4	79	4	112	4	0.76	28350	0.1871	0.0029	14.090	0.270	0.5292	0.0099	0.54	2716	16	2731	41	2749	18	101
BC.31-26C	0.05	182	16	51	4	78	6	0.28	40500	0.1830	0.0037	9.880	0.220	0.3973	0.0092	0.59	2705	20	2155	42	2424	20	80
BC.31-27C	0.05	141	6	118	4	165	6	0.84	36400	0.1853	0.0027	13.310	0.230	0.5044	0.0093	0.58	2723	14	2624	39	2692	17	96
BC.31-28C	0.07	112	3	52	1	77	3	0.47	26550	0.1855	0.0032	12.150	0.230	0.4550	0.0100	0.65	2710	16	2405	45	2618	17	89
BC.31-29C	0.08	91	2	65	1	87	2	0.72	23750	0.1818	0.0028	13.060	0.230	0.5092	0.0091	0.55	2689	16	2657	39	2680	16	99
BC.31-30C	0.28	26	1	9	0	14	1	0.36	6750	0.1846	0.0045	13.110	0.310	0.5060	0.0120	0.50	2724	23	2635	52	2675	22	97
BC.31-31C	0.12	61	4	33	2	48	3	0.55	15350	0.1889	0.0036	13.470	0.280	0.5060	0.0110	0.56	2762	19	2629	45	2711	20	95
BC.31-32C	0.15	57	2	17	1	26	1	0.30	12890	0.1870	0.0042	12.230	0.270	0.4404	0.0099	0.52	2744	22	2351	45	2617	21	86
BC.31-34C	0.10	76	3	46	1	67	2	0.60	18800	0.1829	0.0033	13.050	0.260	0.4849	0.0097	0.61	2695	17	2541	42	2675	19	94
BC.31-35C	0.12	64	3	25	1	43	2	0.39	16200	0.1790	0.0031	13.390	0.320	0.5040	0.0110	0.69	2663	16	2618	47	2695	22	98
BC.31-36C	0.05	122	5	95	4	164	7	0.78	38500	0.2129	0.0032	19.090	0.310	0.6070	0.0110	0.61	2945	14	3047	43	3039	15	103
BC.31-37C	0.08	91	4	56	3	80	4	0.61	22300	0.1884	0.0032	13.650	0.260	0.4906	0.0090	0.55	2743	17	2568	39	2717	18	94
BC.31-38C	0.06	131	7	79	4	110	6	0.60	31850	0.1799	0.0033	12.310	0.280	0.4740	0.0110	0.65	2666	18	2507	48	2634	22	94
BC.31-39C	0.09	86	2	74	3	101	3	0.86	21950	0.1841	0.0030	13.750	0.250	0.5065	0.0094	0.55	2700	17	2630	40	2729	17	97
BC.31-40C	0.05	146	6	88	3	191	10	0.60	34600	0.1918	0.0033	12.900	0.240	0.4693	0.0098	0.63	2783	17	2477	43	2671	18	89
BC.31-41C	0.08	105	6	75	5	91	6	0.72	23800	0.1785	0.0029	10.930	0.200	0.4249	0.0077	0.55	2651	16	2278	35	2514	17	86
BC.31-42C	0.08	96	3	74	2	101	3	0.77	24350	0.1784	0.0029	13.030	0.230	0.5106	0.0092	0.57	2661	16	2643	39	2678	17	99
BC.31-43C	0.21	35	2	15	1	20	1	0.44	8835	0.1839	0.0043	13.450	0.320	0.5170	0.0130	0.54	2722	22	2674	52	2689	22	98
BC.31-44C	0.11	71	3	41	2	59	2	0.58	17750	0.1851	0.0032	13.280	0.260	0.5070	0.0100	0.57	2715	18	2630	43	2694	18	97
BC.31-45C	0.10	74	3	55	3	76	4	0.75	18000	0.1848	0.0036	12.760	0.260	0.4890	0.0110	0.50	2704	18	2551	47	2651	19	94
BC.31-46C	0.09	95	5	61	3	93	6	0.64	21650	0.1843	0.0033	12.440	0.250	0.4760	0.0110	0.70	2720	17	2504	46	2637	18	92

Table S1 continue.

Sample-Spot		Content (mg.g-1)							Isotopic ratios								Isotopic ages (Ma)						% conc
	f206 (%)	U	2s	Th	2s	Pb	2s	Th/U	206Pb/ 204Pb	207Pb/ 206Pb	2s	207Pb/ 235U	2s	206Pb/ 238U	2s	Rho	207Pb/ 206Pb	2s	207Pb/ 235U	2s	206Pb/ 238U	2s	
BC.50-2C	0.03	686	14	70	2	99	4	0.10	67850	0.1751	0.0026	11.200	0.250	0.4500	0.0092	0.73	2610	14	2401	41	2535	21	92
BC.50-6C	0.04	553	19	133	3	116	4	0.24	44600	0.2402	0.0033	13.480	0.210	0.3868	0.0067	0.66	3130	12	2105	31	2716	15	67
BC.50-6R	0.05	395	10	18	1	42	2	0.05	39250	0.2371	0.0032	16.730	0.280	0.4945	0.0091	0.65	3110	12	2591	39	2915	16	83
BC.50-7C	0.09	314	12	175	6	208	7	0.56	20150	0.1714	0.0028	7.740	0.150	0.3180	0.0070	0.65	2574	16	1779	34	2195	17	69
BC.50-8C	0.07	292	9	150	5	201	8	0.51	27200	0.2637	0.0044	17.630	0.330	0.4633	0.0096	0.64	3280	15	2453	41	2969	18	75
BC.50-12C	0.08	255	7	190	4	207	7	0.75	22200	0.1691	0.0026	10.400	0.200	0.4296	0.0082	0.62	2560	15	2299	37	2470	18	90
BC.50-13C	0.09	257	7	139	5	205	10	0.54	21600	0.2830	0.0052	16.850	0.350	0.4232	0.0096	0.62	3393	17	2268	43	2922	20	67
BC.50-15C	0.05	373	8	305	6	321	7	0.82	37650	0.1716	0.0019	13.170	0.160	0.5150	0.0066	0.55	2581	11	2678	28	2688	11	104
BC.50-16R	0.04	422	16	337	13	458	15	0.80	42350	0.1752	0.0026	13.490	0.190	0.5217	0.0089	0.58	2619	15	2701	37	2712	13	103
BC.50-19C	0.22	78	3	47	2	154	8	0.60	8460	0.2261	0.0062	17.990	0.510	0.5520	0.0140	0.57	3056	29	2822	60	2969	27	92
BC.50-21C	0.07	440	11	233	4	283	9	0.53	28700	0.1784	0.0025	9.220	0.140	0.3479	0.0059	0.58	2653	14	1922	28	2360	14	72
BC.50-23R	0.10	409	8	81	4	155	8	0.20	18545	0.1803	0.0040	6.170	0.150	0.2385	0.0060	0.60	2678	21	1381	31	1991	21	52
BC.50-25R	0.07	345	7	113	3	199	7	0.33	26550	0.1843	0.0034	11.680	0.230	0.4205	0.0085	0.56	2712	19	2263	38	2578	19	83
BC.50-26C	0.11	184	5	87	3	156	10	0.47	16450	0.1885	0.0045	12.870	0.300	0.4740	0.0120	0.52	2740	24	2489	53	2661	22	91
BC.50-27C	0.07	299	8	190	5	225	9	0.64	26850	0.1790	0.0027	13.000	0.270	0.4936	0.0097	0.69	2656	14	2579	42	2668	19	97
BC.50-33C	0.10	253	7	104	3	110	4	0.41	18750	0.1635	0.0029	10.430	0.220	0.4336	0.0095	0.62	2512	20	2323	43	2473	19	92
BC.50-38C	0.09	836	19	61	2	176	13	0.07	21950	0.1404	0.0029	3.087	0.079	0.1517	0.0032	0.59	2232	23	910	18	1426	20	41
BC.50-38R	0.11	824	18	75	2	44	3	0.09	16950	0.1125	0.0020	1.891	0.050	0.1195	0.0025	0.68	1855	20	728	15	1072	18	39
BC.50-39R	0.05	1346	27	90	2	60	3	0.07	36450	0.1064	0.0017	2.500	0.046	0.1611	0.0029	0.61	1760	16	962	16	1268	14	55
BC.50-44C	0.07	321	14	171	8	234	10	0.53	26150	0.1705	0.0023	13.090	0.180	0.5089	0.0068	0.50	2570	14	2649	29	2684	13	103
BC.50-45C	0.10	250	7	148	5	275	13	0.59	19600	0.1861	0.0033	12.750	0.280	0.4720	0.0100	0.64	2738	19	2492	43	2659	20	91
BC.50-46C	0.08	912	26	57	2	142	7	0.06	23800	0.1305	0.0027	3.172	0.077	0.1599	0.0035	0.58	2116	23	954	20	1443	19	45
BC.50-47C	0.05	446	16	178	6	258	12	0.40	34650	0.1642	0.0023	12.080	0.260	0.4714	0.0087	0.69	2516	13	2481	38	2605	20	99
BC.50-53C	0.08	883	21	68	2	64	3	0.08	22350	0.1334	0.0024	3.232	0.071	0.1572	0.0031	0.64	2164	18	941	17	1459	17	43
BC.50-53R	0.06	565	9	55	2	102	5	0.10	32900	0.1621	0.0029	8.800	0.280	0.3569	0.0098	0.80	2493	19	1962	46	2294	30	79

Table S1 continue.

Sample-Spot	Content (mg.g-1)								Isotopic ratios								Isotopic ages (Ma)						% conc
	f206 (%)	U	2s	Th	2s	Pb	2s	Th/U	206Pb/ 204Pb	207Pb/ 206Pb	2s	207Pb/ 235U	2s	206Pb/ 238U	2s	Rho	207Pb/ 206Pb	2s	207Pb /235U	2s	206Pb /238U	2s	
BC.23-1C	0.10	336	13	394	13	330	19	1.17	19000	0.1482	0.0031	7.770	0.360	0.3461	0.0093	0.58	2350	59	1909	45	2213	42	81
BC.23-2C	0.08	299	15	433	17	476	26	1.45	22950	0.1520	0.0030	10.850	0.420	0.4720	0.0120	0.66	2328	59	2472	51	2494	38	106
BC.23-3C	27.25	384	14	324	8	1481	56	0.84	69	0.3270	0.0100	12.900	1.000	0.4830	0.0180	0.48	2480	110	2529	78	2779	64	102
BC.23-4C	6.75	293	12	351	12	423	27	1.20	277	0.1764	0.0038	8.190	0.440	0.3460	0.0100	0.54	2448	62	1907	48	2261	46	78
BC.23-5C	21.24	673	31	127	5	371	21	0.19	88	0.2289	0.0055	1.530	0.240	0.0988	0.0032	0.21	2597	97	608	19	1139	68	23
BC.23-5R	6.71	497	24	292	12	394	24	0.59	279	0.1660	0.0032	4.960	0.270	0.2453	0.0065	0.49	2235	67	1413	33	1796	46	63
BC.23-6C	0.11	390	13	241	7	256	13	0.62	17150	0.1565	0.0029	5.880	0.310	0.2756	0.0074	0.51	2331	59	1561	37	1934	47	67
BC.23-7C	9.02	847	43	1043	42	514	35	1.23	207	0.1603	0.0037	2.250	0.210	0.1249	0.0045	0.39	2233	81	754	26	1236	58	34
BC.23-8C	17.34	248	6	167	5	607	28	0.67	108	0.2501	0.0065	9.810	0.710	0.4210	0.0140	0.46	2506	77	2246	66	2441	61	90
BC.23-10C	15.20	401	31	402	22	1148	46	1.00	123	0.2695	0.0076	11.440	0.660	0.4560	0.0120	0.46	2477	74	2400	54	2579	49	97
BC.23-11C	11.16	526	23	686	21	567	29	1.30	168	0.1877	0.0040	3.980	0.270	0.1978	0.0053	0.39	2384	78	1155	28	1649	52	48
BC.23-12C	20.59	416	10	153	5	461	24	0.37	91	0.2309	0.0063	2.810	0.400	0.1940	0.0064	0.23	2380	110	1146	34	1562	76	48
BC.23-13C	17.41	412	14	466	9	786	52	1.13	107	0.2311	0.0069	6.380	0.520	0.2980	0.0110	0.45	2428	73	1652	56	2141	61	68
BC.23-14C	0.07	499	20	1104	34	677	32	2.21	25300	0.1546	0.0028	7.080	0.250	0.3187	0.0074	0.66	2361	50	1773	36	2103	34	75
BC.23-15C	0.06	438	25	681	30	696	43	1.55	31850	0.1546	0.0028	10.000	0.370	0.4360	0.0110	0.68	2366	51	2323	50	2459	33	98
BC.23-16C	11.47	371	18	541	22	503	32	1.46	163	0.2019	0.0041	4.570	0.360	0.2103	0.0065	0.39	2504	82	1234	34	1815	55	49
BC.23-17C	36.23	340	13	480	16	895	52	1.41	52	0.3570	0.0100	5.260	0.660	0.2262	0.0082	0.29	2850	110	1308	43	2066	75	46
BC.23-17R	28.88	255	8	201	5	675	44	0.79	65	0.3044	0.0096	6.880	0.710	0.3130	0.0110	0.34	2690	100	1747	52	2168	80	65
BC.23-18C	0.11	259	13	313	11	344	17	1.21	17250	0.1496	0.0028	10.140	0.410	0.4400	0.0110	0.62	2463	52	2352	47	2431	38	95
BC.23-19C	61.73	231	7	392	10	1821	85	1.70	30	0.5070	0.0120	11.600	1.200	0.3620	0.0140	0.37	3143	99	1992	67	2745	78	63
BC.23-22C	12.52	507	23	758	29	397	21	1.50	149	0.1891	0.0048	2.420	0.250	0.1391	0.0039	0.27	2443	88	839	22	1361	58	34
BC.23-23C	15.09	622	16	384	7	526	30	0.62	124	0.2035	0.0052	3.100	0.250	0.1687	0.0047	0.35	2333	79	1002	26	1513	52	43
BC.23-26C	13.51	489	22	345	12	299	21	0.71	138	0.1834	0.0059	2.110	0.280	0.1341	0.0049	0.28	2500	90	813	28	1382	64	33
BC.23-27C	0.05	452	23	306	13	540	31	0.68	34050	0.1551	0.0041	11.010	0.390	0.4680	0.0130	0.78	2341	55	2461	57	2509	32	105
BC.23-27R	0.06	384	20	223	9	344	21	0.58	28900	0.1511	0.0026	10.920	0.370	0.4690	0.0110	0.69	2349	49	2463	48	2492	34	105
BC.23-29C	0.09	314	14	185	7	345	20	0.59	21300	0.1693	0.0034	9.560	0.450	0.4050	0.0120	0.63	2457	57	2173	53	2366	46	88
BC.23-31C	52.94	316	8	223	5	1378	80	0.71	35	0.4490	0.0130	6.180	0.950	0.2490	0.0110	0.29	2920	140	1443	57	2170	100	49
BC.23-32C	0.18	159	5	167	4	334	11	1.05	10180	0.1888	0.0048	9.110	0.760	0.3920	0.0120	0.37	2737	81	2121	58	2439	63	77
BC.23-33C	9.65	252	7	224	5	614	29	0.89	194	0.1980	0.0052	9.990	0.600	0.4640	0.0130	0.47	2356	79	2452	56	2415	56	104
BC.23-38C	23.96	397	18	393	12	960	56	0.99	78	0.2654	0.0061	6.010	0.480	0.2766	0.0075	0.34	2491	83	1565	38	2079	58	63
BC.23-39C	15.94	543	19	384	16	591	21	0.71	117	0.2289	0.0050	4.040	0.350	0.1845	0.0068	0.43	2446	80	1087	36	1665	66	44
BC.23-40C	3.80	505	19	472	14	540	20	0.93	492	0.1793	0.0059	11.270	0.470	0.4400	0.0130	0.71	2346	69	2359	56	2507	44	101
BC.23-41C	14.26	287	8	619	14	622	39	2.16	131	0.2250	0.0064	8.320	0.500	0.3568	0.0097	0.45	2423	81	1963	46	2317	48	81
BC.23-42C	0.05	531	32	1373	66	567	32	2.59	38750	0.1515	0.0024	11.100	0.320	0.4523	0.0096	0.74	2373	41	2398	42	2533	26	101
BC.23-42R	69.62	305	10	1206	38	1408	73	3.95	27	0.5300	0.0120	3.260	0.960	0.1729	0.0086	0.17	3340	130	1022	47	2050	110	31
BC.23-44C	20.60	338	8	870	23	430	22	2.58	91	0.2549	0.0086	3.390	0.480	0.1581	0.0057	0.25	2822	89	945	32	1746	73	33
BC.23-45C	19.71	330	12	482	17	698	46	1.46	95	0.2476	0.0060	7.120	0.670	0.3170	0.0110	0.37	2476	89	1764	53	2270	64	71

Table S1 continue.

Sample-Spot	Content (mg.g-1)								Isotopic ratios							Isotopic ages (Ma)						% conc
	f206 (%)	U	2s	Th	2s	Pb	2s	Th/U	206Pb/ 204Pb	207Pb/ 206Pb	2s	207Pb/ 235U	2s	206Pb/ 238U	2s	Rho	207Pb/ 206Pb	2s	207Pb /235U	2s	206Pb /238U	2s	
BC.33-1R	0.10	449	10	734	17	424	12	1.63	18950	0.1593	0.0039	6.120	0.160	0.2641	0.0074	0.57	2486	22	1508	38	1994	22	61
BC.33-2C	0.29	122	8	118	6	127	9	0.96	6540	0.1490	0.0041	7.990	0.240	0.3540	0.0100	0.56	2370	27	1940	49	2217	27	82
BC.33-3C	0.14	269	9	74	2	183	7	0.28	13650	0.1453	0.0031	7.010	0.190	0.3168	0.0088	0.75	2323	22	1761	43	2110	24	76
BC.33-3R	0.22	113	3	117	3	137	5	1.04	8635	0.1501	0.0035	10.580	0.260	0.4580	0.0110	0.53	2380	24	2431	51	2477	23	102
BC.33-4C	0.05	791	25	396	7	351	11	0.50	34600	0.1319	0.0024	5.650	0.180	0.2742	0.0072	0.75	2153	19	1556	36	1903	27	72
BC.33-4R	0.08	483	14	236	6	195	8	0.49	22500	0.1376	0.0028	5.770	0.130	0.2818	0.0068	0.59	2211	21	1595	34	1940	20	72
BC.33-5C	0.12	222	7	198	6	361	16	0.89	15300	0.1530	0.0029	9.910	0.250	0.4210	0.0100	0.70	2403	19	2243	46	2412	22	93
BC.33-6C	0.09	286	20	483	29	405	30	1.69	21500	0.1500	0.0028	10.810	0.210	0.4620	0.0100	0.54	2384	17	2446	44	2502	18	103
BC.33-8C	0.15	405	22	277	13	204	14	0.68	12650	0.1309	0.0029	4.070	0.130	0.2022	0.0057	0.73	2146	22	1182	30	1631	27	55
BC.33-9C	0.07	801	24	557	36	433	34	0.70	26200	0.1318	0.0025	4.150	0.210	0.1923	0.0078	0.91	2138	21	1121	41	1592	40	52
BC.33-11C	0.07	470	18	674	17	335	13	1.43	26200	0.1481	0.0025	8.230	0.160	0.3517	0.0078	0.69	2340	16	1937	37	2256	18	83
BC.33-12C	0.18	136	5	134	4	95	3	0.99	10255	0.1516	0.0032	11.250	0.240	0.4780	0.0110	0.57	2387	19	2505	46	2532	20	105
BC.33-13C	0.09	288	11	511	17	417	18	1.77	21800	0.1462	0.0024	10.450	0.230	0.4553	0.0089	0.64	2329	16	2420	39	2463	20	104
BC.33-14C	0.18	159	7	165	6	252	12	1.04	10250	0.1543	0.0034	9.550	0.290	0.3860	0.0110	0.70	2438	22	2110	49	2375	28	87
BC.33-15C	0.10	481	14	181	4	238	10	0.38	18100	0.1339	0.0025	4.950	0.130	0.2368	0.0055	0.69	2173	19	1363	29	1807	22	63
BC.33-16C	0.09	427	15	78	3	138	6	0.18	19750	0.1396	0.0027	6.150	0.210	0.2838	0.0078	0.77	2239	21	1597	39	1965	29	71
BC.33-17C	0.12	270	16	219	9	264	14	0.81	15300	0.1469	0.0027	8.280	0.170	0.3631	0.0076	0.58	2325	19	1995	36	2256	19	86
BC.33-17R	0.08	305	18	246	14	349	21	0.81	22600	0.1479	0.0024	10.650	0.200	0.4627	0.0092	0.56	2336	16	2442	40	2489	17	105
BC.33-18C	0.09	515	15	69	2	106	6	0.13	21850	0.1637	0.0032	6.690	0.150	0.2610	0.0057	0.69	2505	23	1488	29	2065	19	59
BC.33-19C	0.16	398	20	250	7	237	12	0.63	11500	0.1363	0.0030	3.880	0.110	0.1821	0.0051	0.72	2212	23	1075	28	1611	23	49
BC.33-20C	0.09	276	14	50	2	105	4	0.18	20850	0.1529	0.0029	10.760	0.250	0.4520	0.0110	0.66	2406	18	2393	48	2500	21	99
BC.33-21C	0.06	376	11	438	8	507	12	1.16	28800	0.1475	0.0023	11.140	0.190	0.4794	0.0087	0.50	2340	16	2517	38	2530	16	108
BC.33-22C	0.10	288	15	204	9	258	15	0.71	19450	0.1480	0.0027	9.440	0.200	0.4124	0.0080	0.58	2342	18	2219	36	2382	19	95
BC.33-23C	0.08	382	12	120	3	147	7	0.31	23850	0.1442	0.0024	8.770	0.180	0.3845	0.0077	0.68	2308	17	2097	35	2311	19	91
BC.33-26C	0.14	621	23	127	4	150	6	0.20	12980	0.1265	0.0025	2.740	0.110	0.1359	0.0046	0.82	2097	24	817	26	1307	31	39
BC.33-27C	0.10	228	14	388	20	420	29	1.70	18000	0.1491	0.0026	11.060	0.220	0.4718	0.0085	0.55	2345	17	2483	37	2524	19	106

Table S1 continue.

Sample-Spot	Content (mg.g-1)								Isotopic ratios								Isotopic ages (Ma)						% conc
	f206 (%)	U	2s	Th	2s	Pb	2s	Th/U	206Pb/ 204Pb	207Pb/ 206Pb	2s	207Pb/ 235U	2s	206Pb/ 238U	2s	Rho	207Pb/ 206Pb	2s	207Pb /235U	2s	206Pb /238U	2s	
BC.35-1C	0.18	159	5	94	3	60	3	0.59	10135	0.1573	0.0039	6.380	0.150	0.2840	0.0073	0.52	2451	24	1613	37	2023	21	66
BC.35-1R	0.14	154	4	77	2	74	3	0.50	13500	0.1590	0.0038	8.870	0.220	0.3844	0.0099	0.53	2472	23	2090	46	2316	22	85
BC.35-2C	0.13	151	3	68	2	67	3	0.45	14070	0.1605	0.0038	9.610	0.230	0.4060	0.0100	0.56	2491	24	2201	47	2397	22	88
BC.35-3C	0.15	208	5	124	4	89	4	0.59	12680	0.1525	0.0040	5.900	0.150	0.2723	0.0079	0.57	2394	26	1546	40	1961	22	65
BC.35-3R	0.14	115	7	65	4	72	5	0.56	13500	0.1586	0.0029	11.490	0.230	0.5036	0.0099	0.55	2459	17	2631	42	2562	19	107
BC.35-4C	0.23	78	3	79	3	72	4	1.02	8140	0.1641	0.0038	11.060	0.290	0.4660	0.0110	0.60	2520	22	2470	50	2526	23	98
BC.35-5C	0.08	263	9	216	12	185	11	0.82	22900	0.1575	0.0034	9.010	0.220	0.3930	0.0110	0.66	2444	22	2124	50	2339	21	87
BC.35-6C	0.13	243	8	15	1	22	2	0.06	13995	0.1501	0.0039	5.580	0.150	0.2537	0.0070	0.55	2373	27	1454	35	1907	24	61
BC.35-7C	0.18	128	4	56	2	75	4	0.44	10400	0.1666	0.0040	8.830	0.240	0.3690	0.0100	0.64	2546	23	2012	49	2321	25	79
BC.35-9C	0.07	242	13	269	14	302	16	1.11	25150	0.1646	0.0028	11.510	0.200	0.4815	0.0096	0.54	2521	17	2518	41	2563	17	100
BC.35-9M	0.09	192	13	162	12	196	17	0.84	20300	0.1592	0.0031	10.530	0.250	0.4430	0.0100	0.65	2504	20	2352	46	2475	22	94
BC.35-9R	0.05	349	18	325	16	391	21	0.93	39000	0.1618	0.0027	11.530	0.220	0.4870	0.0110	0.67	2487	16	2542	45	2565	17	102
BC.35-10C	0.12	170	4	77	2	76	3	0.45	15485	0.1603	0.0037	9.290	0.220	0.4030	0.0110	0.62	2478	19	2172	50	2362	22	88
BC.35-10R	0.06	305	21	137	8	167	12	0.45	31150	0.1577	0.0035	10.820	0.240	0.4740	0.0130	0.61	2458	21	2500	58	2500	21	102
BC.35-11C	0.12	152	7	118	5	132	9	0.78	15600	0.1547	0.0032	9.250	0.210	0.4150	0.0100	0.66	2416	18	2224	47	2350	21	92
BC.35-11R	0.09	198	11	181	9	219	11	0.91	21000	0.1633	0.0030	11.050	0.200	0.4650	0.0090	0.58	2499	18	2448	40	2525	16	98
BC.35-12C	0.16	201	6	244	6	134	4	1.21	11625	0.1521	0.0033	5.600	0.130	0.2517	0.0061	0.58	2397	22	1446	32	1912	19	60
BC.35-14C	0.13	152	3	80	2	75	3	0.53	14120	0.1618	0.0036	9.180	0.220	0.3930	0.0100	0.60	2493	22	2137	48	2345	22	86
BC.35-14R	0.16	162	4	111	3	80	4	0.69	12045	0.1590	0.0039	7.310	0.180	0.3176	0.0082	0.55	2466	23	1769	40	2149	23	72
BC.35-15C	0.10	155	6	62	4	81	5	0.40	18100	0.1573	0.0031	11.210	0.250	0.4820	0.0110	0.60	2455	20	2546	48	2536	21	104
BC.35-16C	0.11	290	6	178	4	128	4	0.61	17570	0.1399	0.0033	5.260	0.140	0.2511	0.0067	0.60	2264	26	1438	35	1861	22	64
BC.35-16R	0.10	156	6	94	4	98	5	0.60	18150	0.1605	0.0025	11.450	0.190	0.4876	0.0076	0.54	2462	13	2553	33	2558	16	104
BC.35-17C	0.10	487	14	234	6	103	5	0.48	17900	0.1584	0.0042	3.529	0.098	0.1555	0.0046	0.53	2459	29	929	26	1530	22	38
BC.35-18C	0.10	515	18	299	8	135	6	0.58	18600	0.1413	0.0038	3.215	0.097	0.1561	0.0047	0.59	2269	29	931	26	1453	23	41
BC.35-18R	0.08	484	12	96	3	98	5	0.20	24150	0.1517	0.0033	4.680	0.120	0.2121	0.0062	0.65	2381	22	1235	33	1759	22	52
BC.35-19C	0.08	268	6	115	3	94	4	0.43	23000	0.1569	0.0030	8.170	0.170	0.3472	0.0078	0.63	2441	20	1915	37	2244	19	78
BC.35-20R	0.03	552	43	320	23	328	25	0.58	60300	0.1565	0.0030	11.470	0.280	0.5010	0.0120	0.66	2415	19	2603	49	2547	22	108
BC.35-21C	0.14	148	4	55	2	57	3	0.37	13435	0.1545	0.0036	8.170	0.190	0.3544	0.0086	0.55	2428	24	1945	41	2248	21	80
BC.35-22C	0.08	268	8	271	6	243	7	1.01	22550	0.1532	0.0032	7.540	0.200	0.3287	0.0088	0.71	2409	22	1827	43	2172	24	76
BC.35-22R	0.11	180	6	85	3	154	8	0.47	17800	0.1664	0.0031	10.090	0.210	0.4052	0.0090	0.60	2550	19	2184	41	2435	19	86
BC.35-24C	0.08	184	8	195	8	213	9	1.06	22250	0.1602	0.0025	11.640	0.180	0.4949	0.0088	0.52	2467	16	2587	37	2569	14	105
BC.35-25C	0.02	630	38	684	35	755	38	1.09	75400	0.1590	0.0026	11.400	0.200	0.4833	0.0093	0.62	2457	15	2547	40	2559	16	104
BC.35-27C	0.07	221	11	194	11	234	13	0.88	26700	0.1607	0.0026	11.870	0.200	0.4915	0.0088	0.53	2489	17	2582	38	2589	15	104
BC.35-27R	0.13	265	7	159	5	76	3	0.60	14195	0.1445	0.0031	4.660	0.110	0.2186	0.0053	0.63	2293	21	1275	27	1760	20	56
BC.35-29C	0.05	338	21	217	14	239	15	0.64	40450	0.1582	0.0023	11.560	0.180	0.4863	0.0080	0.58	2449	14	2550	35	2568	15	104
BC.35-30C	0.06	262	14	118	6	144	8	0.45	31300	0.1593	0.0022	11.190	0.180	0.4715	0.0086	0.70	2467	13	2482	38	2535	15	101
BC.35-30R	0.36	63	3	9	1	26	2	0.14	5150	0.1533	0.0051	7.330	0.250	0.3190	0.0100	0.53	2417	29	1772	49	2144	30	73
BC.35-31C	0.09	268	6	98	3	78	3	0.36	21760	0.1512	0.0027	7.250	0.140	0.3192	0.0065	0.58	2391	18	1781	32	2139	17	74
BC.35-31R	0.15	140	4	62	3	49	3	0.44	12490	0.1591	0.0033	8.280	0.180	0.3499	0.0080	0.58	2457	19	1929	38	2257	20	79
BC.35-32C	0.06	252	14	261	16	295	18	1.04	30000	0.1569	0.0024	11.240	0.160	0.4842	0.0079	0.53	2438	16	2537	34	2537	13	104
BC.35-33R	0.56	60	1	4	0	12	1	0.07	3350	0.1456	0.0055	4.680	0.180	0.2227	0.0075	0.55	2339	38	1286	39	1756	32	55
BC.35-34C	0.09	192	5	88	2	101	4	0.46	19950	0.1566	0.0030	9.610	0.190	0.4134	0.0092	0.61	2439	18	2221	42	2402	18	91
BC.35-39C	0.10	166	6	78	4	97	5	0.47	18250	0.1581	0.0028	10.400	0.200	0.4365	0.0089	0.61	2458	19	2326	39	2467	17	95
BC.35-40C	0.08	218	6	76	2	126	5	0.35	23400	0.1500	0.0021	9.600	0.170	0.4248	0.0085	0.68	2362	15	2283	38	2398	16	97
BC.35-48R	0.12	238	7	74	2	100	3	0.31	15885	0.1625	0.0032	6.840	0.160	0.2821	0.0068	0.64	2498	21	1594	34	2082	20	64
BC.35-50C	0.07	384	8	144	4	117	4	0.37	28650	0.1498	0.0025	6.750	0.130	0.2972	0.0063	0.67	2353	17	1671	31	2072	18	71
BC.35-53C	0.05	610	16	315	6	203	8	0.52	39800	0.1436	0.0023	5.910	0.130	0.2708	0.0066	0.75	2291	16	1539	34	1966	19	67
BC.35-53R	0.07	429	9	182	4	120	5	0.42	25250	0.1373	0.0025	5.011	0.098	0.2445	0.0054	0.65	2194	18	1406	28	1822	16	64
BC.35-54C	0.07	249	10	217	7	268	13	0.87	28450	0.1610	0.0022	11.490	0.210	0.4761	0.0095	0.74	2480	12	2505	40	2563	17	101

Table S2. Whole-rock geochemistry (major in wt. % (anhydrous calculated oxide) and trace in ppm) concentrations for the TTG gneisses and high-K granitoids from the CBGGT.

Sample	BC.16	BC.19	BC.41	BC.45	BC.60	BC.61
Locality	Baragaon	Mauranipur	Mauranipur	Mauranipur	Charkhari	Charkhari
SiO_2	73.734	68.669	65.521	68.816	72.817	64.842
TiO_2	0.161	0.476	0.558	0.513	0.256	0.549
Al_2O_3	14.534	15.368	16.358	15.617	14.675	15.303
Fe_2O_3	0.473	1.055	1.343	1.007	0.634	1.591
FeO	0.947	2.636	3.356	2.518	1.268	3.980
MnO	0.025	0.076	0.077	0.080	0.033	0.104
MgO	0.435	1.491	1.687	1.437	0.505	2.426
CaO	1.850	3.264	3.678	3.178	2.336	4.740
Na_2O	4.740	5.079	5.577	5.253	4.308	3.739
K_2O	3.043	1.683	1.546	1.346	3.084	2.557
P_2O_5	0.057	0.205	0.301	0.232	0.083	0.166
Total	100	100	100	100	100	100
LOI	0.62	0.73	0.74	0.66	0.62	0.7
Ba	349.957	197.576	127.099	92.201	525.393	198.959
Rb	67.878	141.98	116.018	152.671	106.929	186.012
Sr	321.981	435.786	452.501	396.23	133.208	76.352
Cr	13.254	19.048	12.659	11.813	3.332	76.352
Co	22.245	15.601	14.204	12.998	15.171	13.656
Ni	4.461	11.709	9.771	9.931	1.732	9.94
Cs	5.559	13.908	16.86	17.355	3.029	9.813
Cu	53.153	4.561	8.824	18.291	0.885	10.142
Hf	3.841	5.098	4.733	4.693	4.842	11.344
Nb	6.565	12.706	13.931	14.802	7.603	12.634
Pb	22.739	16.935	16.032	23.288	26.639	31.904
Sb	0.078	0.05	0.057	0.045	0.02	17.026
Sc	1.367	6.645	8.349	6.307	1.656	0.029
Ta	1.391	2.83	2.818	2.495	1.256	13.994
Th	10.722	15.644	14.589	16.121	14.7	2.721
U	2.677	3.653	4.024	7.51	3.051	22.458
V	13.37	52.28	64.738	47.631	10.36	4.614
Y	7.082	31.684	41.306	35.127	5.179	86.263
Zn	24.653	50.778	43.149	54.43	34.314	90.42
Zr	128.225	191.909	177.717	176.641	185.726	105.007
Mo	0.152	0.452	0.406	0.445	0.145	480.102
Sn	3.282	10.108	12.275	5.902	3.178	0.22
La	20.689	46.605	47.613	50.296	35.176	11.286
Ce	31.356	88.464	94.645	99.041	54.709	61.815
Pr	4.055	9.434	10.44	11.231	4.737	127.781
Nd	14.596	35.699	40.604	45.192	14.969	14.287
Sm	2.554	6.596	7.848	9.515	2.037	57.843
Eu	0.592	1.411	1.661	1.694	0.627	12.637
Gd	1.966	5.702	7.046	8.01	1.474	2.239
Tb	0.273	0.929	1.189	1.322	0.181	12.539
Dy	1.46	5.83	7.422	7.733	0.982	2.368
Ho	0.252	1.088	1.425	1.328	0.177	16.045
Er	0.748	3.433	4.436	3.62	0.566	3.239
Tm	0.117	0.545	0.702	0.5	0.083	10.352
Yb	0.839	3.813	4.46	2.984	0.581	1.634
Lu	0.129	0.553	0.608	0.388	0.081	10.795
ΣREE	78.166	204.272	222.677	235.121	115.398	1.572
$(La/Yb)_{CN}$	16.751	8.304	7.252	11.450	41.129	319.101
$(La/Lu)_{CN}$	16.647	8.748	8.128	13.455	45.0763	3.889
$(La/Sm)_{CN}$	5.059	4.413	3.788	3.301	10.783	4.081
$(Gd/Yb)_{CN}$	1.895	1.230	1.278	2.171	2.053	3.054
Nb/Nb*	0.229	0.370	0.447	0.480	0.1688	0.939
Ta/Ta*	0.846	1.437	1.572	1.408	0.485	0.755
Ti/Ti*	0.291	0.286	0.272	0.265	0.485	1.120
Eu/Eu*	0.779	0.688	0.670	0.578	1.057	0.152
Gd/Er	2.629	1.660	1.588	2.212	2.604	0.538
Sr/Y	45.464	13.754	10.955	11.279	25.720	1.211
Nb/Th	0.612	0.812	0.955	0.918	0.517	0.844
La/Yb	24.659	12.222	10.676	16.855	60.543	1.420
Ab	40.112	42.974	47.192	44.449	36.456	5.726
Or	17.979	9.944	9.135	7.955	18.228	31.646
An	8.8067	14.165	15.032	14.253	11.048	15.113
Ba+Sr	671.938	633.362	579.6	488.431	658.601	17.415
K_2O/Na_2O	0.642	0.332	0.277	0.256	0.715	275.311
Mg#	36.066	42.561	39.723	42.796	32.902	0.684
2A/CNK	2.0110	1.908	1.866	1.967	2.00	44.415
ANK	1.3104	1.510	1.509	1.546	1.408	1.745
$FeO_t/(FeO_t+MgO)$	0.7596	0.706	0.730	0.705	0.785	1.715
ASI	1.0150	0.984	0.973	1.019	1.014	0.690

Table S2 continue.

Sample	BC.27	BC.31	BC.50	BC.23	BC.33	BC.35
Locality	Babina	Babina	Kuraicha	Babina	Baghora	Jhansi
SiO_2	66.478	74.377	73.447	78.331	75.382	72.572
TiO_2	0.662	0.242	0.185	0.297	0.157	0.873
Al_2O_3	15.572	13.720	14.533	9.768	12.996	11.337
Fe_2O_3	1.579	0.959	0.539	0.939	0.463	1.631
FeO	3.947	1.919	1.078	1.878	0.927	3.262
MnO	0.085	0.049	0.034	0.387	0.020	0.090
MgO	1.269	0.463	0.853	0.900	0.303	3.004
CaO	4.777	2.629	1.330	3.492	0.615	1.624
Na_2O	4.112	4.623	4.428	2.166	3.160	2.821
K_2O	1.259	0.936	3.483	1.741	5.947	2.689
P_2O_5	0.259	0.079	0.092	0.096	0.025	0.094
Total	100	100	100	100	100	100
LOI	0.57	0.59	1.08	1.08	0.83	0.78
Ba	143.464	106.234	457.631	517.712	235.124	761.056
Rb	43.803	78.382	95.89	72.792	230.157	102.964
Sr	193.694	126.211	194.697	424.902	32.547	382.666
Cr	193.694	126.211	194.697	424.902	32.547	382.666
Co	9.932	2.004	6.453	9.865	1.831	71.864
Ni	13.911	10.54	10.697	16.751	17.849	18.631
Cs	6.554	1.033	3.958	5.483	0.451	16.148
Cu	5.902	3.526	2.703	0.319	0.843	4.385
Hf	35.783	1.74	12.594	1.653	2.099	0.924
Nb	5.15	5.136	4.563	3.445	5.654	4.262
Pb	10.677	9.205	8.068	8.09	9.959	8.082
Sb	7.412	12.753	28.563	222.531	30.594	20.043
Sc	0.097	0.036	0.021	0.045	0.016	0.09
Ta	7.415	3.101	1.158	3.642	0.567	11.982
Th	0.981	1.525	0.977	1.164	1.274	1.174
U	1.631	4.597	19.013	18.602	44.271	14.455
V	0.726	1.953	3.926	6.146	19.98	4.842
Y	52.782	12.582	17.803	50.456	6.039	89.809
Zn	15.066	11.708	8.845	16.423	13.438	18.139
Zr	91.23	56.164	24.066	197.803	16.001	67.943
Mo	198.108	192.386	155.434	111.811	155.209	146.462
Sn	0.137	0.28	0.902	0.091	0.933	0.464
La	1.906	3.191	0.979	2.257	1.719	2.258
Ce	19.825	25.289	37.844	35.427	48.814	33.025
Pr	46.065	52.286	65.812	66.415	53.333	63.016
Nd	5.452	5.564	6.676	6.893	10.04	6.837
Sm	22.024	20.473	22.927	24.79	33.598	25.921
Eu	4.306	3.439	3.483	4.179	5.203	4.824
Gd	1.268	0.857	0.615	0.993	0.422	1.191
Tb	3.747	2.835	2.5	3.497	3.675	4.028
Dy	0.58	0.409	0.328	0.52	0.495	0.622
Ho	3.223	2.37	1.702	3.029	2.664	3.652
Er	0.556	0.413	0.304	0.57	0.483	0.672
Tm	1.587	1.209	0.942	1.83	1.553	2.022
Yb	0.222	0.177	0.144	0.294	0.258	0.298
Lu	1.37	1.206	0.972	1.997	1.808	1.971
ΣREE	0.201	0.175	0.14	0.307	0.285	0.281
$(La/Yb)_{CN}$	107.203	114.332	142.687	147.712	159.967	144.708
$(La/Lu)_{CN}$	9.830	14.244	26.449	12.051	18.341	11.382
$(La/Sm)_{CN}$	10.237	14.999	28.058	11.977	17.778	12.199
$(Gd/Yb)_{CN}$	2.875	4.592	6.785	5.293	5.858	4.275
Nb/Nb*	2.212	1.902	2.081	1.416	1.644	1.653
Ta/Ta*	0.606	0.496	0.188	0.180	0.266	0.144
Ti/Ti*	0.969	1.430	0.396	0.451	0.593	0.364
Eu/Eu*	0.562	0.290	0.304	0.288	0.266	0.727
Gd/Er	0.944	0.816	0.608	0.773	0.280	0.804
Sr/Y	2.361	2.344	2.653	1.910	2.366	1.992
Nb/Th	12.856	10.779	22.012	25.872	2.422	21.096
La/Yb	6.546	2.002	0.424	0.435	0.225	0.559
Ab	14.470	20.969	38.934	17.740	26.998	16.755
Or	34.794	39.126	37.467	18.330	26.744	23.875
An	7.444	5.536	20.586	10.289	35.149	15.895
Ba+Sr	20.308	12.524	6.003	11.787	2.891	7.440
K_2O/Na_2O	337.158	232.445	652.328	942.614	267.671	1143.722
Mg#	0.306	0.202	0.786	0.803	1.881	0.953
2A/CNK	29.658	22.889	49.318	37.093	28.650	53.095
ANK	1.852	2.047	2.157	1.655	2.037	2.158
$FeO_t/(FeO_t+MgO)$	1.915	1.591	1.314	1.793	1.117	1.501
ASI	0.808	0.857	0.646	0.751	0.816	0.611

$Nb/Nb^* = 2*Nb_{PM} / (Ba+La)_{PM}$; $Ta/Ta^* = 2*Ta_{PM} / (Ba+La)_{PM}$
$Ti/Ti^* = Ti_{PM} / ((EU+Y)/2)_{PM}$; $Eu/Eu^* = 2*Eu_{PM} / (Sm+Gd)_{PM}$
$Mg\# = 100 \times (Mg^{2+} / (Mg^{2+} + Fe^{2+}))$
$_{PM}$= Primitive mantle normalized value (taken from McDonough and Sun, 1995),
$_{CN}$= Chondrite-normalized (taken from McDonough and Sun, 1995).

Table S3. Compilation of published ages (Ma) of the plutonic and volcanic rocks from the BC, and comparison with present results.

Sample No.	Locality	Lithology	Formation age	Inherited/ xenocrystic age	Metamorphic age	Method	Reference (s)
			Paleoarchean TTG gneises				
LB13	Babina	TTG gneiss	3440 ± 3	3589 ± 8		LA-ICP-MS (zr)	Saha et al. (2016)
DUR13	Babina	TTG gneiss	3220 ± 79	3368 ± 30		LA-ICP-MS (zr)	Saha et al. (2016)
PN1301B	Babina	TTG gneiss	3397 ± 8	3532 ± 7		SHRIMP (zr)	Nasipuri et al. (2019)
SD1305	Babina	TTG gneiss	3390 ± 16	3409 ± 8		SHRIMP (zr)	Nasipuri et al. (2019)
BK-7	Kuraicha	TTG gneiss	3551 ± 6			LA-ICP-MS (zr)	Kaur et al. (2014)
BM-369	Kuraicha	TTG gneiss	3297 ± 8			Ion microprobe (zr)	Mondal et al. (2002)
BC.16	Baragaon	TTG gneiss	3410 ± 9		3157 ± 13	LA-ICP-MS (zr)	This study
BC.19	Roni	TTG gneiss	3343 ± 85		3097 ± 12 2643 ± 11	LA-ICP-MS (zr)	This study
BC.41	Roni	TTG gneiss	3391 ± 39	3425 ± 16	3203 ± 18	LA-ICP-MS (zr)	This study
BC.45	Roni	TTG gneiss	3364 ± 10	3516 ± 11	3232 ± 12 3318 ± 13	LA-ICP-MS (zr)	This study
2BK-32	Roni	TTG gneiss	3394 ± 9			LA-ICP-MS (zr)	Kaur et al. (2016)
BETTG 107	Mahoba	TTG gneiss	3301 ± 2	3327 ± 5		SIMS (zr)	Joshi et al. (2017)
BM/G-12	Mahoba	TTG gneiss	3270 ± 3			Ion microprobe (zr)	Mondal et al. (2002)
2BK-36	Charkhari	TTG gneiss	3285 ± 7		3185 ± 8	LA-ICP-MS (zr)	Kaur et al. (2016)
BC.60	Charkhari	TTG gneiss	3278 ± 20	3295 ± 10		LA-ICP-MS (zr)	This study
BC.61	Charkhari	TTG gneiss	3346 ± 10		3299 ± 10	LA-ICP-MS (zr)	This study
BM/G-9	Mahoba	Metabasite	3249 ± 5			Ion microprobe (zr)	Mondal et al. (2002)
2BK-48	Rungaon	TTG gneiss	3205 ± 12	3530 ± 10 3330 ± 16	2550	LA-ICP-MS (zr)	Kaur et al. (2016)
			Neoarchean TTG gneises				
BC.27	Babina	TTG gneiss	2669 ± 11			LA-ICP-MS (zr)	This study
BC-04	Babina	TTG gneiss	2669 ± 7	2804 ± 38		LA-ICP-MS (zr)	Verma et al. (2016)
BC.31	Babina	TTG gneiss	2706 ± 11	2975 ± 12		LA-ICP-MS (zr)	This study
MB-245	Babina	Granodiorite	2703 ± 3	2917 ± 25 2818 ± 23		Ion microprobe (zr)	Mondal et al. (1998)
MB-110	Baghora	Granodiorite	2697 ± 3			Ion microprobe (zr)	Mondal et al. (2002)
WS2	Babina	White schist			2785 ± 49	LA-ICP-MS (zr)	Saha et al. (2011)
WS5	Babina	White schist	2733 ± 30			LA-ICP-MS (zr)	Saha et al. (2011)
BC.50	Kuraicha	TTG gneiss	2712 ± 16	3393 ± 17 3280 ± 15		LA-ICP-MS (zr)	This study
			Greenstone sequences				
	Babina	Mafic-ultamafic	3435 ± 161			ID-TIMS (WR-Sm-Nd)	Singh et al. (2019a)
	Mauranipur	Mafic-ultamafic	3435 ± 161			ID-TIMS (WR-Sm-Nd)	Singh et al. (2019a)
M-5/2	Baragaon	Felsic volcanics	2810 ± 13	3242 ± 65		SHRIMP (zr)	Slabunov and Singh, (2018)
M 8/2	Baragaon	Basalts	2687 ± 11			SHRIMP (zr)	Slabunov and Singh, (2018)
M- 18-1	Baragaon	Felsic volcanics	2557 ± 33	2864 ± 46		SHRIMP (zr)	Slabunov and Singh, (2018)
Ba-17/4	Babina	Felsic volcanics	2542 ± 17			SHRIMP (zr)	Singh and Slubanov, (2015)
MB-518	Bansi	Rhyolite	2517 ± 7			Ion microprobe (zr)	Mondal et al. (2002)
La7-1	Girar	Quartzite	3432 ± 70			SHRIMP (zr)	Slabunov et al. (2017)
			High-K granitoids				
BETG 119	Karera	Sanukitoids	2563 ± 2			SIMS (zr)	Joshi et al. (2017)
BC.35	Jhansi	Sanukitoids	2568 ± 12		2487 ± 16	LA-ICP-MS (zr)	This study
BETG 120	Raksa	Sanukitoids	2559 ± 7			SIMS (zr)	Joshi et al. (2017)
BCTG 129	Orccha	Sanukitoids	2560 ± 7	2914 ± 8 2842 ± 3		SIMS (zr)	Joshi et al. (2017)
BC-16-18	Sakrar	Sanukitoids	2577 ± 16	2644 ± 25 2619 ± 24		LA-ICP-MS (zr)	Singh et al. (2019b)
BSTM 104	Khajuraho	Sanukitoids	2544 ± 6			SIMS (zr)	Joshi et al. (2017)
BM-567	Karera	Granodiorite	2561 ± 6			Ion microprobe (zr)	Mondal et al. (2002)
BK-12	Dinara	Granodiorite	2561 ± 11			LA-ICP-MS (zr)	Kaur et al. (2016)

BC.23	Babina	Granodiorite	2556 ± 23			LA-ICP-MS (zr)	This study
2BK-30	Bedaura	Granodiorite	2551 ± 7			LA-ICP-MS (zr)	Kaur et al. (2016)
BK-19	Bilbai	Granodiorite	2566 ± 11			LA-ICP-MS (zr)	Kaur et al. (2016)
2BK-53	Panchora	Granodiorite	2546 ± 6	3119 ± 18 2828 ± 15 2647 ± 15	2002 ± 42	LA-ICP-MS (zr)	Kaur et al. (2016)
BLHM 118	Raksa	Monzogranite	2557 ± 19	2787 ± 3		SIMS (zr)	Joshi et al. (2017)
BLHM 127	Garhmau	Monzogranite	2569 ± 19			SIMS (zr)	Joshi et al. (2017)
BLHM 128	Garhmau	Monzogranite	2571 ± 16			SIMS (zr)	Joshi et al. (2017)
BK-2	Jhansi	Granites	2529 ± 8			LA-ICP-MS (zr)	Kaur et al. (2016)
BK-3	Jhansi	Granites	2566 ± 14			LA-ICP-MS (zr)	Kaur et al. (2016)
SK-27	Dhala	Granites	2553 ± 6			SHRIMP (zr)	Pati et al. (2010)
MCB-10	Dhala	Granites	2563 ± 7			SHRIMP (zr)	Pati et al. (2010)
MB-549	Datia	Biotite granite	2515 ± 5			Ion microprobe (zr)	Mondal et al. (2002)
BK-1	Kalothara	Granites	2583 ± 10			LA-ICP-MS (zr)	Kaur et al. (2016)
2BK-25	Bharthari	Leucogranites	2543 ± 10			LA-ICP-MS (zr)	Kaur et al. (2016)
2BK-26	Vijaipur	Leucogranites	2537 ± 8		2134 ± 19	LA-ICP-MS (zr)	Kaur et al. (2016)
2BK-57	Utwaha	Leucogranites	2554 ± 5			LA-ICP-MS (zr)	Kaur et al. (2016)
BLEM 124	Babina	Monzogranite	2546 ± 3			SIMS (zr)	Joshi et al. (2017)
BLEM 109	Talbehat	Monzogranite	2544 ± 3			SIMS (zr)	Joshi et al. (2017)
BMG 130	Bijoli	Granites	2562 ± 6			SIMS (zr)	Joshi et al. (2017)
BC-01	Bijoli	Pink granites	2531 ± 21			LA-ICP-MS (zr)	Verma et al. (2016)
BC-02	Bijoli	Pink granites	2516 ± 38			LA-ICP-MS (zr)	Verma et al. (2016)
BC-03	Babina	Pink granites	2514 ± 13			LA-ICP-MS (zr)	Verma et al. (2016)
2BK-29	Baghora	Granites	2525 ± 25			LA-ICP-MS (zr)	Kaur et al. (2016)
BC.33	Baghora	Anatectic granites	2557 ± 16			LA-ICP-MS (zr)	This study
BK-13	Dinara	Granites	2563 ± 10			LA-ICP-MS (zr)	Kaur et al. (2016)